OBSERVATIONS, FORECAST, AND MODELING OF 0.5-200 MIN INFRAGRAVITY OSCILLATIONS IN HALE'IWA HARBOR REGION, HAWAI'I

A DISSERTATION SUBMITTED TO THE
GRADUATE DIVISION OF THE
UNIVERSITY OF HAWAIʻI AT MĀNOA
IN PARTIAL FULFILLMENT OF THE
REQUIREMENTS FOR THE DEGREE OF

DOCTOR OF PHILOSOPHY

IN

OCEANOGRAPHY

NOVEMBER 2016

By

Assaf Azouri

Dissertation Committee:

Douglas S. Luther, Chairperson
Mark A. Merrifield
Brian Powell
Jérome Aucan
Kwok Fai Cheung

We certify that we have read this dissertation and that, in our opinion, it is satisfactory in scope and quality as a dissertation for the degree of Doctor of Philosophy in Oceanography.

DISSERTATION
COMMITTEE

Chairperson

I would like to dedicate this work to my wife, Santa, for the tremendous amount of love, patience, and belief in me, providing me the motivation to continue my research work (and occasionally surf), and sacrificing her freedom by taking care of our two kids to allow me to work. My kids, Dante and Niko, for providing me a strong motivation each day to become a better person, and reminding me that all is about loving what you do, having fun, and being happy.
To my mother, Camille, and my brother, Olivier, for believing in me and supporting the choice of my career path.

Finally, to my dad, Ezra Azouri, for showing me how fun and interesting science can be. Your endless love and care are the reason I decided to become a scientist and are standing here today.

ACKNOWLEDGMENTS

I would first like to express special thanks to my advisor, Prof. Doug Luther, for the patience and dedication while guiding me throughout this long journey. The many hours of discussions with you, and insights that followed after each meeting, were invaluable for the growth and success of this research work. Your passion to the field and high professional standards have given me the motivation and confidence that I need to continue to grow and become a good scientist. Thank you for everything!

Many thanks go to my committee members: Prof. Mark Merrifield, for always being available to answer my coding and research questions, as well as providing historical datasets, and instrumentation and manpower for my deployments. Dr. Jérome Aucan, for providing deep-water datasets, helping with field work, and guiding me with my analyses. Prof. Brian Powell, for his valuable tips and comments about my work, especially in regards to numerical modeling. Prof. Kwok Fai Cheung, for reminding me about the importance of numerical modeling, many insightful discussions, and providing us numerical model outputs for our harbor surge forecast.

Special thanks to Dr. Volker Roeber, for providing and allowing me to use his numerical model, BOSZ. Volker has taught me how to prepare bathymetry datasets for modeling, using his numerical model, and understanding many important aspects of his model. Without you, the critical piece of numerical modeling study in this dissertation work would not have been possible.

Many thanks go to Prof. Glenn Carter for allowing me to run the numerical model on Tongariro, his computer cluster, in order to generate all the results of chapter 4. Thank you Tongariro for crunching all the numbers, and to Derek Young for the help and troubleshooting during the numerical modeling runs. Many thanks go to Prof. Eric Firing for being such a great programming mentor. Your assistance and guidance in accelerating my processing codes using Python are invaluable.

I would like to thank Prof. Janet Becker for bringing in her theoretical point of view, helping me better understand the fundamentals of infragravity waves, and providing me historical datasets. Thanks to Dr. Christine Pequignet, for sharing your expertise and knowledge of infragravity waves, as well as providing me various references of infragravity waves. Thanks to Dr. Yoshiki Yamazaki for running NEOWAVE tsunami model and providing me high resolution solutions in my North Shore and harbor domains. Thanks to Prof. Paul Wessel for teaching and assisting me in generating maps using GMT, and manipulate datasets using UNIX. Many thanks to Dr. Martin Guiles for sharing with me your understanding of ocean waves, and creating and maintaining the harbor surge forecast on PacIOOS website.

Special thanks go to Carly Quisenberry, Chris Kontoes, and Christina Comfort, for countless hours assisting me planning, preparing, and executing my deployments and recoveries in Hale'iwa Harbor and along the North Shore coast. Chris and Carly also assisted me during post deployment recoveries processing. Thanks to Joseph Gilmore and Gordon Walker, who also assisted during the execution of the deployments and recoveries.

Many thanks go to NOAA, JIMAR, PacIOOS, and NSF, for providing me the financial support throughout my entire degree. You have provided me and my family the financial security that we needed during this research work. In particular, I would like to thank Chris Ostrander, Melissa Iwamoto, and Fiona Langenberger from the PacIOOS family for all the support.

Many thanks to all the ocean office staff, especially Kristin Momohara for assisting me with meeting all of the degree requirements on time, and for being a great friend; for Catalpa Kong for always being there for a fun conversation and having snacks to help survive the rest of the day. Also thanks for my office mate Seth Travis for all the great discussions we had, including comments and ideas related to my research work, as well as Saulo Soares and many other friends. Finally, thanks to my favorite band, Megadeth, for making the writing process of the dissertation much more enjoyable.

ABSTRACT

The scientific objective of this study is to identify the dominant phenomena, their generation mechanisms, and the corresponding energy pathways that result in 0.5-200 min infragravity (IG) wave energy in Hale'iwa Harbor, North Shore of O'ahu, Hawai'i. We meet these objectives with spectral analysis that is applied to sea level and currents data obtained from historical and recent observations, and high-resolution numerical modeling, inside the harbor and at the coast. Validation and calibration of the model results with harbor and coastal observations have confirmed many of our observational results. Furthermore, analysis of model output from cross-shore and alongshore arrays at several coastal sites has improved our understanding of the generation mechanisms and dynamics of IG waves at the coast; and, detailed maps of energy, coherence amplitude, and coherence phase at the coast and inside the harbor, revealed unique standing wave patterns at several IG periods bands.

Interestingly, the greatest observed variance was found to be in different period bands for sea level and currents; $\sim$5-15 min for sea level, and $\sim$3-8 min for currents. When SS forcing is non existent, we observe a suite of coastal and harbor modes that could potentially be forced in different ways (e.g., wind, internal waves). We find that the coastal modes range between 1$\sim$23 min (in agreement with other model studies in that region), and the harbor modes between $\sim$40 sec and $\sim$6 min. The model results further support observations indicating that the harbor's gravest mode potentially oscillates at $\sim$5-6 min.

As the SS forcing increases to high levels, our anticipation was that the energy of the modes would grow linearly, as was observed in similar studies by others. Surprisingly, we find that the energetic spectra is predominantly non-modal with uniform levels across a wide band of IG periods, suggesting that other processes (non-modal) are at least as important. The observed high spectral levels extend from periods of minutes to several hours, corresponding to scales much longer than the gravest coastal mode of 23 min. The overwhelming amount of energy hitting the North Shore coast and the irregularities of the bottom and the coastline, are likely strong factors in this observed response.

At periods shorter than ∼30 min under strong SS forcing, we obtained abundant evidence of bound IG waves offshore of the SS break point, and dominance of free IG waves within the surf zone. The free IG wave field appears to be mostly composed of leaky waves, but at one site we also found evidence of short-period (∼45-60 sec) low-mode edge waves. Inside the harbor, the IG wave field is free, and could be forced by the leaky or edge waves from the coast. Observational evidence several kilometers from the harbor suggests that a SS-driven setup mechanism drives energetic coastal oscillations at periods from minutes to hours. Modeling results much closer to harbor suggest that such a mechanism could potentially force ($T<20$ min) oscillations inside the harbor.

Overall, the scientific portion of this study suggests that inside the harbor, coastal oscillations may be as important as harbor oscillations. This leads us to the conclusion that, at least for harbors with a similar environment as the one in Hale'iwa Harbor and the North Shore, understanding the dynamics of energetic harbor oscillations requires understanding of the dynamics at the coast.

For the practical objective of this study, we developed a forecasting system of energetic 0.5-40 min IG oscillations that result in large sea level amplitudes and strong currents in Hale'iwa Harbor. Observations of sea level offshore of the harbor and sea level and currents inside the harbor are used to determine a statistically-optimal relationship between offshore SS forcing and harbor IG response. Using this we establish transfer functions relating the offshore sea level with the harbor currents. Given an input of sea level forecast at an offshore site, the transfer functions are used to generate a forecast of surge currents inside the harbor. This output is expressed in terms of an index that, compared against threshold levels, provides a sense of the danger levels inside the harbor given a particular forecast of offshore forcing conditions. The threshold levels were determined using two exceptionally strong SS forcing events during which we documented the aftermath inside the harbor. These SS forcing events serve as calibration of our forecast and provide us a good sense of the response inside the harbor given particular offshore SS forcing conditions.

TABLE OF CONTENTS

Acknowledgments . . . . **v**

Abstract . . . . **vii**

List of Tables . . . . **xiv**

List of Figures . . . . **xv**

List of Abbreviations . . . . **xxii**

List of Symbols . . . . **xxiv**

1 Introduction **1**

2 Infragravity Oscillations in Hale'iwa Harbor Region, Hawai'i. Part I: Observations **7**

2.1 Introduction 7

2.2 Study area and datasets 13

2.3 Analyses leading to hypotheses 15

2.3.1 Response of Hale'iwa Harbor Region to offshore forcing 15

2.3.2 Hypotheses: Pathways of IG wave energy into Hale'iwa Harbor 21

2.3.2.1 None-to-weak Sea/Swell (SS) Forcing 22

2.3.2.2 Moderate Sea/Swell Forcing 23

2.3.2.3 Strong Sea/Swell Forcing 24

2.4 Methods 25

2.4.1 Excitation of Linear Coastal or Harbor Modes (Hypotheses A1, B1, C1, A2, B2, & C2) 26

2.4.2 Bound Wave Impacts; Generation of Leaky and Edge Waves (Hypotheses B3, C3, C4, & C5) 28

2.4.3 The Role of Time-Varying, SS-Driven "Setup" (Hypotheses C6 and D1) 30

2.4.4 Large-Scale Modes of the Hawaiian Islands (Hypothesis D2) 32

2.4.5 Free IG energy from remote sources (Hypothesis A0) 32

2.5 Analysis and results 35

2.5.1 Excitation of Linear Coastal or Harbor Modes (Hypotheses A1, B1, C1, A2, B2, & C2) 36

2.5.2 Bound Wave Impacts; Generation of leaky and edge waves (Hypotheses B3, C3, C4, & C5) 41

2.5.2.1 Auto- and Cross-Spectral Analysis Applied to the Mokuleia Experiment 42

2.5.2.2 Auto- and Cross-Spectral Analysis Applied to the Hale'iwa Harbor Data 48

2.5.3 SS-Forced "Setup" Variability (Hypotheses C6 and D1) 51

2.5.4 Excitation of Normal Modes of the Main Hawaiian Islands (Hypothesis D2) 55

2.5.5 Free IG Energy From Remote Sources (Hypotheses A0a, A0b) 61

2.6 Discussion 65

3 Forecast of Current-Driven Harbor Surges in Hale'iwa Harbor, Hawai'i 132

3.1 Introduction 132

3.2 Study area and datasets 134

3.3 Methods 136

3.3.1 Observations: sea level and currents 136

3.3.2 Analyses: transfer functions 137

3.3.3 Tools/Forecast 138

3.3.4 Testing/Validation 139

3.4 Analysis and results 139

3.4.1 Dominant IG bands in Hale'iwa Harbor 139

3.4.2 Searching for appropriate sea/swell parameter and generating a surge forecast 140

3.4.3 Determine SCI threshold levels 142

3.4.4 Harbor's response versus phase relationships of IG waves 143

3.5 Surge forecast and forecast validation 144

3.6 Discussion 146

4 Infragravity Oscillations in Hale'iwa Harbor Region, Hawai'i. Part II: Numerical Modeling 159

4.1 Introduction 159

4.2 Model Description 162

4.3 Methods 163

4.3.1 Sensitivity tests 163

4.3.2 Observations vs. model comparison 164

4.3.3 Hypotheses testing 164

4.3.3.1 Excitation of Linear Coastal or Harbor Modes (Hypotheses A1, B1, C1, A2, B2, & C2) 164

4.3.3.2 Bound Wave Impacts; Generation of Leaky and Edge Waves (Hypotheses B3, C3, C4, & C5) 165

4.3.3.3 The Role of Time-Varying, SS-Driven "Setup" (Hypothesis C6) 167

4.3.3.4 Large-Scale Modes of the Hawaiian Islands (Hypothesis D2) 168

4.4 Analysis and Results 168

4.4.1 Sensitivity tests 168

4.4.1.1 Model setup and input 168

4.4.1.2 Effect of varying computational time 170

4.4.1.3 Effect of artificial oscillations from the domain boundaries . 171

4.4.1.4 Sensitivity to variation of the friction coefficient 173

4.4.2 Observations vs. model vs. comparison 174

4.4.2.1 Model setup and input 174

4.4.2.2 Comparison with observations 175

4.4.3 Hypotheses testing 176

4.4.3.1 Excitation of Linear Coastal or Harbor Modes (Hypotheses A1, B1, C1, A2, B2, & C2) 177

4.4.3.2 Bound Wave Impacts; Generation of Leaky and Edge Waves (Hypotheses B3, C3, C4, & C5) 180

4.4.3.3 The Role of Time-Varying, SS-Driven "Setup" (T < 30 min; Hypothesis C6) 192

4.5 Discussion 193

5 Conclusions 249

5.1 Summary 249

5.2 Future Research 251

References 253

LIST OF TABLES

2.1 Latitude/Longitude coordinates, and site description of historical, 2011/2012, 2013/2014, and additional deployment sites. 69

2.2 Data specifications. Rows: historical, 2011/2012, 2013/2014, and additional deployments. Columns: site, instrument (Tide Gauge; AQuadopp; BUoy; SeaBird), measurement (η = sea level; p = pressure; u, v = currents), date range/s of data (mm/dd/yy), depth, sampling period, and averaging interval. 70

2.3 Average and standard deviation of the period, T, Quality-factor, Q, and e-folding decay time, τ, for spectral peaks observed inside Hale'iwa Harbor during times of no/weak-SS forcing conditions in the years 1997-2010, and 2014. 71

2.4 Summary of multiple datasets averaged to generate various figures. Columns are: forcing levels and type, site number, data time periods, total number of days, and figures. 72

4.1 Specifications of all BOSZ model runs. Columns are: Run name, SS forcing level, date of SS directional spectra, alongshore domain size (y), cross-shore domain size (x), grid resolution, friction coefficient for bathymetry, friction coefficient for topography. 197

LIST OF FIGURES

1.1 IG-PSD : sea level vs. currents - 2011/2012 datasets 4

1.2 IG-VP : sea level vs. currents - 2011/2012 datasets 5

1.3 Hale'iwa Harbor IG response - 02/22/2016 SS event 6

2.1 North Shore datasets - Hale'iwa Harbor map 73

2.2 North Shore dstasets - Coastal map 74

2.3 Main Hawaiian Islands map - historical and additional datasets 75

2.4 Energy vs. time at Waimea Buoy - 07/2011-07/2014 76

2.5 Distribution of energy from 315° at Waimea Buoy, 07/2011 - 07/2014 77

2.6 IG-PSD vs. SS forcing amplitude - Hale'iwa Harbor - historical datasets . . . 78

2.7 IG-PSD vs. SS forcing amplitude - Hale'iwa Harbor - 2013/2014 datasets . . 79

2.8 IG VP vs. SS forcing amplitude - Hale'iwa Harbor - 2013/2014 datasets . . . 80

2.9 Power spectral density of observed pressure at four locations inside harbor . 81

2.10 Spectrogram and PSD of observed harbor IG - Hale'iwa Harbor, 10 yr Jul-Aug average 82

2.11 PSD of observed pressure at four locations inside harbor 83

2.12 PSD under varying SS forcing amplitude - 2m Mokuleia - historical datasets 84

2.13 PSD under varying SS forcing amplitude - 6m Mokuleia - historical datasets 85

2.14 PSD under varying SS forcing amplitude - 12m Mokuleia - historical datasets 86

2.15 Energy pathways hypotheses - Hale'iwa Harbor 87

2.16 Coastal response of O'ahu Island to the 11/15/06 Kuril Islands tsunami. . . 88

2.17 Spectrogram of observed offshore SS - Waimea Buoy, 01/2002 89

2.18 Spectrogram of observed harbor IG - Hale'iwa Harbor, 01/2002 89

2.19 Spectrogram of observed harbor IG - Hale'iwa Harbor, 11/04/11-03/14/12 . 90

2.20 Spectrogram of observed harbor IG - Hale'iwa Harbor, 11/28/13-05/05/14 . 91

2.21 Spectrogram of observed harbor IG - Hale'iwa Harbor, 11/28/13-05/05/14 - high frequency IG band 92

2.22 Scatter plot of harbor IG sea level PSD versus offshore sea level $F_{ss,cf}$ 93

2.23 Coherence amplitude, coherence phase, amplification, and gain, for sites 1 vs. 6. 94

2.24 Coherence amplitude and phase for sites 1 vs. 6. 95

2.25 PSD of sites 1 and 6. 96

2.26 Variance preserving of sites 1 and 6. 97

2.27 Coherence amplitude, coherence phase, amplification, and gain, for sites 1 vs. 7. 98

2.28 Coherence amplitude, coherence phase, amplification, and gain, for sites 2 vs. 7. 99

2.29 Coherence amplitude, coherence phase, amplification, and gain, for sites 4 vs. 7. 100

2.30 PSD of sites 1, 2, 4, and 7. 101

2.31 Variance preserving of sites 1, 2, 4, and 7. 102

2.32 Coherence amplitude, coherence phase, amplification, and gain, for sites 6 vs. 9. 103

2.33 Scatter plots of $E_{IG,6}$ vs. $E_{IG,12}$ 104

2.34 Scatter plots of $E_{IG,2}$ vs. $E_{IG,6}$ 105

2.35 PSD of η and $\eta_{ss,env}$ at sites 8a-8c 106

2.36 Coherence analysis between $\eta_{ss,env}$ and η, at sites 8a, 8b, and 8c - weak SS . 107

2.37 Coherence analysis between $\eta_{ss,env}$ and η, at sites 8a, 8b, and 8c - weak SS . 108

2.38 Coherence analysis between $\eta_{ss,env}$ and η, sites 8a vs. 8b, 8a vs. 8c, 8b vs. 8c - weak SS 109

2.39 Coherence analysis between $\eta_{ss,env}$ and η, sites 8a vs. 8b, 8a vs. 8c, 8b vs. 8c - strong SS 110

2.40 Coherence amplitude, coherence phase, amplification, and gain, for sites 5 vs. 6. 111

2.41 Coherence amplitude, coherence phase, amplification, and gain, for sites 1 vs. 5. 112

2.42 PSD of η and $\eta_{ss,env}$ at sites 6, 5, and 1 113

2.43 Coherence analysis between $\eta_{ss,env}$ and η, at sites 6, 5, and 1 - weak SS . . . 114

2.44 Coherence analysis between $\eta_{ss,env}$ and η, at sites 6, 5, and 1 - strong SS . . 115

2.45 Wave transformation from offshore through the surf zone - Mokuleia 116

2.46 Cross-shore profiles - Mokuleia 117

2.47 Coherence analysis for η vs. η, and $\eta_{ss,env}$ vs. η, sites 6 and 5 - strong SS . . 118

2.48 Oscillation modes around the Hawaiian Islands - 16, 17, 24, 27, 34, and 42 min 119

2.49 Oscillation modes around the Hawaiian Islands - 33, 42, 52, and 75 min . . . 120

2.50 PSD at sites 1, and 13-15. No tsunami events 121

2.51 PSD at sites 1, and 13-15 during tsunami events 122

2.52 Coherence analysis - Honolulu vs Kawaihae tide gauges 123

2.53 Coherence amplitude and phase - open ocean 124

2.54 Energy vs. time for Honolulu and Kahului modes 125

2.55 Energy vs. time for Honolulu and Kahului modes - zoom in 126

2.56 Time series of deep-water offshore, coastal, and harbor H_{sig} in the 1-20 min band 127

2.57 Time series of deep-water offshore and harbor H_{sig} in the 1-20 min band . . 128

2.58 PSD and Coherence analysis - deep water sites 11 & 12 129

2.59 Projected PSDs from sites 9 to 11 - weak SS 130

2.60 Projected PSDs from sites 9 to 11 - weak SS 131

3.1 Building blocks of a surge forecast 147

3.2 Power spectral density of observed pressure at four locations inside harbor . 148

3.3 Power spectral density of observed currents at four locations inside harbor . 149

3.4 Times series of sea level and uv currents at site 1 inside Hale'wa Harbor . . . 150

3.5 Scatter of harbor infragravity vs. parameters of offshore sea/swell 151

3.6 Scatter of harbor infragravity vs. parameters of offshore sea/swell, including fitted curves 152

3.7 Mean infragravity standard deviation vs. parameters of offshore sea/swell . . 153

3.8 SCI of all tsunami events and two strongest SS events per year during 1997-2010, and one strong SS event during 2014. 154

3.9 High-pass filtered sea level time series during a large SS event and a tsunami 155

3.10 SCI versus maximum RMS of all tsunamis and two strongest sea/swell events per year during 1997-2010, and one strong SS event during 2014. 156

3.11 Hale'iwa Harbor SCI forecast 157

3.12 Surge impact in Hale’iwa Harbor - 02/22/16 SS event 158

4.1 Map of BOSZ model domains - North Shore 198

4.2 Map of BOSZ model domains - Mokuleia 199

4.3 Map of BOSZ model domains - Kaiaka Bay 200

4.4 Map of BOSZ model domains - Waialua Bay 201

4.5 Map of BOSZ model domains - Pua’ena 202

4.6 PSD of model data at site 1, using data from model runs ST2, ST3, ST4, and ST5 203

4.7 PSD of model data at site 3, using data from model runs ST2, ST3, ST4, and ST5 204

4.8 PSD of model data at site W14, using data from model runs ST2, ST3, ST4, and ST5 205

4.9 PSD of model data at site 7, using data from model runs ST2, ST3, ST4, and ST5 206

4.10 Maps of potential energy in the 1-2 min band 207

4.11 Maps of coherence phase in the 1-2 min band 208

4.12 Maps of potential energy in the 2-4 min band 209

4.13 Maps of coherence phase in the 2-4 min band 210

4.14 Maps of potential energy in the 4-8 min band 211

4.15 Maps of coherence phase in the 4-8 min band 212

4.16 Maps of potential energy in the 8-17 min band 213

4.17 Maps of coherence phase in the 8-17 min band 214

4.18 Energy map for friction sensitivity test: 1-2 min 215

4.19 Energy map for friction sensitivity test: 2-4 min 216

4.20 Energy map for friction sensitivity test: 4-8 min 217

4.21 Energy map for friction sensitivity test: 8-17 min 218

4.22 Model vs. observational PSDs - site 3 219

4.23 Model vs. observational PSDs - site 4 220

4.24 Model vs. observational PSDs - site 7 221

4.25 Model vs. observational PSDs - sites 1, 2, 4, 5, 6, 7 222

4.26 Model vs. observational coherence - sites 1 vs 2, and 1 vs 4 223

4.27 Model vs. observational coherence - sites 1 vs 5, and 1 vs 6 224

4.28 Maps of energy, coherence amplitude squared, and coherence phase, inside Hale'iwa Harbor - harbor model run 225

4.29 Model vs. observed PSDs under weak, moderate, and strong SS forcing conditions 226

4.30 Directional spectra of all SS forcing events 227

4.31 Maps of potential energy, coherence amplitude squared, and coherence phase in the 5-30 sec SS band 228

4.32 Maps of potential energy, coherence amplitude squared, and coherence phase in the 0.5-1 min band 229

4.33 Maps of potential energy, coherence amplitude squared, and coherence phase in the 1-2 min band 230

4.34 Maps of potential energy, coherence amplitude squared, and coherence phase in the 2-4 min band 231

4.35 Maps of potential energy, coherence amplitude squared, and coherence phase in the 4-8 min band 232

4.36 Maps of potential energy, coherence amplitude squared, and coherence phase in the 8-17 min band 233

4.37 Maps of potential energy, coherence amplitude squared, and coherence phase in the 0.5-1 min band - Hale'iwa Hbr. 234

4.38 Maps of potential energy, coherence amplitude squared, and coherence phase in the 1-2 min band - Hale'iwa Hbr. 235

4.39 Maps of potential energy, coherence amplitude squared, and coherence phase in the 2-4 min band - Hale'iwa Hbr. 236

4.40 Comparison of γ^2 in the 1-2 min band, using different reference points - Hale'iwa Hbr. 237

4.41 Energy vs. distance from shore - Mokuleia 238

4.42 Maps of total energy in the 5-30 sec, 0.5-1, 1-2, 2-4, 4-8, and 8-17 min bands - model run R2 239

4.43 Maps of energy flux in the 5-30 sec, 0.5-1, 1-2, 2-4, 4-8, and 8-17 min bands - model run R2 240

4.44 Maps of energy flux in the 5-30 sec, 0.5-1, 1-2, 2-4, 4-8, and 8-17 min bands - model run R2 - Hale'iwa Hbr. 241

4.45 Incoming and outgoing energy flux vs. distance from shore - Mokuleia 242

4.46 Incoming and outgoing energy flux vs. distance from shore - Pua'ena Point . 243

4.47 Frequency-wavenumber PSD - Mokuleia 244

4.48 Frequency-wavenumber PSD - Pua'ena Point 245

4.49 Cross-shore profiles - Mokuleia vs. Pua'ena 246

4.50 Coherence amplitude and coherence phase of envelope vs. sea level for for single sites at Waialua 247

4.51 Coherence amplitude and phase of envelope vs. sea level for for single sites and pairs of sites at Waialua 248

LIST OF ABBREVIATIONS

ARSHSL	Archive of Rapidly-Sampled Hawaiian Sea Level
BOSZ	Boussinesq Ocean and Surf Zone
CDIP	Coastal Data Information Program
FFT	Fast Fourier Transform
HMRG	Hawai'i Mapping Research Group
HOME	Hawai'i Ocean Mixing Experiment
IG	Infragravity
IG-PSD	Infragravity power spectral density
Lidar	Light Detection and Ranging
MLE	Maximum Likelihood Estimate
MSL	Mean sea level
NOAA	National Oceanic and Atmospheric Administration
PacIOOS	Pacific Islands Ocean Observing System
PSD	Power spectral density
PTWC	Pacific Tsunami Warning Center
RMS	Root Mean Square
SCI	Surge Current Index
SHOALS	Scanning Hydrographic Operational Airborne Lidar Survey
SIO	Scripps Institute of Oceanography
SS	Sea/Swell

ST	Sensitivity Test
USACE	United States Army Corps of Engineers
VP	Variance preserving
WW3	WAVEWATCH III

LIST OF SYMBOLS

A	Energy amplification
γ_b	Breaker height index
$\gamma_{x,y}$	Coherence amplitude between variables x and y
γ^2	Coherence amplitude squared (variance explained)
$\phi_{x,y}$	Coherence phase between variables x and y
r	Correlation coefficient
$F_{ss,cf}$	Cosine-filtered sea/swell energy flux
$P_{ss,cf}$	Cosine-filtered sea/swell power spectral density
$\vec{F}$	Energy flux vector
η_{hf}	High-frequency free surface elevation
f	Frequency
Δf	Difference frequency; Frequency bandwidth
hf	High-frequency
lf	Low-frequency
$G_{xy}(f)$	Gain (frequency domain) between input (x) and output (y) signals
g	Gravitational acceleration
$\hat{H}$	Hilbert transform
T_{IG_a}	2-4 min infragravity period band
T_{IG_b}	4-10 min infragravity period band
T_{IG_c}	10-15 min infragravity period band
T_{IG_d}	15-40 min infragravity period band
E_{IG,h_1}	Total infragravity energy at depth h_1

E_{IG,h_2}	Total infragravity energy at depth h_2
ρ	Short wave envelope
$SL_{rms,max}$	Maximum of the root-mean-square of sea level swing
SL_{max}	Maximum sea level swing
T_p	Peak period
Φ	Phase lag
C	Phase speed
C_∞	Phase speed at infinity
S_{xx}	One-sided auto-spectra for variable x
S_{xy}	One-sided cross-spectra between sites x and y
IG_a	Power spectral density of the 2-4 min infragravity period band
IG_b	Power spectral density of the 4-10 min infragravity period band
IG_c	Power spectral density of the 10-15 min infragravity period band
IG_d	Power spectral density of the 15-40 min infragravity period band
n	Manning roughness coefficient
η	Sea level
$\bar{\eta}$	Mean water level/sea level
$\eta_{ss,env}$	Sea level sea/swell wave envelope
E_{ss}	Sea/swell energy
P_{ss}	Sea/swell power spectral density
H_∞	Deep-water significant wave height (at infinity)
H_{off}	Offshore significant wave height
H_{sz}	Surf-zone significant wave height
ξ_i	i^{th} site
$slope_{ss}$	Slope of SCI vs. maximum root-mean-square for tsunami events
$slope_{tsu}$	Slope of SCI vs. maximum root-mean-square for tsunami events
Co	One-sided co-spectral density

SCI_{ss}	Surge Current Index of sea/swell
SCI_{tsu}	Surge Current Index of tsunami
$TF1$	Transfer function 1, relating offshore sea level to harbor sea level
$TF2$	Transfer function 2, relating harbor sea level to harbor currents
$\hat{E}$	Maximum Likelihood Estimate of the variance
u	Zonal velocity component
v	Meridional velocity component
h	Local water depth
d	Mean water level + local water depth
T	Wave period
L	Wavelength
k	Wavenumber

CHAPTER 1
INTRODUCTION

This study combines observations and numerical modeling results to address questions about the origins of water surges within Hale'iwa Harbor, near the middle of the North Shore of O'ahu. The focus is on infragravity (IG) waves with periods from 0.5 min to ∼200 min that are forced by short-period gravity waves with periods less than 0.5 min. The latter are called "sea" and "swell", or sea/swell (SS) for short, hereafter. The investigation described herein is organized around a set of hypotheses of possible energy pathways linking the offshore SS forcing to intermediary coastal and harbor processes, and then linking these to the observed response inside Hale'iwa Harbor. The main goal of this study is to identify the intermediary processes that occur, and are most dominant, in our study area. Various studies in relatively small harbors have found that, energetically, the 30∼300 sec IG period band is typically the most relevant under strong SS forcing conditions (e.g., *McComb et al.* (2015), *Thotagamuwage and Pattiaratchi* (2014a), *Okihiro et al.* (1993)). This is not what we see in Hale'iwa Harbor, even though it is a small harbor where we originally did not anticipate to observe significant energy levels at periods longer than ∼2-3 min. The sea level and currents spectra that we observe in Hale'iwa Harbor, reveal various significant spectral peaks in the period band ranging from 40 sec to 23 min (see Fig. 1.1). As is seen in the variance preserving plots of Fig. 1.2, the period band that contains most of the variance is ∼5-15 min for sea level, and ∼3-8 min for currents (Figs. 1.1 and 1.2 were generated using five 4-day long sea level and currents data under strong SS forcing conditions at site 2 during our 11/2013 - 05/2014 deployment. These spectra are representative of all other datasets that were available to us. Calculation details are described in Section 2.4).

Another goal is to combine the observational results with a long-term forecast of offshore SS conditions from a high-resolution model, to create a forecasting system of SS-driven harbor surges at IG periods inside Hale'iwa Harbor. This forecast is intended to provide the general public and researchers user-friendly tools to identify ahead of time SS events that could potentially result in damage to harbor infrastructure and/or boats. As an example, Fig. 1.3 shows the sea level response inside the harbor during a very powerful SS event on 02/22/2016. The oscillations that generated these large sea level swings had periods in the order of 4-6 minutes. Note how the small dock was flooded during high sea level, and how high the boat has reached. Such large sea level swings that repeatedly occur for many hours can cause significant damage to the boats and harbor infrastructure, and are therefore important to predict.

At the start of this project, the available observations inside the harbor and at the coast were insufficient to adequately address the hypotheses, since these were limited to a single observation point inside the harbor and one small cross-shore array at the coast, at a site several km from the harbor. Additional high-frequency sea level and surface current data inside the harbor was also needed for creating the harbor surge forecast. These needs for greater spatial and temporal resolution in the harbor and at the coast provided the motivation for instrument deployments during two winter SS seasons affecting the north shore. These deployments provided observations of high frequency sea level and horizontal velocity at multiple harbor and coastal sites.

In Chapter 2 of this dissertation we address the hypotheses of energy pathways through interpretations of analyses of the different observations. In Chapter 3 we describe the observation-based data analysis and results that are used to establish an empirical relationship between the offshore SS forcing and the harbor response at IG periods. The harbor surge forecast is then created by combining this derived empirical relationship with an output from an available numerical model that provides a forecast of the relevant SS conditions at an appropriate offshore location.

Although the different observations were sufficient for establishing the solid empirical relationships necessary for the creation of the harbor surge forecast described in Chapter 3, the observational work of Chapter 2 only partially discriminated the important hypotheses. Additional spatial and temporal resolution was required to fully address many of the hypotheses. This led us to employ a numerical model. Starting with a thorough sensitivity testing stage, followed by validation and calibration, the numerical model was then used to force a domain that includes our study area. Several SS forcing events were used, during times when observations were available. Chapter 4 describes the numerical model testing, validation, calibration, and results, which provided many of the missing links in Chapter 2 that were required to fully discriminate the important hypotheses.

Nearly all geographical maps throughout this dissertation were generated using the Generic Mapping Tools (GMT; *Wessel and Smith* (1991)). In Chapter 4, all of the spectral maps were generated by processing the model output and plotting it using Python programming language.

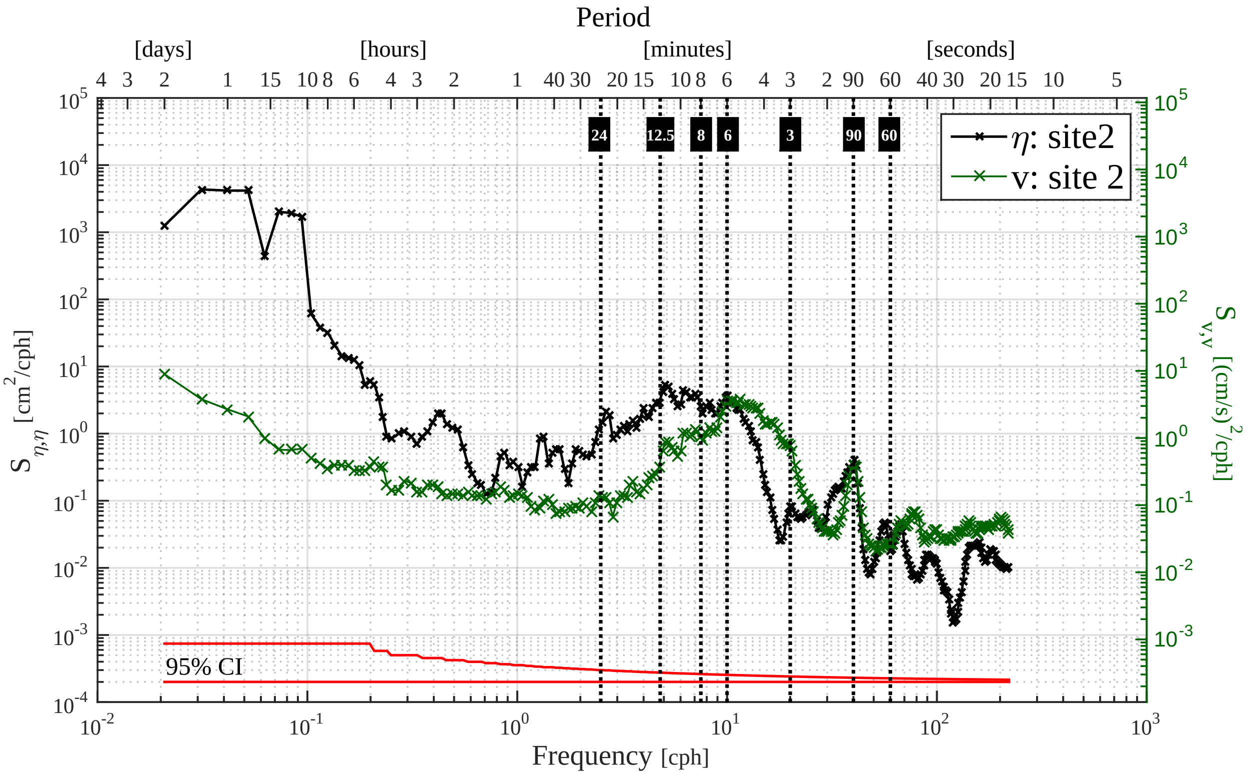

Figure 1.1: Power spectral density using datasets from site 2 of the 11/2013 - 05/2014 deployment in Hale'iwa Harbor. Each curve was generated from five 4-day long sea level (black curve), and along-channel velocity (green curve) data segments (see Table 2.4 for exact time periods). The 95% confidence interval for each independent spectrum estimate is shown at the bottom. *The approximate periods of statistically significant spectral peaks (60 sec, 90 sec, 3, 6, 8, 12.5, and 23 min) are labeled and indicated by the vertical black dotted lines.*

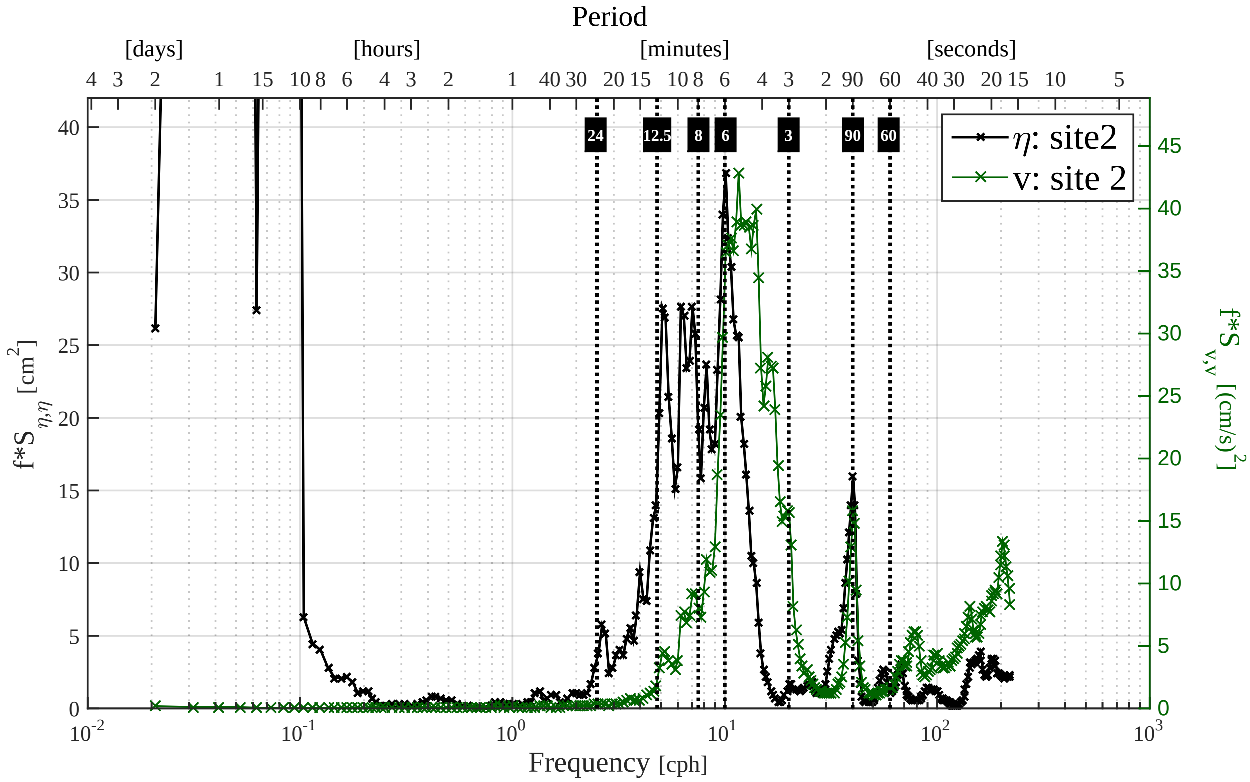

Figure 1.2: Variance preserving spectra using datasets from site 2 of the 11/2013 - 05/2014 deployment in Hale'iwa Harbor. Each curve was generated from five 4-day long sea level (black curve), and along-channel velocity (green curve) data segments (see Table 2.4 for exact time periods). *The approximate periods of statistically significant spectral peaks (60 sec, 90 sec, 3, 6, 8, 12.5, and 23 min) are labeled and indicated by the vertical black dotted lines.*

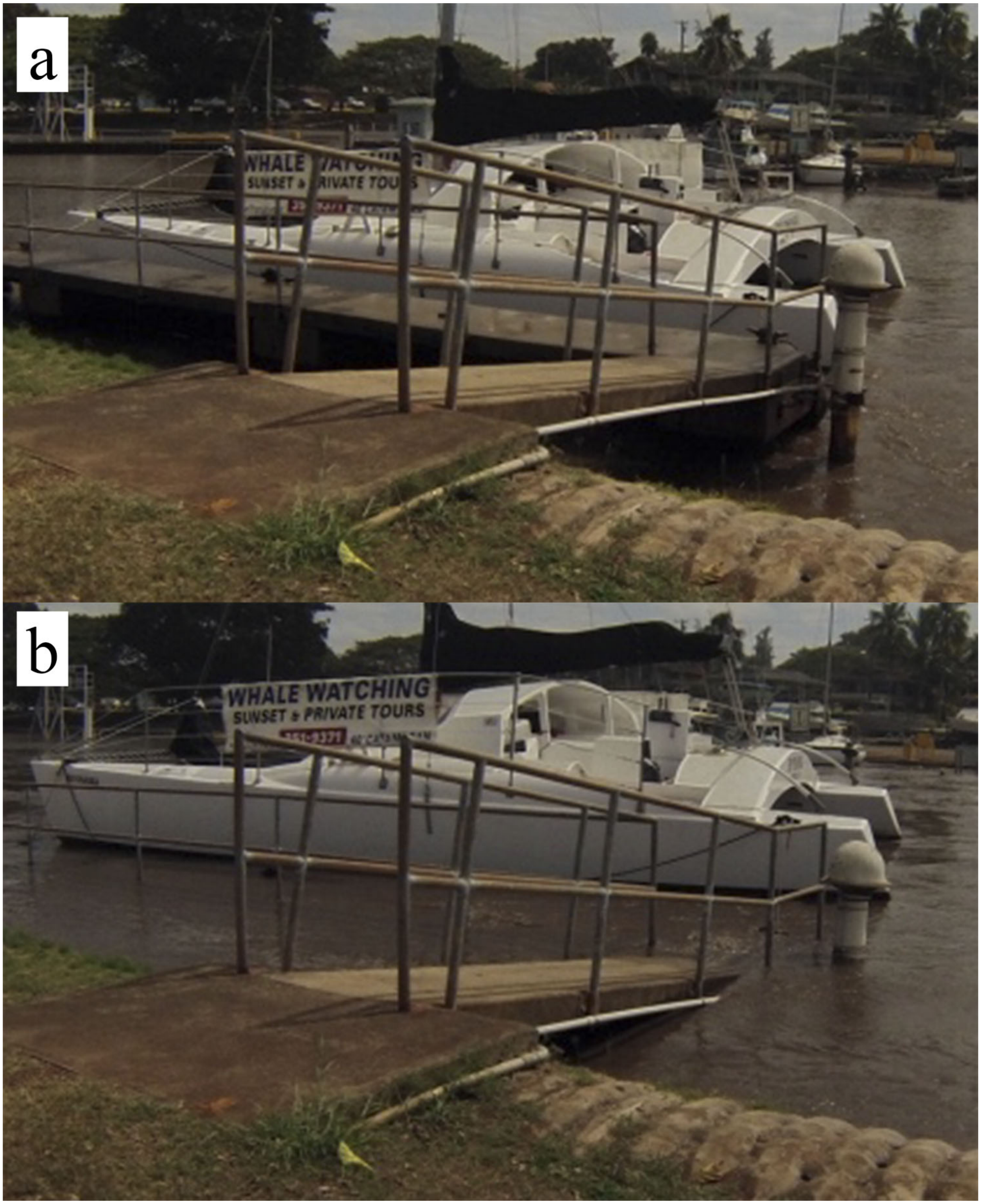

Figure 1.3: Sea level response inside Hale'iwa Harbor during the strong 02/22/2016 SS event.

CHAPTER 2
INFRAGRAVITY OSCILLATIONS IN HALE'IWA HARBOR REGION, HAWAI'I. PART I: OBSERVATIONS

2.1 Introduction

From approximately October to April, coastal regions of the Hawaiian Islands facing the west to north directional window are exposed to highly energetic sea/swell (SS) gravity wave activity that originates from North Pacific storms (*Caldwell and Aucan* 2007). As these waves shoal and break, much of the energy is dissipated, but a large portion is also nonlinearly transferred to low frequency motions with periods ranging from 30 sec to several hours. These long waves, also known as infragravity (IG) waves, contribute significantly to the spectra along the coast, especially within the surf zone, and play an important role in various coastal processes (e.g., *Baldock et al.* (2010), *Bowen* (1967), *Bowen and Inman* (1969)).

The earliest observations of waves having IG periods were made at the coast by *Munk* (1949), who also called them "*surf-beat*", and *Tucker* (1950). As IG waves propagate into shallow depths they become shallow water waves and their amplitudes may reach variances of the order of 1 m (*Wright et al.* 1982). Such oscillations may result from free waves (*Eckart* 1951), or forced (also known as *bound*) waves (*Longuet-Higgins and Stewart* 1962; *Hasselmann* 1962), both of which have gravity as the restoring force. The free waves can be further categorized into *edge-waves* that are trapped to the coastline between the shoreline and an offshore turning point by reflection and refraction processes, exponentially decay offshore of the turning point, and progressively propagate in the alongshore; and, *leaky-waves* that do not return to the shoreline by refraction and therefore escape to deep water.

In deep water, bound IG waves arise from, and are phase coupled to, groups of SS waves by weak nonlinear interaction. For unidirectionally propagating groups, the sea level displacements associated with the bound IG waves and the magnitudes of the SS waves within the groups are out of phase (180° phase difference). The bound IG waves are forced to propagate at the group speed of the short SS waves, which is different than the actual group speed that a free IG wave with the same wavelength would have. *Longuet-Higgins and Stewart* (1962) hypothesized that these groups of SS waves may release their bound IG waves as free IG waves in the surf zone, where they would subsequently reflect from the shoreline.

Using results from field observations, *Elgar and Guza* (1985) were able to find evidence for phase coupling between SS wave groups and long waves with IG periods. They also found that the phase relationship between the two gradually changes during the shoaling process, shifting from 180° towards 90°. *Longuet-Higgins and Stewart* (1962) could not predict this phase shift since their model was developed only for waves traveling in deep water.

Observations made by *Herbers et al.* (1995a) and *Masselink* (1995) showed that bound waves are released as free IG waves in the surf zone, and are subsequently reflected at the shoreline. *Masselink* (1995) reported that the decoupling of bound waves from SS wave groups is a process that starts at the beginning of the breaker zone and is completed at the end of the breaker zone. His particular results further suggested that the reflection occurs around 5 m from the shoreline at about 0.25 m water depth, resulting in standing oscillations at IG wave periods in the surf zone.

Results from laboratory experiments done by *Baldock and Huntley* (2002) found very little evidence in favor of the bound wave release mechanism. They found that the amplitude of the released free long wave will be small when the bound wave is released before it became a shallow water wave. In a review of laboratory datasets, *Baldock* (2012) claimed that the evidence suggests that bound waves are not released as free waves during SS wave breaking, their amplitude is decreased during SS wave breaking and they remain bound throughout much of the surf zone. Once the SS waves become shallow water waves, the free wave dispersion relationship is satisfied by the bound IG waves and they progressively become free IG waves. *Baldock* (2012) also states that the phase shift findings of *Elgar and Guza*

(1985) provide evidence that bound waves may be decoupled from the SS waves even before SS wave breaking. Laboratory results analyzed by *Janssen et al.* (2003) were in agreement with the evolving phase lag found by *Elgar and Guza* (1985) outside the surf zone, between the SS wave groups and bound IG waves.

Gallagher (1971) extended the theoretical work of *Longuet-Higgins and Stewart* (1962) and *Hasselmann* (1962) from normal incidence (2-D) to oblique incidence (3-D) of SS waves. His theory predicts that given certain combinations of frequencies and directions, nonlinear triad interactions of the obliquely incident SS waves will trigger freely propagating edge wave modes that resonantly grow. In a comparison of his theory with data during three SS events that approached the coastline at different angles, by obtaining similar theoretical and observational energy levels, *Gallagher* (1971) was able to qualitatively confirm the resonant growth amplitudes at particular frequencies.

Bowen and Guza (1978) have also tested Gallagher's theory using laboratory experiments that were carried out in a wave tank. They confirmed that edge waves resonantly grow as they move along the beach, and that their energy at IG frequencies increases with distance down the beach. These experiments also showed that the edge wave resonance does not disappear during wave breaking.

In a theoretical study, *Symonds et al.* (1982) found a new generation mechanism of IG waves at the coast. By considering the amplitude variation of incoming waves, the breakpoint position (and the surf zone width) will vary with time at the group period. IG waves are radiated from the breakpoint forcing region shoreward and seaward. Upon reflection at the shoreline, the shoreward propagating wave propagates seaward through the breakpoint forcing region. Assuming no dissipation, the resulting pattern is a standing IG wave oscillating between the breakpoint forcing region and the shoreline, and a progressive IG wave propagating seaward of the breakpoint forcing region. Bound IG waves were neglected in this model. Various laboratory experiments carried out by *Kostense* (1984), *Baldock et al.* (2000), and *Baldock and Huntley* (2002), were able to validate the time-varying breakpoint mechanism of *Symonds et al.* (1982).

A theoretical study developed by *Schäffer* (1993) suggested that the dynamic set-up generated by the time-varying breakpoint mechanism and the dynamic set-down of bound waves, are almost of equal importance. In a theoretical study by *Lippmann et al.* (1997) they describe a resonant edge wave mechanism in the nearshore by extending Gallagher's generation of edge wave theory into the surf zone, and the time-varying breakpoint theory from two to three dimensions. A simple linear analytical model by *Becker et al.* (2016) was able to explain a large portion of the IG variability over a steep reef environment, by adding a damping term to the time-varying breakpoint model of *Symonds et al.* (1982).

In a numerical study, *List* (1992) compared the relative importance between the bound wave release and the time-varying breakpoint mechanisms. He found that the amplitude of IG waves generated by the former mechanism are greater than the ones generated by the latter mechanism. In his review of laboratory datasets, *Baldock* (2012) also compared the bound wave release and time-varying breakpoint mechanisms, and identified the relative beach slope and short wave steepness to be important in the generation of IG waves. He found that the bound wave release mechanism is more important when the beach slope and wave conditions are mild, and the time-varying breakpoint mechanism is more important when the beach slope and wave conditions are steep.

Molin (1982) developed a theory that describes generation of IG waves by discontinuities in the bottom slope. When groups of SS waves and the bound waves that are coupled to them meet a region of variable depth, additional free long waves with SS difference frequency are generated if the region's length scale is comparable to the group length.

Another source of nearshore oscillations at IG wave periods is known as *shear waves* (also called *vorticity waves*). First observed by *Oltman-Shay et al.* (1989), these waves were found in the surf zone only in the presence of a mean longshore current, and have periods of 100 - 1000 sec. In a theoretical work, *Bowen and Holman* (1989) identified conservation of potential vorticity as the underlying mechanism for generating these waves (hence, the restoring force is vorticity rather than gravity), and suggested that they are generated by the shear instability of the mean longshore current. Additional theoretical work by *Shrira et al.*

(1997) suggested explosive instability processes as an alternative generation mechanism, and *Haller et al.* (1999) expanded the shear instability theory of *Bowen and Holman* (1989) by including a wave group forcing term in the nearshore potential vorticity balance.

Various observational studies have shown that the energy levels of both free and bound IG waves increase with increasing sea/swell (SS) energy levels and decreasing water depth, but their relative contributions to the total IG energy varies depending on the SS energy levels (*Okihiro et al.* 1992; *Elgar et al.* 1992, among others). In the surf zone, in most cases it was found that free wave energy dominates bound wave energy (*Okihiro et al.* 1992; *Bowers* 1992; *Herbers et al.* 1992, 1994, 1995b, among others). Outside the surf zone, bound wave energy levels were found to be comparable or even higher than those of free waves, under strong SS conditions (*Okihiro et al.* 1992; *Elgar et al.* 1992). Observations made by *Huntley and Kim* (1984) outside the surf zone in a relatively steep beach showed that low frequency motions in the 30 - 300 sec period band were dominated by bound waves. In the case of the freely propagating edge and leaky waves, the relative contribution to the total IG energy depends on the geometry of a given coastline (*Munk et al.* 1964; *Huntley* 1976).

When resonantly excited, standing long waves in semi-enclosed basins (known as *seiches*) such as ports and harbors, may result in significant vertical displacements of the free surface, and strong horizontal currents. Such conditions could lead to delays in harbor operations, and in some cases could even result in significant damage to moored ships and harbor infrastructure (*Morison and Imberger* 1992; *Lopez et al.* 2014). *Morison and Imberger* (1992), *Okihiro et al.* (1993), *Okihiro and Guza* (1996), *Bellotti and Franco* (2011), and *Thotagamuwage and Pattiaratchi* (2014a), have all observed SS (generated by non-local atmospheric disturbances) exciting harbor seiches. *Okihiro et al.* (1993), and *Okihiro and Guza* (1996) also show that the resonant response of several small harbors is frequency dependent, with the strongest amplification occurring at the gravest normal modes of these harbors. The harbor IG responses in these studies were shown to be triggered primarily by free waves; however, it was theoretically shown that the mismatch of bound-wave-induced set-down across a harbor mouth introduces free long waves inside the harbor that can excite harbor resonances (*Bowers* 1977). *Douyere* (2003) used an extended Boussinesq model to study the resonant oscillations in Barbers Point and Kahului Harbors in Hawai'i. The model results identified modal oscillations at IG periods that agree well with the ones found in published results of linear models, but the nonlinear model also generated additional modes that were not found by the linear models. Other processes that were shown to excite harbor seiches include: local atmospheric disturbances (*Okihiro et al.* 1993; *De Jong et al.* 2003; *De Jong and Battjes* 2004), internal tides (*Giese et al.* 1990; *Chapman and Giese* 1990; *Grimshaw and Chapman* 1992; *Giese et al.* 1998), and tsunamis (*Wilson* 1971; *Heath* 1974; *Okihiro and Guza* 1996). As an example from a recent study, *Park et al.* (2016) used tide gauge sea level data from several harbors in the Pacific Ocean to study large-scale seiches of bays that persist continuously in time. Using spectral techniques they were able to provide sowas inme evidence supporting their hypothesis that the continuous source of forcing could potentially be driven by tidal waves that force a shelf to resonate.

The goal of this study is to learn more about the different processes that lead to modal and non-modal oscillations at IG periods along the North Shore coast of O'ahu Island and in Hale'iwa Harbor. We are especially interested in those processes converting SS wave energy into IG wave energy (as opposed to direct forcing of IG waves by wind or air pressure, or forcing by tsunamis). As briefly reviewed above, there are various mechanisms by which IG oscillations are generated along a given coast upon the arrival of SS waves, and different ways by which energy can flow into the harbor. Some of this energy may even excite resonant harbor seiches, resulting in amplified IG oscillations in the harbor. All these processes were considered during an initial analysis of historical datasets to delineate the more likely processes for exciting IG waves in Hale'iwa Harbor. Additional data collection and analyses produced both refinements of the relevant processes and limited conclusions.

The study areas and datasets are described in Section 2.2, the initial analyses and hypotheses are described in Section 2.3, the methods used in this study are outlined in Section 2.4, and the analysis and results are presented in Section 2.5. We then provide a short discussion in Section 2.6.

2.2 Study area and datasets

Hale'iwa Harbor region (facing $\sim 315°$ relative to geographic north) is exposed to the very large North Pacific winter swells arriving from the west to north directional windows, from October through April (*Caldwell and Aucan* 2007). The bathymetry along this stretch of coast is composed of an uneven volcanic reef with a relatively steep slope and channels that cross the reef at several locations along the coast. The contour of the coastline is tortuous and contains numerous small-scale embayments that, depending on the local bathymetry, could potentially trap and amplify oscillations at particular IG periods. The scale of these embayments ranges from less than 100 m to 1-2 km (which translates into IG waves having periods as long as ~5 min). All of these features make this site particularly interesting for studying IG waves.

Lengthy sea level records that were available to us inside Hale'iwa Harbor (and other Hawaiian Harbors), at the offshore location of Waimea Buoy, and short high-resolution records at Mokuleia, were a good starting point for this study, but data from additional deployments were eventually deemed necessary for attacking the important research questions. The datasets used in this study are described below.

At the early stages of this study we were limited to the use of sea level datasets from existing monitoring systems (see Fig. 2.1, Fig. 2.2, Table 2.1, and the rows under historical deployments in Table 2.2):

1. Data from a stilling-well tide gauge located inside Hale'iwa Harbor (site 1) were obtained from the Archive of Rapidly-Sampled Hawaiian Sea Level (ARSHSL, *Luther et al.* (1998)). This tide gauge is operated and maintained by the Pacific Tsunami Warning Center (PTWC), providing samples every 2 minutes (data points are not averaged) since 1997 to present.

2. A Datawell directional wave buoy located at a depth of 200 m, at site 10, ~ 6.5 km WNW of Waimea Bay and ~ 8.5 km N of Hale'iwa Harbor (also known as *Waimea Buoy*), operated and maintained by the Pacific Islands Ocean Observing

System (PacIOOS) with data processing by the Center for Data and Information Program (CDIP) in Scripps Institution of Oceanography (SIO). Operating since 2001 to date, the buoy samples at 1.28 Hz and every 30 min it produces an analysis of 1600 sec ($\sim$ 26.6 min) of data to provide sea/swell (SS) spectral products such as wave energy density and mean direction.

3. Several five-week records in '07-'08 of pressure and currents sampled every second at a cross-shore array near Mokuleia on the North Shore of O'ahu ($\sim$5.5 km west of Hale'iwa Harbor), at depths of 2m, 6m, and 12m.

Although the available datasets inside the harbor were found to be very useful to this research, the 2 min sampling frequency was too slow to detect the highest frequency IG oscillations (0.5-4 min), and horizontal current data were not available. We therefore executed a small scale six-month long experiment where we deployed two pressure sensors and one current meter inside the harbor, and two pressure sensors offshore (sites 1, 5, 6, and 9). The deployment was done during the winter swell season months, between 11/2011 - 05/2012 (see Fig. 2.1, Fig. 2.2, Table 2.1, and the rows under 2011/2012 deployments in Table 2.2).

Since the spatial coverage inside the harbor was limited to only two locations, and additional datasets of horizontal currents were deemed necessary after initial analyses of the existing data described above, we executed a second, larger scale six-month long experiment during 11/2013 - 05/2014, in which we deployed four pressure sensors and current meters at four locations inside the harbor (sites 1-4), and two pressure sensors and one current meter at offshore sites 7 and 9 (see Fig. 2.1, Fig. 2.2, Table 2.1, and the rows under 2013/2014 deployments in Table 2.2).

In the later stages of our study we also used historical datasets from tide gauges in other Hawaiian Harbors (sites 13-15), and datasets from additional deployments in deep water offshore of O'ahu Island (sites 11 and 12; see Fig. 2.3, and Tables 2.1 and 2.2). When necessary, several segments of data are averaged in order to increase the number of degrees of freedom in the spectral analyses, and represent a larger portion of a given dataset. The time periods when averaging was applied are representative of the entire available dataset/s.

These time periods are summarized in Table 2.4.

2.3 Analyses leading to hypotheses

2.3.1 Response of Hale'iwa Harbor Region to offshore forcing

In this section we present analyses and different results from the early exploratory stages of this study. The analyses involve plotting the power spectral density (PSD) of 2-min pressure datasets at site 1 in Hale'iwa Harbor (see Fig. 2.1), and 1-sec datasets at coastal sites 8a - 8c of the Mokuleia stretch of coast (Fig. 2.2), under different SS forcing levels.

We define the SS forcing levels using 3 years of sea level data from site 10 between 07/01/11 - 07/01/14. The time series of energy in the 2-30 sec SS period band is shown in Fig. 2.4, for SS arriving from (a) 315° from north, representing Hale'iwa Harbor and the coastline northeast of it, and; (b) 360° from north, representing Mokuleia coastline. Horizontal dashed red lines represent the cutoffs between weak, moderate, and strong SS forcing levels, and were determined from the distribution of energy in the SS band (E_{SS}) seen in Fig. 2.5. From left to right in Fig. 2.5, we define the ranges of E_{SS} as follows: (i) no SS: $0 < E_{SS} < 1000$ cm^2 (magenta bars, $\sim$ 67% of the distribution); (ii) weak SS: $1000 < E_{SS} < 2500$ cm^2 (blue bars, $\sim$ 20% of the distribution); (iii) moderate SS: $2500 < E_{SS} < 6000$ cm^2 (black bars, $\sim$ 10% of the distribution); (iv) strong SS: $E_{SS} > 6000$ cm^2 (red bars, $\sim$ 3% of the distribution). These definitions of no-SS (or, minimal SS), weak, moderate, and strong SS forcing levels will be used in the remainder of this dissertation. They were arbitrarily chosen, but are appropriate for the North Shore of O'ahu, which is a unique environment that is known to be exposed to exceptionally strong SS forcing levels during the North Pacific winter season (October - April). For comparison, in their study of IG oscillations in Barbers Point, *Okihiro et al.* (1993) used pressure data (converted to sea level) from a site located at a depth of $\sim$ 8.5m and a distance of $\sim$ 200m offshore of the harbor entrance, and defined $0 < E_{SS} < 156$ cm^2 as "calm" SS conditions, and $E_{SS} > 625$ cm^2 as "energetic" SS conditions.

A sea level PSD plot at site 1 is seen in Fig. 2.6, showing the harbor's IG response to no-SS, weak, moderate, and very strong SS forcing. Each curve was generated by averaging five 4-day long data segments (i.e., 20 days of data), from the years 2002/2003. What immediately stood out, was the different character of harbor IG responses under varying SS forcing levels. During times of no-SS forcing, the sea level response of the harbor is characterized by amplified oscillations at rather discrete IG periods from 6 to 23 min that suggest normal mode oscillations of the harbor, coast, or the combined system (Fig. 2.6, magenta curve). When the SS forcing rises to weak levels, several of the same spectral peaks still appear but PSD levels have increased broadly over the short-period end of the IG band (Fig. 2.6, blue curve). With moderate SS forcing levels (Fig. 2.6, green curve), some of the peaks are still distinct, but overall they start to lose their modal character. Once SS levels reach high values (Fig. 2.6, red curve), PSD levels are significantly increased and the IG response of the harbor no longer appears to be dominated by modal oscillations, as deduced from the lack of spectral peaks; instead, PSD levels are relatively uniform across a wide IG band even up to periods of several hours. The question then arose: how do the IG waves at periods unresolved by the 2-min historical sea level data respond to the different SS forcing strengths? This is a particularly interesting question because it has been reported that in some harbors the shortest period IG waves ($0.5 \sim 1$ min) are the most energetic IG waves (*McComb et al.* 2015; *Guedes et al.* 2015). The high frequency datasets from the 2011/2012 and 2013/2014 field deployments were used to test the possibility of aliasing from unresolved high frequency oscillations (periods shorter than 4 min). We found that the energy levels of such oscillations are very weak by the time they reach site 1, and that the tide gauge does a good job in filtering out any high frequency oscillations.

The question above, and others, led to the two field deployments accomplished under this study. Especially, the datasets obtained during the 2^{nd} experiment, from 11/2013 - 05/2014, are particularly useful, allowing us to see the harbor's response at the shortest periods. Fig. 2.7 provides an example of the harbor's IG response to no-SS, weak, moderate, and very strong SS forcing, using datasets that were collected at site 2 (see Fig. 2.1). Also here, each curve was generated by averaging five 4-day long data segments (i.e., 20 days of data). The sampling periods of these datasets vary between 8-10 sec, enabling us to resolve the spectral content down to periods of 16-20 sec, therefore adding new information to Fig. 2.6 at periods shorter than 4 min. Here, we chose to use datasets from site 2 instead of site 1 for the following reasons: (i) at site 1, all strong SS events occurred during the first deployment, except the strongest event that occurred during the second deployment. In order to avoid the need to interpolate a dataset and reduce its sampling period from 8 sec to 14 sec, we chose not to use the dataset from site 1 for this particular analysis. (ii) at site 2, all strong SS events occurred during a single deployment (8 sec sampling period), and therefore did not require any interpolations. (iii) site 2 is located very close to site 1 and the spectra at these two locations are qualitatively very similar.

Although the SS events used in Figs. 2.6 and 2.7 are entirely different, the character of the harbor's IG response to no-SS, weak, moderate, and strong SS forcing (at periods of 4 min and longer) are qualitatively very similar. Note that there are several statistically significant spectral peaks in the 40 sec - 3 min period band; however, with the exception of the 90 sec peak, the PSD levels of the peaks in this band are much lower compared to the PSD levels of the 6 - 12.5 min period band. The relative importance of the peaks in terms of their contribution to the IG variance in the harbor can be better seen using a variance-preserving (VP) spectral plot. Fig. 2.8 is a variance-preserving version of Fig. 2.7 and it clearly reveals that most of the IG sea level variance is at periods of 5 to 15 min. Within the weaker IG band at periods shorter than 4 min, almost all of the variance is contained in the 90 sec oscillations. Fig. 2.9 shows sea level PSDs at four different sites inside the harbor using data from the time period 11/28/13 - 01/20/14. It shows us that at periods longer than ~ 5 min, the same spectral peaks appear at the different locations inside the harbor; however, at periods shorter than ~ 5 min we note that although a spectral peak of a particular period may appear to be strong at one site, at another site it may be absent if it is located at a node of that period. A good example is the 90 sec mode that is very energetic at sites 1 and 2, weaker at site 4, and completely absent at site 3. As will be shown in Chapter 4, subsection 4.4.3.1, this result is consistent with the spatial distribution of the 90 sec mode, showing that sites 1 and 2 are located at an antinode, site 3 is located at a node, and site 4 is located at an antinode, but is also nearby a node.

As was mentioned above, the spectral peaks seen in the 6-23 min period band in the spectra of Figs. 2.6-2.9, appear in all of our sea level spectra between 1997 - 2010. As an example, the upper panel of Fig. 2.10 shows a spectrogram generated by averaging the spectra of 10 two-month long time segments during the months of July-August at site 1 in Hale'iwa Harbor, when the SS forcing levels fall into our definition of no-SS (see Fig. 2.5). We can clearly identify several horizontal ridges where the PSD levels are elevated. By averaging this spectrogram over time, we obtain the PSD plot seen in the lower panel of Fig. 2.10. The spectral ridges/peaks in these two plots can be qualitatively classified as: 23, 12.5, 8, and 6 min, being the main periods, followed by 18 and 15 min. The spectrogram plot also shows that the spectral levels of these modes are persistent in time, similar to the findings of *Park et al.* (2016) in several Pacific Ocean bays.

Fig. 2.11 contrasts Hale'iwa Harbor's IG response to two very different types of forcing: (i) tsunami forcing (black curve; 06/25/01 tsunami event); and, (ii) strong SS forcing (red curve; 01/04/03 SS event). Each of these curves was generated using 2-day long sea level datasets. Note the different spectral character of the two curves. The tsunami spectra contains relatively narrow, well-defined, peaks at the periods of: 23, 18, and 12.5, 8, and 6 min (as well as other smaller, secondary, peaks). The spectra of the strong SS, on the other hand, contains no feature that could clearly be considered as being statistically significant.

To see how the coast responds to varying levels of SS energy forcing, we look at the historical datasets from a cross-shore array in Mokuleia at depths of 12m, 6m, and 2m (sites 8a - 8c in Fig. 2.2, respectively). PSD plots at those three sites can be seen in Figs. 2.12 - 2.14. For each curve we use two 3-day long datasets from times of weak, moderate, and strong SS forcing (see Table 2.4 for the exact time periods). The IG band response to varying levels of offshore SS forcing at each of these sites has interesting qualitative similarities to the response seen inside the harbor (compare Figs. 2.12 - 2.14 with Fig. 2.7). Even though the SS events of Figs. 2.12 - 2.14 are entirely different from the SS events used in Fig. 2.7, the relative IG-PSD changes from no-SS through strong SS are qualitatively very similar. Note that the 12.5 and 23 min peaks appear at all three depths in Mokuleia, but the remaining peaks seen in Fig. 2.7 do not appear at the 2m and 12m Mokuleia sites. This could result from these Mokuleia sites being located at nodes in the spatial structure of coastal modes at certain periods (e.g., see *Munger and Cheung* (2008)). The lack of spectral peaks at shorter periods (< 4 min) at the coast suggests that the short period harbor peaks could be the result of the harbor resonating on its own. However, at the 6m Mokuleia site (Fig. 2.13), we do see statistically significant peaks at 3 and 1.5 min (which match the periods of peaks inside the harbor), as well as peaks at periods of ~ 60 sec and ~ 50 sec.

In Fig. 2.12 (2m depth), we also see several large broadband peaks at ~ 50 sec, ~ 25 sec, and shorter periods that appear to be part of a broad-band oscillatory function of frequency, which is reminiscent of nodes and antinodes resulting from the superposition of incoming and reflecting waves in shallow water within the surf zone, and are very much site-dependent (personal communication with Mark Merrifield). It seems clear from Figs. 2.12 - 2.14 that the spatial structure of high-frequency IG waves near the coast is complex. Adequately exploring and describing these structures requires more data than is available. We'll return to this issue in Chapter 4 during the analysis of numerical simulations of SS-forced IG waves on the North Shore of O'ahu.

Prior to generating spectral plots such as Fig. 2.6, our expectation was that inside the harbor any peaks indicating normal modes in the $6 \sim 23$ min band would grow in magnitude and remain quite distinct as SS levels increased. We based this expectation on the intuition derived from a simple harmonic oscillator with one or more natural frequencies, as well as from the work on harbor modes by *Okihiro et al.* (1993) and *Okihiro and Guza* (1996) at Barbers Point Harbor, O'ahu. In fact, at periods shorter than 4 min, the differences among the four curves in Fig. 2.7 (corresponding to the different SS forcing amplitudes), reveal very good agreement with our expectation. As SS forcing levels increase, the different modes in this band become more energetic and their spectral shape remains nearly unchanged.

However, at periods longer than 4 min in Figs. 2.6 and 2.7, the differences among the curves suggest that this system does not remain linear once the SS spectral levels become high on the North Shore; the modal character is lost and the spectra under high SS levels becomes uniform across the entire IG period band extending from $\sim$ 4 min up to several hours. Qualitatively, very similar results are obtained at the coast, as can be seen from the spectral analysis at Mokuleia (sites 8a-8c). The spectral peaks that appear at periods shorter than $\sim$ 4 min in Figs. 2.12 and 2.13, grow in energy and maintain their spectral shape as SS forcing levels grow. At periods longer than $\sim$ 4 min, Figs. 2.12-2.14 show for the most part a uniform, non-modal, spectra under strong SS forcing levels.

If common to other harbors, this result, where the spectra at periods longer that $\sim$ 4 min evolves from being modal-dominated to being uniform and non-modal, has significant implications for how harbor designs should be evaluated for maximum surge amplitudes (e.g., *Briggs et al.* (1994)). Harbor sea level and current variability in the presence of strong forcing is not simply due to a summation of appropriately scaled linear normal mode amplitudes.

At least for the no-SS and weak SS forcing, which appears to excite coastal and harbor modes, it is useful to ask: how fast do the excited modes decay? Such numbers can be used to validate numerical models, for instance. For the case of weak SS forcing conditions, the quality factor, Q, of the system and the e-folding decay time, τ, were estimated by assuming that the North Shore harbor-coastal system responds to weak impulse forcing like a damped oscillator, with a resistive force proportional to the velocity and opposite in direction. The envelope of this oscillating system decays exponentially as $Ae^{-\frac{t}{2Q/\omega_1}}$, where $\tau = 2Q/\omega_1$, $Q = \omega_1/\Delta\omega$, ω_1 is the radian frequency of the oscillation (shifted to a slightly lower frequency compared to an undamped oscillator), and $\Delta\omega$ is the half-power radian frequency bandwidth. We also calculate the periods of the spectral peaks (T) that appear in our spectra from the different harbor and coastal sites. This is done using the two lowest order spectral moments: $T = \frac{m_0}{m_1}$, where $m_k \simeq \sum_{i=1}^{N/2} f_i^k S(f_i)\Delta f$, $N/2$ is the number of spectral estimates, $k = 0, 1, 2, \ldots$, and Δf is the frequency resolution. Table 2.3 summarizes the mode periods, quality factors and corresponding e-folding decay times, that were calculated from a large number of week-long spectra during no-SS and weak SS time periods from the years 1997-2010 at site 1, and 2014 at sites: 1, 2, 3, 4, and 7 (see Figs. 2.1 and 2.2). The uncertainty of each of these quantities is the standard deviation.

The results show that $Q \sim 7 - 14$ for all modal peaks in the 55.3 sec - 22.7 min period band, with a small tendency toward larger values at the shortest periods. The 14.5 min, and 22.7 min oscillations have the lowest $Q's$, and the 65.7 sec and 91.5 sec oscillations have the highest $Q's$. High/low Q's suggest low/high rates of energy loss relative to the energy stored in the system, thus the shorter-period IG modes are slightly less damped than the longer-period modes. The e-folding decay times are seen to generally increase with increasing period, principally as a result of the inverse dependence of τ on frequency.

Our observed large-scale periods: 14.5 ± 0.3, 18 ± 0.2, and 22.5 ± 0.3 min, agree with the values modeled by *Munger and Cheung* (2008), but overall, the periods of the model-predicted modes appear to be slightly longer than our observed values (e.g., see the spectra of Mokuoloe and Kahului in *Munger and Cheung* (2008), Fig.3). For example, the observed modal peak at 22.5 ± 0.3 min was identified by *Munger and Cheung* (2008) as 24 min. In a later study by *Cheung et al.* (2013), they identified this mode to be 22.5 min, which overlaps with the value from our observations.

2.3.2 Hypotheses: Pathways of IG wave energy into Hale'iwa Harbor

In order to organize the various questions that arose from these observations, we formulated several hypotheses representing the most likely pathways of IG energy into the harbor, given different offshore SS forcing levels. The hypotheses, which will be described in detail in the following subsections, are represented graphically in Fig. 2.15. Each hypothesis links an offshore forcing to a coastal or harbor process, and the latter is then linked to a harbor response. The forcing is based on observations that were so far presented in this chapter (i.e., SS forcing), or other studies (i.e., forcing by open ocean processes). The coastal/harbor processes are based on observational, theoretical, or numerical modeling work done by others and that can be found in the literature. The harbor response is based on sea level observations that were described earlier in this chapter (see Figs. 2.6-2.7).

2.3.2.1 None-to-weak Sea/Swell (SS) Forcing

1. **IG offshore**: The offshore IG and SS wave fields contain mostly random, broadband, small amplitude waves, which we'll call the background IG/SS wave fields. The IG wave field is composed mostly of free waves originating from open ocean processes. The bound IG waves are very weak because the swell is very weak (*Okihiro et al.* 1992, 1993). The free IG waves are known to be extremely weak themselves and therefore are not expected to excite significant IG oscillations (e.g., *Okihiro et al.* (1992); *Webb et al.* (1991); *Herbers et al.* (1995b); *Filloux et al.* (1991)). Amplitude estimates of the offshore IG wave field are presented in Section 2.5.5.

2. **IG at the coast and harbor**: The offshore small-amplitude, low-energy, background IG wave field may (i) directly reach the harbor mouth without any coastal mode excitation and subsequently force harbor oscillations like impulse forcing of a linear harmonic oscillator (Hypothesis A0a); or, (ii) force coastal leaky waves and/or modes, and/or coastal edge waves and/or modes, via impulse forcing of the coastal system, and then this coastal IG energy will reach the harbor mouth (Hypothesis A0b). Similarly, the offshore small-amplitude, low-energy, background SS wave field may (i) directly reach the harbor mouth without any coastal mode excitation and subsequently force harbor oscillations like impulse forcing of a linear harmonic oscillator (Hypothesis A1); or, (ii) force coastal leaky waves and/or modes, and/or coastal edge waves and/or modes, via impulse forcing of the coastal system, and then this coastal IG energy will reach the harbor mouth (Hypothesis A2). The primary question under Hypothesis A2 is whether the harbor responds passively to the input of coastal IG energy, or whether the harbor's own free oscillations are excited and amplify. The expectation is that this co-oscillation could happen at the shorter periods, perhaps in the 0.5 min to 3 min band, where the harbor's natural frequencies should lie. An important goal of this work

is to understand if and when the harbor's own natural frequencies are independent of coastal natural frequencies.

Since the modal oscillations appear to dominate the non-modal signals under weak SS forcing, the coherence amplitudes of IG waves along the coast and between the harbor IG waves and the coastal IG waves is expected to be high. This will be discussed further in Section 2.5.1.

2.3.2.2 Moderate Sea/Swell Forcing

1. **IG offshore**: The IG wave field energy has increased both because the winds that force SS also force free IG waves and because there is now IG-scale energy bound to SS wave groups; it is expected that the IG wave field is still composed mostly of free waves (*Okihiro et al.* 1992).

2. **IG at the coast**: The offshore SS wave field may (i) directly reach the harbor mouth without any coastal mode excitation and subsequently force harbor oscillations like impulse forcing of a linear harmonic oscillator (Hypothesis B1); or, (ii) force coastal leaky waves and/or modes, and/or coastal edge waves and/or modes, via impulse forcing of the coastal system, and then this coastal IG energy will reach the harbor mouth (Hypothesis B2). The additional SS energy also corresponds to an increase in energy of the high-frequency end of the IG band. Longest period modes may still appear as pronounced peaks, but an increase in leaky wave and/or edge wave energy may mask some of the modes in the high frequency IG band (Hypothesis B3). The spectrum appears to contain non-modal as well as modal oscillations.

3. **IG in the harbor**: In addition to excitation of the harbor modes by impulse forcing (either directly, or indirectly) of the background IG/SS energy levels, the energy levels of the short period harbor modes have increased. Following the early analysis results presented in section 2.3.1 (e.g., see Fig. 2.7), we expect that the spectrum contains mostly modal oscillations. Non-modal energy will likely be very weak by the time it reaches the harbor.

2.3.2.3 Strong Sea/Swell Forcing

The energy of the IG wave field is significantly elevated above background levels. Results from observations in shallow water (*Okihiro et al.* 1993) have shown that as SS energy levels increase, the portion of bound IG energy out of the total IG energy is increasing. This is also true in deep water (*Okihiro et al.* 1992). Since bound IG wave energy is approximately proportional to the square of the SS energy, there is now a greater portion of IG wave energy that increases quadratically with SS energy. The energy of free IG waves, on the other hand, is linearly related to SS energy (*Okihiro et al.* 1992; *Elgar et al.* 1992; *Herbers et al.* 1995b). The IG energy is now significantly increased in a very wide IG period band extending from short to long IG periods. Following the early analysis results of Section 2.3.1 that revealed elevated spectral levels at periods longer than $\sim$ 30 min under strong SS forcing, we will define this period band as far-IG.

1. **IG offshore**: The IG wave field energy has increased both because the winds that force SS also force free IG waves and because there is now IG-scale energy bound to SS wave groups; it is expected that the IG wave field is still composed mostly of free IG waves, although the portion of bound IG out of the total IG wave field has increased (*Okihiro et al.* 1992).

2. **IG at the coast**: The energy of the IG wave field has increased, and is composed of comparable levels of free and bound waves (*Okihiro et al.* 1992), with possible dominance of bound IG waves outside the surf zone (*Elgar et al.* 1992). The offshore SS wave field may (i) directly reach the harbor mouth without any coastal mode excitation and subsequently force harbor oscillations as an impulse forcing of a linear harmonic oscillator (Hypothesis C1); or, (ii) force coastal leaky waves and/or modes, and/or coastal edge waves and/or modes, via impulse forcing of the coastal system, and then this coastal IG energy will reach the harbor mouth (Hypothesis C2). Although the coastal modes may still be excited, they no longer dominate the non-modal energy that has become very energetic. The IG wave field may still contain energetic free leaky waves

and/or edge waves (Hypothesis C3), but mostly bound waves. These bound waves could be traveling shoreward via deep channels without wave breaking (*Bowers* 1977) (Hypothesis C4), or could be released before/during/after wave breaking (Hypothesis C5). At the longest IG periods, variable set-up due to SS groupiness and bathymetric irregularities may also contribute to variability of the North Shore of O'ahu, at IG periods (Hypotheses C6, D1), and the gravest modes of the Hawaiian Islands Chain (*Munger and Cheung* 2008; *Cheung et al.* 2013) may be excited (Hypothesis D2).

3. **IG in the harbor**: The harbor modes are still excited but no longer dominate the non-modal energy that has become very energetic.

Following the early analysis results presented in section 2.3.1 (e.g., see Fig. 2.7), we expect that under these conditions the modal and non-modal signals may be comparable, and the coherence amplitude along the coast and between the harbor and the coast to be reduced due to destructive interference among the IG waves. This will be discussed further in Section 2.5.1.

2.4 Methods

In this section we describe the analysis tools that are used to address the various hypotheses previously outlined, and discriminate their relative importance. Nearly all of the data analysis presented in this chapter involves the use of data from pressure that was measured at different water depths. The pressure data in this study were measured in units of dbar, which according to linear wave theory approximately equals to the water depth in units of meters. Because the pressure signal of ocean SS decays with depth (it is a function of local water depth and wavenumber), at a given depth we adjust our pressure records in the frequency domain (for all wavenumbers) to provide the pressure at the surface. Hereafter, we will refer to all pressure records as sea level records.

Most of the analyses in this chapter involve auto- and cross-spectral calculations to generate power spectral density (PSD), spectrogram, and coherence plots. For the PSD and coherence, the autospectrum and cross-spectrum are calculated using the frequency band averaging method, as described in *Thomson and Emery* (2014), with the exception that here we increase the number of spectral estimates within the frequency bands as we go to higher frequencies; this results in a relatively uniform spectra across the entire logarithmic frequency range of a given dataset, and decreasing confidence intervals going to higher frequencies (since the number of degrees of freedom increases). The PSD is normalized so that the variance of a unit amplitude sine wave is 1/2, and the 95% confidence intervals for independent spectrum estimates are calculated following *Thomson and Emery* (2014). For the coherence amplitude function, $\gamma_{x,y}$, the 95% level of no significance is calculated following *Thompson* (1979), and the sign convention used here for the coherence phase function is such that a positive phase difference between sites ξ_1 and ξ_2 implies that the signal at ξ_2 is leading the signal at ξ_1. All auto- and cross-spectral estimates are calculated by applying 50% overlap between adjacent spectral estimates. To minimize spectral leakage, we apply a 10% cosine-taper Tukey window, as described in *Thomson and Emery* (2014).

The spectrograms are calculated by calculating PSDs using the block averaging method (also known as Welch's method), using a 10% cosine-taper Tukey window, as described in *Thomson and Emery* (2014). We do that for 6-hour long segments of data every 3 hours (i.e., resulting in a 50% temporal overlap between adjacent spectral estimates). We then smooth the resulting two dimensional PSD matrix in both time and frequency domains by convolving it with a 3×3 Hamming window (three point smoothing in the time and frequency domains), where its weights were normalized to 1.

2.4.1 Excitation of Linear Coastal or Harbor Modes (Hypotheses A1, B1, C1, A2, B2, & C2)

In order to test these hypotheses we first need to determine whether the free IG oscillations of the harbor and coastal linear systems are separated by some frequency cutoff, or maybe an overlap exists between the frequencies of the harbor and coastal modes that will permit energy exchange between them. In case no overlap exists between the two systems, each one may be excited independently, depending on the SS forcing character. In case the harbor and coastal modal systems are connected, they may excite each other by exchanging energy at particular frequencies or frequency bands. In that case, for a given frequency of oscillation, the relative energy levels between the two systems may provide an indication of the direction of energy flow, assuming the damping rate in each system is roughly the same.

While the longest period peaks seen in Fig. 2.7 are likely coastal modes, and the shortest period peaks are likely harbor modes, these conjectures need to be demonstrated with high certainty. *Munger and Cheung* (2008) used a nonlinear shallow-water model to reconstruct the amplification and oscillation patterns that resulted from the Kuril Islands tsunami that hit the Hawaiian Islands on November 15, 2006. Their model results around O'ahu Island (see Fig. 2.16) indicate that the tsunami excited coastal modes at a number of IG periods ranging from 6 min to 24 min, where the latter appears to be the gravest mode of the North Shore of the island. These modes have relatively strong amplitudes on the North Shore of O'ahu and occur at periods similar to those observed in the IG band of Hale'iwa sea level spectra (e.g., see Figs. 2.6, 2.7, and 2.14).

To begin the process of sorting out coastal from harbor modes, we calculate coherence amplitude and coherence phase between a site in the harbor and another site at the coast, during times of weak-to-moderate SS forcing when oscillations in the harbor and at the coast are primarily modal (see Section 2.3.1). Subsequently, using the method employed by *Okihiro et al.* (1993), we calculate the averaged spectrum of energy amplification, A, between the harbor and the coast, as a further test of the existence of harbor modes:

$$\langle A(\xi_1, \xi_2, f)\rangle = \frac{1}{N}\sum_{j=1}^{N}\left(\frac{S^j_{\xi_2}(f)}{S^j_{\xi_1}(f)}\right), \tag{2.1}$$

where $S^j_{\xi_i}(f)$ is the smoothed power spectral density at site ξ_i $(i = 1, 2)$ and frequency f, and N is the number of independent spectra to be averaged.

For a particular pair of harbor and coastal sites, we try to identify frequencies (or frequency bands) with statistically significant high coherence amplitudes and corresponding coherence phases that are stable around 0° or 180°, which would tell us that the harbor and the coast (at these particular sites) are connected with a simple modal spatial structure. In addition, the corresponding energy amplification, A, will help determine whether the oscillations are dominant in the harbor (high amplification), or at the coast (low amplification). If for given frequencies (or frequency bands) the coherence amplitudes are low and the corresponding coherence phases are random, this tells us that the two systems are independent, as long as neither site is located at a node (the spatial distribution of nodes/antinodes of several period bands of interest, is determined in Chapter 4). The corresponding energy amplification will then tell us whether the oscillations are purely of the harbor (high amplification), or purely coastal (low amplification).

Another useful variable is the cross-spectral gain, $G_{xy}(f)$, for a pair of forcing/input and response/output sites:

$$G_{xy}(f) = \frac{|S_{xy}|}{S_{xx}}, \tag{2.2}$$

where S_{xy} is the one-sided cross-spectrum between the forcing/input (x) and the response/output (y), and S_{xx} is the one-sided autospectrum of the forcing/input. The 95% error bars for independent spectrum estimates are calculated following Eq. 4.1 in *Walden* (1986). Through the cross-spectrum term, the gain provides information regarding whether the input (x) and the output (y), are connected.

2.4.2 Bound Wave Impacts; Generation of Leaky and Edge Waves (Hypotheses B3, C3, C4, & C5)

To test these hypotheses we first follow a qualitative analysis (*Elgar et al.* 1992; *Ruessink* 1998) that will allow us to see whether the total IG wave energy is composed mostly of free or bound waves under particular SS conditions. This method involves calculating the total IG energy at two different depths (E_{IG,h_1} and E_{IG,h_2}, where $h_1 < h_2$), plotting the scatter between these energies, and observing where the cloud of data lies with respect to theoretical curves for free and bound IG waves.

The energy at a given depth is calculated following the same procedure that was described earlier in this section for the spectrograms. For a given time step, we then sum the energies in the 30 sec - 6 hr period band. The theoretical relationship between the total IG energy at depths h_1 and h_2 for the case of bound waves forced by normally-incident long waves (*Longuet-Higgins and Stewart* 1962), is

$$\frac{E_{IG,h_1}}{E_{IG,h_2}} = \big(\frac{h_1}{h_2}\big)^{-5}. \tag{2.3}$$

For normally-incident free waves (*Eckart* 1951), the relationship is

$$\frac{E_{IG,h_1}}{E_{IG,h_2}} = \big(\frac{h_1}{h_2}\big)^{-1/2}. \tag{2.4}$$

Taking the log on both sides of Eq.(2.3), and define $x = log(E_{IG,h_2})$, and $y = log(E_{IG,h_1})$, we obtain an equation of a straight line, $y = ax + b$, where $a = 1$ and $b = log\big[\big(\frac{h_1}{h_2}\big)^{-5}\big]$. Following a similar derivation for the case of freely propagating edge waves, we find that the y-intercept is $b = log\big[\big(\frac{h_1}{h_2}\big)^{-1}\big]$, and for the case of freely propagating leaky waves it is $b = log\big[\big(\frac{h_1}{h_2}\big)^{-1/2}\big]$. Therefore, on a loglog plot the theoretical lines of the free edge, free leaky, and bound waves, have the same slopes but different y-intercept values, resulting in the lines of free IG waves lying below the line of bound IG waves. The location of the scatter of data relative to the lines of free and bound waves will tell us whether free waves, bound waves, or a mixture of the two, best describe the wave field around these depths.

Next, we seek to determine whether the free IG wave energy was generated by the release of bound waves from the SS groups, or by some other non-linear mechanism such as the time-varying breakpoint mechanism described by *Symonds et al.* (1982). This can be done by calculating the coherence amplitude and coherence phase of the SS wave envelope ($\eta_{ss,env}$) versus the sea level signal η at IG periods. (*Masselink* 1995; *Baldock and Huntley* 2002; *Péquignet et al.* 2009; *Contardo and Symonds* 2013).

A signature of bound waves is obtained if the coherence amplitude at IG periods between $\eta_{ss,env}$ and η at the same location is statistically significant, and the corresponding coherence phase is near 180°, with a possible shift towards 90° as we get closer to shore (*Elgar and Guza* 1985; *Baldock* 2012).

In the case of free waves that were released from bound waves, $\eta_{ss,env}$ and η at the same location are expected to be statistically incoherent. However, $\eta_{ss,env}$ at an offshore site outside the surf zone and η at shoreward sites within the surf zone should be statistically coherent with a coherence phase near 180°, with a possible shift towards 90°.

We calculate the SS wave envelope, ρ, using the surface elevation and its Hilbert transform (*Janssen et al.* 2003):

$$\rho = |\eta_{hf} + i\hat{H}(\eta_{hf})|_{lf}, \tag{2.5}$$

where hf is high frequency ($T \leq 30$ sec), lf is low frequency ($T > 30$ sec), η_{hf} is the high frequency sea level, and $\hat{H}$ is the Hilbert transform operator.

To obtain additional clues regarding the type of IG wave that triggers the harbor oscillations, we will contrast the coherence analyses between the sea level observations from available harbor and coastal sites (the same analyses employed to evaluate hypotheses A1, A2, B1, B2, C1, and C2) with coherence analyses between the envelope of offshore SS amplitude, $\eta_{ss,env}$, and sea level, η, from sites inside the harbor.

2.4.3 The Role of Time-Varying, SS-Driven "Setup" (Hypotheses C6 and D1)

To test these hypotheses we will be applying a coherence analysis to a cross-shore array that extends offshore of the surf zone during large SS forcing conditions. To find a signature of setup that was induced by the breaking of SS wave groups, we are looking for the following evidence:

1. High coherence amplitude and coherence phase near 180°, between the sea level height offshore of the breakpoint and the sea level height shoreward of the breakpoint, since

there is a set-down offshore of the breakpoint and setup seaward of the breakpoint (*Bowen et al.* 1968).

2. High coherence amplitude and ∼ 0° coherence phase at IG periods between the envelope of SS wave amplitudes ($\eta_{ss,env}$) outside the breakpoint, and sea level, η, within the surf zone. This is what we would expect if the setup is induced by the SS wave groups.

Given a deep-ocean significant wave height (H_∞) and a peak period (T_p) for the SS waves, the set-down of the sea level offshore of the breaking wave zone, the location and wave height at the point of wave breaking, and the setup within the surf zone, can be calculated as follows:

1. Apply conservation of energy flux and use linear wave theory to calculate the evolution of the offshore significant wave height, H_{off}, and the set-down, $\bar{\eta}$, up to the breakpoint:

$$H_{off} = H_\infty \sqrt{\frac{C_\infty}{2Cn}}, \tag{2.6}$$

   where $C = \frac{gT}{2\pi} tanh\left(\frac{2\pi h}{L}\right)$ is the phase speed, C_∞ is the phase speed at infinity, T is the wave period, $n = \frac{1}{2}\left(1 + \frac{2kh}{sinh(2kh)}\right)$, $k = \frac{2\pi}{L}$ is the wavenumber, L is the wavelength, and h is the local water depth.

$$\bar{\eta} = -\frac{kH_{off}^2}{8sinh(2kh)}, \tag{2.7}$$

   where the mean water level here, $\bar{\eta}$, is the wave-induced set-down (*Longuet-Higgins and Stewart* 1964).

2. Use the breaker height index, $\gamma_b = \left(\frac{H}{h}\right)_b$ and set it to $\gamma_b \simeq 0.78$ (*Thornton and Guza* 1982) to find the breakpoint location and the wave height at the breakpoint. Using Eq.(2.6) and taking set-down into account, we obtain:

$$\gamma_b = \left[\frac{H_\infty}{d}\sqrt{\frac{C_\infty}{2Cn}}\right]_b \simeq 0.78, \tag{2.8}$$

where $d = \bar{\eta} + h$ is the mean water level plus the local water depth.

3. Find the wave height decay through the surf zone using the similarity method (*Thornton and Guza* 1982), and calculate the setup within the surf zone:

$$H_{sz} \simeq 0.42d, \tag{2.9}$$

where H_{sz} is the surf zone significant wave height, and H_{sz}/d approaches 0.42 for a saturated inner surf zone.

The setup within the surf zone is (*Longuet-Higgins and Stewart* 1964):

$$\bar{\eta} = -\int dx \left(\frac{3}{16} \frac{1}{\bar{\eta} + h} \frac{d(H_{sz}^2)}{dx} \right). \tag{2.10}$$

2.4.4 Large-Scale Modes of the Hawaiian Islands (Hypothesis D2)

We apply a coherence analysis for pairs of sea level sensors at different sides of O'ahu Island and between several Hawaiian Islands. We look for high coherence amplitude values with corresponding coherence phases around 0° or 180°. We apply this analysis for data collected during times of weak and strong SS forcing, in order to see whether any such island-wide modes are triggered under minimal background SS forcing levels (e.g., by local winds), or maybe strong SS forcing levels are needed to trigger them. We also generate PSD plots for each site to identify the dominant spectral peaks. Any spectral peaks identified from the above auto- and cross-spectral analyses are compared to model-predicted modes from the studies of *Munger and Cheung* (2008) and *Cheung et al.* (2013).

2.4.5 Free IG energy from remote sources (Hypothesis A0)

By combining coastal sea level records and deep-water sea level records (obtained from bottom pressure measurements) from sites that are exposed to the NW and NE of O'ahu

Island, we will look for a signature of free IG waves that arrive from remote sources such as the Northwest U.S. coast (*Webb et al.* 1991; *Aucan and Ardhuin* 2013).

Under SS forcing that arrives from the NW direction, the free IG wave field along the north shore coast is mostly generated locally, either by nonlinear interactions (among SS waves or with the local bathymetry) at the coast, or as released bound waves. When SS is relatively weak, there may be times when IG waves generated remotely (such as on the northwest shores of North America) are strong enough to be an important forcing source of coastal and harbor IG waves on the North Shore of O'ahu. When investigating this path of IG energy, we look at the significant wave height in the 1-20 min IG period band ($H_{sig,IG}$) at each deep-water site (sites 11 & 12 in Fig. 2.3), and identify time periods when SS levels are minimal and $H_{sig,IG}$ at the NE site ($H_{sig,IG;NE}$) is greater than $H_{sig,IG}$ at the NW site ($H_{sig,IG;NW}$). Under such conditions, free IG waves arriving from remote sources could potentially be important and maybe even dominate the locally-generated IG waves. IG wave energy at the deep-water ($\sim$ 2000m) sites is most likely dominated by free, rather than bound, IG waves, since the bound waves decay quickly in the vertical like the SS waves in the groups to which the IG waves are bound.

We calculate $H_{sig,IG}$ by applying a 4^{th}-order Butterworth band-pass filter to isolate only variability in the 1-20 min period band, and then every 15 min averaging 30 min of data (i.e., resulting in 50% overlap between adjacent data points). For the case of $H_{sig,IG;NE} > H_{sig,IG;NW}$ under minimal SS conditions, a coherence analysis between sites 11 and 12 is being used to identify coherent signals where site 12 (located northwest of O'ahu) leads site 11 (located northeast of O'ahu), which would support the idea that the free IG wave field arrives somewhere from the west coast of America. To further try and estimate the region from which the free IG waves arrives, we follow *Filloux et al.* (1991) and assume plane wave propagation to calculate the phase lag between the two stations (Φ):

$$\Phi(\omega) = \frac{360}{2\pi} Dkcos(\theta), \tag{2.11}$$

where D is the distance between the two sites, $k = k(\omega)$ is the wavenumber of the gravity waves, θ is the propagation angle of the waves relative to the line connecting the two sites, and ω is the radian frequency and is calculated from the dispersion relation of gravity waves:

$$\omega^2 = gktanh(kH), \tag{2.12}$$

where g is the gravitational acceleration, and H is the local ocean depth at the location of the sites (assuming the sites are located at the same depth). By calculating Φ for several possible propagation angles (θ), we overlay Φ on the observed coherence phase ($\phi_{\eta,\eta}$) to find the value of θ that results in the best fit. Finally, we use this value of θ to estimate the region from which the free IG waves arrived.

Alternatively, simple concepts from linear wave theory can be applied to the shallow- and deep-water sea level datasets to determine whether the offshore IG wave field contains sufficient energy to trigger the observed response at the coast at particular IG period band/s. We start by assuming that the energy flux (F) of the gravity wave field is conserved as the waves propagate from deep to shallow water. Assuming a unidirectional wave field, the energy fluxes at the shallow water site (1) and deep water site (2), are:

$$F_1 = (EC_g)_1 = E_1 C_{g;1}, \tag{2.13}$$

$$F_2 = (EC_g)_2 = E_2 C_{g;2}, \tag{2.14}$$

where E is the energy density, C_g is the gravity wave group velocity, and the subscripts 1 and 2 represent the shallow and deep water sites, respectively. Then setting $F_1 = F_2$ yields the following relationship:

$$E_2 = \frac{C_{g;1}}{C_{g;2}} E_1, \tag{2.15}$$

where $C_{g;1,2}$ is obtained from the kinematics of linear gravity waves:

$$C_{g;i} = \left(\frac{gT}{4\pi}\right) tanh\left(\frac{2\pi h_i}{L}\right)\left[1 + \frac{\frac{4\pi h_i}{L}}{sin(\frac{4\pi h_i}{L})}\right], \tag{2.16}$$

where $i = 1, 2$, T is the period of the gravity wave, and h_i is the water depth at site i. The same relationship holds if the energy density, $E_{1,2}$, is replaced with the power spectral density, $PSD_{1,2}$, since they only differ by a normalization factor.

Using the PSD at the shallow water site, PSD_1, Eqs.(2.15) and (2.16) can be used to calculate a hypothetical spectra at a deep water site, PSD_2. Note that PSD_2 is the hypothetical spectra at site 2, but at depth h_1, and it needs to be adjusted to account for the depth decay of the pressure signal to yield PSD_2 at depth h_2.

If for a given deep-water site (sites 11 or 12) the projected deep-water spectra is significantly greater than the observed deep-water spectra at the IG band of interest, that means that it is unlikely that the energy of the offshore IG wave field significantly contributes to the coastal IG response. On the other hand, if the levels of the hypothetical and observed spectra at the deep-water site are comparable, that would suggest that the observed coastal IG oscillations could possibly be triggered by the offshore IG wave field.

2.5 Analysis and results

For initial exploration of Hale'iwa Harbor's response to offshore SS forcing we generated monthly spectrogram plots. Using sea level datasets at sites 10 and 1, Figures 2.17 and 2.18 clearly reveal a one-to-one correspondence between the offshore SS forcing and the IG response in Hale'iwa Harbor. There are also faint horizontal ridges of PSD that at all times appear at the approximate periods of 6, 8, 12.5, 18, and 23 min. These appear to be the fundamental modes of oscillations of Hale'iwa Harbor region (harbor and/or coast), and are excited even when SS forcing amplitudes are minimal. The one-to-one correspondence between offshore SS forcing and harbor IG response, and the horizontal ridges of PSD, are seen in all of our spectrogram plots when both offshore SS and harbor IG data were available between the years 2001 - 2010. The high-frequency datasets from the 2011/2012 and 2013/2014 deployments at sites inside the harbor have also revealed the same faint horizontal ridges of PSD in the 6-23 min period band (see Figs. 2.19 and 2.20). In addition, they also reveal a horizontal ridge near 90 sec, but it is nearly absent during times when SS forcing levels become minimal. The low frequency band of energetic spectra slightly past day 90 in Fig. 2.20, is the result of a magnitude 8.2 tsunami event that originated from Northern Chile. Focusing on the short-period IG band from 0.5-2 min in the 2013/2014 dataset, the spectrogram in Fig. 2.21 reveals additional ridges with the strongest one at 47 min, a weaker one at 66 min, and a faint hint of what could potentially be an additional ridge at 43 min. The same results (not shown here) are obtained in the 0.5-2 min period band of the 2011/2012 dataset.

As will be shown in greater detail in Chapter 3, the correspondence between the coastal and harbor IG energy response to the energy of the offshore SS forcing, E_{ss}, does not appear to be very tight. The relationship is greatly improved when taking into account the periodicity and direction of the incoming SS wave field, incorporating them into a new SS parameter, $F_{ss,cf}$, the energy flux propagating perpendicular to shore.

In Fig. 2.22 we see a scatter plot between $F_{ss,cf}$ at site 10 and the harbor IG sea level response at site 1 (Harbor $S_{\eta,\eta}$). It shows that there is a white noise level in each of these IG period bands. In the high frequency IG band (4-10 min), the initial increase in the harbor spectra above the white noise level occurs at relatively low SS forcing levels, whereas this initial increase shifts to higher SS forcing levels at the lower frequency IG bands (10-15 min and 15-40 min). The relationships are better defined after bin-averaging is applied to the cloud of data (while keeping a fixed number of data points), and then a curve is fit through the averages using the smoothing spline interpolation technique (MATLAB function: spaps). The resulting curve fits are the red curves in Fig. 2.22.

2.5.1 Excitation of Linear Coastal or Harbor Modes (Hypotheses A1, B1, C1, A2, B2, & C2)

In this section we search for evidence showing that the free IG oscillations have a cutoff frequency separating purely coastal and purely harbor oscillations; or, possibly a range of frequencies exists where there is overlap between the coastal and harbor oscillations, meaning that the coastal and harbor systems are connected and may exchange energy. Sea level records from the 11/2011 - 05/2012 deployment are used to look at the coherence amplitude, coherence phase, and amplification, between the harbor and a nearby offshore site (we average spectra from five three-day long blocks taken from the strongest/weakest SS events during 11/04/11 - 01/31/12). As was described above in Section 2.4.1, the coherence amplitude and phase can provide information regarding the possible existence of modes, and whether the oscillations of the coastal and harbor systems are connected (high coherence amplitude and in/out of phase), or possibly the systems oscillate independently (statistically insignificant coherence amplitude, as long as neither site is located at a node). The amplification, A, will determine whether the oscillations are more energetic at the coast or within the harbor, and the gain will add information (through the cross-spectrum term) regarding whether the forcing at the coastal site, and the response at the harbor site, are connected.

The coherence amplitude ($\gamma_{\eta,\eta}$), coherence phase ($\phi_{\eta,\eta}$), amplification (A), and gain (G) between sites 1 and 6, approximately 2 km apart (see Figs. 2.1 and 2.2 for exact locations), are seen in Fig. 2.23. Under weak SS forcing conditions (blue curves), oscillations at periods longer than ∼12 min are highly coherent having coherence phase values that are stable around 0°, indicating a harbor-coastal system that exchanges energy. Under strong SS forcing conditions (red curves) the coherence amplitude is greatly reduced at periods longer than ∼12 min, possibly due to the nonlinear excitation by SS of a broad spectrum (in wavenumber) of IG waves along the coast. The exceptions are at particular periods, i.e., ∼23 min and ∼18 min, where large scale coastal modes of the north shore coast have been identified (e.g., Fig. 2.6, Fig. 2.7, and Fig. 2.16). At these periods, the coherence remains high under strong SS forcing.

In the 3 ∼ 12 min period band, the coherence amplitude is lower but still above the 95% level of no significance, with similar levels under weak and strong SS forcing. The coherence phase in this period band has several 180° transitions that are accompanied by sharp decreases in coherence amplitudes, an indication of possible nodes that are being introduced between the two sensor sites as frequency increases. Such transitions most clearly occur at the approximate periods of 12 min and 6 min. To further explore that, we look at

Fig. 2.24, which focuses on the 1-40 min period band in the coherence amplitude and phase plots from Fig. 2.23. The coherence phase here is unwrapped in order to identify periods where sharp transitions occur. Under weak SS we identify 180° transitions at periods of 12 min and 6 min. Under strong SS there is only one clear transition at around $\sim$ 9 min. The greater variability and lower levels of coherence amplitude under strong vs. weak SS forcing, are likely the cause of the shift in the first 180° transition under strong SS forcing. All of these 180° transitions are accompanied by sharp drops in coherence amplitude to the 95% level of no significance, or below it. These phase transitions seen in Fig. 2.24 suggest that the wavelengths of the waves having periods shorter than $\sim$12 min are shorter than the distance between sites 1 and 6, and are at most comparable to the distance between these two stations. This is also supported qualitatively by the numerical model results of *Munger and Cheung* (2008) (compare the panels of the 6 min & 10 min oscillations with the 15 min oscillations around Kaiaka Bay in Fig. 2.16), where we see that the oscillations are confined to a short distance offshore from the coast. In this region, there is significant reflection of IG waves from the shoreline (as will be supported by numerical model results in Chapter 4), which results in destructive interference of the IG waves.

The amplification in the 4 $\sim$ 15 min period band (Figs. 2.23 and 2.24) reveals much higher energy levels inside the harbor, although at this stage it seems like oscillations at these long periods are likely governed by the coastal system and may not be harbor modes, since their corresponding wavelengths are possibly too long to be trapped in a harbor as small as Hale'iwa. A plausible explanation for these high amplification levels that were observed in the harbor at these long periods, is that the water is converging (horizontally and vertically) as it enters the small volume of the harbor, resulting in vertical sea level displacements that are much greater compared to the displacements observed at the coast. This was further studied and supported using numerical model results that are presented in Chapter 4, although it will also be shown that the gravest mode of Hale'iwa Harbor potentially oscillates at a relatively long period of $\sim$6 min. Figs. 2.25 and 2.26 confirm that the variance inside the harbor is greatest in the approximate 5 $\sim$ 15 min period band, and is much smaller in this period band outside the harbor at site 6. This was further studied and supported using numerical model results that are presented in Chapter 4. Another possibility is that the location of site 6 at the coast is where the sea level variability in the 4 $\sim$ 15 min band is relatively weak. The numerical model results of Chapter 4 qualitatively suggest that this is possible. The bottom panel of Fig. 2.23 shows that there is very little cross-spectral gain between sites 1 and 6, meaning that the forcing at site 6 does not contribute much to the response at site 1 in this particular period band. As was mentioned above, this result could be sensitive to the position of site 6 at the coast.

In the 75 sec $\sim$ 3 min period band (Figs. 2.23 and 2.24), the coherence amplitudes are very close to the 95% level of no significance, an indication of decoupling in this band between the harbor and coastal systems. The corresponding amplification in this band, being generally less than 1, suggests that oscillations in this period band are primarily coastal. An exception is the 90 sec period where the harbor is more energetic, and the amplification exceeds 1, although the gain does not. The concomitant slightly higher coherence amplitudes imply that around this period energy is possibly being exchanged between the harbor and the coast. Fig. 2.26 confirms that the variance at 90 sec is relatively high inside the harbor. At periods shorter than 75 sec in Fig. 2.23, the coherence amplitude is statistically insignificant, and the corresponding coherence phase varies in a random fashion. This implies that the harbor and coastal systems are not exchanging energy. Other than at 90 sec, the amplification in this band indicates more energy at the coast, and no gain from site 6 to site 1.

To identify any spatial variation in the coherence amplitude, coherence phase, amplification, and gain, between the harbor and offshore, we used datasets from the 11/2013 - 05/2014 deployment (see Figs. 2.1 and 2.2 for exact locations), and applied a similar spectral analysis between harbor sites 1, 2, and 4, versus offshore site 7, which is about 50% further west from the harbor than site 6 discussed above. We averaged spectra from four three-day long blocks during strong and weak SS events in that time period (see Table 2.4 for exact time periods).

The coherence, amplification, and gain analyses at these four harbor sites are seen in

Figs. 2.27-2.29, and reveal results that are qualitatively very similar to the ones seen with the 2011/2012 datesets (Fig. 2.23). The lower values of coherence amplitudes in the 30 min to ∼ 4 hr period band, and the difference between the amplifications during weak and strong SS at periods longer than ∼30 min, are all likely due to the greater distance that exist between these pairs of sites as compared to the distance between sites 1 and 6. Again here, the PSD and variance preserving plots (Figs. 2.30 and 2.31) reveal the dominant period bands inside the harbor and at the coast.

To get an idea of the coherence along the coast under weak and strong SS forcing, we applied a coherence analysis between sites 6 and 9, about 7 km apart. Despite the larger distance, the result (Fig. 2.32) is qualitatively quite similar to the harbor versus near-coast coherences under weak and strong forcing. Under weak SS forcing, Fig. 2.32 shows that the coherence amplitude is very high at periods longer than ∼15 min, and is greatly reduced at shorter periods. There are, however, particular peaks in the coherence amplitude that appear to be separated by relatively sharp minima. Those minima occur around the approximate periods of: 12, 9.5, 7.5, 5.5, 3.5, 2.5 min, and possibly others, and some of them (e.g., 9.5, 5.5, 3.5, and 2.5 min) also appear to be accompanied by relatively sharp coherence phase jumps near ∼ 180°, indicating the possible existence of modes. We previously identified signatures of modes near these particular periods. At shorter periods, the coherence amplitude is much lower, but still statistically significant down to ∼1 min. During strong SS forcing, the coherence is greatly reduced compared to the weak SS forcing case, as in the harbor versus coast coherence, with the exception of the 23 min period where the coherence is very high, being nearly 1. Fig. 2.32 shows that the coherence along the coast, like the harbor versus coast coherence, is reduced once SS forcing levels become large.

The qualitative difference between the coherence amplitude levels during weak and strong SS forcing is not expected to change significantly for pairs of sensors closer together along the coast. The distance of the sites 6 and 9 from shore should also lower the coherence amplitude levels of short oscillation periods of the order of minutes, since oscillations at short periods will not extend far offshore and may not reach sites 6 and 9. Both these conjectures of the

IG variability can be tested with the model described in Chapter 4.

The evidence presented so far - observed auto-spectra, coherences, amplification factors and gains - in conjunction with published model-data comparisons during the occurrences of tsunamis at Hawai'i, supports the conclusion that a spectrum of *discrete* natural frequencies, of coastal and perhaps harbor modes, does exist for periods from the "gravest" normal mode of the North Shore of O'ahu at a period of 23 min (*Munger and Cheung* 2008) down to periods as short as perhaps 3 min or even shorter.

The spectra within the harbor (e.g., Figs. 2.7, 2.25 and 2.30), that are based on data collected from the high-sampling-rate sensors deployed in the winters of 2011/2012 and 2013/2014, along with the lack of coherence between harbor and coastal sensors at periods shorter than ~3 min (e.g., Figs. 2.23, 2.27- 2.29), strongly suggest that the harbor has its own natural modes at several periods $\leq$ 3 min, with the best example at 90 sec period. The amplification factor suggests a resonance of the harbor at 90 sec (e.g., Figs. 2.23, 2.27, 2.28), but the gain does not. However, these metrics are subject to a great deal of positional dependence within the harbor (as seen in the variations among the amplification factors in Figs. 2.27- 2.29), and probably outside the harbor as well. The numerical model presented in Chapter 4 permits quantification of the positional changes in spectra and coherences of modal and non-modal IG variability.

Most importantly, the spectra and coherences clearly indicate that whatever modes might be excited by weak SS forcing, in the harbor or at the coast, these modes become nearly irrelevant for explaining the broad-banded suite of IG oscillations that tend to smooth out the auto-spectra and greatly reduce horizontal coherence under strong SS forcing.

2.5.2 Bound Wave Impacts; Generation of leaky and edge waves (Hypotheses B3, C3, C4, & C5)

To build an understanding of the processes that determine the IG wave field variability in Hale'iwa Harbor and its vicinity, we need to have an array of SS and IG wave observations from the nearshore to offshore. Such observations were not available to us near the harbor, but observations collected from a cross-shore array ~ 5.5 km west of the harbor (Mokuleia stretch of coast, sites 8a-8c in Fig. 2.2), were given to us by Mark Merrifield and Janet Becker. Much of the analyses in this section involve the use of datasets from these observations at Mokuleia, and these are complemented with observations from inside the harbor and one outside (from the 2011/2012 deployment), in order to shed some light on the variability of the IG wave field closer to the harbor.

2.5.2.1 Auto- and Cross-Spectral Analysis Applied to the Mokuleia Experiment

The 12m and 6m Mokuleia datasets (sites 8a and 8b in Fig. 2.2) were used to explore the relative strengths of bound and free IG waves per the relationship described in Section 2.4.2. For each of the weak, moderate, and strong SS cases we use two 3-day long time series (see Table 2.4 for exact time periods). The IG energies, $E_{IG,6}$ and $E_{IG,12}$, at these two sites are contrasted in scatter plots in Fig. 2.33, where the IG energies have been sorted according to the strength of SS forcing: weak (panel a), moderate (panel b), and strong (panel c) SS. Power law fits (two straight lines: $y = f(x)$ and $x = g(y)$, ploted on loglog axes, with corresponding slope and y-intercept values indicated on each plot), and correlation coefficient (r), are shown on each plot. The possible theoretical relationships between the IG energies at 6m and 12m (see Section 2.4.2) are plotted as straight dotted lines for the case of bound waves, $\left(\frac{h_6}{h_{12}}\right)^{-5}$, edge waves, $\left(\frac{h_6}{h_{12}}\right)^{-1}$, or leaky waves, $\left(\frac{h_6}{h_{12}}\right)^{-1/2}$.

From Fig. 2.33, we see that under weak and moderate SS conditions the IG wave field is composed mostly of free waves as the cloud of data are lined up with the theoretical lines for edge and leaky waves. Under strong SS conditions we see that the cloud of data and the corresponding fitted lines are lying between the theoretical lines of bound and free waves, implying that the IG wave field is composed of a mixture of free and bound waves. These results agree with observations made by *Elgar et al.* (1992) at two sites, one in the Pacific and another in the Atlantic. In their study, they found that under weak SS conditions bound waves contributed less than 10% at both 8m and 13m, and under strong SS conditions bound waves contributed about 30% at 13m and 70% – 100% at 8m depth.

Note that in the strong SS case in Fig. 2.33, the group of most energetic data points ($E_{IG,12} > 40$ cm^2) were excluded from the line fit as they do not follow the trend of the remaining cloud of data. We believe that during these strongest SS energy levels the SS breaking point is located between sites 8a & 8b (12m & 6m depths, respectively), in which case the most energetic waves will break further offshore from site 8b and will show more energy loss by the time they reach site 8b. In fact, we calculated the wave transformation for these weak, moderate, and strong SS conditions, and we found that the breaking point lies between sites 8b and 8c under weak and moderate SS conditions (not shown), and between sites 8a and 8b under strong SS conditions (see subsection 2.5.3).

Fig. 2.34 shows results from the same analysis, applied to the pair of sites that are located closest to shore: 8b & 8c (6m & 2m depths, respectively). Here, we see that under weak and moderate SS forcing conditions the IG wave field is composed of leaky waves. Under strong SS forcing conditions, the cloud of data shifts away from all three theoretical lines, but it remains closest to the line of leaky waves. Since in subsection 2.5.3 we show that under similar SS forcing conditions sites 8b and 8c are located well within the surf zone, the above results suggest that any bound wave energy arriving from offshore transforms into freely propagating waves that are predominantly leaky well within the surf zone.

Sea level datasets from the cross-shore array at sites 8a, 8b, and 8c, (12m, 6m, and 2m, respectively) at Mokuleia, are used to calculate the coherence amplitude and coherence phase between the SS wave envelope ($\eta_{ss,env}$) and sea level (η) at each of these locations and for pairs of locations, for weak and strong SS forcing cases (see Table 2.4 for exact time periods). Using these we are looking for signatures of free or bound IG waves. Here, we follow a methodology similar to the one employed by *Contardo and Symonds* (2013). At a single site, given high levels of coherence amplitude of $\eta_{ss,env}$ vs. η: (i) a corresponding coherence phase near/at 0° would be the expected signature of locally generated IG waves (leaky or edge); and, (ii) a corresponding coherence phase near/at 180° would be the expected signature of bound IG waves. For a pair of sites, given high coherence amplitude of $\eta_{ss,env}$ at a seaward site vs. η at a shoreward site: (i) a corresponding coherence phase near/at 0° would be the expected signature of free IG waves (leaky or edge); and, (ii) a corresponding coherence phase near/at 180° would be the expected signature of IG waves that are either bound IG, or are release-bound (i.e., free). For the latter case, if in addition $\eta_{ss,env}$ and η are coherent at the seaward site and (iia) coherent at the shoreward site, then it is the signature of bound IG waves; (iib) incoherent at the shoreward site, then it could potentially be the signature of released-bound IG waves. We should keep in mind, however, that the expected coherence phase of 180° for bound waves is based on the assumption that the IG wave field is unidirectional.

The PSD of $\eta_{ss,env}$ and η at a given site, under weak (left column), and strong (right column) SS forcing, are seen in Fig. 2.35. We first note the clear expression of the free IG modes at 12.5 and 23 min periods under weak SS forcing at sites 8a (12m depth; Fig. 2.35a, dark red curve), and 8b (6m depth; Fig. 2.35b, dark red curve). Under strong SS forcing, the two mode peaks have effectively disappeared at the offshore-most site, 8a (Fig. 2.35d, dark red curve). Under strong SS forcing, the spectral levels of $\eta_{ss,env}$ are nearly two orders of magnitude higher at the offshore-most site, 8a (compare black curves in Fig. 2.35a and d)), about an order of magnitude higher at the middle site, 8b (compare black curves in Fig. 2.35b and e), and less than an order of magnitude higher at the site closest to shore, 8c (compare black curves in Fig. 2.35c and f).

For a given site (at each of the sites 8a-8c), under weak SS forcing, the coherence between $\eta_{ss,env}$ and η, is shown in Fig. 2.36. At site 8a (12m), the coherence amplitude is weak at the 12.5 and 23 min mode peak periods (Fig. 2.36a), as would be expected if a free coastal mode is dominant. At shorter periods, the coherence amplitude is stronger and significant, but does not imply a dominant relationship between the SS waves and IG waves. The phase at these shorter periods, when the coherence amplitude is well above the 95% level of no significance, fluctuates around 180°, indicative of the presence of bound waves. Very similar results are obtained for site 8b (6m) at periods shorter than ∼8 min (Fig. 2.36c,d). At site 8b in the 8-120 min period band, $\eta_{ss,env}$ and η are incoherent. This lack of coherence could be explained as being due to the release of IG variability that had been bound to SS variability at site 8a, but was then released and propagated freely between sites 8a and 8b. At site 8c (2m), $\eta_{ss,env}$ and η are incoherent at nearly all periods, except at periods shorter than ~ 90 sec (Fig. 2.36e,f). This suggests that most bound waves have been released as free IG waves offshore of site 8c. In addition, the IG wave field at site 8c may contain free waves that are generated locally during SS wave breaking (*Péquignet et al.* 2014). As stated earlier, the breakpoint for any non-trivial SS waves arriving at Mokuleia is expected to almost always be offshore of site 8c.

For a given site (at each of the sites 8a-8c), under strong SS forcing, the coherence between $\eta_{ss,env}$ and η, is shown in Fig. 2.37. At site 8a (12m), the coherence amplitude between $\eta_{ss,env}$ and η is now very high at periods of $\sim$3 hours and less (Fig. 2.37a). The corresponding coherence phase is consistently near or at 180° (Fig. 2.37b), suggesting that bound waves are the dominant form of IG waves at this site under strong SS forcing conditions. Since the spectrum of the SS envelope was found to be two orders of magnitude higher under strong SS forcing and has a relatively uniform value in the coastal mode period band of 6-23 minutes (Fig. 2.35, compare black curves in panels a and d), it's clear that the bound IG wave energy is overwhelming the free IG mode peaks that are so clearly present under weak SS forcing conditions. The only hints of the existence of the two IG modes under strong SS forcing are the slight dips of the coherence amplitude around the periods of 12.5 and 23 min (Fig. 2.37a). At site 8b (6m), $\eta_{ss,env}$ and η are significantly but not strongly coherent for periods shorter than ~ 8 min, and the corresponding coherence phase is generally close to 180°, with some shift towards 90° (Fig. 2.37c,d). This result is very similar to the one obtained at this site under weak SS forcing (Fig. 2.36c,d), suggesting that at periods shorter than ~ 8 min the IG variability may be generated by bound waves, but these are likely not the dominant form of IG waves at site 8b. Across most of the 8-120 min period band, $\eta_{ss,env}$ and η are significantly but not strongly coherent, and the corresponding coherence phase fluctuates between $120° - 180°$. This suggests that the IG variability at this site may be composed of bound waves, but some forms of free IG waves may be important as well (i.e., leaky, edge). At site 8c (2m), the coherence amplitude between $\eta_{ss,env}$ and η is significantly high at periods shorter than $\sim$ 20 min, and the corresponding coherence phase is, on average, close to 0°. This suggests that bound waves are no longer important at the shallow site 8c, that free waves dominate the IG oscillations, and that those free waves are somehow linked to the local SS waves. One possibility is that those free IG waves are generated by the time-varying breakpoint mechanism of *Symonds et al.* (1982) (also, *Péquignet et al.* (2009); *Contardo and Symonds* (2013)).

For pairs of sites, under weak SS forcing, Fig. 2.38 shows the coherence amplitude and phase between η vs. η (orange curves), and $\eta_{ss,env}$ at a seaward site vs. η at a shoreward site (black curves). For the pair of sites 8a & 8b, the coherence amplitude of η vs. η is very high at long periods, and is sharply dropping at certain periods (e.g., at $\sim$3.5 min, and 1 min, in Fig. 2.38a, orange curve). The corresponding coherence phase is stable around 0° at long periods, and jumps by $\sim$ 180° at the periods where the coherence amplitude sharply drops (e.g., at $\sim$3.5 min, and 1 min, in Fig. 2.38b, orange curve). The PSD at site 8b under weak SS forcing conditions (Fig. 2.13, blue curve) shows broad spectral peaks around 3.5 min and 1 min, suggesting that the drops in coherence amplitude and corresponding coherence phase transitions seen in Fig. 2.38a,b are the result of modal oscillations. The corresponding coherence amplitude of $\eta_{ss,env}$ vs. η is low and significant only at periods shorter than $\sim$8 min (Fig. 2.38a, black curve), where the corresponding coherence phase varies from positive to negative phases continuously (negative phase difference), implying propagation towards shore (Fig. 2.38b, black curve) at these periods. Very similar results are obtained for the pairs of sites 8a and 8c (Fig. 2.38c,d), and 8b and 8c (Fig. 2.38e,f), except that the coherence amplitude in the $\sim$15-200 min period band has decreased for η vs. η and increased for $\eta_{ss,env}$ vs. η (except for the strong minimum near 23 min that is likely due to the oscillations of the 23 min North Shore mode). The corresponding coherence phases (for η vs. η and $\eta_{ss,env}$ vs. η) in the $\sim$15-200 min period band fluctuate around 0°. In section 2.5.3 we will discuss the possibility that this is SS-induced "setup" variability. For the pairs of sites in Fig. 2.38, the relatively low coherence amplitude levels of $\eta_{ss,env}$ vs. η do not allow us to identify an energy pathway that involves a particular type of IG waves (i.e., bound, leaky, edge); however, the higher coherence amplitude levels of η vs. η with corresponding 0° coherence phase and subsequent 180° transitions that coincide with broad spectral peaks, are an indication that the local mode structure is dominant at these Mokuleia sites under weak SS forcing conditions. At periods shorter than $\sim$4 min, we see high coherence and clear directional phase propagation (e.g., see Fig. 2.38c,d). As the period of the SS wave groups becomes shorter, the wavelengths shorten to be of the order of the distance between the above pairs of sites, and shorter. For progressive IG waves, if the signals between a given pair of sites are coherent, the corresponding coherence phase will be continuously varying in a certain direction. The phase propagation in the example of Fig. 2.38c,d is shoreward. A detailed investigation of the origin and type of these IG waves will require future analyses.

For pairs of sites, under strong SS forcing, Fig. 2.39 shows the coherence amplitude and phase between η vs. η, and $\eta_{ss,env}$ at a seaward site vs. η at a shoreward site. In Fig. 2.39a,b we see that $\eta_{ss,env}$ at 8a vs. η at 8b (black curve) have relatively low coherence levels that are statistically significant in the $\sim$8-200 min period band, with corresponding coherence phase values fluctuating close to 0° across most of that band (with an exception around 55 min). At periods shorter than $\sim$8 min the coherence amplitude and phase suggest waves propagating shoreward. For η at 8a vs. η at 8b (orange curve), the coherence amplitude behaves very similar to the black curve, but the coherence phase is closer to 180° across much of the 15-150 min period band. Qualitatively, very similar results are obtained for the pairs of sites 8a vs. 8c, as can be seen in Fig. 2.39c,d. Here, the coherence amplitude levels between $\eta_{ss,env}$ at 8a vs. η at 8c are slightly higher than the case described above, and the coherence phases are more stable around 0° for $\eta_{ss,env}$ at 8a vs. η at 8c, and 180° for η at 8a vs. η at 8c. Again, similar results are qualitatively obtained for the pair of sites 8b and 8c (Fig. 2.39e,f), except that here the coherence phase is stable near zero for $\eta_{ss,env}$ at 8b vs. η at 8c, and η at 8b vs. η at 8c. As was seen for the case of weak SS forcing (Fig. 2.38), here, under strong SS forcing conditions, we also see directional phase propagation towards shore at periods shorter than ~4 min. As was mentioned above, a detailed investigation of the origin and type of these IG waves will require future analyses.

The above coherence analysis results of $\eta_{ss,env}$ at a seaward site vs. η at a shoreward site, under strong SS forcing conditions, suggest that the IG waves between the different pairs of sites are likely free, generated by the time-varying breakpoint mechanism, or by some other mechanism that is tied to the SS wave groupiness at the offshore site 8a. Nevertheless, the coherence amplitude levels are not very high (especially for the pair of sites 8a vs. 8b), and at most explain 65% of the variance (between sites 8a and 8c). The evidence for the existence of bound IG waves at site 8a (Fig. 2.37), combined with results from the present analysis for pairs of sites (Fig. 2.39), suggests that the bound waves were released as free waves somewhere between sites 8a and 8b. Since we are dealing with very high SS forcing levels, it is likely that the group structure is dramatically altered after wave breaking. Each wave-group bore may become independent of other wave-bores, resulting in wave-groups being randomized as they approach site 8b.

2.5.2.2 Auto- and Cross-Spectral Analysis Applied to the Hale'iwa Harbor Data

In the previous subsection we looked at the IG variability at the coast using the cross-shore array of three sites at Mokuleia. However, these are located ~ 5.5 km west of Hale'iwa Harbor and do not provide us any information regarding the IG variability in the vicinity of the harbor, and how it may be connected to the IG variability inside the harbor. Although the datasets from our 2011/2012 deployment are from only two sites inside the harbor and one ~2 km offshore, these are the best available datasets that we have with a relatively short distance between the harbor and a site at the coast (i.e., the pairs of sites 5 and 6, or 1 and 6). At a given site (done separately for sites: 1, 5, and 6), we look at the PSD of $\eta_{ss,env}$ and η, and coherence analysis between $\eta_{ss,env}$ and η, in order to determine whether the IG variability at these sites is dominated by bound or free IG waves. High coherence between $\eta_{ss,env}$ and η at a given site, with corresponding coherence phase near/at 180°, would suggest the existence of bound IG waves. If the corresponding coherence phase is near/at 0°, that would suggest the existence of free IG waves that were not bound to groups of SS waves. We note that since the 23 min oscillation appears to be the gravest mode of the north shore (e.g., see Figs. 2.7, 2.10, 2.14, and 2.16), it does not seem to be appropriate to use the term ”wave” for oscillations having periods longer than 23 min. An exception is large-scale island-wide and inter-island modes of oscillations, which will be described in Section 2.5.4.

Figs. 2.23 and 2.24 showed the coherence analysis for sites 1 vs. 6. The coherence amplitude is very high at periods longer than ∼12 min with coherence phase near 0°, dropping to lower levels down to ∼3 min with coherence phase changing sharply 180° at ∼12 min and ∼6 min, indicating that at these periods nodes are being introduced between the sites, and changing more gradually at shorter periods, an indication of progressive waves. At periods shorter than ∼3 min, the coherence amplitude is close to the 95% level of no significance, with the exception near 90 sec where it is higher. As can be seen in Fig. 2.40, similar results are qualitatively obtained for the pair of sites 5 and 6, which spans a slightly shorter distance. Nevertheless, the amplification and gain between sites 5 and 6 do not reveal the same pronounced peaks that were seen for the pair of sites 1 and 6, at the periods: 50, 65, and 90 sec. These differences are likely because of the strong positional dependence of the modes, as will be further explored in more detail in the numerical modeling study in Chapter 4. The coherence between sites 1 and 5 inside the harbor is seen in Fig. 2.41. The coherence amplitude is near 1 at periods longer than ∼3 min, with a small dip at a period slightly shorter than 6 min. At the approximate periods of 5-6 min, 90 sec and 60 sec, we identify sharp drops in coherence phase and corresponding ∼ 180° coherence phase transitions that reflect standing wave mode structure. The results are nearly identical under weak and strong SS forcing. Since sites 1 and 5 are located at the inner and outer basins of the harbor, respectively, this result suggests that the mode oscillating around ∼6 min could potentially be a harbor mode. As was mentioned previously, the modes inside the harbor are subject to positional dependence, and the numerical modeling results presented in Chapter 4 will reveal the spatial distribution of certain period bands inside the harbor.

The PSD of $\eta_{ss,env}$ and η at a given site (for sites 1, 5, and 6), under weak (left column), and strong (right column) SS forcing, are seen in Fig. 2.42. Offshore of the harbor at site 6 (17m), we note a clear expression of the free IG mode at 23 min under weak SS forcing (Fig. 2.42a, dark red curve). Even though the spectral levels have increased by about an order of magnitude under strong SS forcing (Fig. 2.42d), the spectral levels of the 23 min mode have barely changed, and it is still pronounced. The spectral levels of the SS envelope has also increased by an order of magnitude between the weak and strong SS cases. Qualitatively, the results inside the harbor (sites 5 and 1; Figs. 2.42b,c,e,f) are very similar, except that there are more peaks as we enter the harbor, and the spectra of the SS envelope (black curves) have significantly lowered to minimal levels at site 1.

The coherence between $\eta_{ss,env}$ and η, at sites 6, 5, and 1, under weak SS forcing, is shown in Fig. 2.43. At site 6 (Fig. 2.43a,b), we see significant but low coherence amplitude levels at periods shorter than $\sim$15 min, with corresponding coherence phase fluctuating in a semi-random fashion, but is also near 180° when the coherence amplitude levels are higher, a possible signature of bound waves. At harbor sites 5 and 1, the coherence is mostly insignificant, suggesting that the IG variability inside the harbor under weak SS forcing is free and not bound.

The coherence analysis between $\eta_{ss,env}$ and η at the same sites, under strong SS forcing levels, is shown in Fig. 2.44. At site 6, Fig. 2.44a,b clearly reveals that at periods shorter than $\sim$ 1.5 hr under strong SS forcing, $\eta_{ss,env}$ and η are coherent and out of phase, except for particular periods that correspond to modes where we see sharp dips in coherence amplitude levels (e.g., around 23, 6, and 3 min). At site 5, Fig. 2.44c,d shows that the coherence amplitude between $\eta_{ss,env}$ and η is significant under strong SS forcing, but relatively low at periods shorter than 30 min, with corresponding coherence phase lying between $45° - 90°$, suggesting that the IG variability is no longer bound but mostly free leaky/edge. In the 30-200 min period band the coherence amplitude is relatively high, with corresponding coherence phase fluctuating closer to 0°. Oscillations in the 30-200 min period band are possibly the result of swell-induced "setup", which will be discussed in detail in Section 2.5.3. At site 1,

Fig. 2.44e,f shows that $\eta_{ss,env}$ and η here are incoherent at nearly all periods under strong SS forcing, except several isolated periods in the 30-200 min period band (30, 40, 60, 70, and 100 min) where the coherence amplitude varies between 0.4 to nearly 0.8, and the coherence phase lies between 0° and 45°. As in the case of site 5, the oscillations at these periods are possibly the result of swell-induced "setup", as will be discussed in detail in subsection 2.5.3.

The variance-preserving sea level and current spectra in Hale'iwa Harbor (Fig. 1.2), showed that the energetic period band of interest in this harbor (where most of the variance of these two quantities is contained) appears to be ∼3-8 min. For this period band, the coherence analysis in this section provided significant evidence for the existence of bound IG waves at the offshore-most site in the vicinity of Hale'iwa Harbor (site 6), and free IG waves (leaky/edge) inside the harbor.

The high coherence amplitude and near zero coherence phase between $\eta_{ss,env}$ and η at site 5 in the 30-200 min period band, suggests that a swell-induced "setup" could possibly be generating these long period oscillations. However, this will be further explored in section 2.5.3. To improve the spatial resolution of the observations in this study, we use a numerical model in order to help us better understand which generation processes produce the IG waves that are dominant inside the harbor and at the coast under weak/strong SS forcing conditions. The numerical model results will be presented in Chapter 4.

2.5.3 SS-Forced "Setup" Variability (Hypotheses C6 and D1)

In this section we examine the possibility that strong SS forcing induces in Hale'iwa Harbor "setup" variability at IG periods shorter than 30 min (hypothesis C6), or longer than 30 minutes (hypothesis D1). We first test the possibility of such energy pathway inducing "setup" variability at the coast, using sea level records from Mokuleia cross-shore array (sites 8a-8c) during times of strong SS forcing conditions. This is done by looking at the coherence of η vs. η, and $\eta_{ss,env}$ vs. η, among the pairs of sites: 8a vs. 8b, 8a vs. 8c, and 8b vs. 8c (Fig. 2.39). Then, we complement results from these Mokuleia datasets with a coherence analysis between a harbor site (site 5) and the nearest coastal site with available sea level observations (site 6), in order to test the possibility that the harbor would respond to such "setup" variability at periods longer than 30 min. For a setup/set-down forced by SS wave groups at the coast, we consider the following scenarios: (i) if the SS breakpoint region lies between two given sites, we are looking for high coherence between η vs. η with corresponding 180° coherence phase, since the site offshore of the breakpoint region experiences a set-down, and the site within the surf zone experiences a setup; and, we are also looking for high coherence between $\eta_{ss,env}$ at the seaward site vs. η at the shoreward site, with corresponding coherence phase of 0°, since the site within the surf zone experiences the setup that was induced by the SS wave groups. (ii) if the SS breakpoint region lies seaward of the two sites, we are looking for high coherence of η vs. η with corresponding coherence phase of 0°, since the two sites are within the surf zone and experience a setup. Also in this case, the coherence phase between $\eta_{ss,env}$ at the seaward site vs. η at the shoreward site is expected to be 0°.

A coherence analysis for the pair of sites 8a and 8b, is seen in Fig. 2.39a,b. Here we see that the coherence amplitudes of η vs. η and $\eta_{ss,env}$ vs. η are relatively high within much of the 30∼200 min period band, and they overlap each other across much of this period band (panel a). In this period band we identify broad peaks in coherence amplitudes that appear at $\sim$ 40 min, $\sim$ 50 min, $\sim$ 1.25 hrs, and $\sim$ 2 hrs. The corresponding coherence phase across this period band is mostly near 180° for η vs. η, and near 0° for $\eta_{ss,env}$ vs. η (panel b), with a few exceptions, for instance, at the periods of ∼55 min, and ∼100 min, where the coherence amplitude shows a sharp dip and the coherence phase shifts. At periods shorter than 30 min, the coherence amplitude levels of η vs. η and $\eta_{ss,env}$ vs. η are relatively high, except for a significant decrease in the 5-25 min band for η vs. η and in the 5-12 min for $\eta_{ss,env}$ vs. η. The corresponding coherence phase of η vs. η lies near 180° within most of the 15-30 min period band, and shows propagation towards shore at periods shorter than ∼3 min. At periods longer than ∼15 min, the coherence phase of $\eta_{ss,env}$ vs. η fluctuates near 0°, and it shows propagation towards shore at periods shorter than ∼15 min. Qualitatively, similar results are obtained in the coherence analysis for the pair 8a and 8c (Fig. 2.39c,d), except that overall, the coherence amplitude levels of η vs. η and particularly $\eta_{ss,env}$ vs. η are slightly higher for this pair of sites, and the corresponding coherence phase values are much more stable around 180° for η vs. η and 0° for $\eta_{ss,env}$ vs. η. The results observed for the pair of sites 8b vs. 8c (Fig. 2.39e,f) show high coherence amplitude of η vs. η across most of the spectrum, except for several sharp drops at: ∼5 min, ∼55 min, ∼90 min, and ∼200 min. Overall, the coherence amplitude of $\eta_{ss,env}$ vs. η is lower, but significant across most of the spectrum. The corresponding coherence phases of η vs. η and $\eta_{ss,env}$ vs. η are consistently close to 0° across much of the spectra from periods of ∼200 min down to ∼6 min, consistent with the scenario of a setup/set-down mechanism with the SS breakpoint lying offshore of sites 8b and 8c. At periods shorter than ∼6 min, we also see a signature of seaward propagation that could be the result of reflections that occur near the coast.

For Mokuleia sites in the period band starting from several minutes to ∼200 min, these results qualitatively provide the signature we expect to see for SS-forced setup/set-down oscillations, if under similar SS forcing conditions the SS breakpoint lies between sites 8a (12m) and 8b (6m). To support such energy pathway, we determine the SS breakpoint location under SS forcing conditions similar to the ones observed and used to generate Fig. 2.39. Using $H_\infty = 6$ m for the deep water significant wave height, and $T_p = 20$ sec for the peak period (parameters of the strong SS event during 01/13/08 - 01/15/08), the wave transformation from offshore through the surf zone was calculated for Mokuleia site using Eqs. (2.6), (2.7), (2.8), (2.9), and (2.10). The result can be seen in Fig. 2.45, where the SS breakpoint position appears to be located around 850 m from shore. 21 cross-shore profiles separated by 11m and spanning 220m in the alongshore (Fig. 2.46a), were chosen to calculate cross-shore depth profiles (Fig. 2.46b). An average depth profile (see thicker line in panel b) was calculated by averaging these 21 profiles. Using Fig. 2.46b and the result we obtained for the SS breakpoint position, we can estimate that the water depth relative to mean sea level at the breakpoint position is slightly shallower than ∼10 m. For clarity, the locations of sites 8a-8c, are indicated on Fig. 2.45 as vertical dotted lines, and on Fig. 2.46 as red circles.

The above results suggest that under strong SS conditions the SS breakpoint lies between sites 8a and 8b, and, and combined with the coherence analysis results of Fig. 2.39, the evidence supports the energy pathway of SS-induced setup/set-down at Mokuleia sites, ∼5.5 km west of Hale'iwa Harbor.

In search of evidence for SS-induced setup/set-down that triggers IG variability at periods shorter than ∼200 min inside Hale'iwa Harbor, we use Fig. 2.47. This figure shows the coherence analysis of η vs. η and $\eta_{ss,env}$ vs. η for sites 6 (17m) vs. 5 (2m). In the 30-200 min period band, η vs. η shows significant, but relatively low coherence amplitude levels, and the corresponding coherence phase fluctuates between 20° and -50°. The coherence amplitude levels of $\eta_{ss,env}$ vs. η in the 30-200 min period band are low and not significant across the entire period band of interest. At periods shorter than 30 min, η vs. η show significant and relatively high coherence amplitude levels down to ∼4 min, with the exception of 10 min, where there is a sharp drop in coherence amplitude levels, likely due to the presence of a node at site 6 (from high-resolution numerical model results forcing the island of O'ahu with the 2011 Tohoku tsunami, courtesy of Yoshiki Yamazaki; not shown here). The corresponding coherence phase fluctuates near 0° only down to ∼12 min. The coherence amplitude levels of $\eta_{ss,env}$ vs. η at periods shorter than 30 min are very low, except near 5 min where it increases significantly. The low levels of coherence amplitude in the 8-30 min band are accompanied by coherence phase that fluctuates significantly.

Results from the above analyses at the Mokuleia sites, showed that under strong SS forcing conditions the SS breakpoint is expected to lie about 850m offshore, between the two offshore-most sites: 8a and 8b. The relatively high coherence amplitude levels in the period band ranging from several minutes to 150-200 min, accompanied by coherence phase values consistently near 180° for η vs. η, and 0° for $\eta_{ss,env}$ vs. η, reflects the signature we had anticipated to see for a SS-induced setup/set-down scenario between the offshore-most site (8a) and the two offshore sites (8b and 8c). In addition, the coherence analysis between the two sites shoreward of the SS breakpoint (8b and 8c) revealed that the coherence amplitude is significant and relatively high in most of this period band and is accompanied by coherence phases of 0° for both η vs. η, and $\eta_{ss,env}$ vs. η. These findings support the existence of a pathway of SS-induced "setup" at the coast in the period band ranging from several minutes to 150-200 min. These sites, however, are located ~5.5 km west of Hale'iwa Harbor and are not sufficient to prove that this pathway is also responsible for the variability observed in Hale'iwa Harbor. The coherence results between sites 6 (offshore of harbor, 17m) and 5 (inside harbor, 2m) do not provide the evidence necessary for proving the "setup" hypotheses in Hale'iwa Harbor region. This is possibly due to the non-ideal, indirect, pathway formed by sites 5 and 6, and the large distance between these two sites. This energy pathway will be re-visited in Chapter 4 using numerical model datasets.

2.5.4 Excitation of Normal Modes of the Main Hawaiian Islands (Hypothesis D2)

In this section we test our hypothesis of a different energy pathway that could possibly explain the energetic long period oscillations that we observe in the 30-200 min band (e.g., Figs. 2.6, 2.7, 2.13). This hypothesis considers a pathway where large-scale normal modes that are trapped to the Hawaiian Islands could be excited and resonate under strong SS forcing conditions. The signatures of such large scale normal modes around, and among, the Main Hawaiian Islands, were found in the numerical model studies of *Munger and Cheung* (2008) and *Cheung et al.* (2013), under tsunami forcing conditions. Results form these studies suggest that, around Kaua'i Island and the North Shore of O'ahu, minimal energy levels are expected at periods longer than ~ 30 min (see Figs. 2.48 and 2.49). They also indicate that on O'ahu Island, most of the energy at these long periods is expected to be trapped between the south/southeastern portion of the island (Barbers Point to Kane'ohe Bay) and northwestern portion of the Big Island (around Kawaihae). We test this hypothesis using datasets from four Hawaiian harbors: Hale'iwa Harbor (O'ahu Island), Honolulu Harbor (O'ahu Island), Kahului Harbor (Maui Island), and Kawaihae Harbor (Big Island) sites (see Fig. 2.3 for exact locations). The PSDs at each of these sites are used to identify any significant peaks, and coherence analyses between the different pairs of sites are used to determine whether some of the identified spectral peaks are potentially modal. We compare our observations with the numerical model results of *Munger and Cheung* (2008) and *Cheung et al.* (2013).

In Fig. 2.50 we have a sea level PSD plot for each of the above harbor sites: (a) site 1, Hale'iwa Hbr.; (b) site 13, Honolulu Hbr.; (c) site 14, Kahului Hbr.; and, (d) site 15, Kawaihae Hbr. Blue curves were generated using multiple 3-month long datasets during the North Pacific summertime (Jun, Jul, Aug; 5 seasons for Hale'iwa, and 13 for the other harbors), and red curves were generated using multiple 3-month long datasets during North Pacific wintertime (Nov, Dec, Jan; 5 seasons for Hale'iwa, and 11 for the other harbors). All data containing tsunami events (2 from summertime and 4 from wintertime) were excluded from this analysis. The large-scale modes from the model results of *Munger and Cheung* (2008) and *Cheung et al.* (2013), are marked with vertical dashed lines (27, 33, 43, 52, and 75 min). Periods shorter than 27 min are not labeled, although we know that modes exist at these periods. We use these plots to identify any significant peaks that could potentially be large-scale island or inter-island modes. In addition, from these plots we can learn about the relative spectral levels of a given mode at a given harbor sites. In Hale'iwa Harbor, except for a few small peaks, the only peak that stands out is at 22.7 ± 0.3 min (Fig. 2.50a). This is the gravest mode of oscillation of the North Shore of O'ahu, as was seen in all of our prior observations (e.g., see Figs. 2.7, 2.10). *Munger and Cheung* (2008) suggest that this North Shore mode is actually part of a mode that co-oscillates at many locations within the main Hawaiian Islands (Fig. 2.48). Whether the locations of the relative maximum amplitudes of this mode shown in Fig. 2.48 (e.g., North Shore, O'ahu; Penguin Bank, west of Molokai) can actually oscillate independently of each other, or whether excitation at one location results in excitation at all other locations, remains to be determined with better datasets than are yet available. In Honolulu Harbor (Fig. 2.50b), we see a large peak with a period of 21.3 ± 0.2 min. This peak is not one of the model-predicted inter-island modes, and therefore is likely a local harbor mode. It does not appear at the Kilo Nalu observatory site just outside the harbor entrance (*Munger and Cheung* (2008)). The shorter period 17 min mode (Fig. 2.48) does appear at Kilo Nalu, but not within Honolulu Harbor (*Munger and Cheung* (2008)).

Another significant peak in Honolulu Harbor appears at 46.8 ± 0.8 min, which is not too far off from the model-predicted 43 min mode. A smaller, but statistically significant peak, occurs at a period of 27 min, coinciding with the period of another model-predicted mode. In Kahului Harbor (Fig. 2.50c), the most dominant peak is at 35.0 ± 0.2 min, close to the model-predicted 33 min mode. There is a broad peak centered at 22.2 ± 1.0 min, which is in agreement with observations (*Munger and Cheung* (2008)). A small peak also appears at 50.1 ± 0.4 min, close to the model-predicted 52 min mode. None of these modes overlap with the gravest harbor mode of $\sim$ 15 min (*Douyere* 2003). In Kawaihae Harbor (Fig. 2.50d), we see the strongest peak at 26.4 ± 0.2 min. Although much weaker, a somewhat broad peak appears at 54.2 ± 0.9 min.

It is not surprising that the spectral levels of certain modes are very high at one location, but are weak, or even appear to be absent at another location. This occurs when, for a given mode, one site is located at/near an antinode, and another site is located at/near a node. Also, depending on the direction from which the forcing (e.g., SS, tsunami, wind) arrives, sites that are located on a coast that is directly exposed to the forcing may result in higher spectral levels than sites located on coasts that are located on the opposite side of an island. One such example is the significant separation between the summer and winter spectra at Hale'iwa Harbor, at periods longer than $\sim$30 min. This harbor is directly exposed to the strong North Pacific winter swells arriving from northwest, whereas Honolulu Harbor is mostly shadowed form these swell events (except for a partial exposure to swells having strong westerly component), but it is exposed to swells arriving from the South Pacific. For this reason, there is minimal separation between the summer and winter spectra at Honolulu Harbor.

We contrast the above PSDs with ones during times of tsunami forcing (Fig. 2.51). At each of the above harbor sites, we average multiple two-day long sea level data segments, where each includes a tsunami event. 7 events were included in the analysis for Hale'iwa Harbor (start times: 06/25/01, 09/25/03, 11/17/03, 05/06/06, 11/15/06, 01/13/07, and 09/29/09), and 11 in Honolulu, Kahului, and Kawaihae Harbors (the same tsunami events that were used for Hale'iwa Harbor, including events having start times: 12/05/97, 08/15/07, 02/27/10, and 03/11/11). For each of the harbor sites, Fig. 2.51 shows that the spectral response under tsunami forcing still excites the dominant peaks that were identified in Fig. 2.50, except that the response to tsunami forcing results in spectral levels that are ~1-2 orders of magnitude higher (note the different scales in the ordinates of Figs. 2.50 and 2.51). In addition, there are several spectral peaks that were hard to identify in the PSDs of Fig. 2.50, and become more pronounced under tsunami forcing (i.e., in Fig. 2.51). One such example is the peak near 27 min in Honolulu Harbor (Fig. 2.51b), near 52 min in Kahului Harbor (Fig. 2.51c), and the broad peak around 38 min in Kawaihae Harbor (Fig. 2.51d). We also note that the periods of those peaks line up quite nicely with the model-predicted ones of *Munger and Cheung* (2008) and *Cheung et al.* (2013) (see vertical dotted lines in Fig. 2.51).

To determine whether oscillations at a site on one island are connected to oscillations at a site on another island, we look at the coherence between the different pairs of sites. We calculate the coherence amplitude and coherence phase using six 3-month long 2 min sea level datasets from Hale'iwa Harbor (O'ahu Island, site 1; Fig. 2.1), and fifteen 3-month long 6 min sea level datasets from Honolulu Harbor (O'ahu Island, site 13; Fig. 2.3), Kahului Harbor (Maui Island, site 14; Fig. 2.3), and Kawaihae Harbor (Hawai'i Island, site 15; Fig. 2.3), during times of minimal North Pacific SS forcing levels (months of June, July, and August), and strong SS forcing levels (months of November, December, and January). Fig. 2.52 shows one such example for the Honolulu-Kawaihae pair during (a) summertime, and (b) wintertime. The dashed red line in each of the coherence amplitude plots indicates the 95% level of no significance, and for comparison purpose, the vertical dashed lines mark the periods of the inter-island normal modes that were found from the numerical model results of *Munger and Cheung* (2008) and *Cheung et al.* (2013). During summertime and wintertime, we see peaks in coherence amplitude near the model-predicted periods of 43 min and 52 min. These peaks are clearly statistically significant at the 95% level. There are, however, other peaks that do not line up with the periods of the predicted modes (e.g., at

$\sim$ 38 min). At 75 min, we see a broad-band bulge that is more likely the result of some other process. This broad band bulge drops to zero coherence amplitude around $\sim$ 68 min. Around the 68 min period we see a sharp 180° transition in coherence phase. We also note little difference in the coherence amplitude levels and corresponding coherence phase values between summertime and wintertime. This latter result is possibly because these two sites are relatively protected from the direct impact of winter swells which typically force a broad band of IG oscillations (e.g., recall the impact of strong SS forcing on alongshore coherence on the North Shore of O'ahu described in Section 2.5.1 and shown in Fig. 2.32). Similar results (not shown here) are obtained for the other pairs of sites used in this study.

We believe that Fig. 2.52 is exhibiting the result of a mixture of two coherent processes that are independent of each other. One process is the system of inter-island modes, the other process involves open ocean IG oscillations that are possibly generated from nonlinear tide interactions at continental coasts (*Luther et al.* 2014). When we have two competing processes - one is narrow banded (the inter-island modes), the other is broad banded (open ocean process) - that are coherent between two sites, the two may destructively interfere near the peaks of the narrow banded process. Fig. 2.53 is taken from a study by *Luther et al.* (2014), using deep-ocean bottom pressure datasets from the Hawai'i Ocean Mixing Experiment (HOME). Here, they plotted the coherence amplitude and phase between two HOME sites. The coherence amplitude is statistically significant across most of the spectrum, but we can see the pattern where it periodically goes to zero at certain frequencies, with corresponding coherence phase jumps of 180°.

As an attempt to isolate the inter-island modal phenomenon, we select the largest spectral peaks from Honolulu and Kahului, and apply the complex demodulation method to generate time series of potential energy for a given frequency of oscillation. Fig. 2.54a shows the energy time series of the 44.8 min period of oscillation in Honolulu Harbor. Fig. 2.54b shows the energy time series of the 35.3 min period of oscillation in Kahului Harbor. We clearly identify certain time periods where the energy is particularly high, but these correspond to very short lived events. After a careful check, we find that all of the large energy peaks in Honolulu and

Kahului Harbors, correspond to tsunami events. We therefore took these short time periods and used them to generate coherence amplitude and phase plots. The results (not shown here) did not reveal anything new, as they turned out to be very similar to the ones using the full time series lengths.

Since the energy levels in Fig. 2.54a,b are so high under tsunami forcing compared to SS forcing, we generate a modified version of that figure where we limit the y-axis to a smaller range. This clearly ignores the high energy levels due to tsunamis, but highlights the variability due to all non-tsunami forcing mechanism/s. The result, seen in Fig 2.55, reveals what appears to be a semi-annual signature in Honolulu Harbor (panel a) and Kahului Harbor (panel b), with peaks around mid-summer and mid-winter, but that signal appears to be more pronounced in Kahului Harbor. Since Honolulu Harbor is exposed to SS forcing from the southern hemisphere, it is expected to have elevated levels of SS energy during the summertime months. During wintertime, this site is occasionally exposed to northern hemisphere SS forcing when the SS has a strong west component. Kahului Harbor, on the other hand, is exposed to SS energy arriving from the northern hemisphere (i.e., wintertime), but not to SS energy from the southern hemisphere (i.e., summertime). In addition, this site is exposed to the trade winds which are prevalent year-round, but strongest during wintertime months (*Wyrtki and Meyers* 1976). These sources of energy, however, do not explain the relatively high energy levels at this site during summertime months. It is possible that the apparent semi-annual signature is due to open ocean processes, since these are forced by nonlinear interactions among the tides. This possibility will not be further explored here.

The auto- and cross-spectral analyses of Hale'iwa, Honolulu, Kahului, and Kawaihae Harbors, provides good evidence of several long-period spectral peaks that could be large-scale modes around, or among, the islands. However, the envelope of the coherence amplitude and the corresponding coherence phase show patterns that resemble the ones of long-period open ocean IG waves, as was shown in other studies (e.g., *Luther et al.* (2014)). Compared to the periods of the observed spectral peaks, we find that the periods of the model-predicted modes (of *Munger and Cheung* (2008) and *Cheung et al.* (2013)), are slightly off. For certain peaks, we also find a mismatch between the observed and model-predicted periods of several peaks. Isolating the energy time series for the main modes of a given harbor shows that the energy levels of these long period oscillations are much higher under tsunami forcing than under SS forcing. Compared to the PSDs of the remaining three harbors, the summertime PSD in Hale'iwa Harbor reveals minimal spectral levels and no apparent peaks of what could potentially be island or inter-island modes in the 30-200 min period band. Therefore, it is highly likely that the high spectral levels seen in Hale'iwa Harbor during wintertime (i.e., strong SS forcing levels on the North Shore of O'ahu; for example, see red curve in Fig. 2.7) are not the result of any large-scale modes.

2.5.5 Free IG Energy From Remote Sources (Hypotheses A0a, A0b)

In the previous sections we focused on free IG energy that was generated locally at the coast, either by nonlinear interactions, or bound waves released from the SS wave groups. In this section, we search for evidence of free IG energy that arrives from remote sources (not generated locally) and excites modal oscillations of Hale'iwa Harbor. The main North Pacific source of this free IG wave field was found to be the Northwest U.S. coast, and is strongest during the North Pacific winter season (*Webb et al.* 1991; *Aucan and Ardhuin* 2013). In the present analysis we use datasets from two pressure sensors at deep water sites around O'ahu Island (pressure data was converted to sea level using linear wave theory). One site (site 12, see Fig. 2.3) is located ∼20 km ENE offshore of O'ahu island at a depth of 1940m, and the other site (site 11, see Fig. 2.3) is located ∼26 km NNW of Hale'iwa Harbor at a depth of 2016m. Both instruments collected data for nearly three months. To look at the response inside Hale'iwa Harbor we use sea level datasets from the 2013/2014 deployment.

In this analysis we focus on IG periods in the 1-20 min band, as was done by *Aucan and Ardhuin* (2013) who observed this band to be energetic at various spectra from 3-4 km ocean depths. The deep-water sea level datasets (from sites 11 & 12) were used to look at the significant wave height in the 1-20 min IG period band at the northeastern site (site 12),

$H_{sig,IG;NE}$, and northwestern site (site 11), $H_{sig,IG;NW}$. At the great depths of sites 11 & 12 (~2000m), the IG wave energy is most likely dominated by free, rather than bound, IG waves, since the bound waves decay quickly in the vertical like the SS waves in the groups to which the IG waves are bound. A situation where $H_{sig,IG;NE} > H_{sig,IG;NW}$ under minimal SS forcing levels during the North Pacific winter season, could potentially suggest that the locally-generated free IG wave field is dominated by waves arriving from remote sources (nonlocally-generated). If the remote source of this free IG wave field is the Northwest U.S. West Coast, then a coherence analysis between sites 11 & 12 should show that site 12 is leading site 11 at certain periods or period bands.

A challenging task here is to identify time periods of minimal SS forcing levels, since we are dealing with datasets that were recorded during the peak North Pacific SS season. We do that using Fig. 2.56a,b by qualitatively identifying several times where $H_{sig,IG;NW} < H_{sig,IG;NE}$ (marked as vertical dotted lines). In Fig. 2.56c,d, we use the corresponding SS peak direction (D_p) and significant wave height ($H_{sig,SS}$) datasets at Waimea Buoy (site 10, 200m water depth, ~8.5 km north of Hale'iwa Harbor), to identify times of minimal SS forcing conditions that do not arrive from the northwest. Fig. 2.56e,f, shows the corresponding response at Waimea Bay (17m water depth), and at several locations inside the harbor, respectively. From Fig. 2.56a-d we choose 01/13/2014-01/15/2014 as the best candidate for a time period where $H_{sig,IG;NW} < H_{sig,IG;NE}$ and SS forcing conditions are minimal.

In Fig. 2.57a we overlap $H_{sig,IG}$ at site 11 on $H_{sig,IG}$ at site 12 to make it easier to see the occasions where $H_{sig,IG;NW} < H_{sig,IG;NE}$. The corresponding significant wave height ($H_{sig,IG}$) levels inside the harbor are seen in Fig. 2.57b. As expected, we note that during the times where $H_{sig,IG;NW} < H_{sig,IG;NE}$, $H_{sig,IG}$ levels are indeed minimal inside Hale'iwa Harbor, assuring us that the offshore SS conditions are minimal.

Fig. 2.58a shows that the PSD levels at sites 11 and 12 are nearly identical across the spectrum range, except at particular periods that could be attributed to positional differences. In particular, around 23 min we see a small bump in PSD levels at site 11, whereas the spectral levels are smaller and nearly flat at site 12. This difference could be due to the fact that site 11 is located near the edge of the 23 min coastal mode of the North Shore, whereas the 23 min oscillation is at a minimum at site 12 (see Figs. 2.3 and 2.48).

The coherence amplitude between sites 11 and 12 is seen in Fig. 2.58b. Although it shows significant coherence amplitude at periods longer than $\sim$20 min, here we focus on periods shorter than 20 min. We identify relatively small but significant broad peaks centered around 10 min and 4 min, where the corresponding coherence phase (Fig. 2.58c) suggests a westward component of propagation, i.e., from site 12 to 11. Using Eqs. (2.11) and (2.12) we calculate the phase lag, Φ, between sites 11 and 12. The two curves of Φ that bracket the observed coherence phase ($\phi_{\eta,\eta}$) are overlayed on Fig. 2.58c (see magenta curves). The corresponding range of θ values is $60^\circ < \theta < 80^\circ$. Using this range of values of θ, we then estimate that the region from which the waves arrived is the stretch of coast from Oregon to the middle of British Columbia on the north (approximate latitudes: $44^\circ N - 53^\circ N$).

By assuming conservation of energy flux, Eqs.(2.15)-(2.16) are used to project the observed spectra from 17m water depth to the corresponding spectra that would be expected at site 11 (2016m water depth). We use this approximation to determine the spectral levels that need to be available at site 11 in order to generate the spectral levels that are observed at site 9 (17m depth). We do that for the cases of weak and strong SS forcing conditions.

The result under weak SS forcing conditions (2 day time period: 01/14/2014 - 01/15/2014) is seen in Fig. 2.59. The black curve is the observed spectra at the shallow-water site (site 9, 17m depth). Projecting this spectra to the same depth at the location of the offshore deep-water site (site 11, 17m depth) results in the magenta curve. By correcting the latter for depth attenuation, we obtain the red curve, which is the projected spectra at the bottom of the ocean at site 11 (2016m depth). Finally, the blue curve shows us the observed PSD at the bottom of the ocean at site 11 (2016m depth). By comparing the observed (blue curve), and projected (red curve) spectra at the bottom of the ocean at site 11 (2016m), we see that in the period band of interest (1-20 min) the observed spectral levels are slightly lower than the projected ones, but are also roughly the same order of magnitude, or even slightly higher, near certain periods or period bands (e.g., around 3-5 min, 8 min). The distinct peaks and valleys seen in the red curve (e.g., peak centered around 7 min and valley around 3.5 min) are the result of the local bathymetry amplifying the IG energy at particular periods or period bands, and are typically absent at deep-water spectra, as can bee seen in the blue curve (also see *Filloux et al.* (1991) and *Aucan and Ardhuin* (2013)). Overall, this result suggests that under minimal SS levels, the IG energy that is available offshore may not be sufficient to trigger the spectral levels that we observe in shallow-water in the 1-20 min IG band. However, this offshore energy could possibly trigger oscillations in the 3-5 min period band. On the other hand, the same analysis during a time period of strong SS levels (Fig. 2.60; 5 day time period: 12/14/2013 - 12/18/2013), reveals that the projected spectral levels in the 1-20 min period band at site 11 (red curve), are about 1-2 orders of magnitude higher than the observed spectral levels at this site (blue curve). This clearly suggests that under such SS conditions, the IG energy available offshore at the location of site 11 is insufficient to produce the IG spectral levels that are observed at the 17m shallow-water site (site 9).

In Figs. 2.59 and 2.60 we also note a clear spectral peak around a periods of 5 sec. We believe that it is the signature of microseisms, a seismic noise signal on the seafloor that is believed to be primarily generated by non-linear interactions among surface gravity waves of similar frequencies. When the wavelengths of these resulting waves are long enough, their pressure fluctuation signals can penetrate all the way to the ocean bottom (*Webb and Cox* 1986). In our spectra, however, the spectral gap between 10 $\sim$ 60 sec is not as deep as the spectral gaps seen in other seafloor observations such as in *Webb and Cox* (1986). The reason for this could potentially be high noise level of our instrument. If that is the case, that noise level appears to lie around 2×10^{-4} cm^2/cph.

During a time period when $H_{sig,IG;NW} < H_{sig,IG;NE}$, the coherence analysis between deep-water sites 11 & 12 provided evidence of free IG waves that potentially originated from the West Coast of North America, the region extending from Oregon to British Columbia (approximate latitudes: $44°N - 53°N$). This result agrees with other studies (*Aucan and Ardhuin* 2013) who found that the main offshore IG wave field could originate from remote sources of free IG waves in this period band is the northwestern U.S.

Under the assumption of conservation of energy flux, the observed shallow-water spectra (site 9, at 17m) was used to yield the projected spectra at the deep water site (site 11, 2016m). A comparison of the projected and observed spectra at site 11 (2016m) under weak SS forcing levels, suggested that the observed spectral levels at this offshore site might be too weak to generate the spectral levels observed at the shallow-water site in most of the the 1-20 min period band. One exception that we find is in the 3-5 min period band, where the observed and projected spectral levels are of the same order of magnitude, meaning that at least in this period band, the energy levels available offshore could be sufficient to force the harbor when SS levels are minimal.

2.6 Discussion

Preliminary analysis of the various observational datasets that were collected prior to the beginning of this study, yielded some very interesting results that seem to be unique to the particular stretch of coast of the North Shore of O'ahu Island, Hawai'i. Following these results, several fundamental questions arose regarding the possible generation mechanisms of IG waves and energy flow at this stretch of coast. We formulated these questions as hypotheses and tried to address them using the historical datasets and datasets that we collected during two deployments that we planned and executed. Below is a summary of what we have learned about these hypotheses from the different observational results.

1. **Excitation of linear coastal or harbor modes**: The observational evidence presented in this chapter, in conjunction with published model-data comparisons during the occurrences of tsunamis at Hawai'i, supports the conclusion that a spectrum of *discrete* natural frequencies, of coastal and perhaps harbor modes, does exist for periods from the "gravest" normal mode of the North Shore of O'ahu at a period of 23 min (*Munger and Cheung* 2008) down to periods as short as perhaps 50 sec. The analyses of spectra within the harbor and coherence between the harbor and the coast, strongly suggest that the harbor has its own natural modes at several periods $\leq$ 3 min, with the

best example at 90 sec period. The results suggest that the most dominant spectral peaks appearing at: 23, 12, 8, and 6 min, and the secondary peaks appearing at: 18 and 15, are likely coastal modes. The spectral peaks that appear at: 3 min, and 91, 66, and 55 sec, are likely harbor modes. However, it is still not clear whether the coast has modes at periods shorter than 3 min, or maybe that period is a cutoff between the harbor and coastal modes. In addition, a coherence analysis inside the harbor also suggests the potential existence of a long period harbor mode near ∼6 min. Most importantly, the spectra and coherences clearly indicate that whatever modes might be excited by weak SS forcing, in the harbor or at the coast, these modes become nearly irrelevant for explaining the broad-banded suite of IG oscillations that tend to smooth out the auto-spectra and greatly reduce horizontal coherence under strong SS forcing.

2. **Bound wave impacts; generation of leaky and edge waves**: The coherence analysis results at Mokuleia provided clear evidence of bound IG waves at the offshore-most site (12m depth), a mix of free and bound IG waves shoreward of that site in the surf zone, and mostly free IG waves further closer to shore. The free IG wave field could be generated by the time-varying breakpoint mechanism or by some other mechanism that is tied to the SS wave groupiness at the offshore site, released-bound free IG, or some combination of these. In the ∼3-8 min period band, where the sea level and current variability were found to be greatest inside Hale'iwa Harbor, we find significant evidence for the existence of bound IG waves at the offshore-most site in the vicinity of Hale'iwa Harbor (17m depth), and free IG waves (free leaky/edge) inside the harbor.

3. **The role of time-varying, SS-driven "setup"**: At Mokuleia site (located ∼5.5 km west of Hale'iwa Harbor), the coherence analysis findings and the calculated location of the SS breakpoint under strong SS forcing conditions, support the existence of a pathway of SS-induced "setup" at the coast in the period band ranging from several minutes to 150-200 min. In the vicinity of Hale'iwa Harbor, however, the results do not provide the evidence necessary for proving that SS-induced "setup" is responsible for the IG variability observed in Hale'iwa Harbor. This lack of conclusive evidence is

possibly due to the non-ideal, indirect, pathway formed by the available sites in the vicinity of the harbor, and the large distance they are located relative to the harbor.

4. **Excitation of normal modes of the Main Hawaiian Islands**: Good evidence was collected regarding several long-period spectral peaks that could be large-scale modes around, or among, the Hawaiian Islands. However, the patterns of the coherence amplitude envelope and the corresponding coherence phase, resemble the ones of long-period open ocean IG waves, as was shown in other studies (*Luther et al.* 2014). There is agreement between some of our observed spectral peaks and the model-predicted peaks of *Munger and Cheung* (2008) and *Cheung et al.* (2013); for instance, 44.8 min observed vs. 43 min modeled in Honolulu Harbor, and 35.3 min observed vs. 33 min modeled in Kahului Harbor. Overall, our observed spectral peaks occur at periods that are slightly off from the model-predicted periods of *Munger and Cheung* (2008) and *Cheung et al.* (2013). Isolating the energy time series for the main modes of Honolulu and Kahului Harbors shows that the energy levels are much larger under tsunami forcing than under SS forcing. During summertime, when SS levels are minimal on the North Shore of O'ahu, the spectral levels in the 30-200 min period band are very weak in Hale'iwa Harbor as compared to the ones observed in Honolulu, Kahului, and Kawaihae Harbors. The spectra in Hale'iwa Harbor also lacks any structure that could potentially be identified as spectral peaks of island or inter-island modes. Therefore, it is highly likely that the high spectral levels seen in Hale'iwa Harbor during wintertime (i.e., strong SS forcing levels on the North Shore of O'ahu) are not forced by any large-scale island/inter-island modes.

5. **Free IG energy from remote sources**: The coherence analysis between deep-water sites 11 & 12 provided evidence of free IG waves that potentially originated from the region extending from Oregon to British Columbia (approximate latitudes: $44°N - 53°N$), a result that is in good agreement with the findings of *Aucan and Ardhuin* (2013). Under the assumption of conservation of energy flux, we were able to calculate the projected spectra at a deep water site offshore of O'ahu's North Shore (2016m

depth), given the observed spectra at a shallow water site (17m depth). Comparing this projected spectra with observations at the deep water site under weak SS forcing conditions, suggested that the observed spectral levels at this offshore site might be too weak to generate the spectral levels observed at the shallow-water site in most of the 1-20 min period band, except in the 3-5 min period band, where the observed and projected spectral levels are of the same order of magnitude, suggesting that the energy of free IG waves that arrive from remote sources could potentially force the harbor when SS levels are minimal.

In the numerical modeling study of Chapter 4 we revisit all of the above hypotheses. We force the numerical model with various levels of SS forcing conditions over a domain that contains a large portion of the North Shore with Hale'iwa Harbor located near the middle of the domain. The high spatial and temporal resolution of the model are used to answer the questions that were not fully addressed in Chapter 2 due the spatial and temporal limitations that are inherent in observations.

Table 2.1: Latitude/Longitude coordinates, and site description of historical, 2011/2012, 2013/2014, and additional deployment sites.

Site	**Lon (deg)**	**Lat (deg)**	**Site Description**
1	-158.105571	21.593051	Hale'iwa inner hbr.
2	-158.106406	21.593392	Hale'iwa inner hbr.
3	-158.105701	21.594202	Hale'iwa middle hbr.
4	-158.105857	21.594902	Hale'iwa middle hbr.
5	-158.105606	21.595063	Hale'iwa outer hbr.
6	-158.115000	21.603000	outside and ∼2 km west of Hale'iwa Hbr.
7	-158.133850	21.594990	outside and ∼3 km west of Hale'iwa hbr.
8a	-158.157230	21.588180	∼5.5 km west of Hale'iwa hbr.
8b	-158.157250	21.583980	∼5.5 km west of Hale'iwa hbr.
8c	-158.157270	21.581880	∼5.5 km west of Hale'iwa hbr.
9	-158.069400	21.642600	Waimea Bay
10	-158.117111	21.670549	Waimea Buoy - ∼6.5 km WNW of Waimea Bay
11	-158.205000	21.800000	bottom pressure gauge site - ∼22 km NW of O'ahu
12	-157.760000	21.710000	bottom pressure gauge site - ∼20 km NE of O'ahu
13	-157.866700	21.306700	Honolulu Hbr.
14	-156.476700	20.895000	Kahului Hbr.
15	-155.830000	20.036700	Kawaihae Hbr.

Table 2.2: Data specifications. Rows: historical, 2011/2012, 2013/2014, and additional deployments. Columns: site, instrument (Tide Gauge; AQuadopp; BUoy; SeaBird), measurement (η = sea level; p = pressure; u, v = currents), date range/s of data (mm/dd/yy), depth, sampling period, and averaging interval.

Deployment	**Site**	**Inst**	**Meas**	**Dates**	**h (m)**	**Samp (s)**	**Avg (s)**
Historical	1	TG	η	01/01/97-10/19/10	0	120	1
	8a	AQ	p	12/14/07-01/17/08	12	1	1
	8b	AQ	p	12/14/07-02/24/08	6	1	1
	8c	AQ	p	12/14/07-02/25/08	2	1	1
	10	BU	p	12/16/01-to date	200	1	26 min
	13	TG	η	11/01/94-to date	0	360	181
	14	TG	η	01/01/96-to date	0	360	181
	15	TG	η	01/01/96-to date	0	360	181
2011/2012	1	AQ	p, u, v	11/03/11-01/17/12 01/18/12-03/14/12	1	10	5
	5	SB	p, u, v	10/28/11-01/13/12 01/18/12-03/24/12	2	1	1
	6	SB	p	10/28/11-04/12/12	17	1	1
	9	SB	p	10/28/11-02/03/12	17	1	1
2013/2014	1	AQ	p, u, v	11/28/13-01/20/14 01/21/14-05/05/14	0.75	8 14	3 14
	2	AQ	p, u, v	11/28/13-01/27/14 02/20/14-05/06/14	1.5 1.7	8 10	3 10
	3	AQ	p, u, v	11/28/13-02/15/14 03/25/14-04/27/14	1.8 2	3 1	1
	4	AQ	p, u, v	11/28/13-02/10/14 02/20/14-05/22/14	4 4	3 2	1
	7	AQ	p, u, v	12/04/13-05/14/14	25	3	1
Additional	9	SB	p	12/06/13-03/05/14	17	1	1
	11	SB	p	11/12/13-02/07/14	2016	1	1
	12	SB	p	11/12/13-02/07/14	1940	1	1

Table 2.3: Average and standard deviation of the period, T, Quality-factor, Q, and e-folding decay time, τ, for spectral peaks observed inside Hale'iwa Harbor during times of no/weak-SS forcing conditions in the years 1997-2010, and 2014.

T	ΔT	Q	ΔQ	τ **(min)**	$\Delta\tau$ **(min)**
55.3 sec	0.4 sec	10.18	0.85	2.30	0.27
65.7 sec	0.5 sec	13.61	1.55	5.64	2.76
91.5 sec	0.7 sec	13.11	4.87	6.32	2.33
3 min	0.1 min	8.53	2.00	8.18	1.88
6.0 min	0.1 min	8.82	2.54	16.99	4.90
8.1 min	0.1 min	8.62	2.69	22.27	6.76
12.4 min	0.2 min	9.05	2.29	35.75	9.24
14.5 min	0.3 min	7.76	0.99	35.31	4.05
18.0 min	0.2 min	8.15	2.48	46.96	14.62
22.7 min	0.3 min	7.85	1.96	57.00	13.95

Table 2.4: Summary of multiple datasets averaged to generate various figures. Columns are: forcing levels and type, site number, data time periods, total number of days, and figures.

Forcing levels and type	**Site/s**	**Data time periods**	**Days total**	**Figure/s**
no SS	1	Jul-Aug, years: 1997, 1999-2003, 2005-2006, 2008, and 2010	3650	2.10
no SS	1	05/21/02-05/24/02; 06/07/02-06/10/02; 06/23/02-06/26/02; 06/27/02-06/30/02; 07/27/02-07/30/02	20	2.6
weak SS	1	04/23/02-04/26/02; 01/31/02-02/03/02; 01/15/02-01/18/02; 03/18/02-03/21/02; 09/20/02-09/23/02	20	2.6
moderate SS	1	03/02/02-03/05/02; 03/15/02-03/18/02; 02/04/02-02/07/02; 12/19/02-12/22/02; 10/14/02-10/17/02	20	2.6
strong SS	1	01/03/03-01/06/03; 01/07/03-01/10/03; 01/14/03-01/17/03; 01/05/02-01/08/02; 01/18/03-01/21/03	20	2.6
no SS	2	03/24/14-03/27/14; 04/14/14-04/17/14; 04/18/14-04/21/14; 04/26/14-04/29/14; 03/30/14-04/03/14	20	2.7, 2.8
weak SS	2	02/21/14-02/24/14; 04/12/14-04/15/14; 04/23/14-04/26/14; 03/20/14-03/23/14; 04/02/14-04/05/14	20	2.7, 2.8, 2.27-2.31
moderate SS	2	12/04/13-12/07/13; 12/18/13-12/21/13; 12/22/13-12/25/13; 01/01/13-01/04/13; 01/08/13-01/11/13	20	2.7, 2.8
strong SS	1, 2, 4, 7	12/11/13-12/14/13; 12/26/13-12/29/13; 01/02/14-01/05/14 (11/28/13-12/02/13 for site 2); 01/15/14-01/18/14; 01/20/14-01/23/14 (not for site 2)	20	2.7, 2.8, 2.27-2.31
weak SS	8a-8c	12/14/07-12/17/07; 12/17/07-12/20/07	6	2.12, 2.13, 2.14, 2.33, 2.35, 2.36, 2.38
moderate SS	8a-8c	12/25/07-12/28/07; 01/06/08-01/08/08	6	2.12, 2.13, 2.14, 2.33
strong SS	8a-8c	01/10/08-01/13/08; 01/13/08-01/16/08	6	2.12, 2.13, 2.14, 2.33, 2.35, 2.37, 2.39
weak SS	1, 5, 6	11/04/11-11/07/11; 11/07/11-11/10/11; 11/15/11-11/18/11; 12/13/11-12/16/11; 01/22/12-01/25/12	15	2.23, 2.24, 2.25, 2.26, 2.32, 2.40-2.44
strong SS	1, 5, 6	11/27/11-11/30/11; 12/01/11-12/04/11; 12/06/11-12/09/11; 12/16/11-12/19/11; 01/28/12-01/31/12	15	2.23, 2.24, 2.25, 2.26, 2.32, 2.40-2.44, 2.47
summer SS	1, 2, 4, 7	06/01-08/31, 1997 and 1999-2012	1380	2.50, 2.52a
winter SS	1, 2, 4, 7	11/01-01/31, 1997 and 1999-2012	1380	2.50, 2.52b

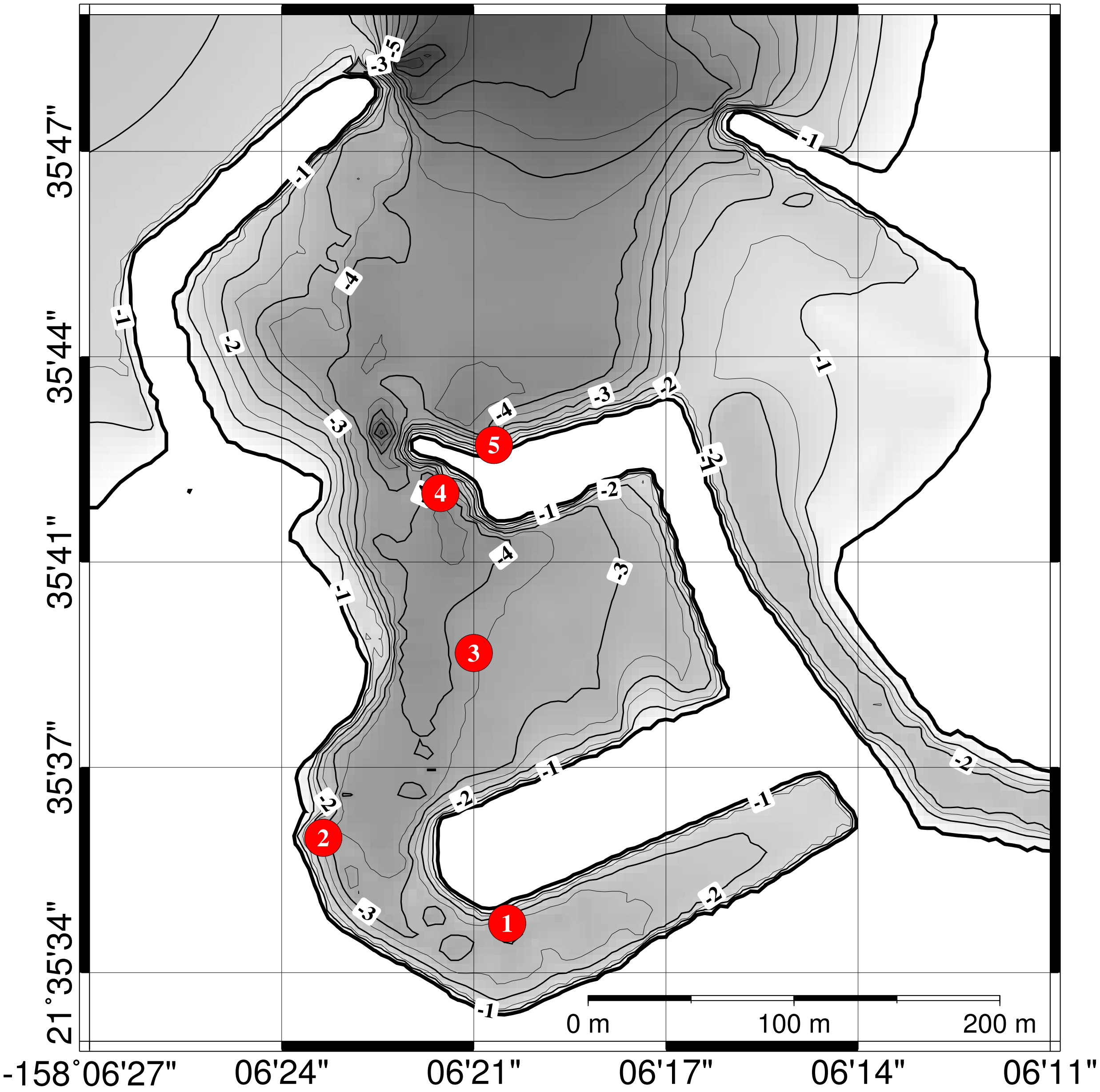

Figure 2.1: Sites of tide gauge, pressure sensors, and current meters in Hale'iwa Harbor. Units of contour lines are meters, and an identification number was assigned to each site.

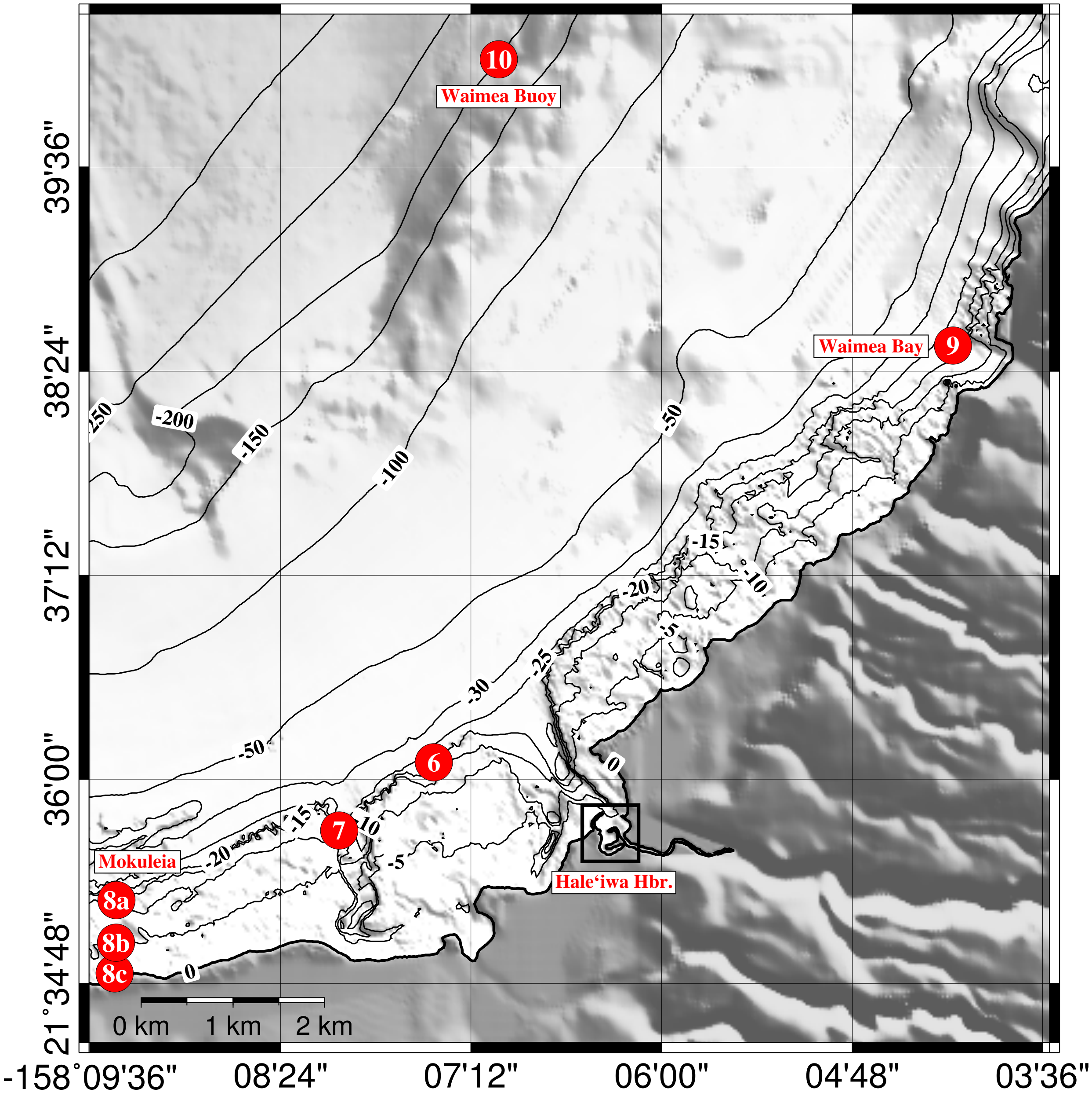

Figure 2.2: Sites of pressure sensors, currents meters, and wave buoy along the North Shore coast in the vicinity of Hale'iwa Harbor. Units of contour lines are meters, and an identification number was assigned to each site.

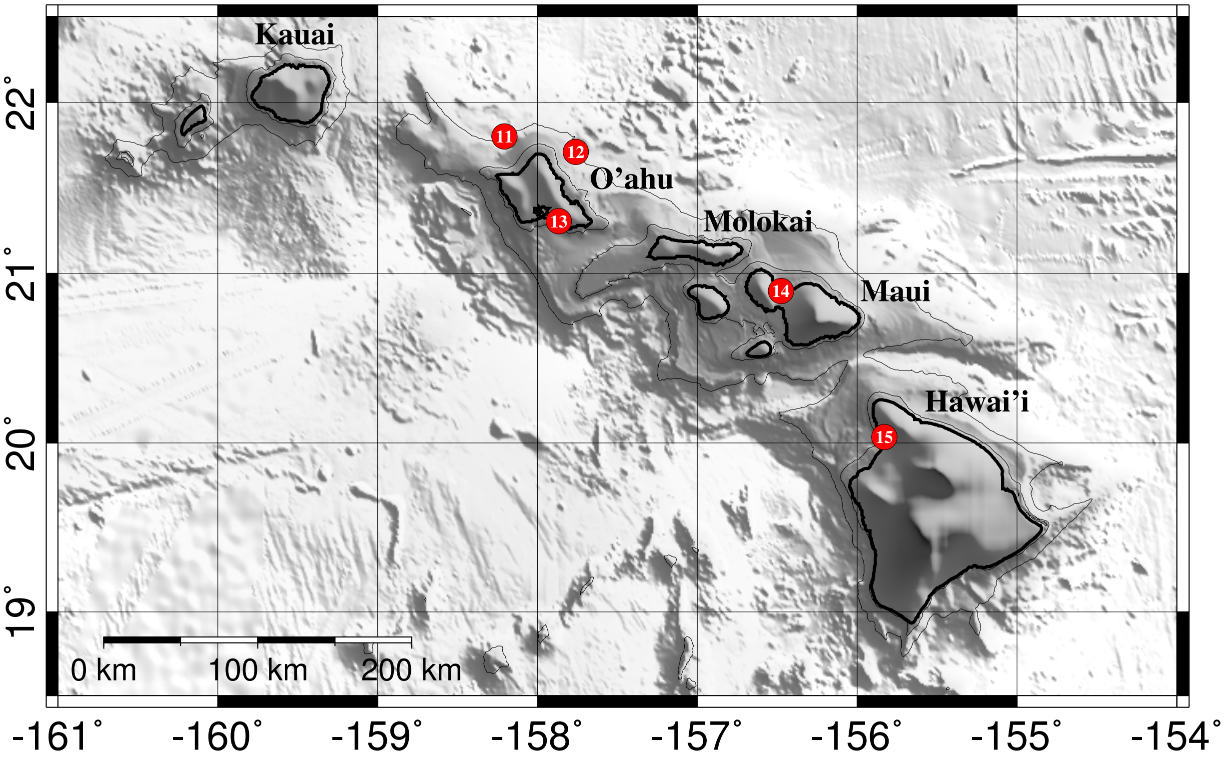

Figure 2.3: Sites of tide gauges at several harbors in the Main Hawaiian Islands, and deep water pressure sensors offshore of O'ahu Island. Contours of 200m and 2000m are plotted, and an identification number was assigned to each site.

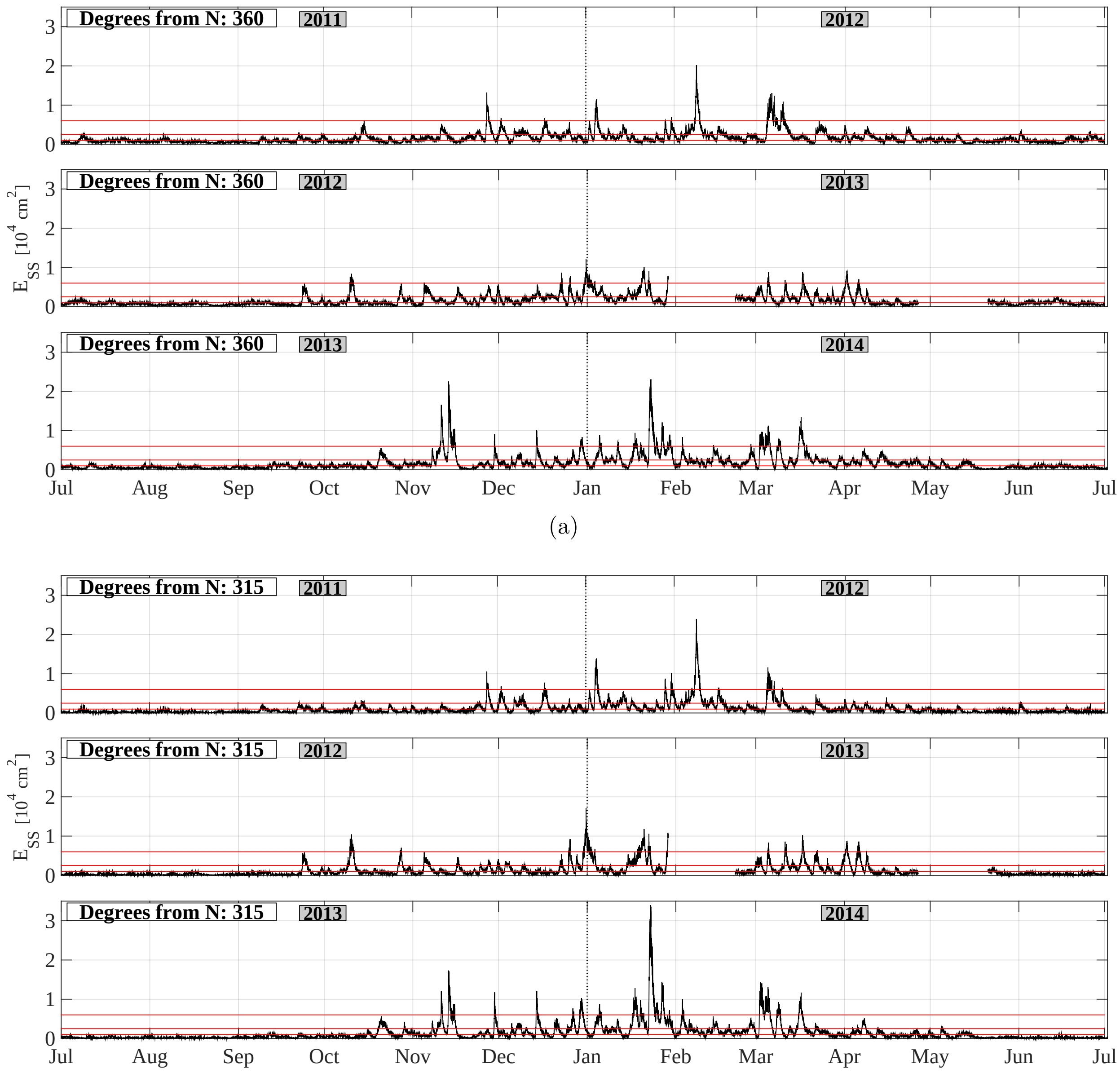

(a)

(b)

Figure 2.4: Energy vs. time at Waimea Buoy site during 07/2011-07/2014 for SS arriving (a) 360°, and (b) 315° from geographical north. From bottom to top, the horizontal dashed red lines represent the cutoffs between no-SS, weak, moderate, and strong SS forcing levels, as determined using the following figure.

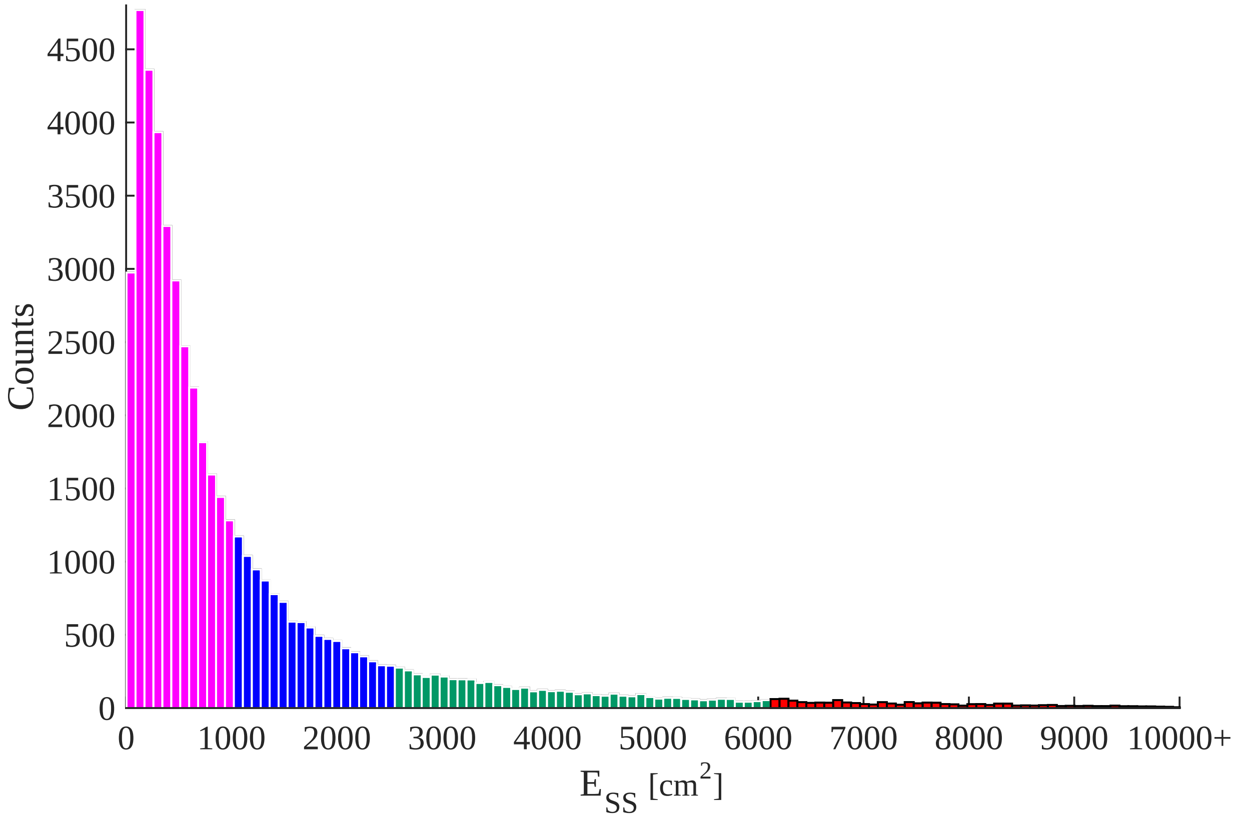

Figure 2.5: Distribution of energy in the SS band flowing towards shore from 315°, at site 10 between 07/2011 - 07/2014. From left to right, the ∼ 67%, next ∼ 20%, next ∼ 10%, and last ∼ 3% of the distribution represent the range of energy levels for the cases of: (i) no/minimal SS (magenta bars); (ii) weak SS (blue bars); (iii) moderate SS (green bars); and, (iv) strong SS (red bars), respectively.

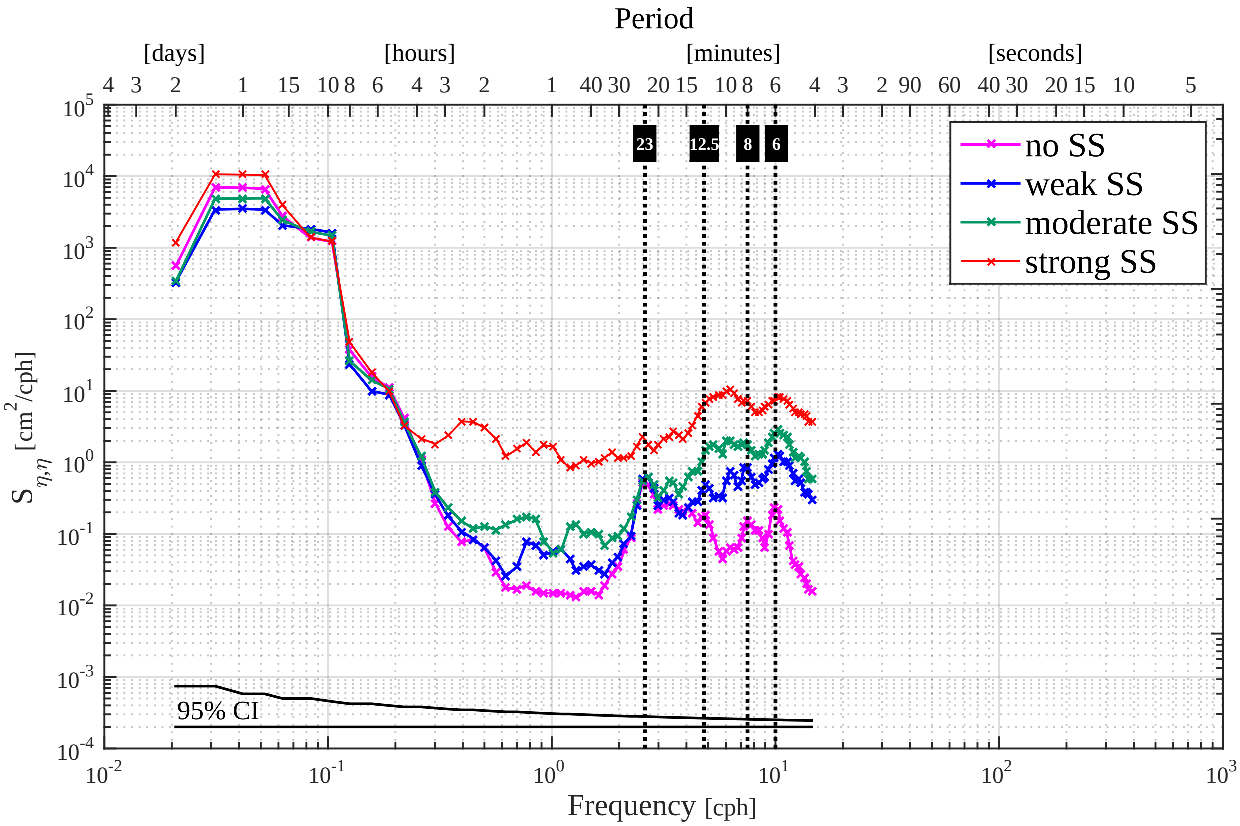

Figure 2.6: Power spectral density using historical datasets at site 1 sampled at 2 min intervals in Hale'iwa Harbor during times of no SS (magenta curve), weak (blue curve), moderate (green curve), and strong (red curve) SS forcing events. Each curve was generated using five 4-day long sea level data segments (see Table 2.4 for exact time periods). The 95% confidence interval for each independent spectrum estimate is shown at the bottom. *The approximate periods of statistically significant spectral peaks found in at least one of the spectra (6, 8, 12.5, and 23 min) are labeled and indicated by the vertical black dotted lines.*

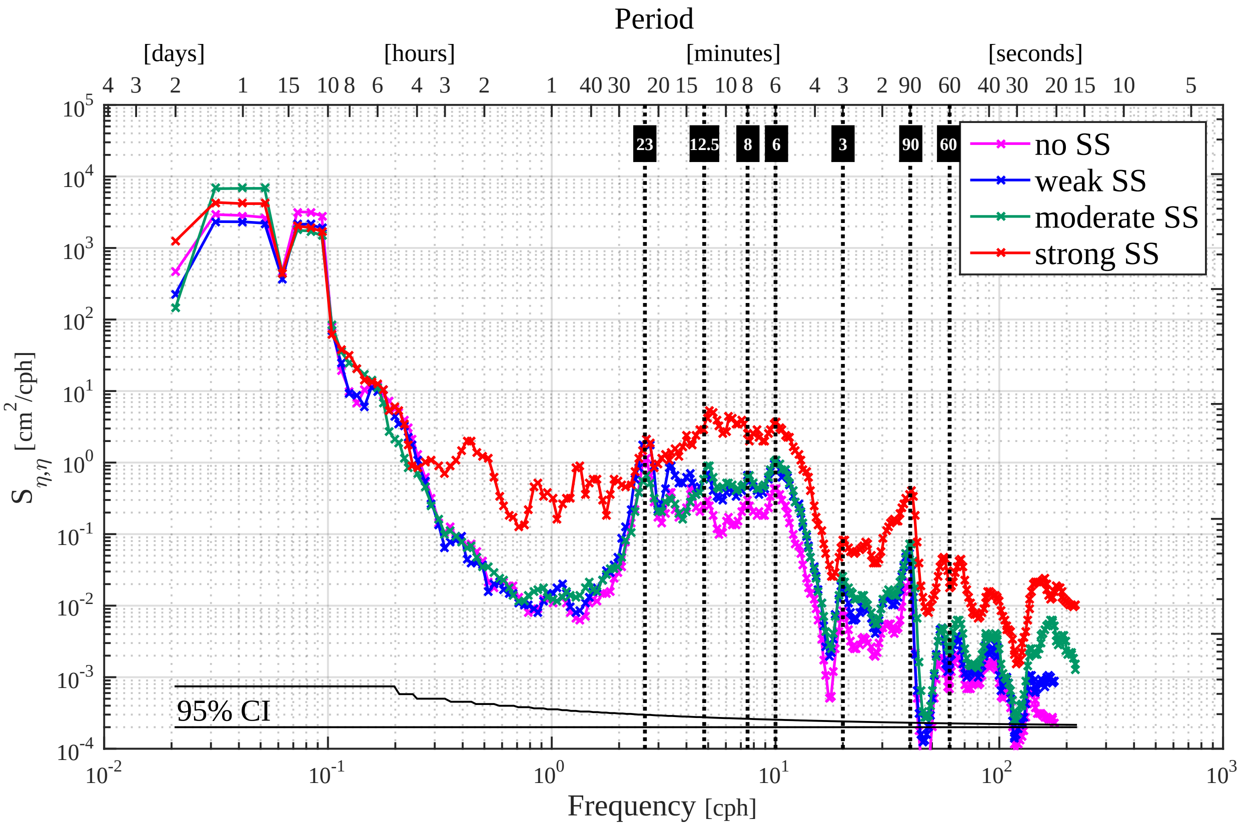

Figure 2.7: Power spectral density using datasets from site 2 of the 11/2013 - 05/2014 deployment in Hale'iwa Harbor during times of no SS (magenta curve), weak (blue curve), moderate (green curve), and strong (red curve) SS forcing events. Each curve was generated using five 4-day long sea level data segments (see Table 2.4 for exact time periods). The 95% confidence interval for each independent spectrum estimate is shown at the bottom. *The approximate periods of statistically significant spectral peaks (60 sec, 90 sec, 3, 6, 8, 12.5, and 23 min) are labeled and indicated by the vertical black dotted lines.*

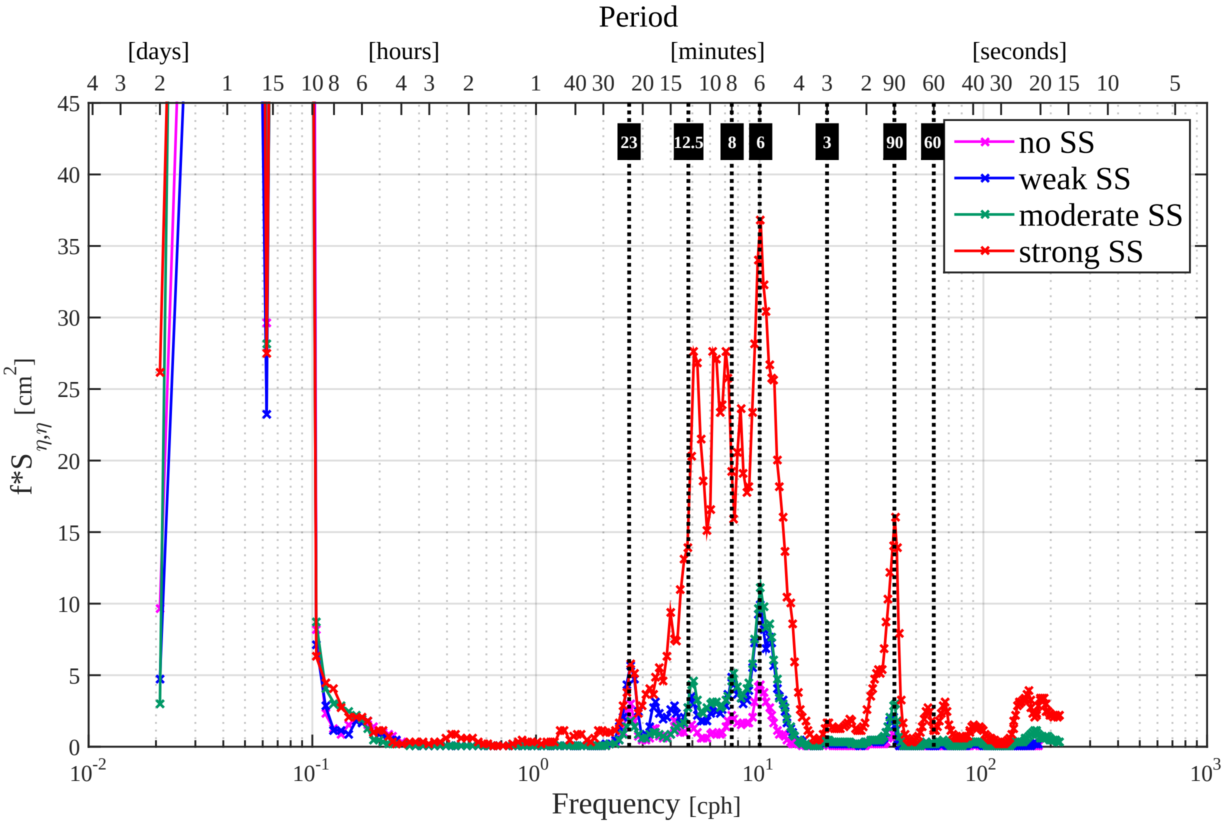

Figure 2.8: Variance preserving spectra using datasets from site 2 of the 11/2013 - 05/2014 deployment in Hale'iwa Harbor during times of no SS (magenta curve), weak (blue curve), moderate (green curve), and strong (red curve) SS forcing events. Each curve was generated using five 4-day long sea level data segments (see Table 2.4 for exact time periods). The 95% confidence interval for each independent spectrum estimate is shown at the bottom. *The approximate periods of statistically significant spectral peaks (60 sec, 90 sec, 3, 6, 8, 12.5, and 23 min) are labeled and indicated by the vertical black dotted lines.*

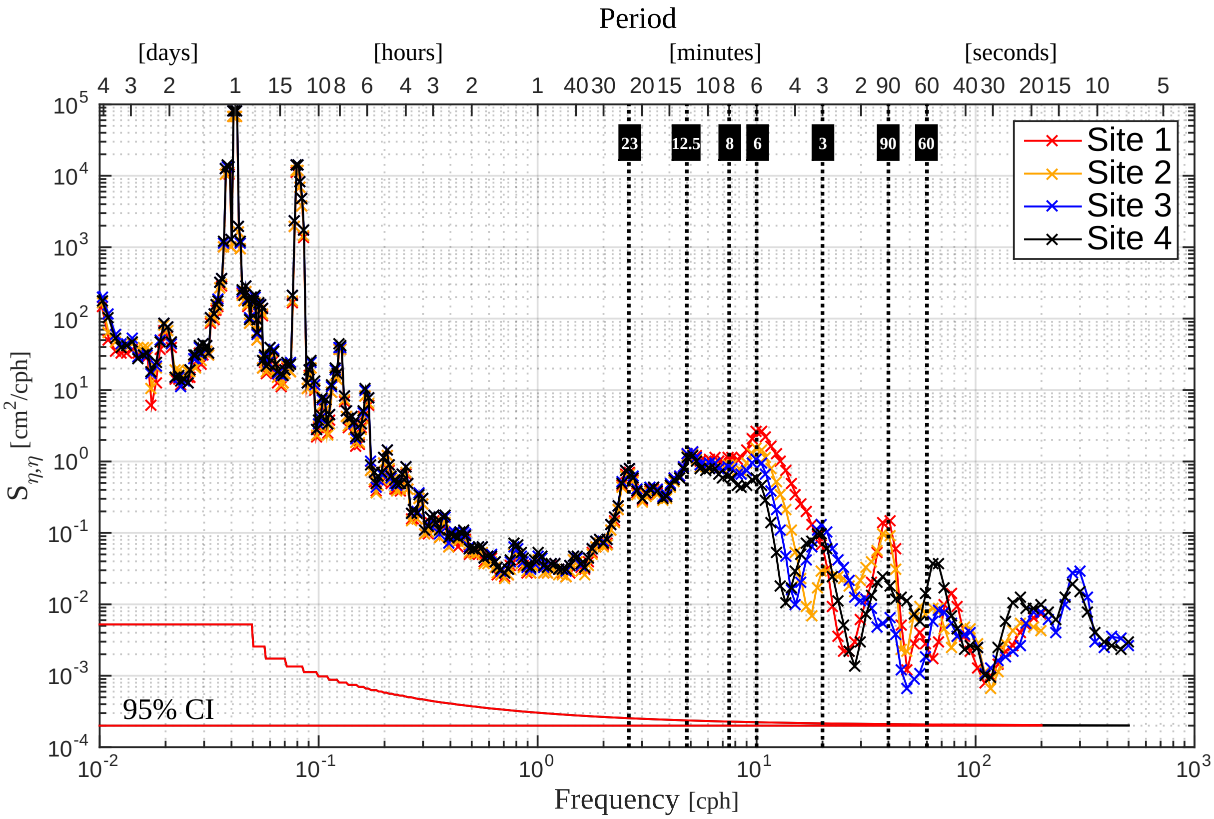

Figure 2.9: Power spectral density of observed sea level at the locations of the four sensors inside Hale'iwa Harbor during 11/28/13 - 01/20/14. The 95% confidence interval for each independent spectrum estimate is shown at the bottom.

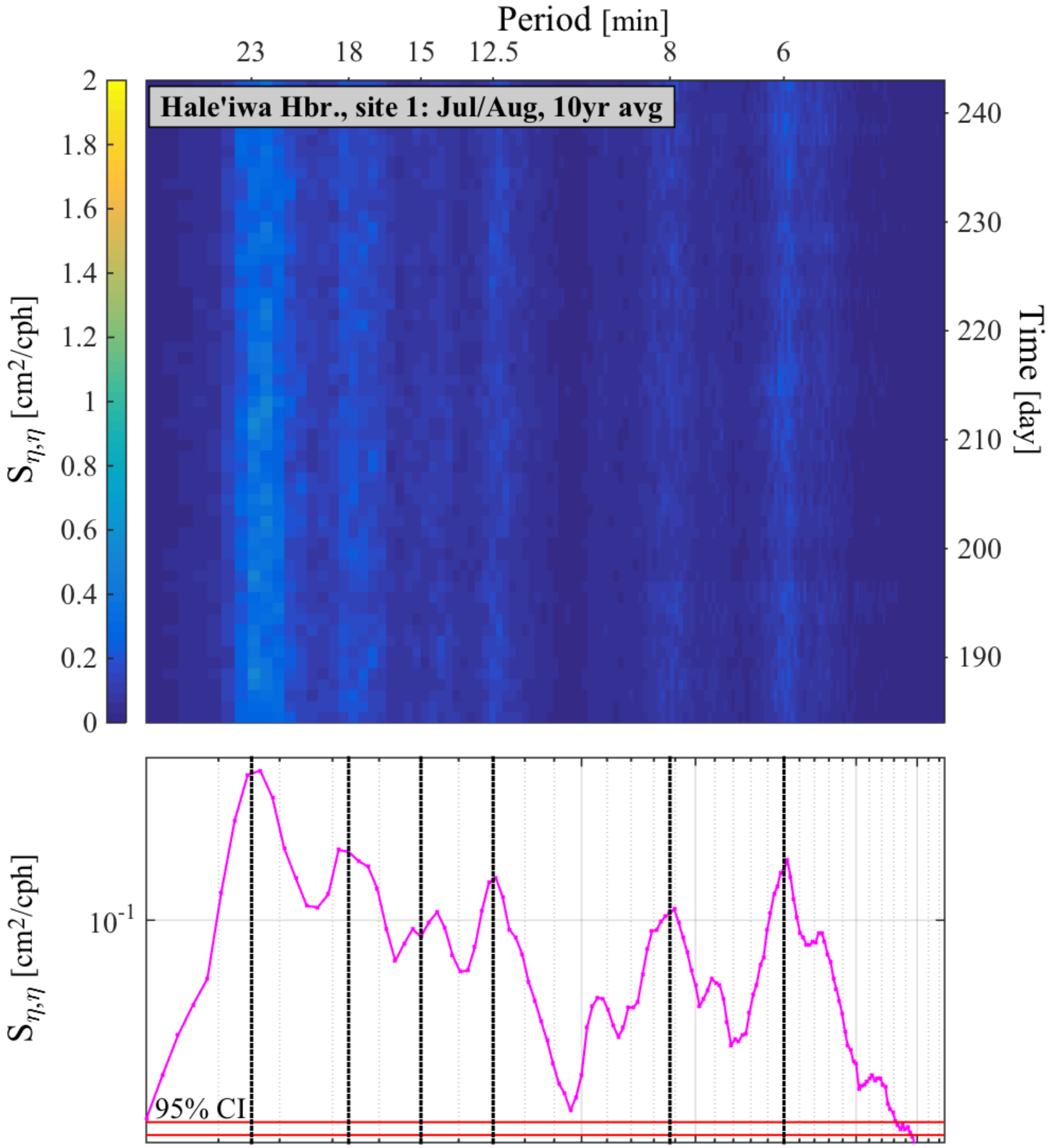

Figure 2.10: Upper panel: spectrogram of observed IG-PSD during July-Aug summertime months, generated by averaging two-month long data segments from 10 years. Lower panel: PSD, generated by applying a time average to the above spectrogram. The 95% confidence interval for each independent spectrum estimate in the PSD plot is shown at the bottom.

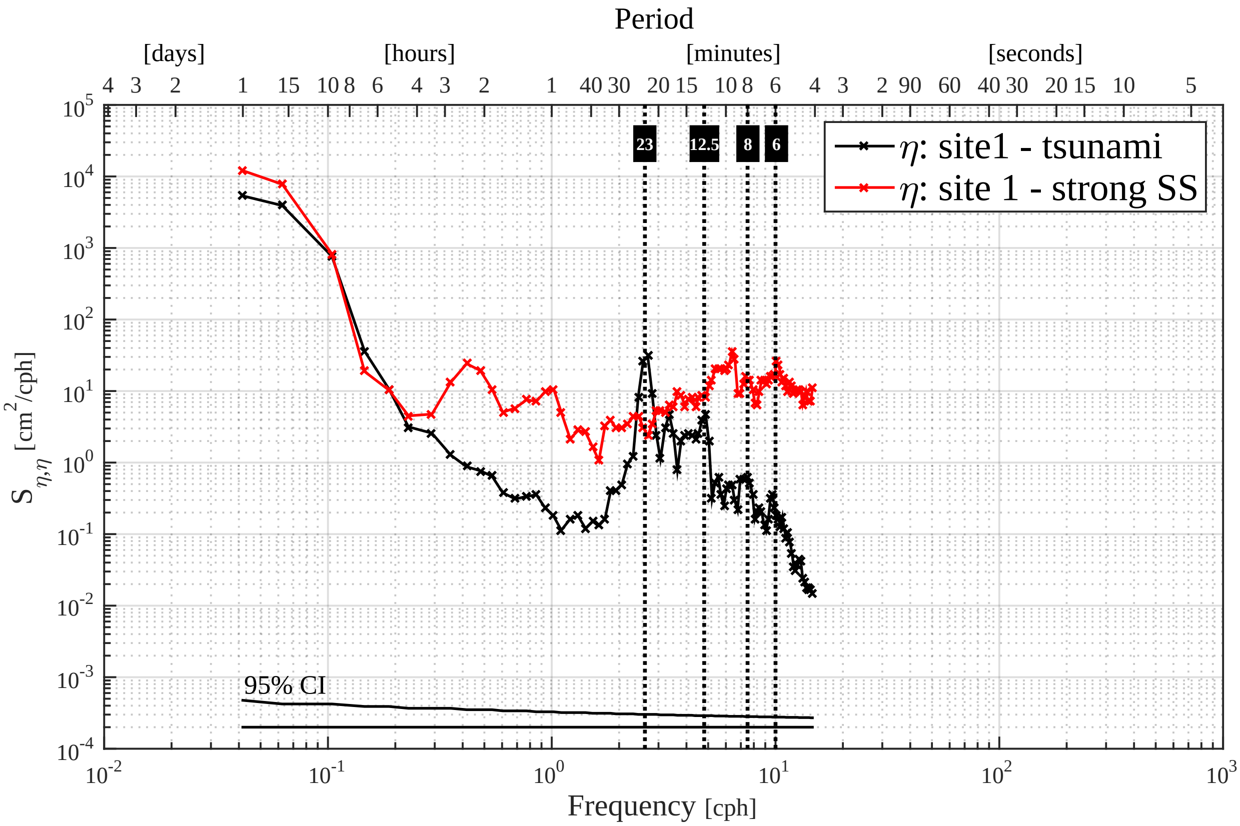

Figure 2.11: Power spectral density curves of observed sea level at site 1 inside Hale'iwa Harbor. The 2-day long dataset used to generate the black curve includes a tsunami event on 06/25/01. The 2-day long dataset used to generate the red curve includes a large SS event from 01/04/03. The 95% confidence interval for each independent spectrum estimate is shown at the bottom. *The approximate periods of statistically significant spectral peaks identified in other spectra (6, 8, 12.5, and 23 min) are labeled and indicated by the vertical black dashed-dotted lines.*

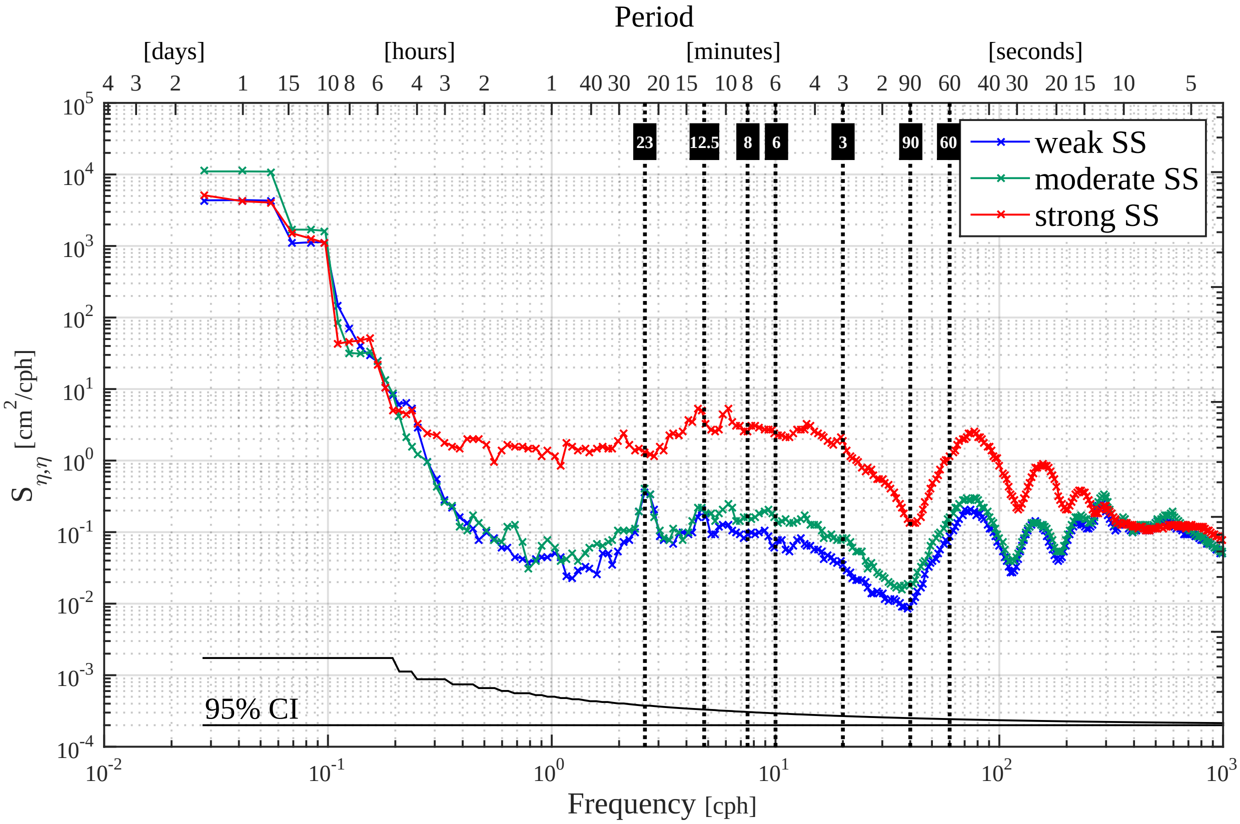

Figure 2.12: Power spectral density using historical datasets at Mokuleia site 8c sampled at 1 sec intervals during times of weak (blue curve), moderate (green curve), and strong (red curve), SS forcing events. Each curve was generated using two three-day long sea level data segments (see Table 2.4 for exact time periods). The 95% confidence interval for each independent spectrum estimate is shown at the bottom. *The approximate periods of statistically significant spectral peaks identified in other spectra (60 sec, 90 sec, 3, 6, 8, 12.5, and 23 min) are labeled and indicated by the vertical black dashed-dotted lines.*

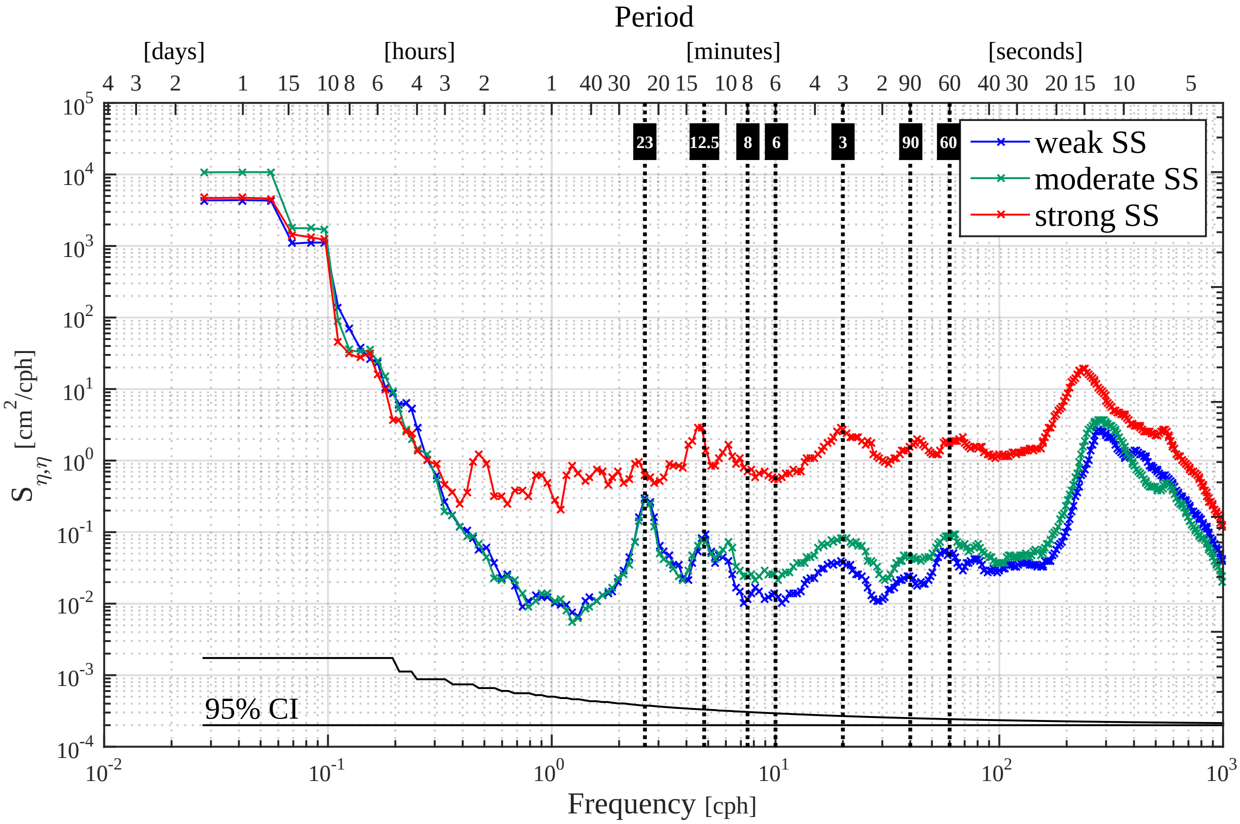

Figure 2.13: Power spectral density plots using historical datasets at Mokuleia site 8b sampled at 1 sec intervals during times of weak (blue curve), moderate (green curve, and strong (red curve), SS forcing events. Each curve was generated using two three-day long sea level data segments (see Table 2.4 for exact time periods). The 95% confidence interval for each independent spectrum estimate is shown at the bottom. *The approximate periods of statistically significant spectral peaks identified in other spectra (60 sec, 90 sec, 3, 6, 8, 12.5, and 23 min) are labeled and indicated by the vertical black dashed-dotted lines.*

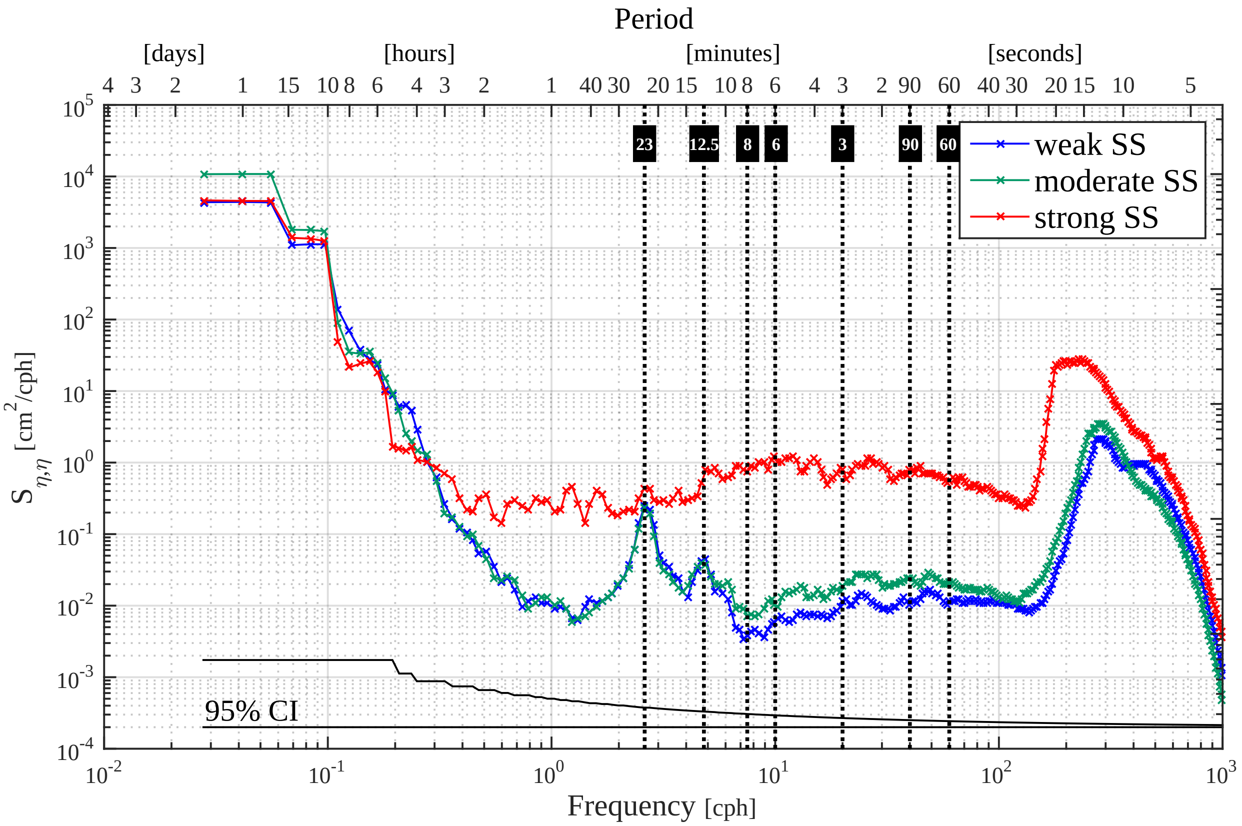

Figure 2.14: Power spectral density plots using historical datasets at Mokuleia site 8a sampled at 1 sec intervals during times of weak (blue curve), moderate (green curve), and strong (red curve), SS forcing events. Each curve was generated using two three-day long sea level data segments (see Table 2.4 for exact time periods). The 95% confidence interval for each independent spectrum estimate is shown at the bottom. *The approximate periods of statistically significant spectral peaks identified in other spectra (60 sec, 90 sec, 3, 6, 8, 12.5, and 23 min) are labeled and indicated by the vertical black dashed-dotted lines.*

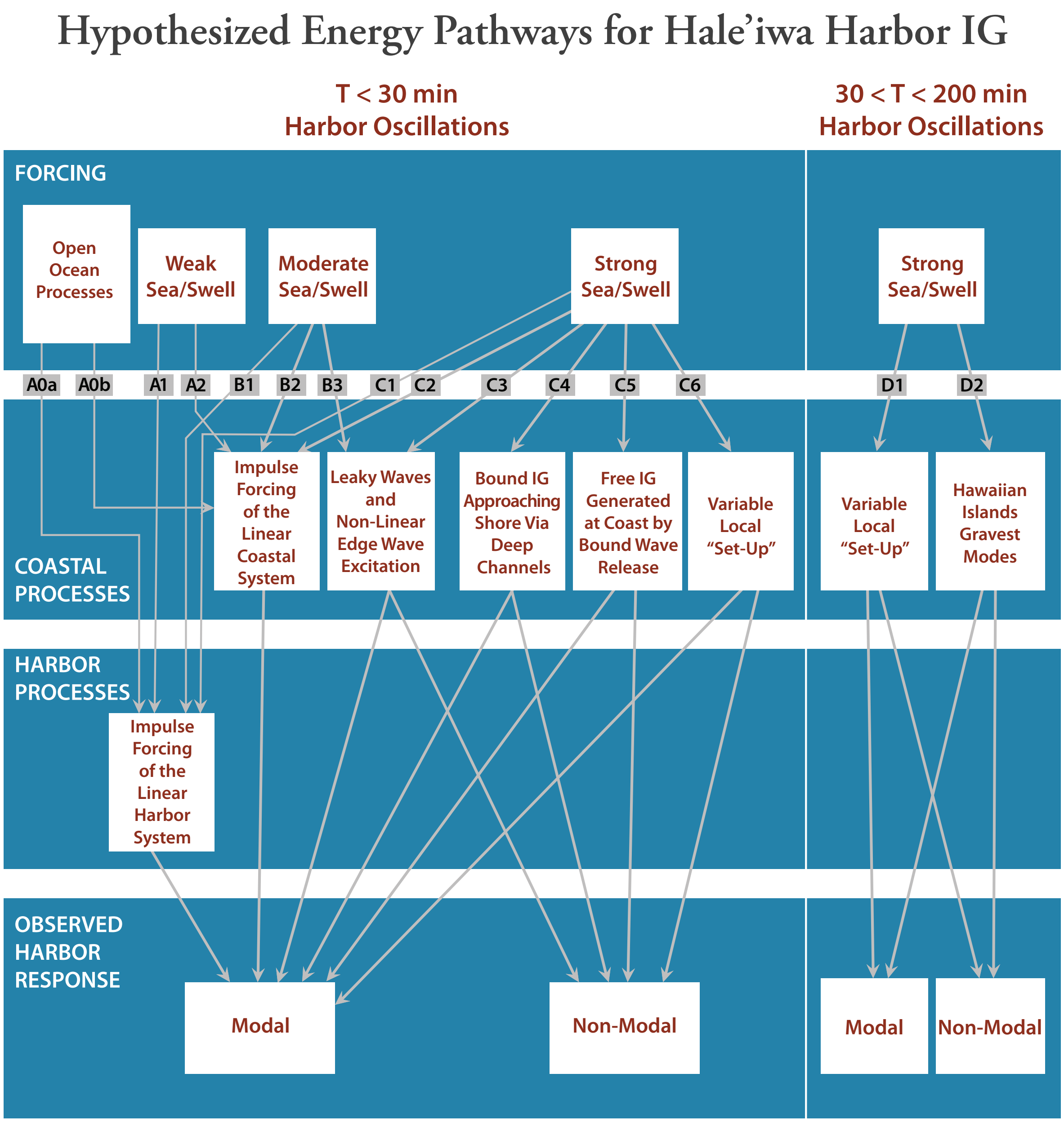

Figure 2.15: Hypotheses of possible energy pathways of IG waves into Hale'iwa Harbor. The top row contains the forcing sources, second and third rows contain the intermediary coastal and harbor processes, respectively, and the bottom row contains the observed harbor response.

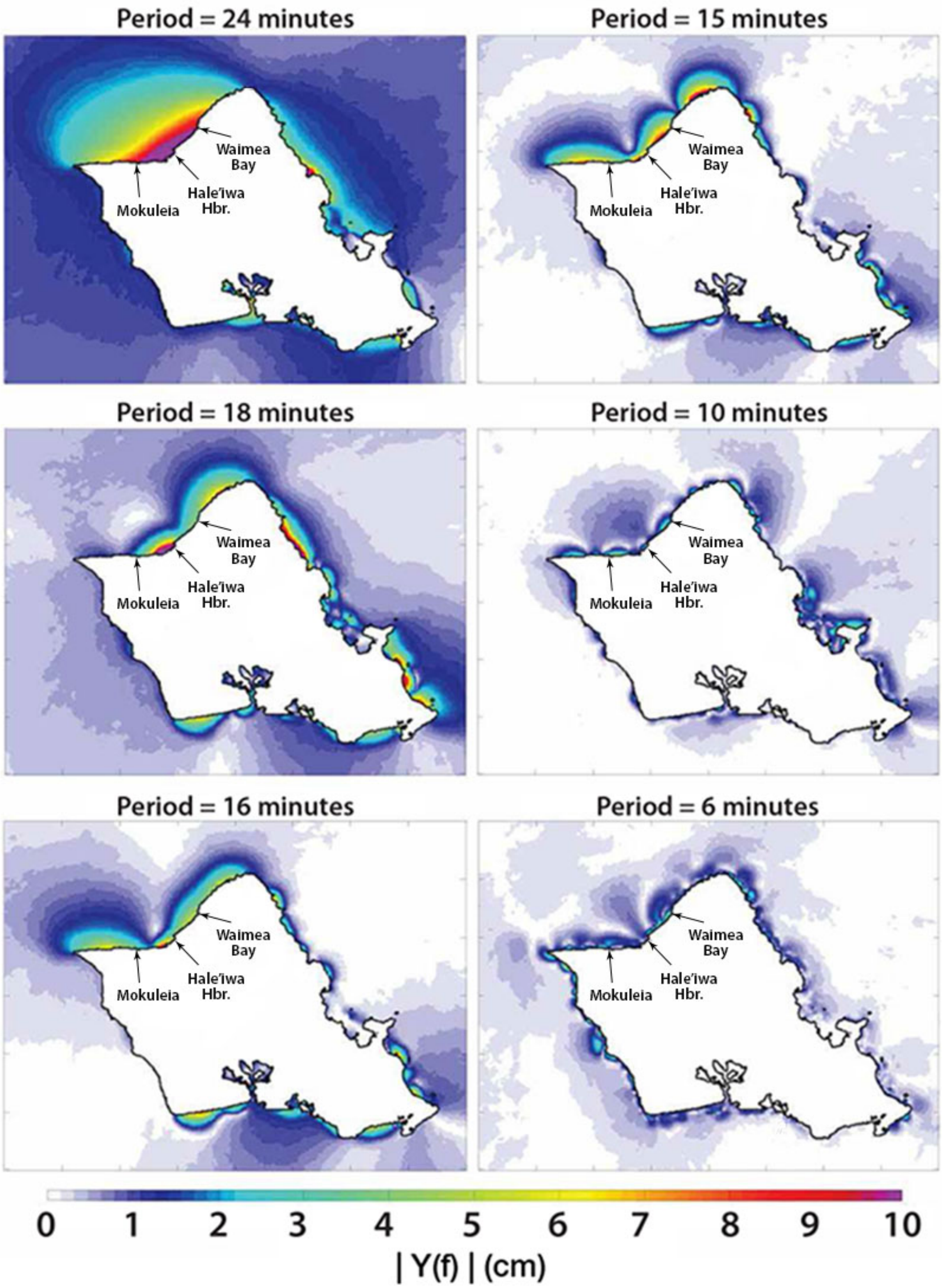

Figure 2.16: Amplitudes of oscillations for several coastal modes around O'ahu Island, as a result of the Kuril Island tsunami forcing that hit Hawai'i on 11/15/2006. Figure taken from *Munger and Cheung* (2008), and modified by Assaf Azouri.

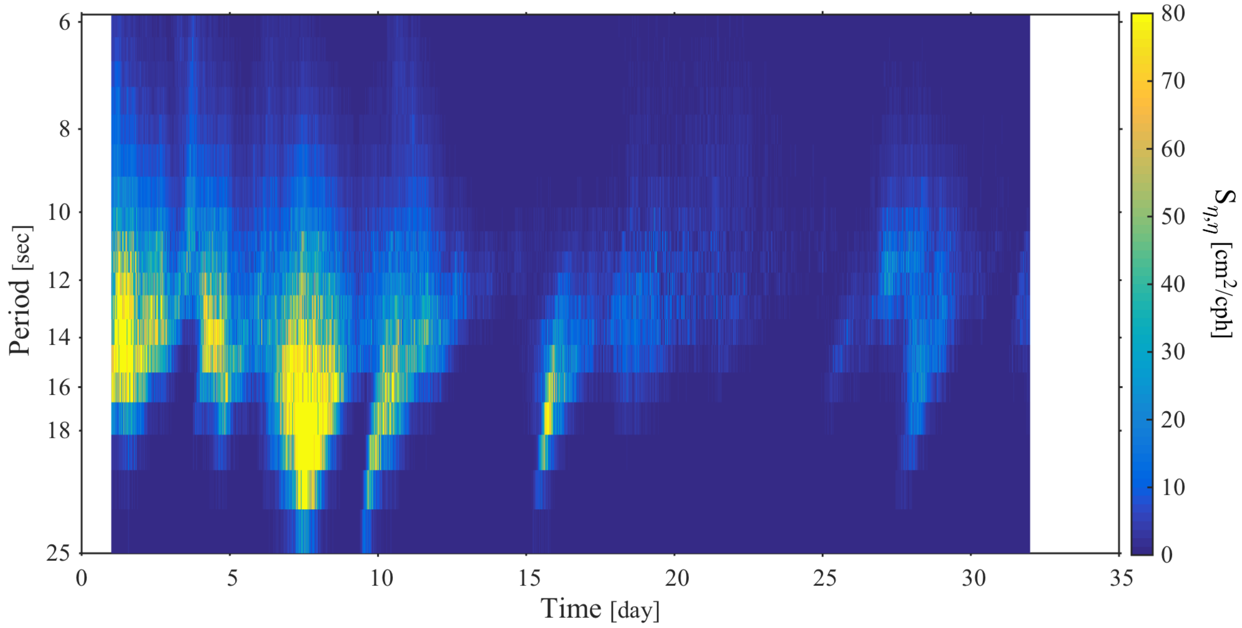

Figure 2.17: Spectrogram of offshore SS PSD during the month of 01/2002 as observed at site 10 (Waimea Buoy).

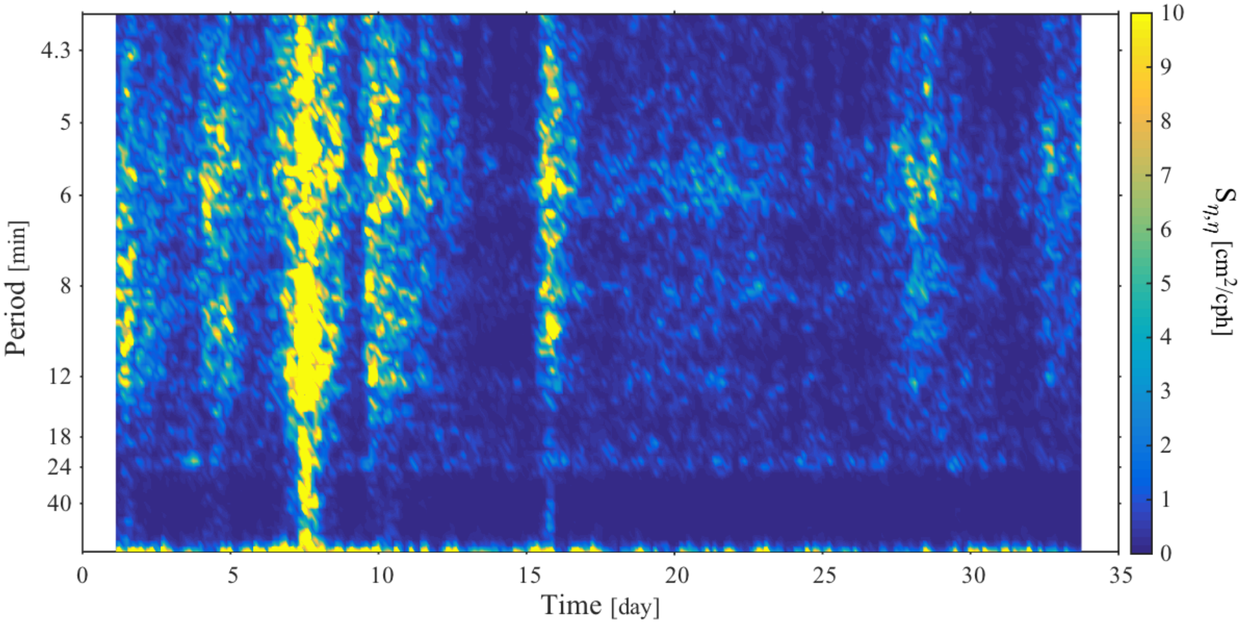

Figure 2.18: Spectrogram of observed IG-PSD during the month of 01/2002 at site 1 in Hale'iwa Harbor.

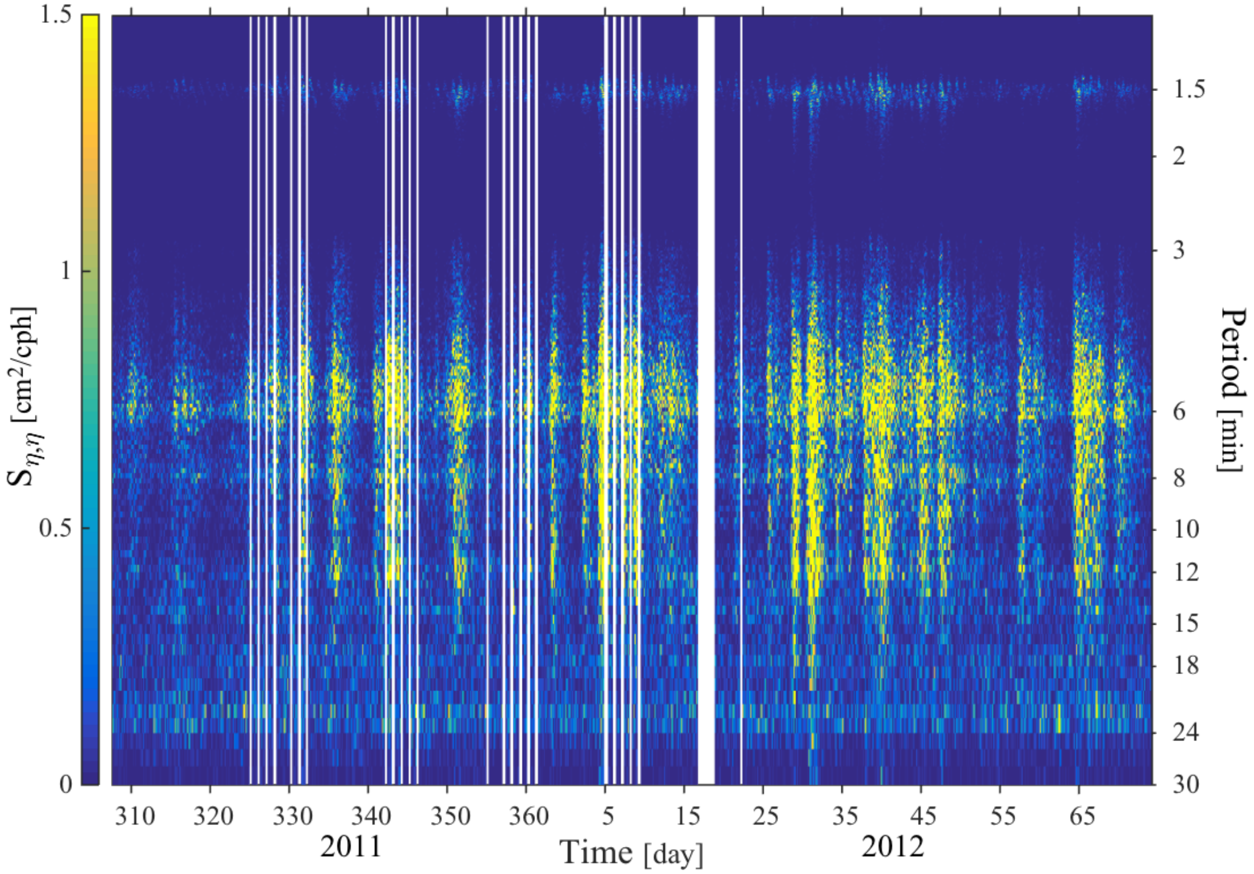

Figure 2.19: Spectrogram of observed IG-PSD during 11/04/11-03/14/12 at site 1 in Hale'iwa Harbor, in the 0.5-30 min period band.

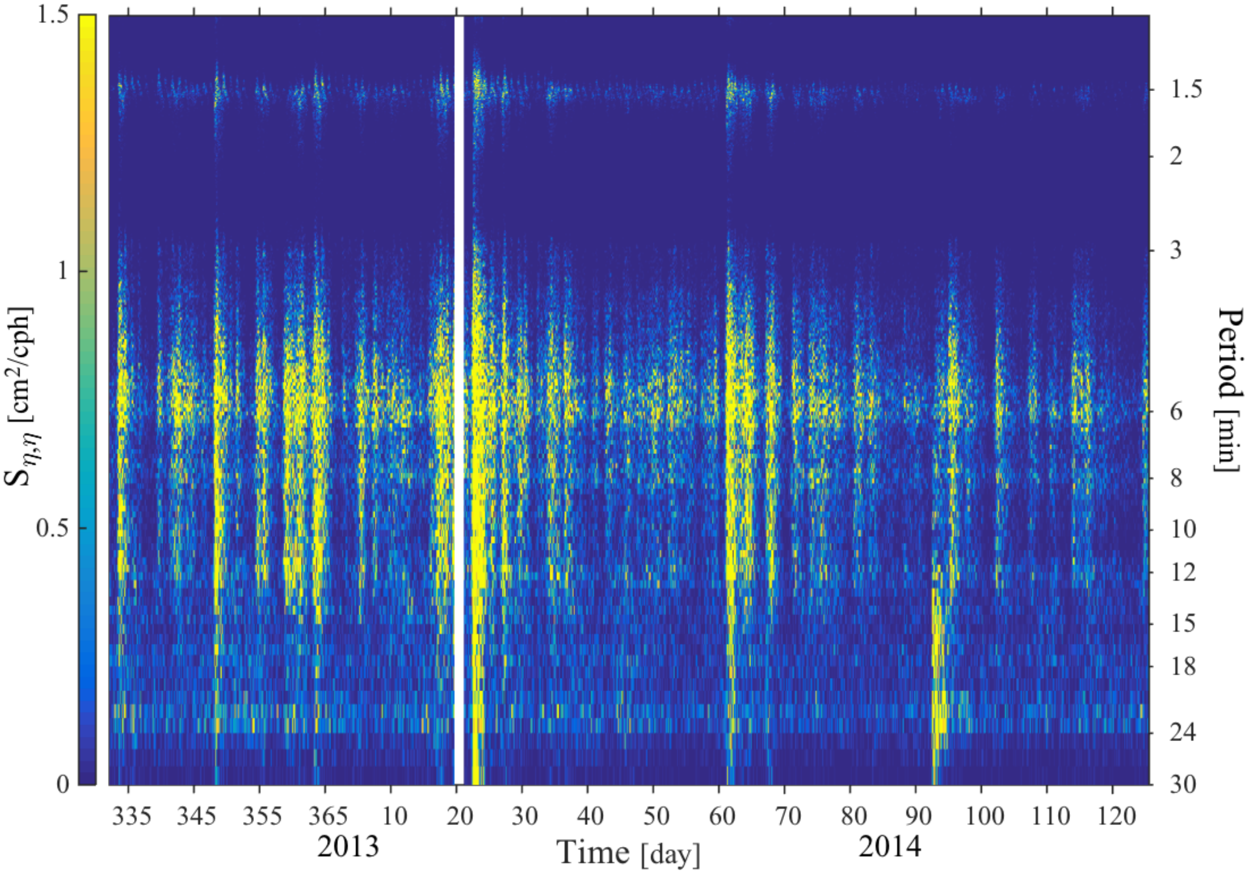

Figure 2.20: Spectrogram of observed IG-PSD during 11/28/13-05/05/14 at site 1 in Hale'iwa Harbor, in the 0.5-30 min period band.

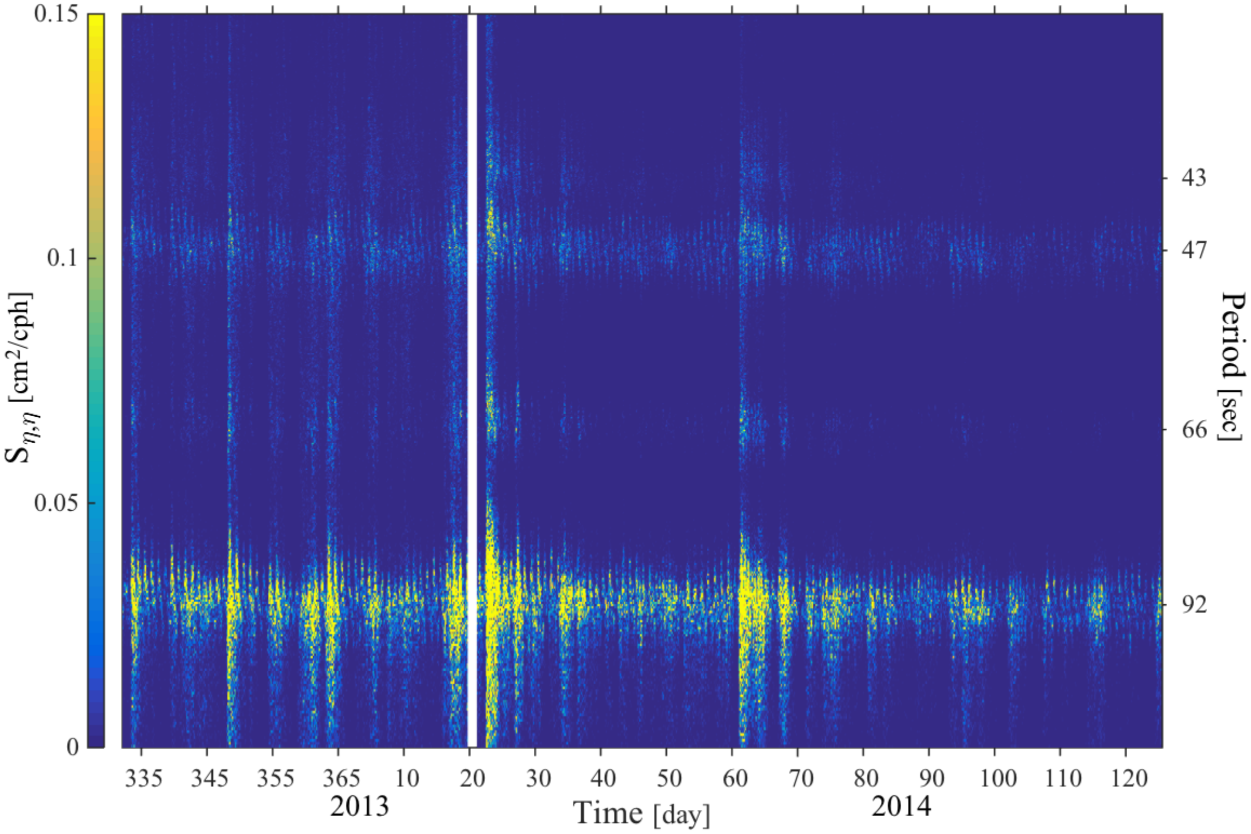

Figure 2.21: Spectrogram of observed IG-PSD during 11/28/13-05/05/14 at site 1 in Hale'iwa Harbor, in the 0.5-2 min period band.

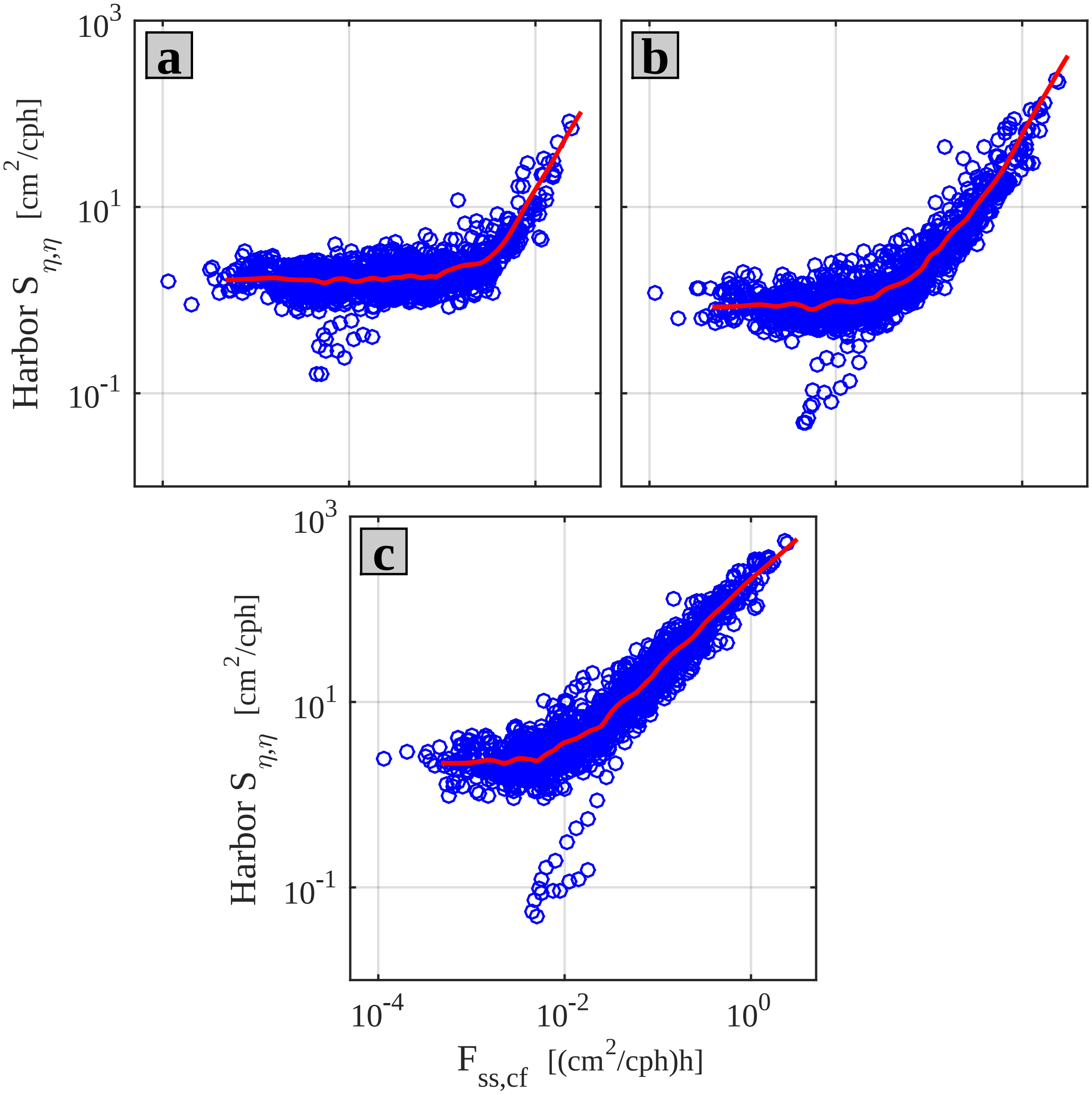

Figure 2.22: Scatter plot of harbor IG sea level PSD at site 1 versus offshore SS sea level energy flux propagating towards shore ($F_{ss,cf}$) for (a) 15-40 min, (b) 10-15 min, and (c) 4-10 min period bands. Each plot was generated using 1392 data points from a year-long dataset during the year 2002. The red curve was fitted to the data using piecewise interpolation technique.

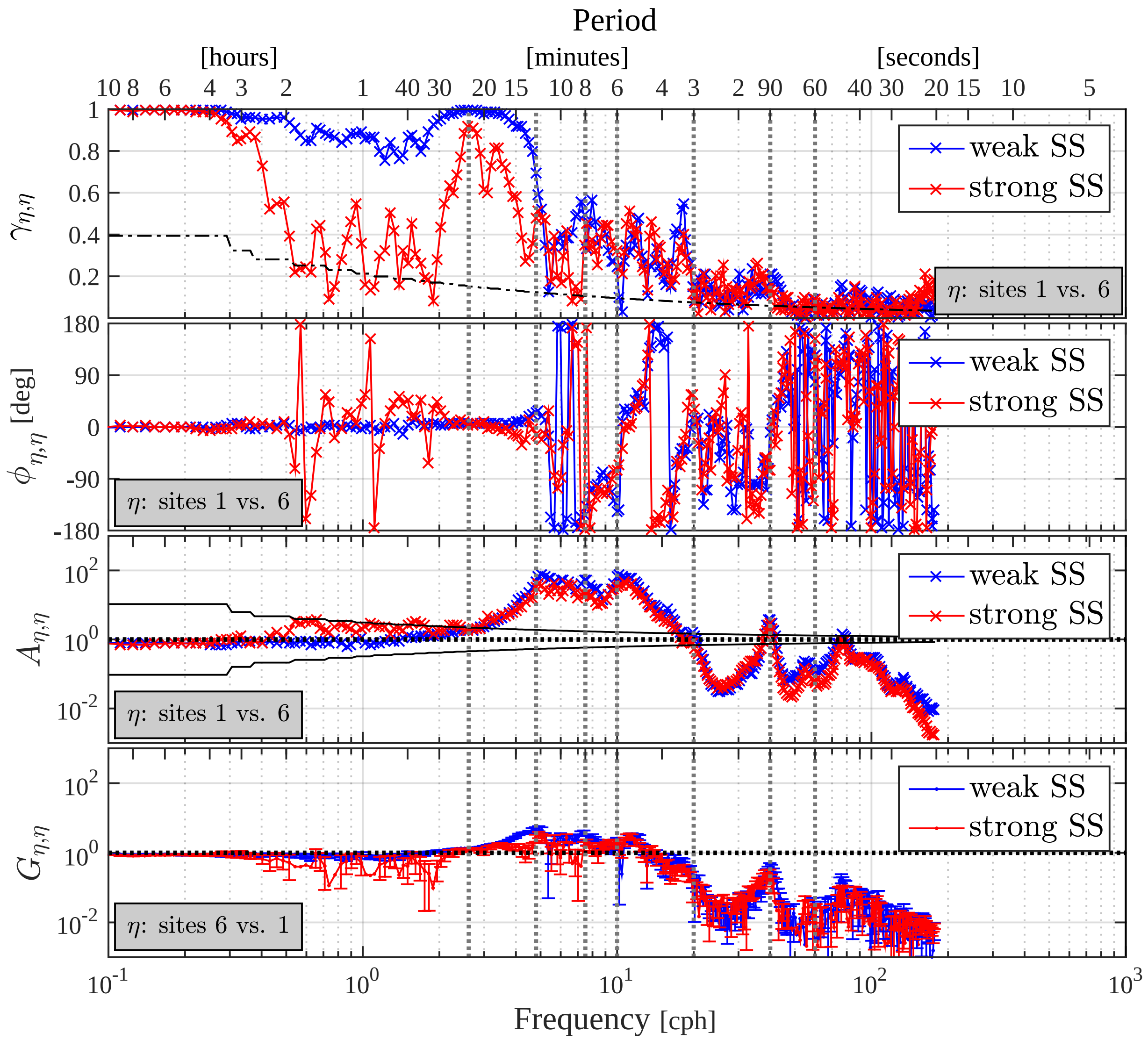

Figure 2.23: Coherence amplitude, $\gamma_{\eta,\eta}$, coherence phase, $\phi_{\eta,\eta}$, amplification, $A_{\eta,\eta}$, and gain ,$G_{\eta,\eta}$, for sites 1 vs. 6. Blue/red curves were derived from five three-day long sea level data segments during 11/04/11 - 01/31/12 (see Table 2.4 for exact time periods). The dashed dotted line in the coherence amplitude plot is the 95% level of no significance. The 95% confidence interval for each independent spectrum estimate is the vertical distance between the continuous black lines in the amplification plot, and the error bars in the gain plot. *The vertical black dotted lines indicate significant spectral peaks identified in other spectra.*

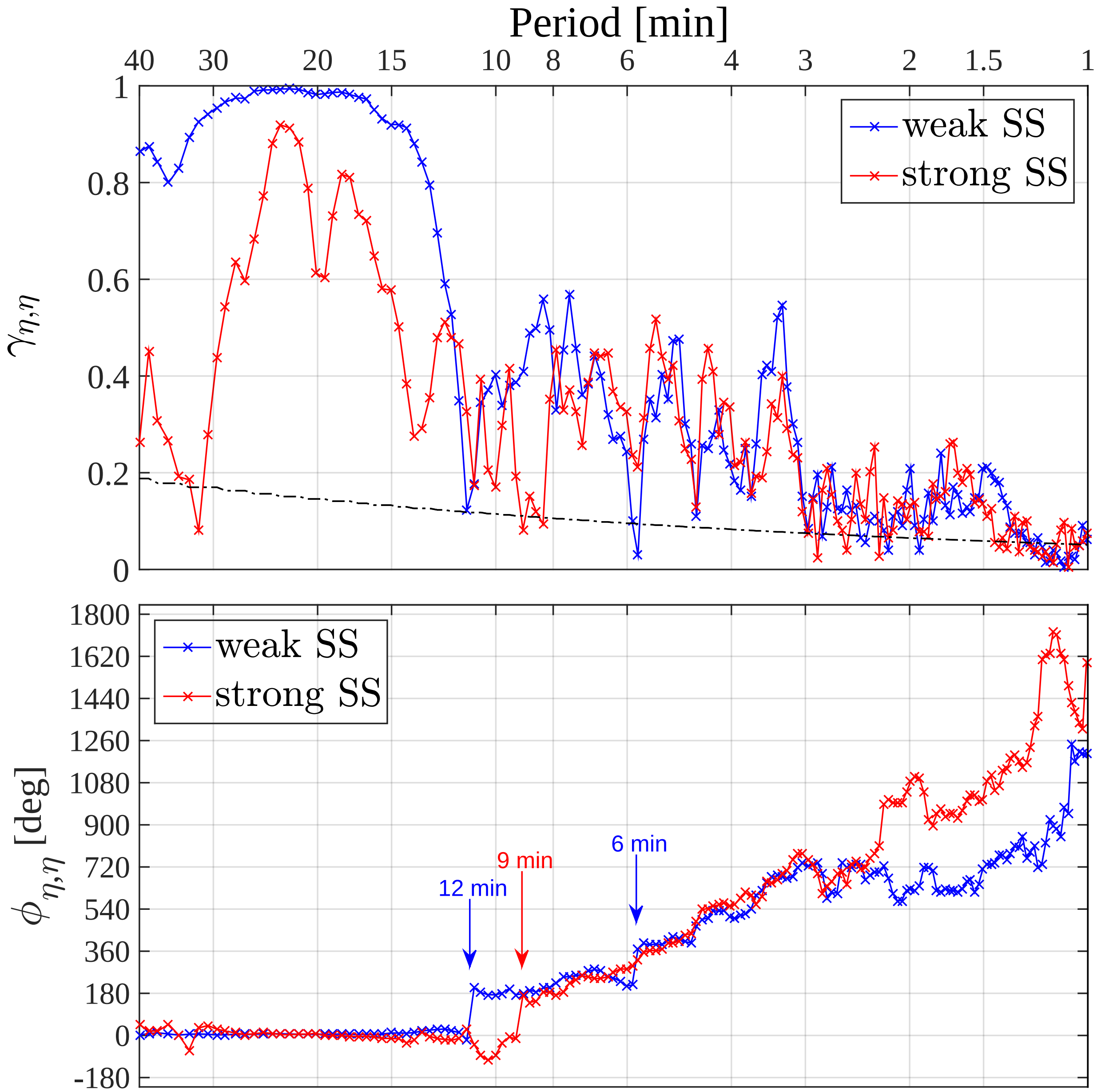

Figure 2.24: Coherence amplitude, $\gamma_{\eta,\eta}$, and coherence phase, for sites 1 vs. 6, focusing on the 1-40 min period band. Blue/red curves were derived from five three-day long sea level data segments during 11/04/11 - 01/31/12 (see Table 2.4 for exact time periods). The dashed dotted line in the coherence amplitude plot is the 95% level of no significance. The coherence phase was unwrapped to help reveal any sharp transitions.

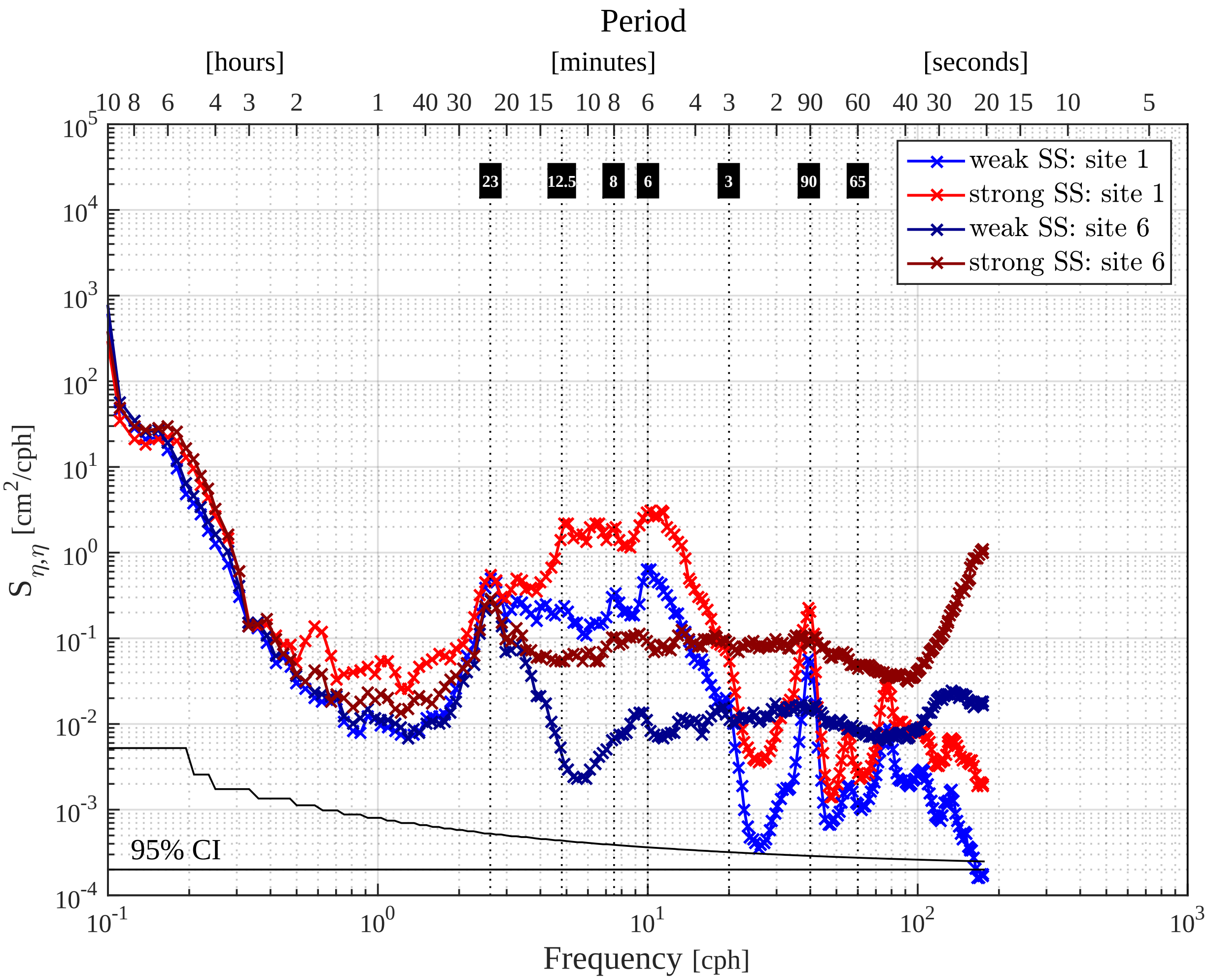

Figure 2.25: PSD curves of sea level derived from bottom pressure for sites 1 and 6 under strong and weak forcing. Strong forcing is shown by red hues; weak forcing by blue. Site 6, well outside the harbor, is shown in the darker hues; site 1, within the inner harbor, is shown by lighter hues. Blue/red curves were derived from five three-day long sea level data segments during 11/04/11 - 01/31/12 (see Table 2.4 for exact time periods). The frequency-dependent 95% confidence interval for each independent spectrum estimate is shown at the bottom. *The approximate periods of statistically significant spectral peaks identified in other spectra (60 sec, 90 sec, 3, 6, 8, 12.5, and 23 min) are labeled and indicated by the vertical black dashed-dotted lines.*

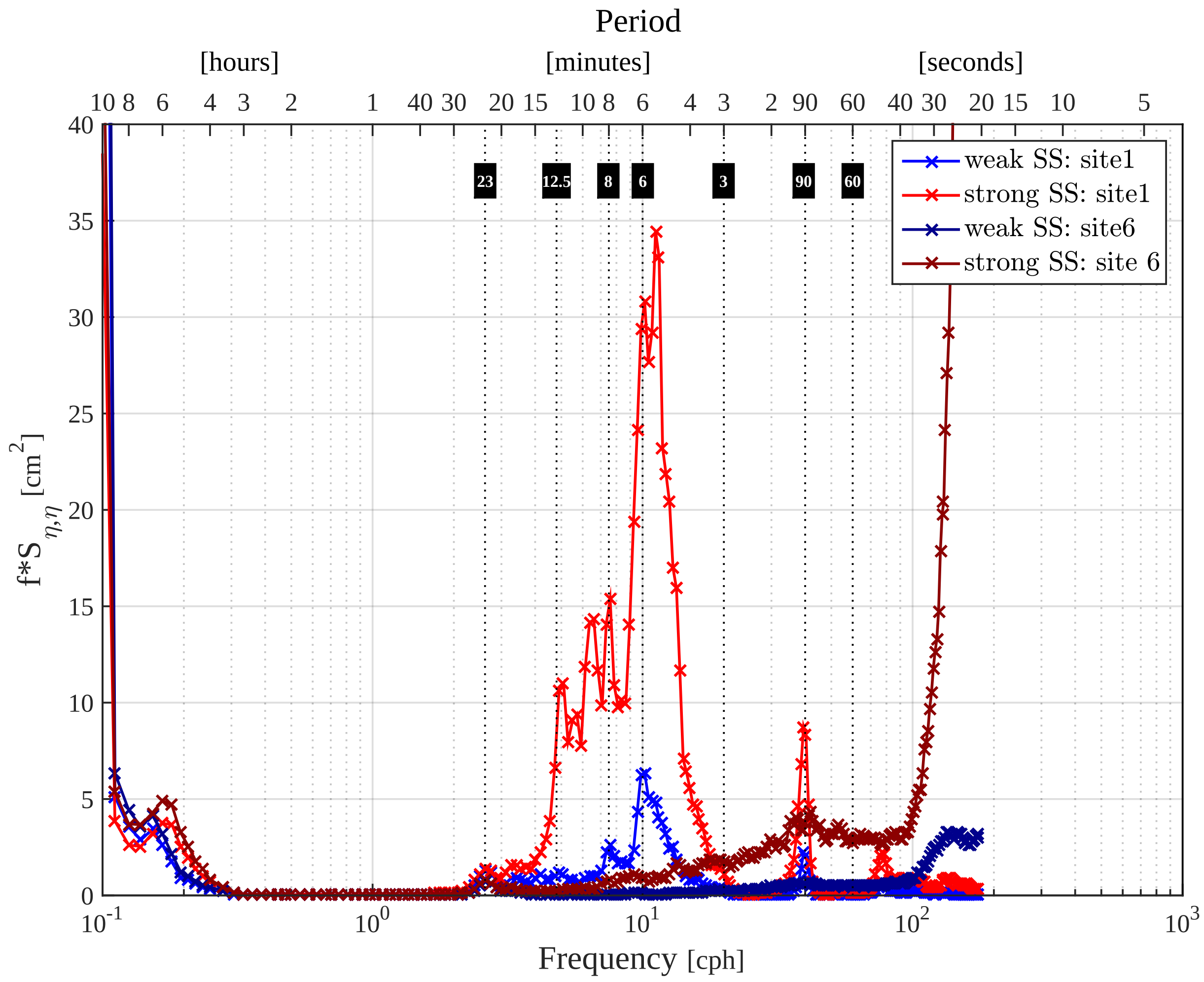

Figure 2.26: Variance preserving curves for sites 1 and 6. Blue/red curves were derived from five three-day long sea level data segments during 11/04/11 - 01/31/12 (see Table 2.4 for exact time periods). *The approximate periods of statistically significant spectral peaks identified in other spectra (60 sec, 90 sec, 3, 6, 8, 12.5, and 23 min) are labeled and indicated by the vertical black dashed-dotted lines.*

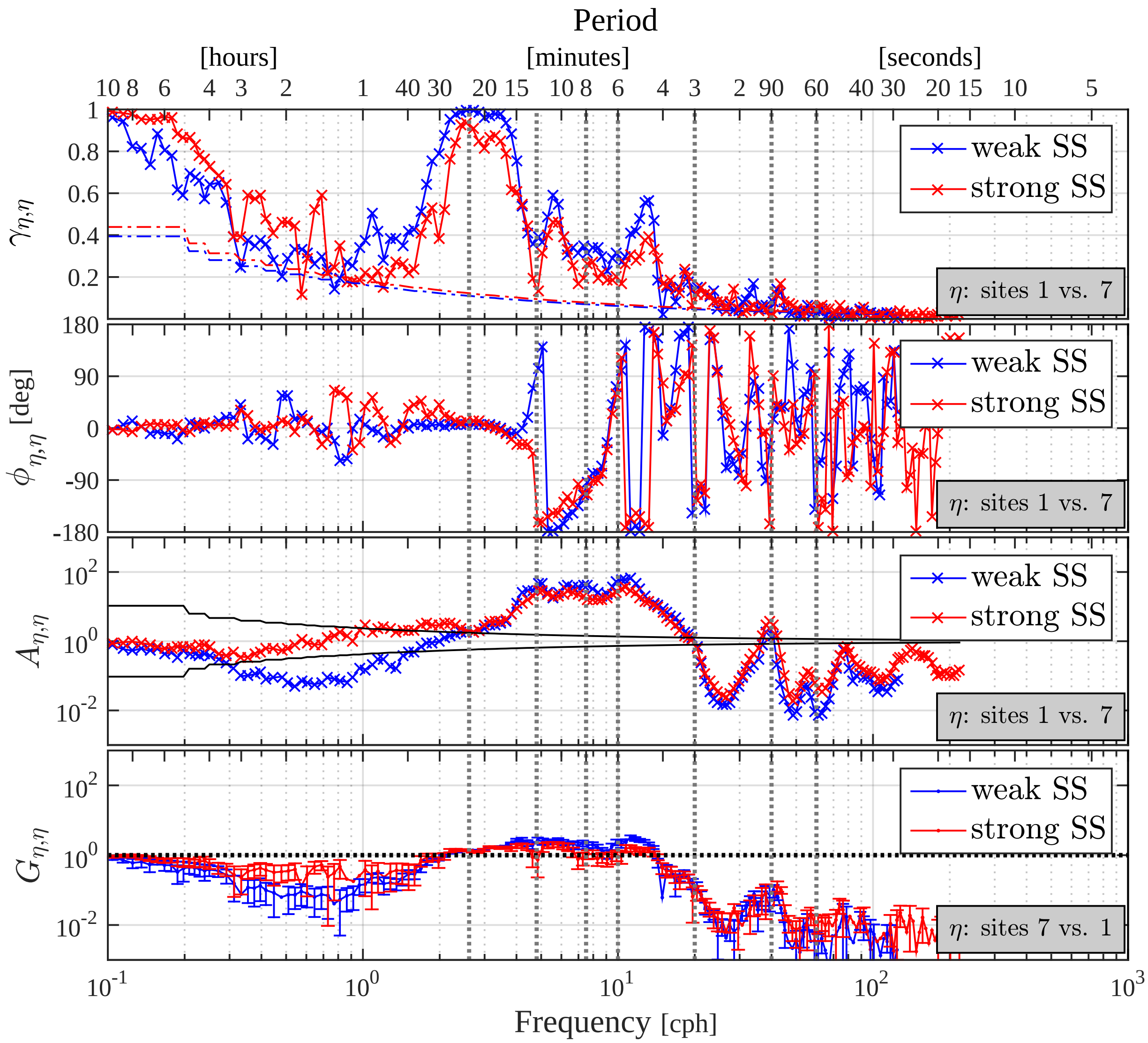

Figure 2.27: Coherence amplitude, $\gamma_{\eta,\eta}$, coherence phase, $\phi_{\eta,\eta}$, amplification, $A_{\eta,\eta}$, and gain, $G_{\eta,\eta}$, for sites 1 vs. 7. Blue/red curves were derived from five three-day long sea level data segments during 12/11/13 - 03/18/14 (see Table 2.4 for exact time periods). The dashed dotted line in the coherence amplitude plot is the 95% level of no significance. The 95% confidence interval for each independent spectrum estimate is the vertical distance between the continuous black lines in the amplification plot, and the error bars in the gain plot.

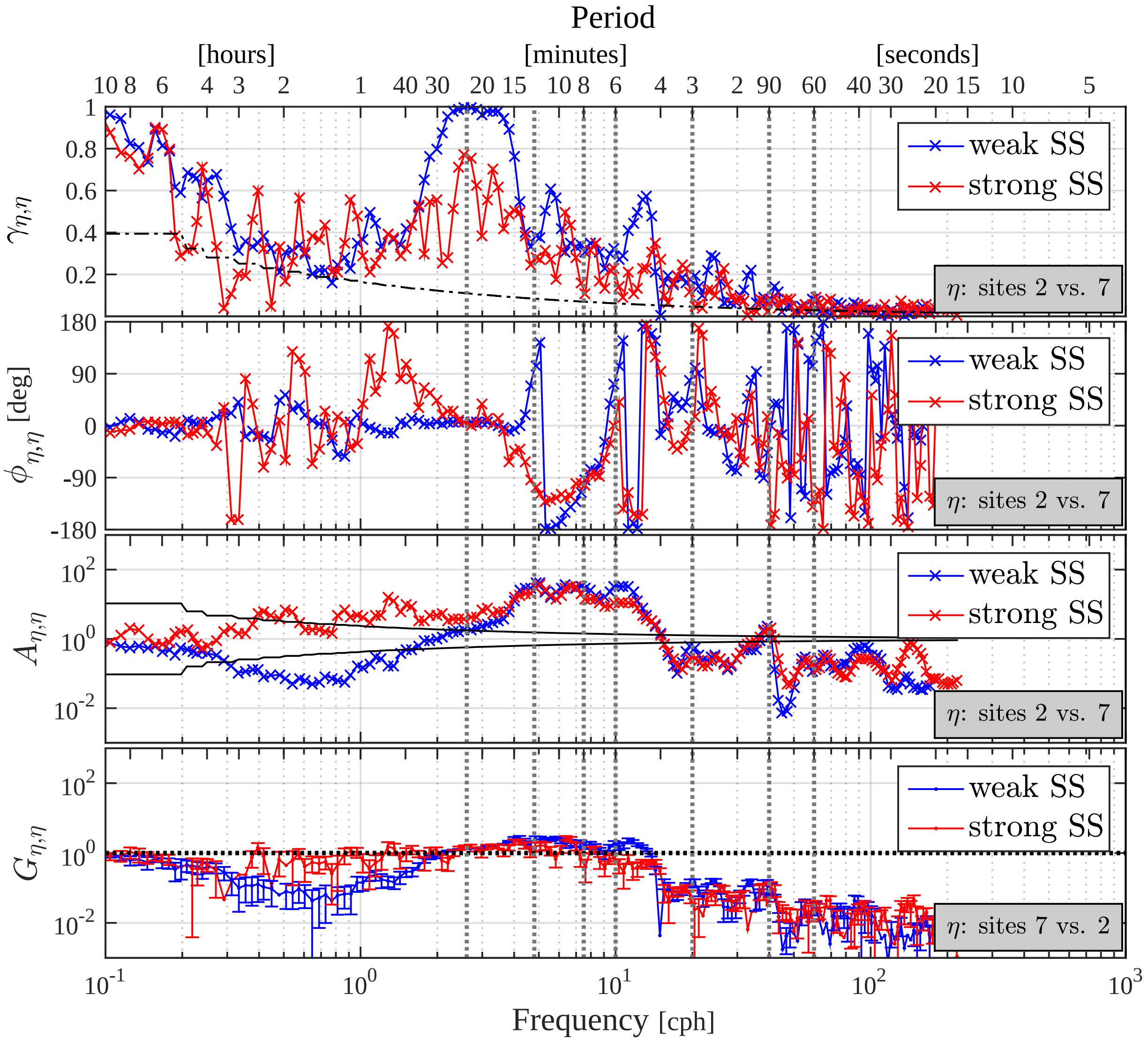

Figure 2.28: Coherence amplitude, $\gamma_{\eta,\eta}$, coherence phase, $\phi_{\eta,\eta}$, amplification, $A_{\eta,\eta}$, and gain, $G_{\eta,\eta}$, for sites 2 vs. 7. Blue/red curves were derived from five three-day long sea level data segments during 12/11/13 - 03/18/14 (see Table 2.4 for exact time periods). The dashed dotted line in the coherence amplitude plot is the 95% level of no significance. The 95% confidence interval for each independent spectrum estimate is the vertical distance between the continuous black lines in the amplification plot, and the error bars in the gain plot.

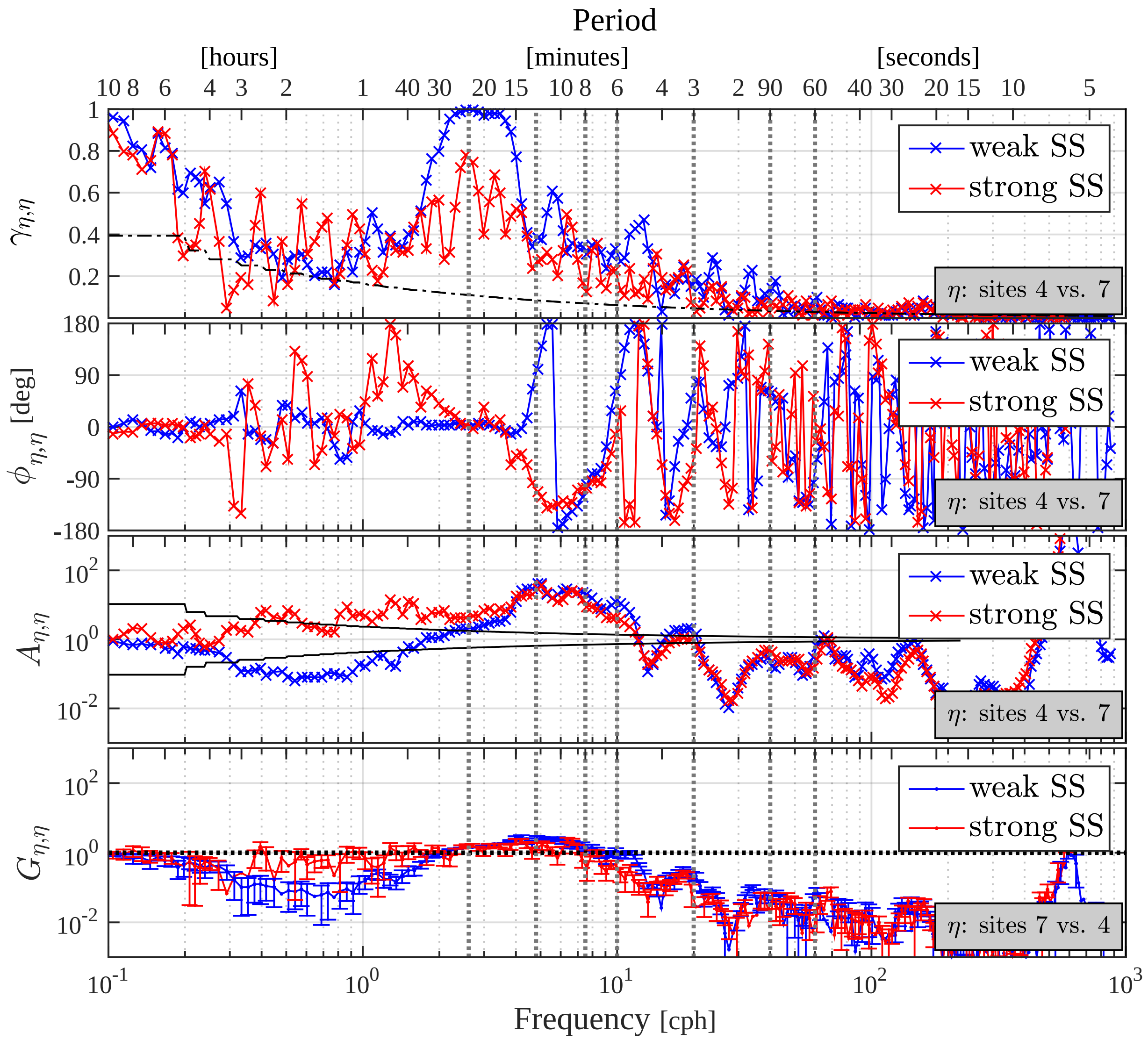

Figure 2.29: Coherence amplitude, $\gamma_{\eta,\eta}$, coherence phase, $\phi_{\eta,\eta}$, amplification, $A_{\eta,\eta}$, and gain, $G_{\eta,\eta}$, for sites 4 vs. 7. Blue/red curves were derived from five three-day long sea level data segments during 12/11/13 - 03/18/14 (see Table 2.4 for exact time periods). The dashed dotted line in the coherence amplitude plot is the 95% level of no significance. The 95% confidence interval for each independent spectrum estimate is the vertical distance between the continuous black lines in the amplification plot, and the error bars in the gain plot.

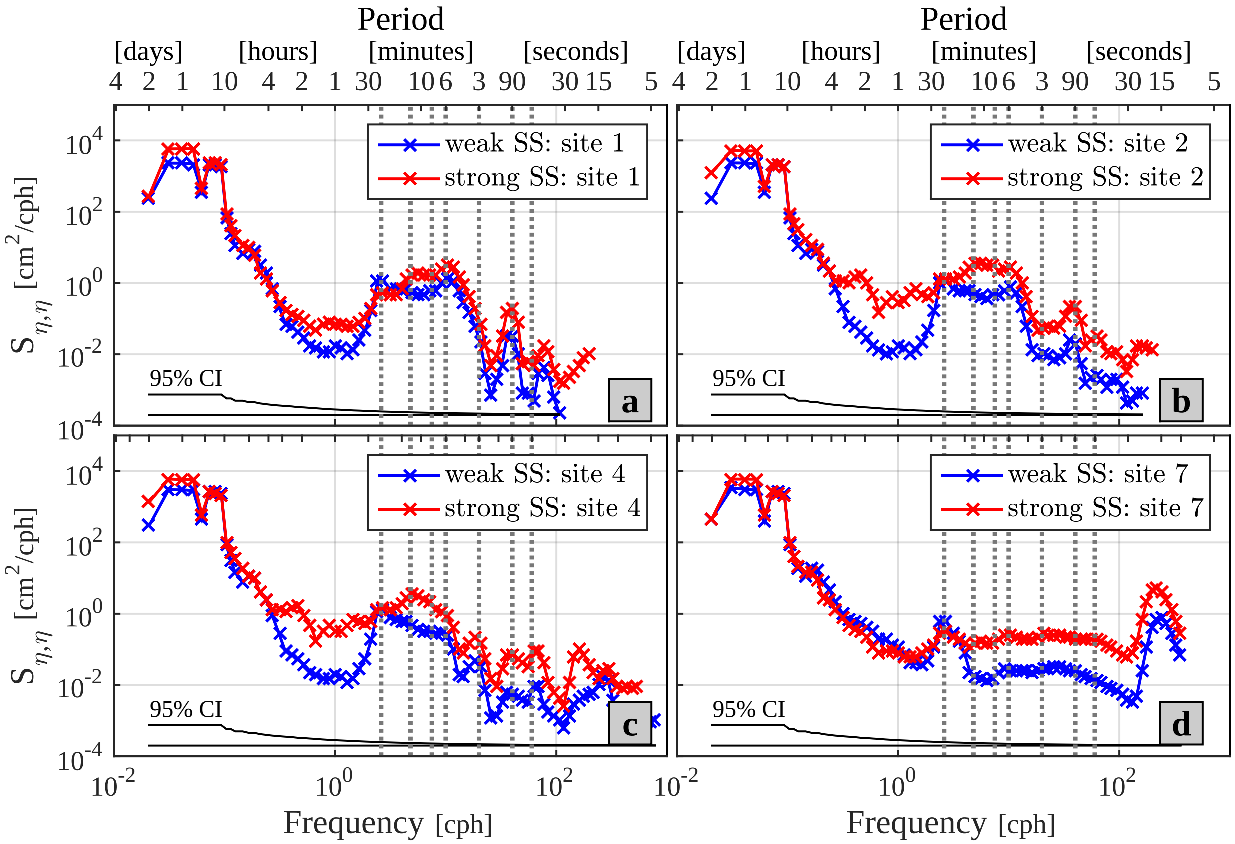

Figure 2.30: PSD curves for sites (a) 1; (b) 2; (c) 4; and, (d) 7. Blue/red curves were derived from five three-day long sea level data segments during 12/11/13 - 03/18/14 (see Table 2.4 for exact time periods). The 95% confidence interval for each independent spectrum estimate is shown at the bottom.

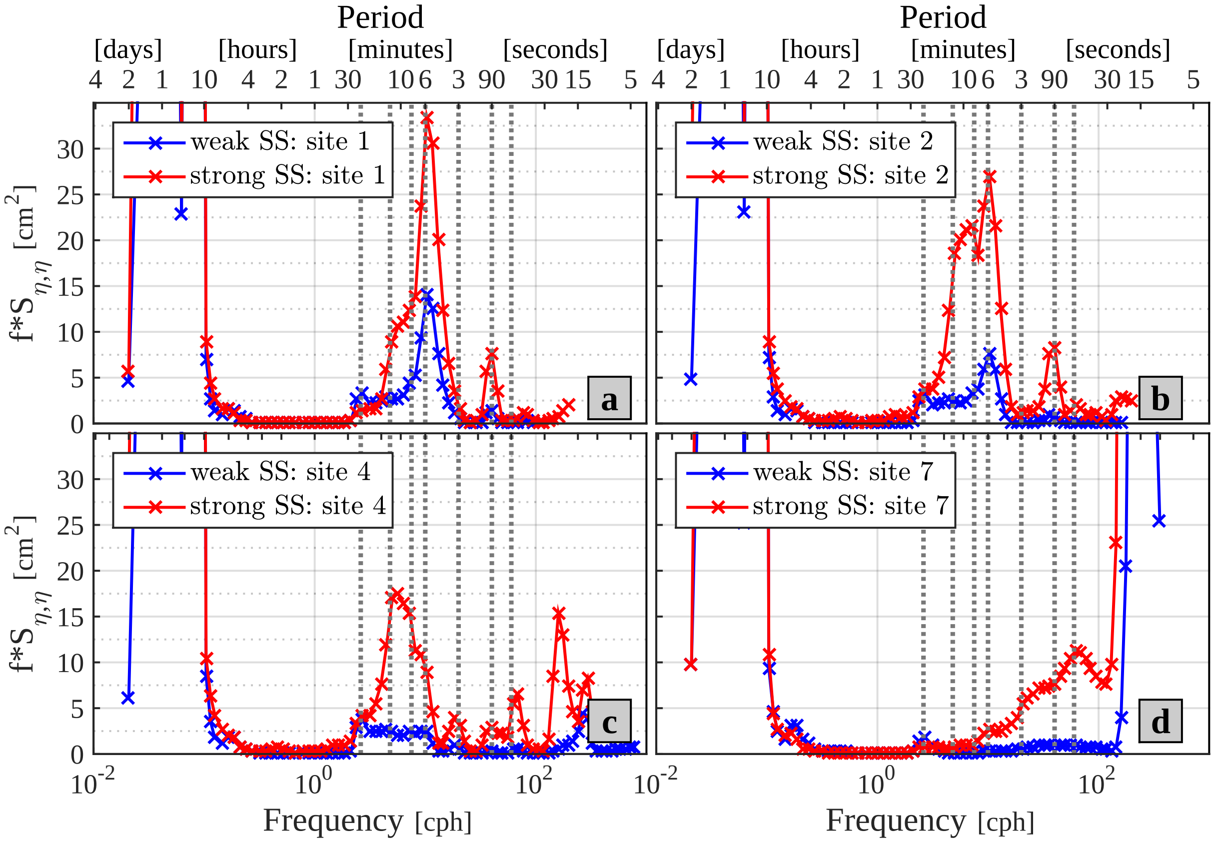

Figure 2.31: PSD curves for sites (a) 1; (b) 2; (c) 4; and, (d) 7. Blue/red curves were derived from five three-day long sea level data segments during 12/11/13 - 03/18/14 (see Table 2.4 for exact time periods).

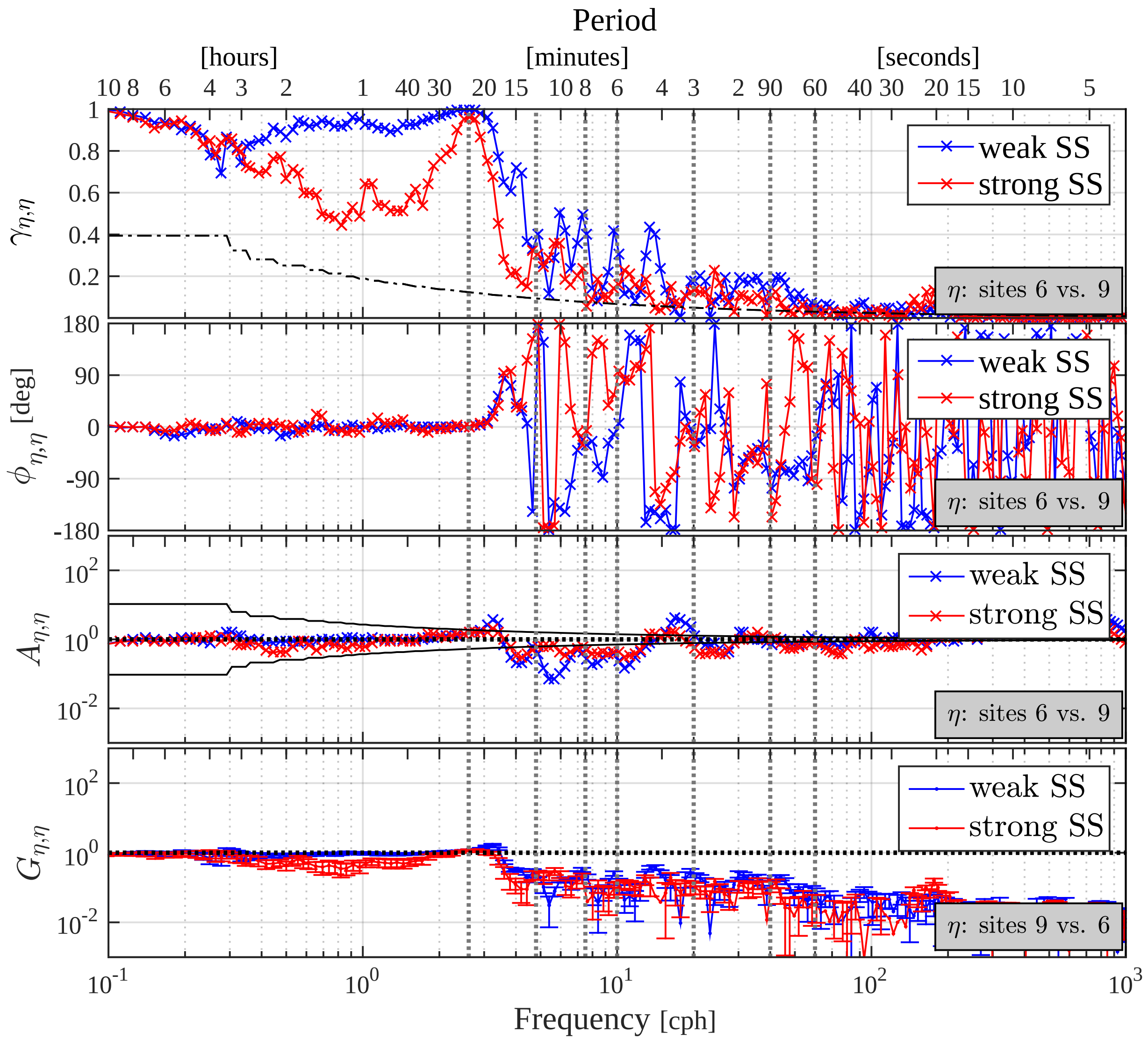

Figure 2.32: Coherence amplitude, $\gamma_{\eta,\eta}$, coherence phase, $\phi_{\eta,\eta}$, amplification, $A_{\eta,\eta}$, and gain ,$G_{\eta,\eta}$, for sites 6 vs. 9. Blue/red curves were derived from five three-day long sea level data segments during 11/04/11 - 01/31/12 (see Table 2.4 for exact time periods). The dashed dotted line in the coherence amplitude plot is the 95% level of no significance. The 95% confidence interval for each independent spectrum estimate is the vertical distance between the continuous black lines in the amplification plot, and the error bars in the gain plot.

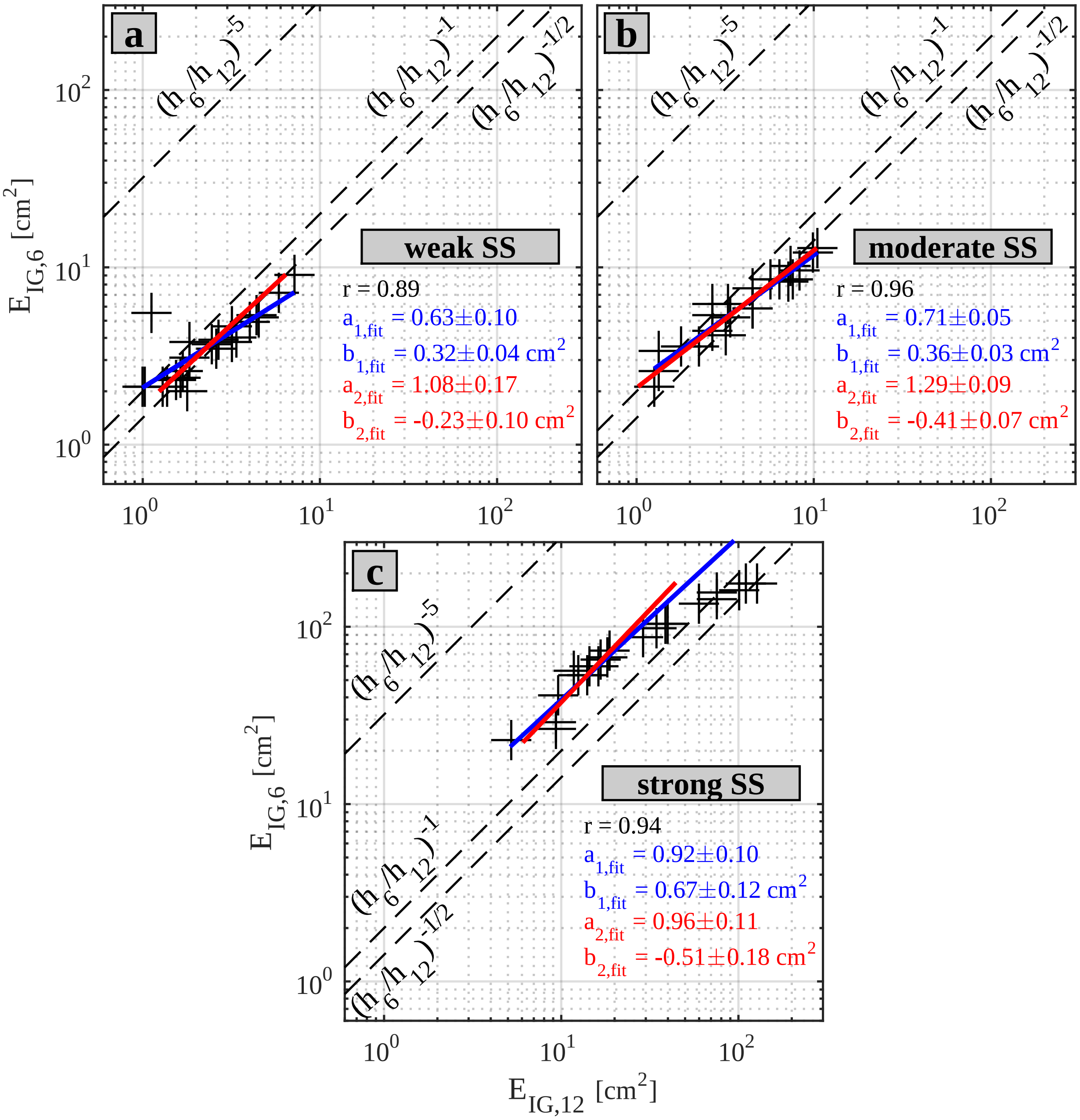

Figure 2.33: Scatter plots of $E_{IG,6}$ (6m depth) vs. $E_{IG,12}$ (12m depth) for (a) weak, (b) moderate, and (c) strong, SS events. In each of the above cases, two 3-day long sea level data segments are averaged (see Table 2.4 for exact time periods).

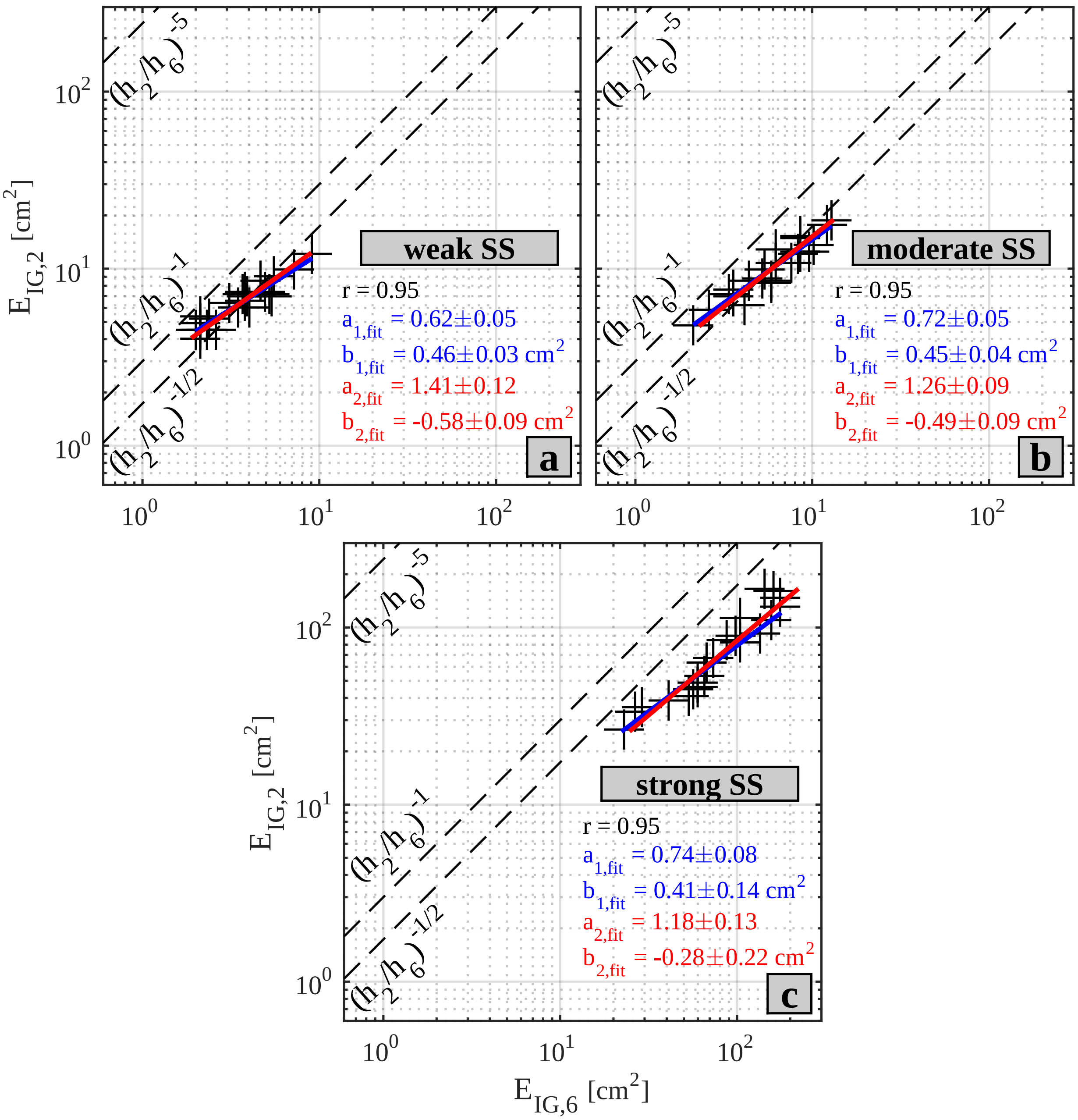

Figure 2.34: Scatter plots of $E_{IG,2}$ (2m depth) vs. $E_{IG,6}$ (6m depth) for (a) weak, (b) moderate, and (c) strong, SS events. In each of the above cases, two 3-day long sea level data segments are averaged (see Table 2.4 for exact time periods).

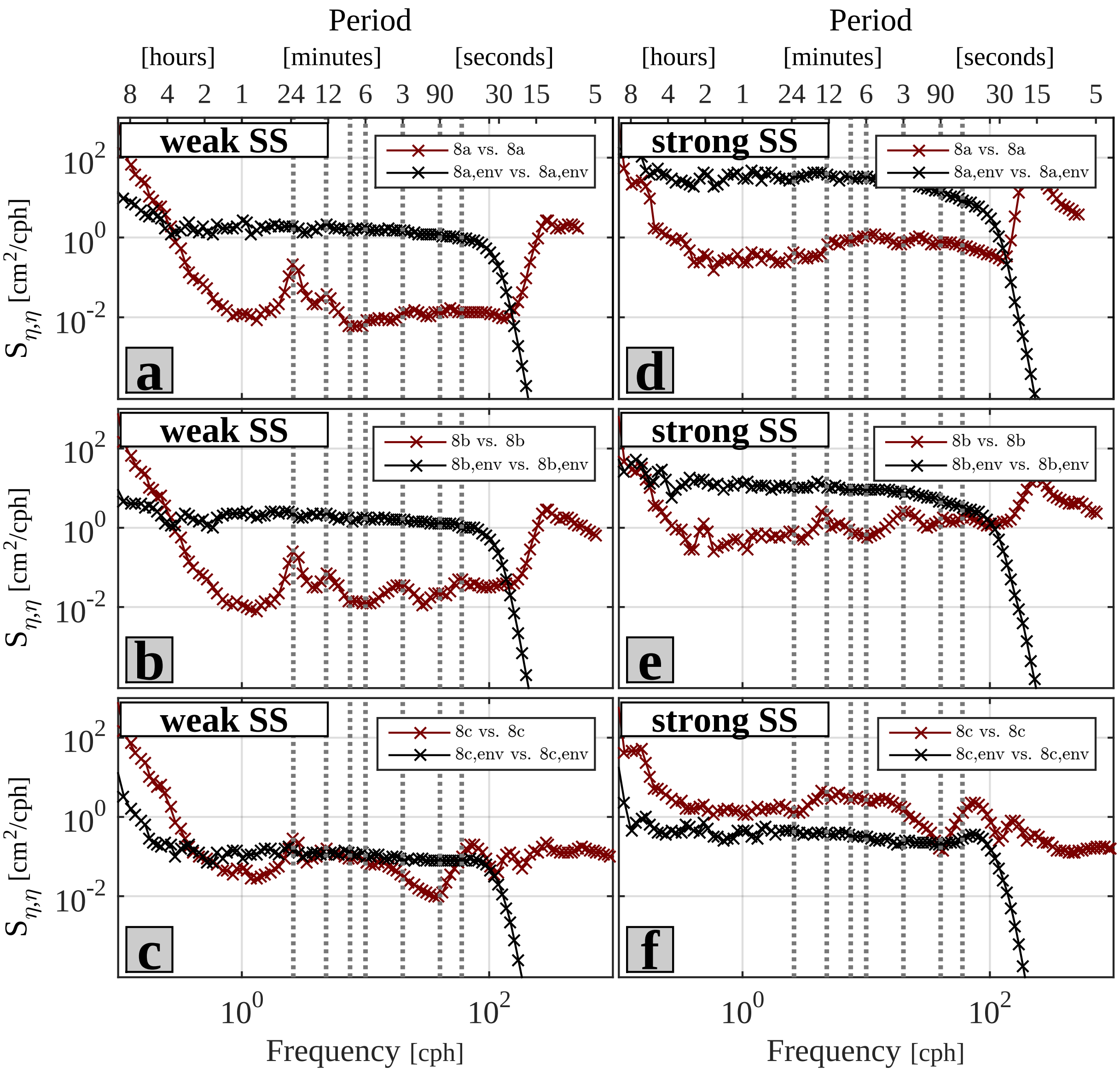

Figure 2.35: PSD of η and $\eta_{ss,env}$ under weak (left column), and strong (right column) SS forcing, at sites 8a (top row), 8b (middle row), and 8c (bottom row). See Table 2.4 for exact time periods.

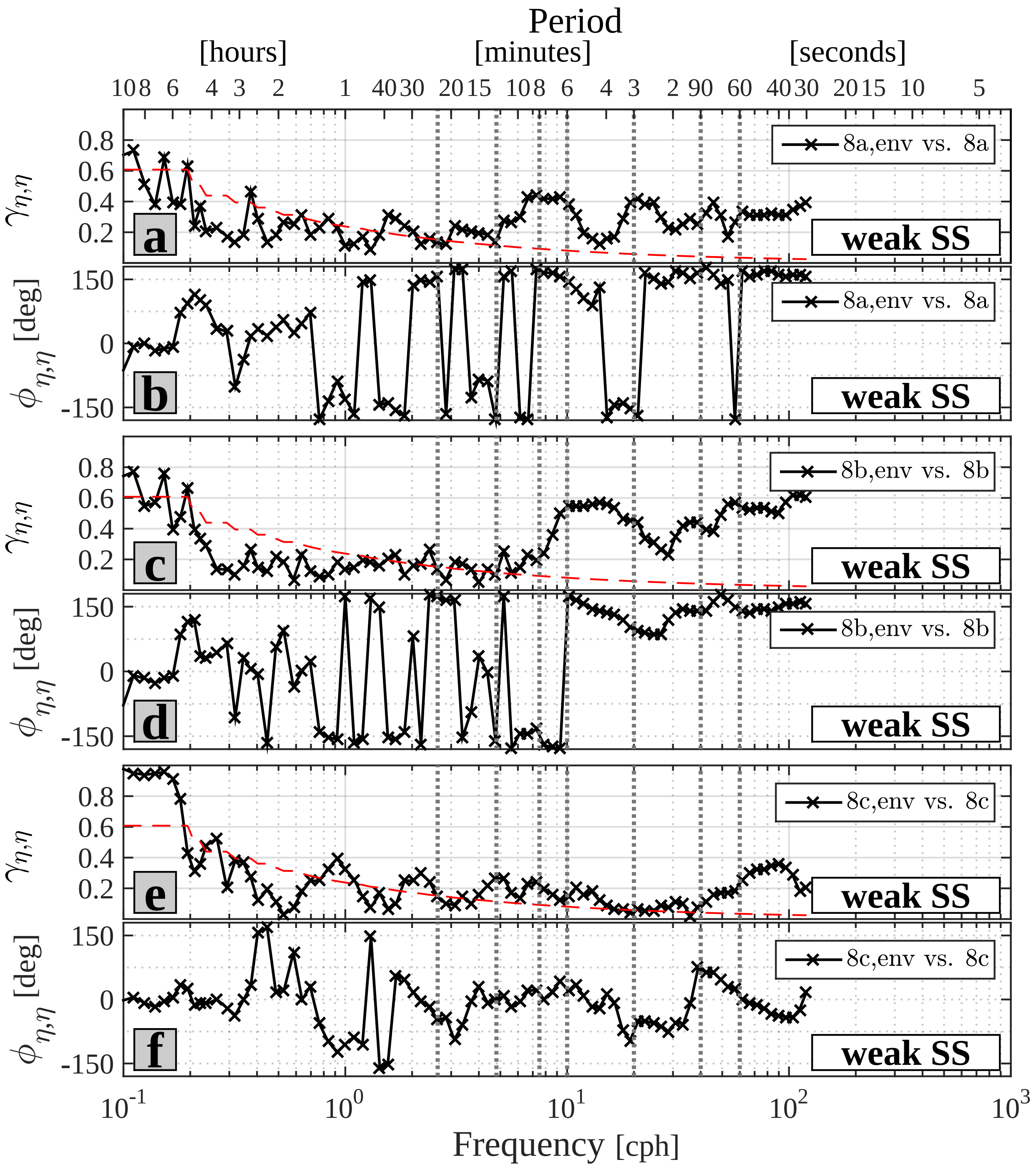

Figure 2.36: Coherence amplitude and phase between $\eta_{ss,env}$ and η at sites 8a (panels a and b), 8b (panels c and d), and 8c (panels e and f), under weak SS forcing conditions (see Table 2.4 for exact time periods). The dashed dotted line in the coherence amplitude plot is the 95% level of no significance.

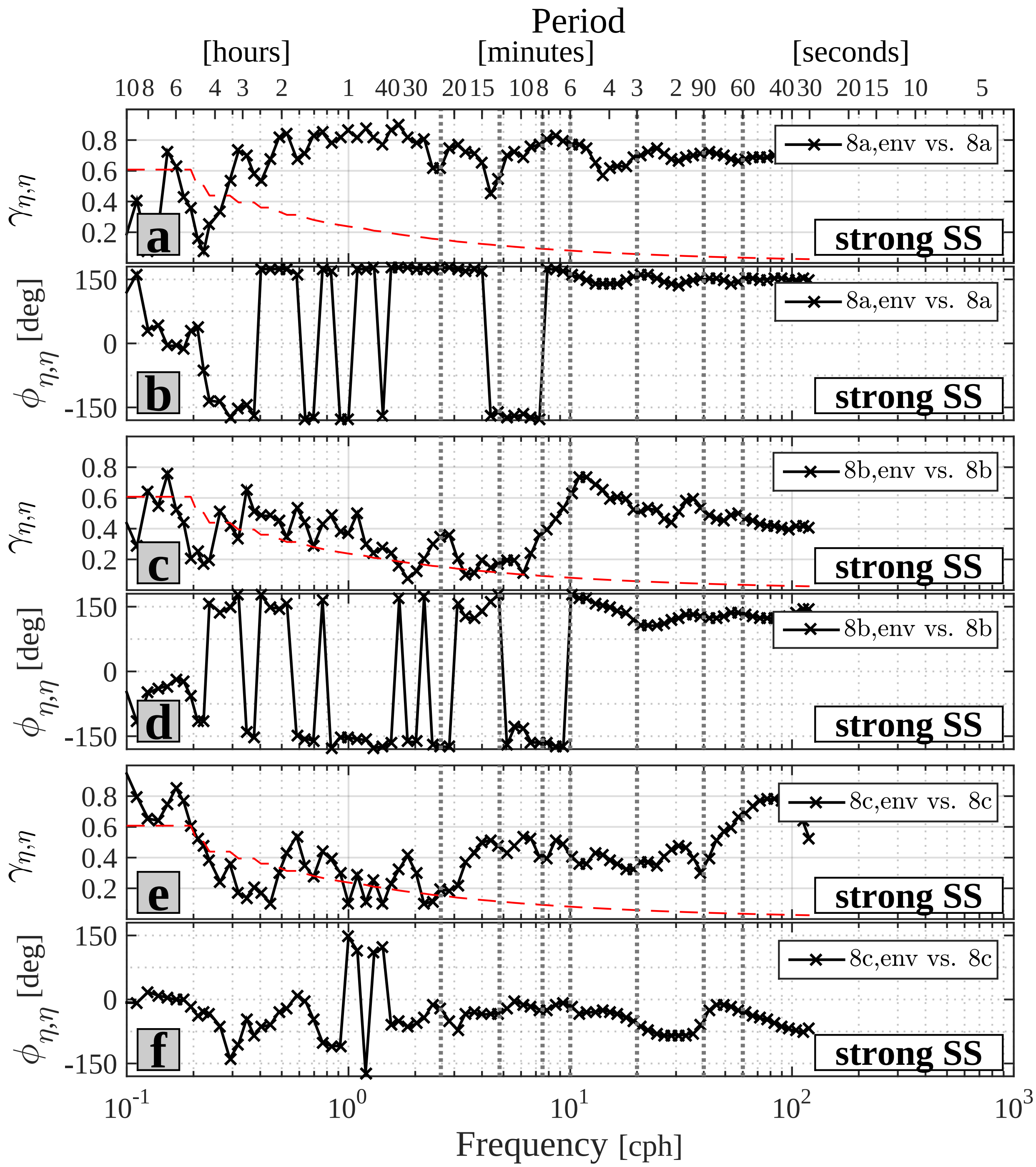

Figure 2.37: Coherence amplitude and phase between $\eta_{ss,env}$ and η at sites 8a (panels a and b), 8b (panels c and d), and 8c (panels e and f), under strong SS forcing conditions (see Table 2.4 for exact time periods). The dashed dotted line in the coherence amplitude plot is the 95% level of no significance.

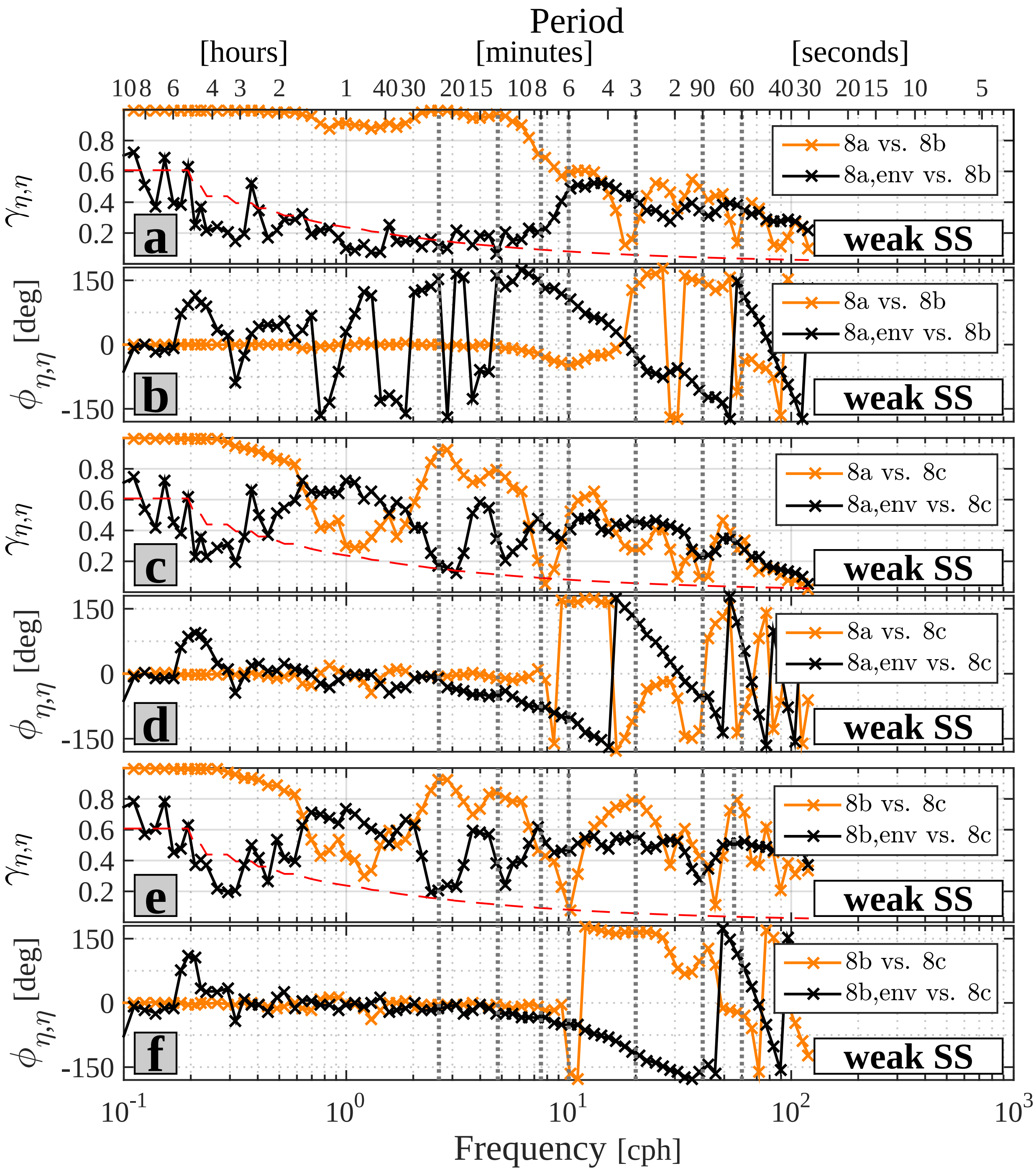

Figure 2.38: Coherence amplitude and phase between $\eta_{ss,env}$ and η for sites 8a vs. 8b (panels a and b), sites 8a vs. 8c (panels c and d), and sites 8b vs. 8c (panels e and f), under weak SS forcing conditions (see Table 2.4 for exact time periods). The dashed dotted line in the coherence amplitude plot is the 95% level of no significance.

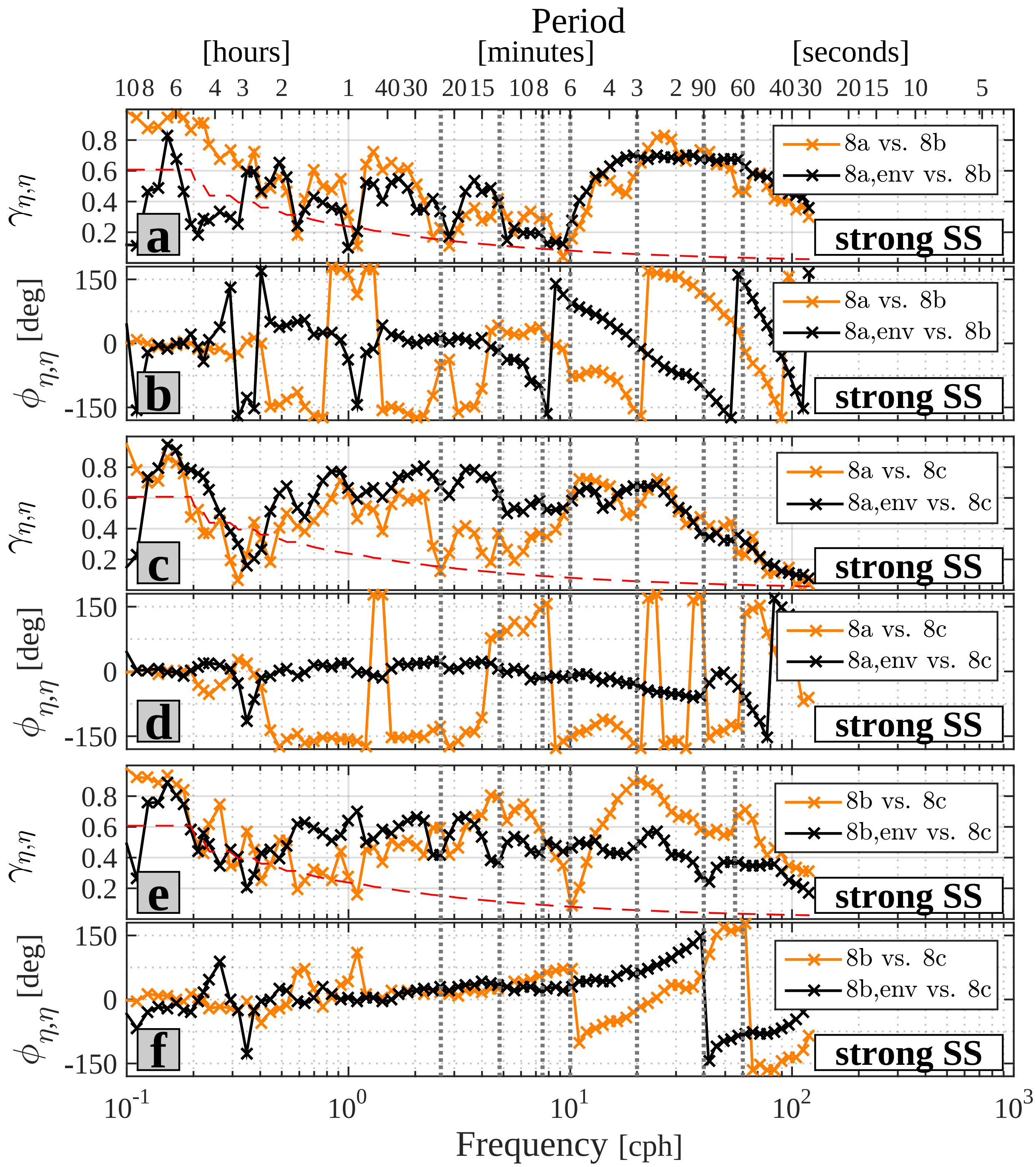

Figure 2.39: Coherence amplitude and phase between $\eta_{ss,env}$ and η for sites 8a vs. 8b (panels a and b), sites 8a vs. 8c (panels c and d), and sites 8b vs. 8c (panels e and f), under strong SS forcing conditions (see Table 2.4 for exact time periods). The dashed dotted line in the coherence amplitude plot is the 95% level of no significance.

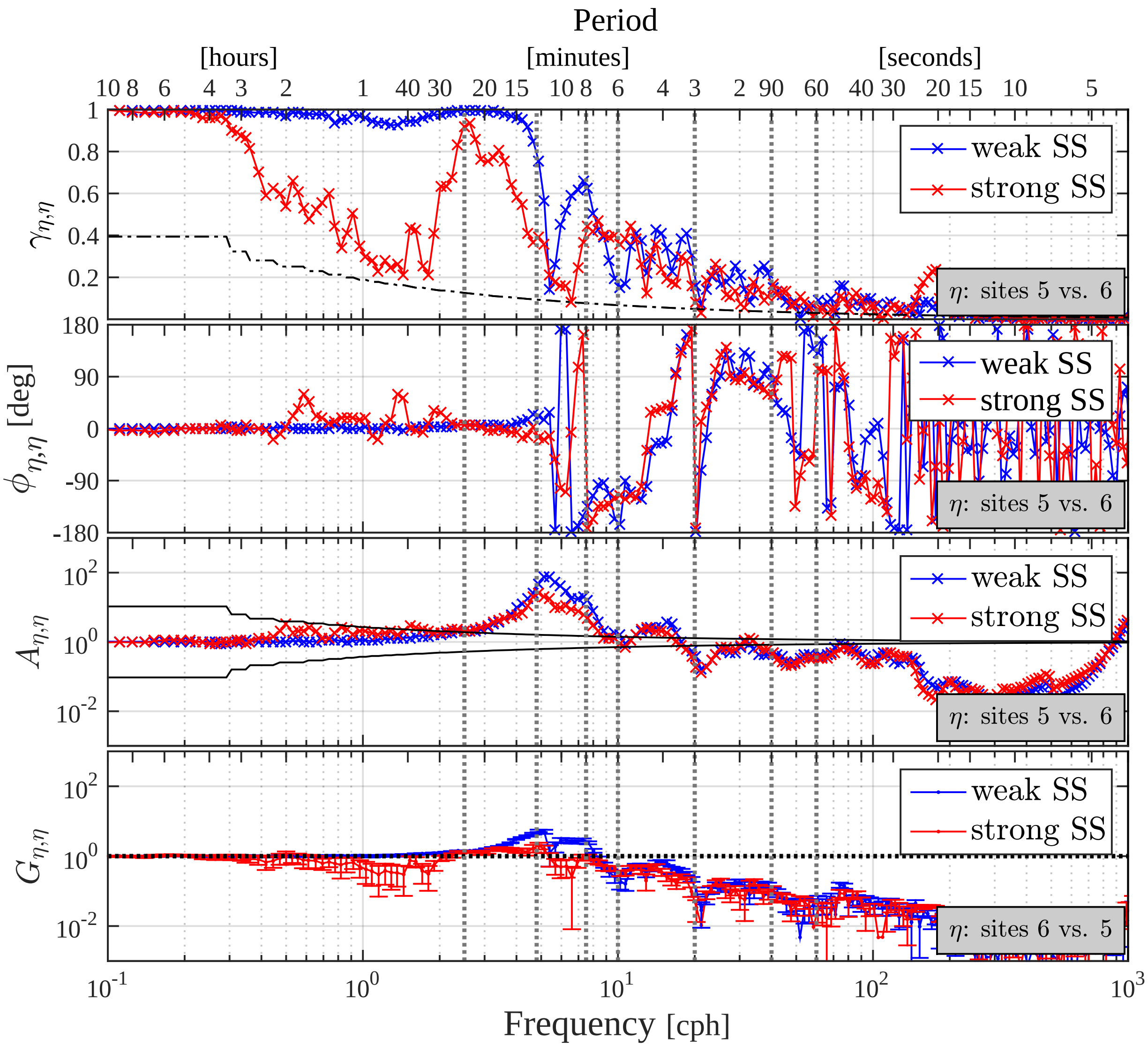

Figure 2.40: Coherence amplitude, $\gamma_{\eta,\eta}$, coherence phase, $\phi_{\eta,\eta}$, amplification, $A_{\eta,\eta}$, and gain ,$G_{\eta,\eta}$, for sites 5 vs. 6. Blue/red curves were derived from five three-day long sea level data segments during 11/04/11 - 01/31/12 (see Table 2.4 for exact time periods). The dashed dotted line in the coherence amplitude plot is the 95% level of no significance. The 95% confidence interval for each independent spectrum estimate is the vertical distance between the continuous black lines in the amplification plot, and the error bars in the gain plot.

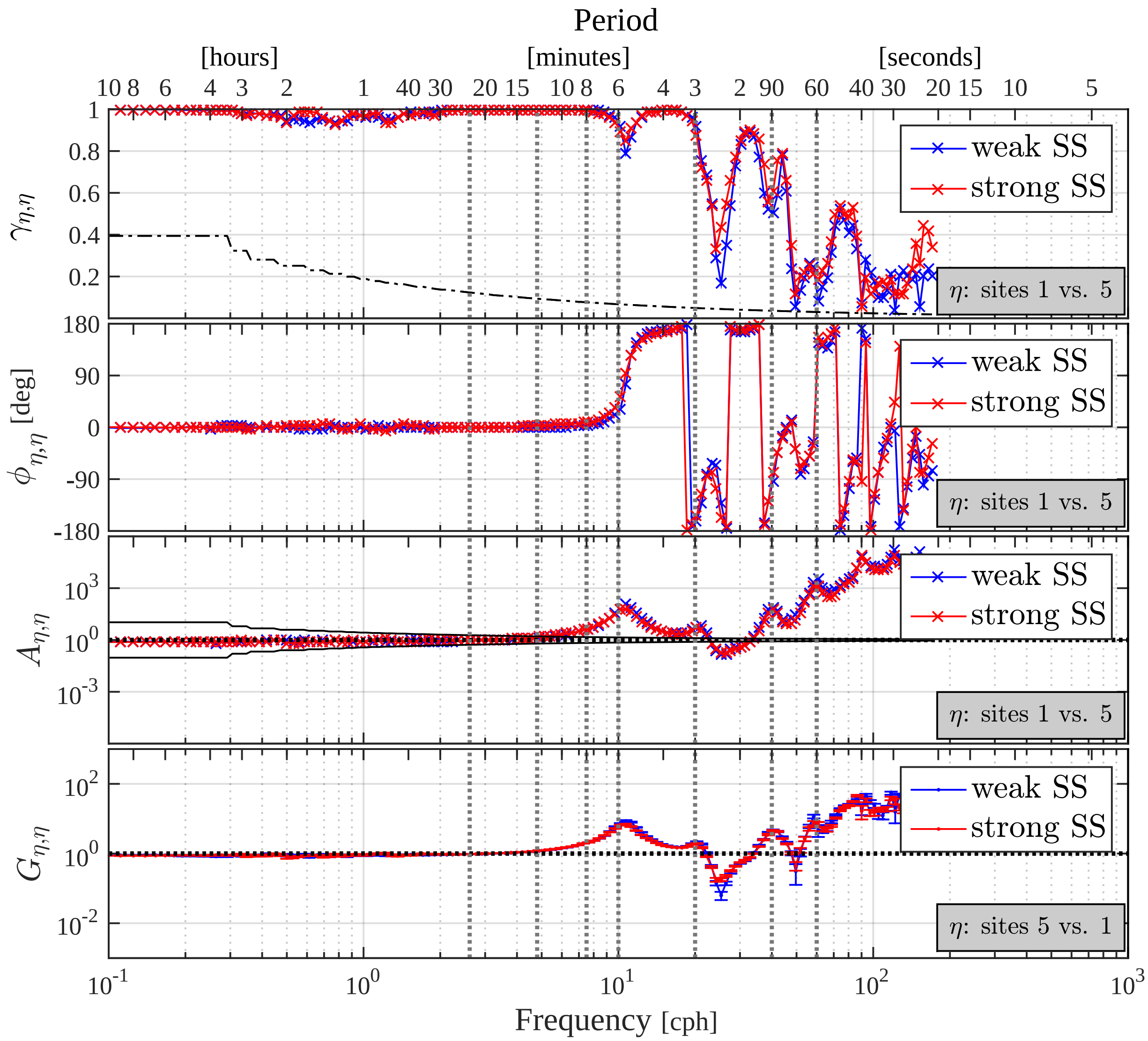

Figure 2.41: Coherence amplitude, $\gamma_{\eta,\eta}$, coherence phase, $\phi_{\eta,\eta}$, amplification, $A_{\eta,\eta}$, and gain ,$G_{\eta,\eta}$, for sites 1 vs. 5. Blue/red curves were derived from five three-day long sea level data segments during 11/04/11 - 01/31/12 (see Table 2.4 for exact time periods). The dashed dotted line in the coherence amplitude plot is the 95% level of no significance. The 95% confidence interval for each independent spectrum estimate is the vertical distance between the continuous black lines in the amplification plot, and the error bars in the gain plot.

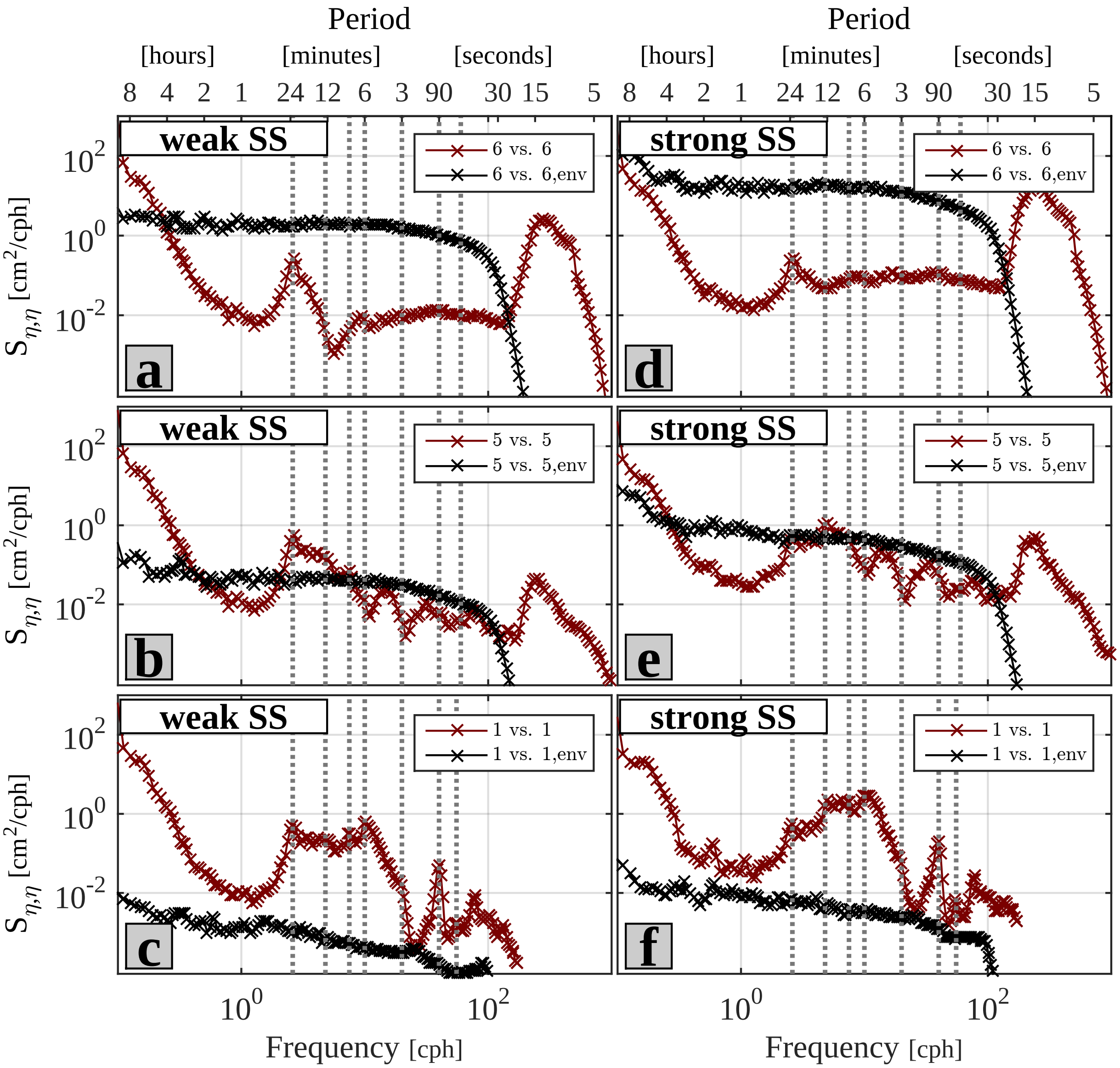

Figure 2.42: PSD of η and $\eta_{ss,env}$ under weak (left column), and strong (right column) SS forcing, at sites 6 (top row), 5 (middle row), and 1 (bottom row). See Table 2.4 for exact time periods.

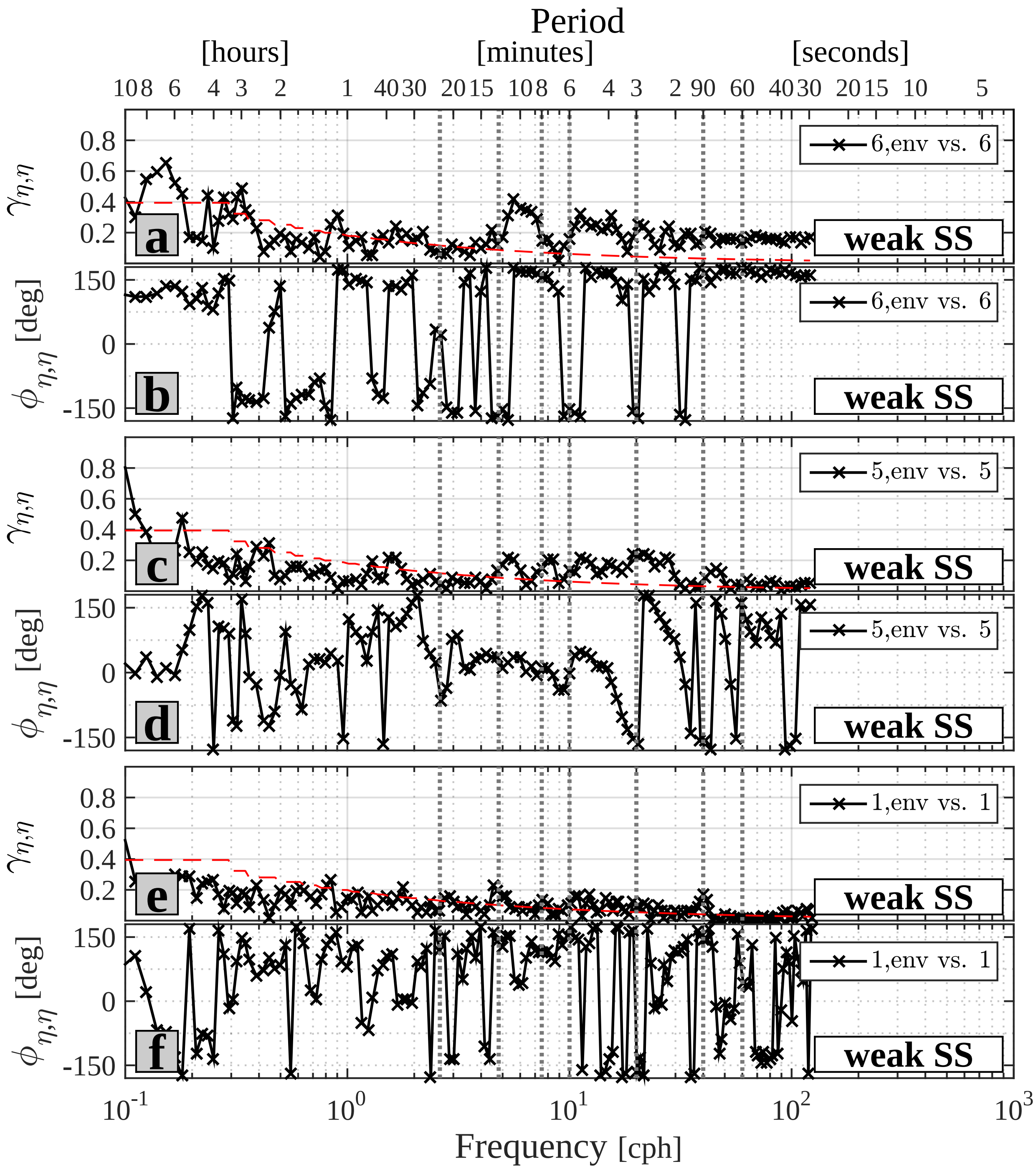

Figure 2.43: Coherence amplitude and phase between $\eta_{ss,env}$ and η at sites 6 (panels a and b), 5 (panels c and d), and 1 (panels e and f), under weak SS forcing conditions (derived from five three-day long blocks of sea level data segments during 11/04/11 - 01/31/12; see Table 2.4 for exact time periods). The dashed dotted line in the coherence amplitude plot is the 95% level of no significance.

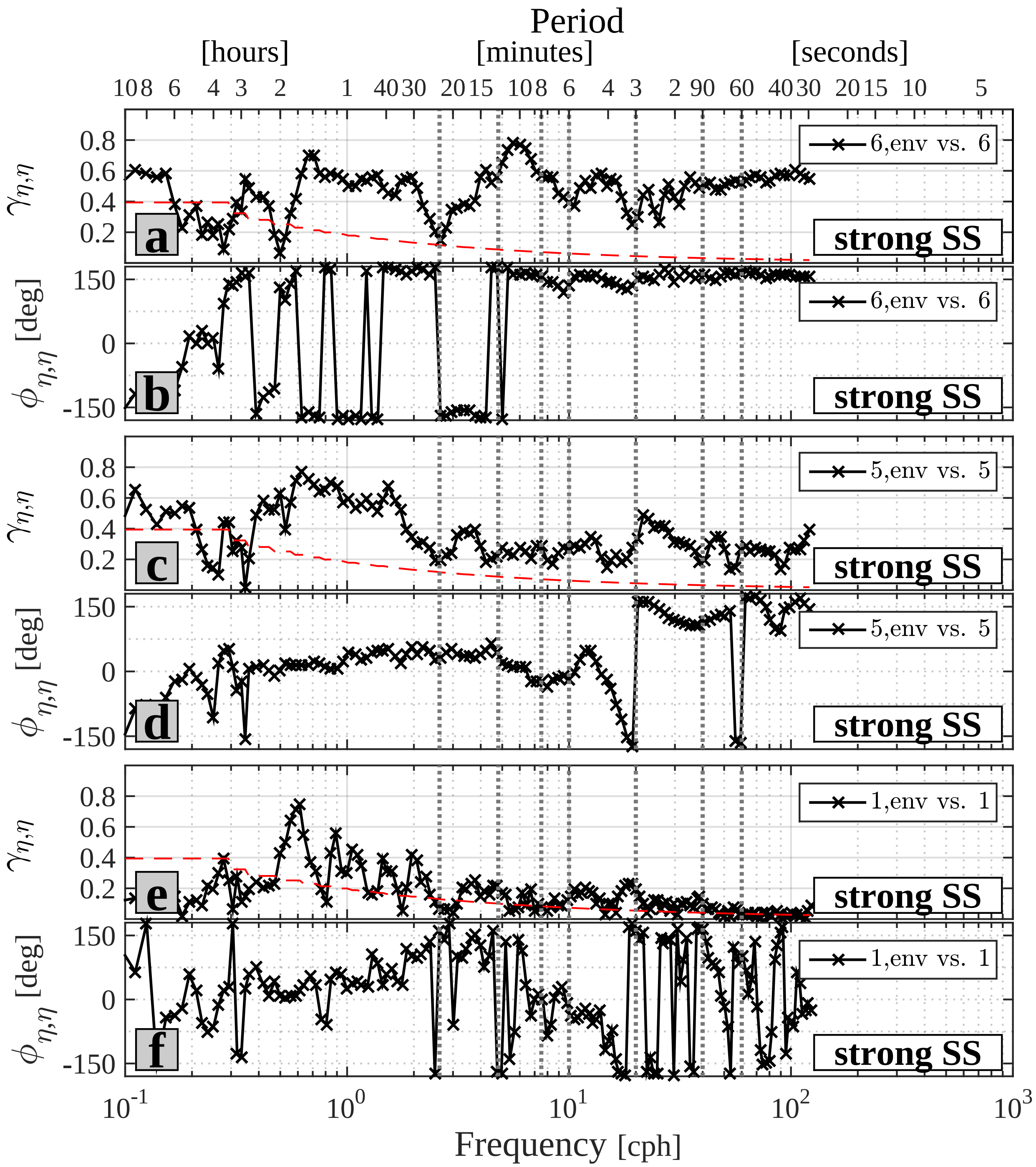

Figure 2.44: Coherence amplitude and phase between $\eta_{ss,env}$ and η at sites 6 (panels a and b), 5 (panels c and d), and 1 (panels e and f), under strong SS forcing conditions (derived from five three-day long blocks of sea level data segments during 11/04/11 - 01/31/12; see Table 2.4 for exact time periods). The dashed dotted line in the coherence amplitude plot is the 95% level of no significance.

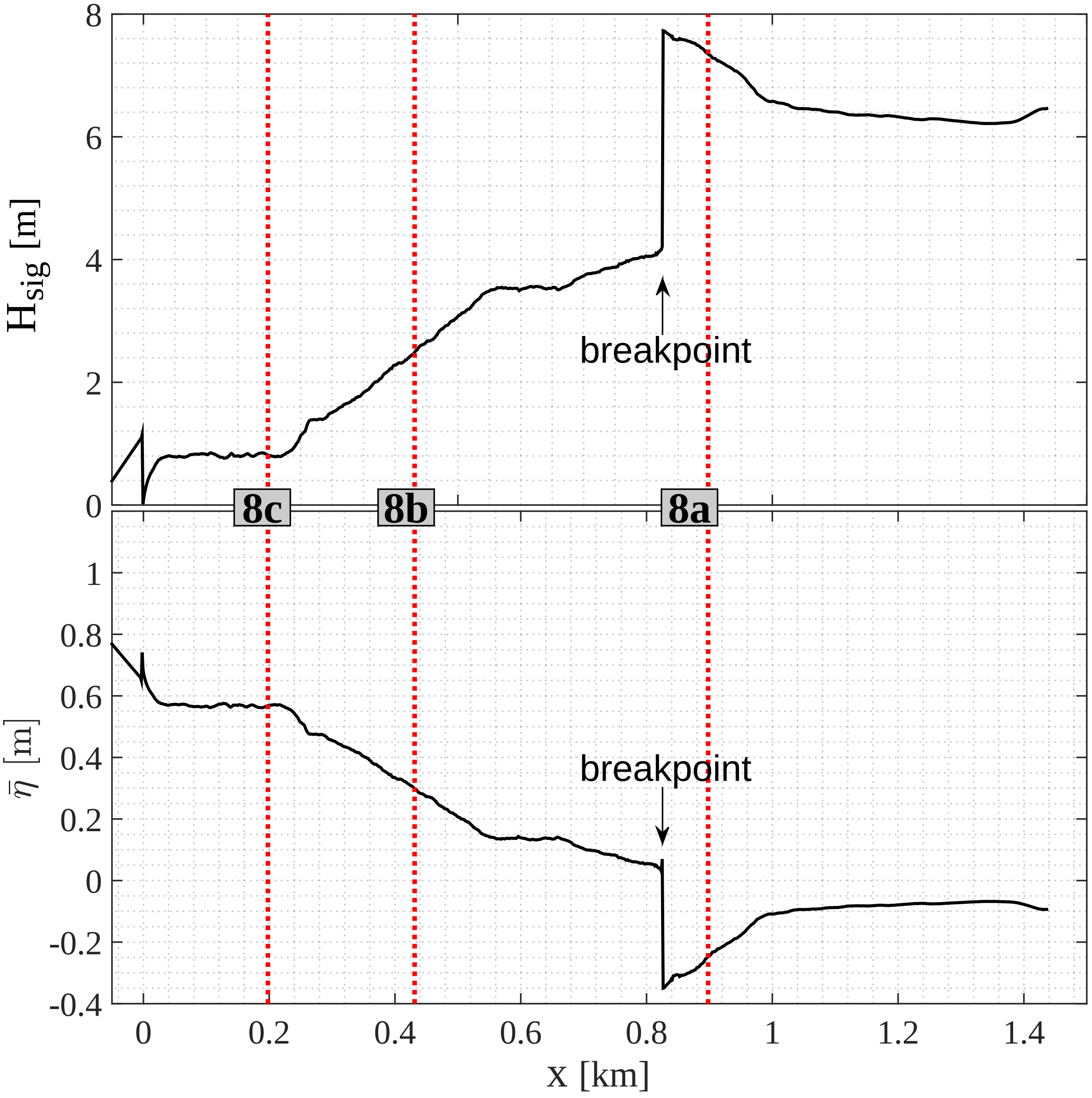

Figure 2.45: Analytical calculation of wave transformation from offshore through the surf zone at Mokuleia using $H_\infty = 6$ m and $T_p = 20$ sec of the strong SS event during 01/13/08 - 01/16/08. The significant wave height (upper plot), and the setup/set-down of mean sea level (lower plot), are plotted against the distance from the shoreline. The dashed red-dotted lines mark the locations of the cross-shore array at sites 8a, 8b, and 8c.

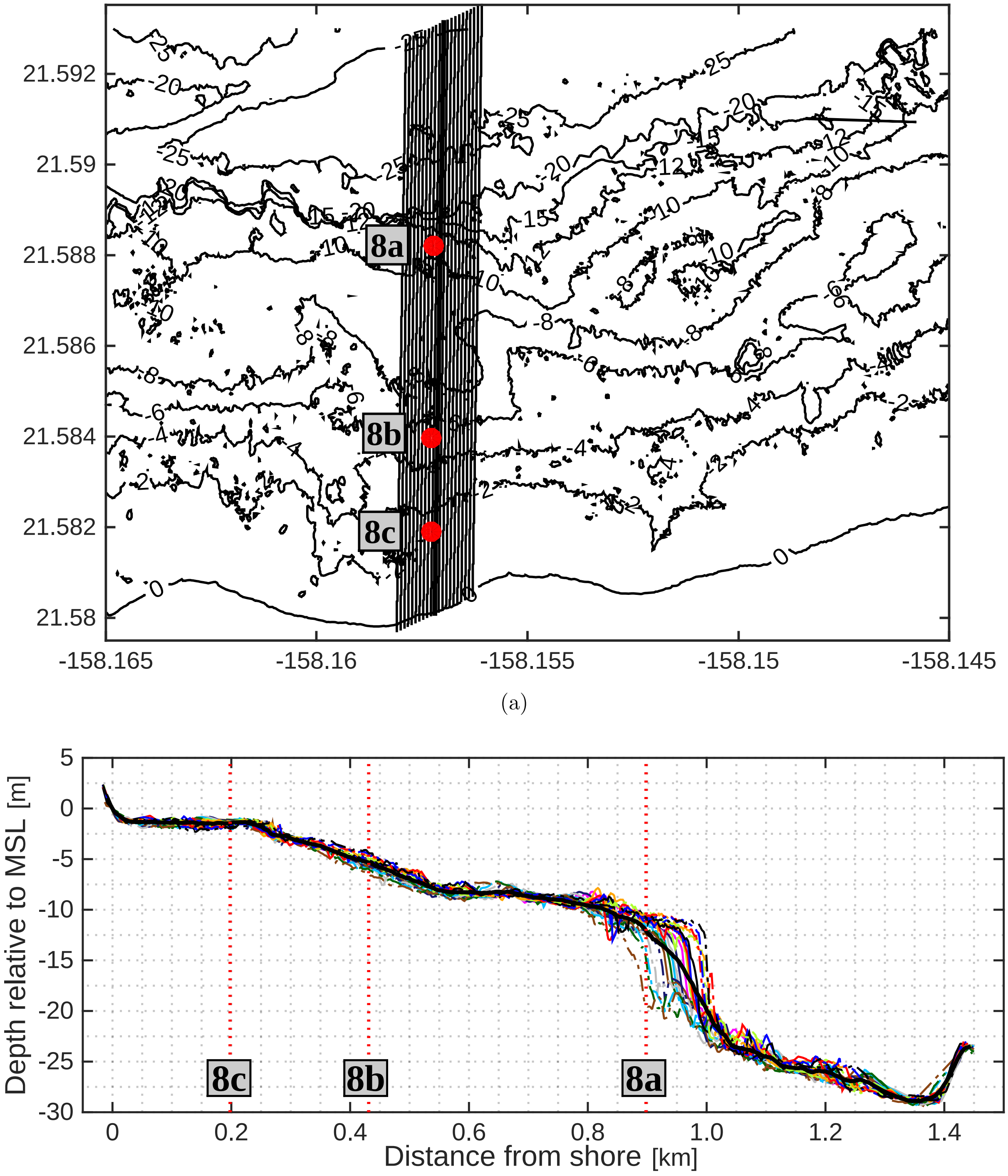

(a)

(b)

Figure 2.46: (a) cross-shore lines, and (b) cross-shore depth profiles vs. distance from the shoreline, at Mokuleia site. The crosses and dashed red-dotted lines mark the locations of the cross-shore array at sites 8a, 8b, and 8c. The thicker curve is the average profile.

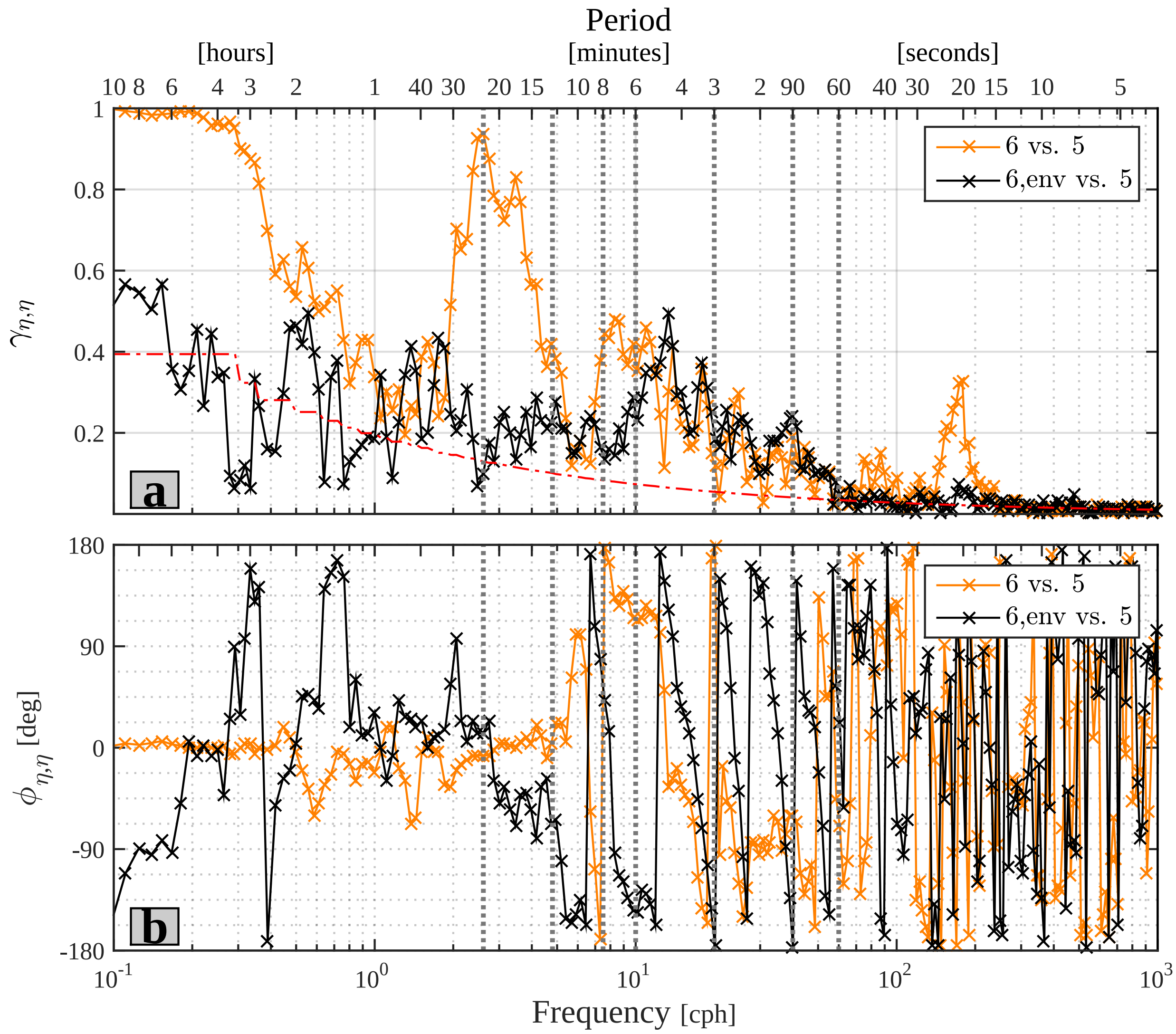

Figure 2.47: Coherence amplitude and phase for η vs. η and $\eta_{ss,env}$ vs. η for sites 6 vs. 5, under strong SS forcing conditions. The dashed dotted line in the coherence amplitude plot is the 95% level of no significance.

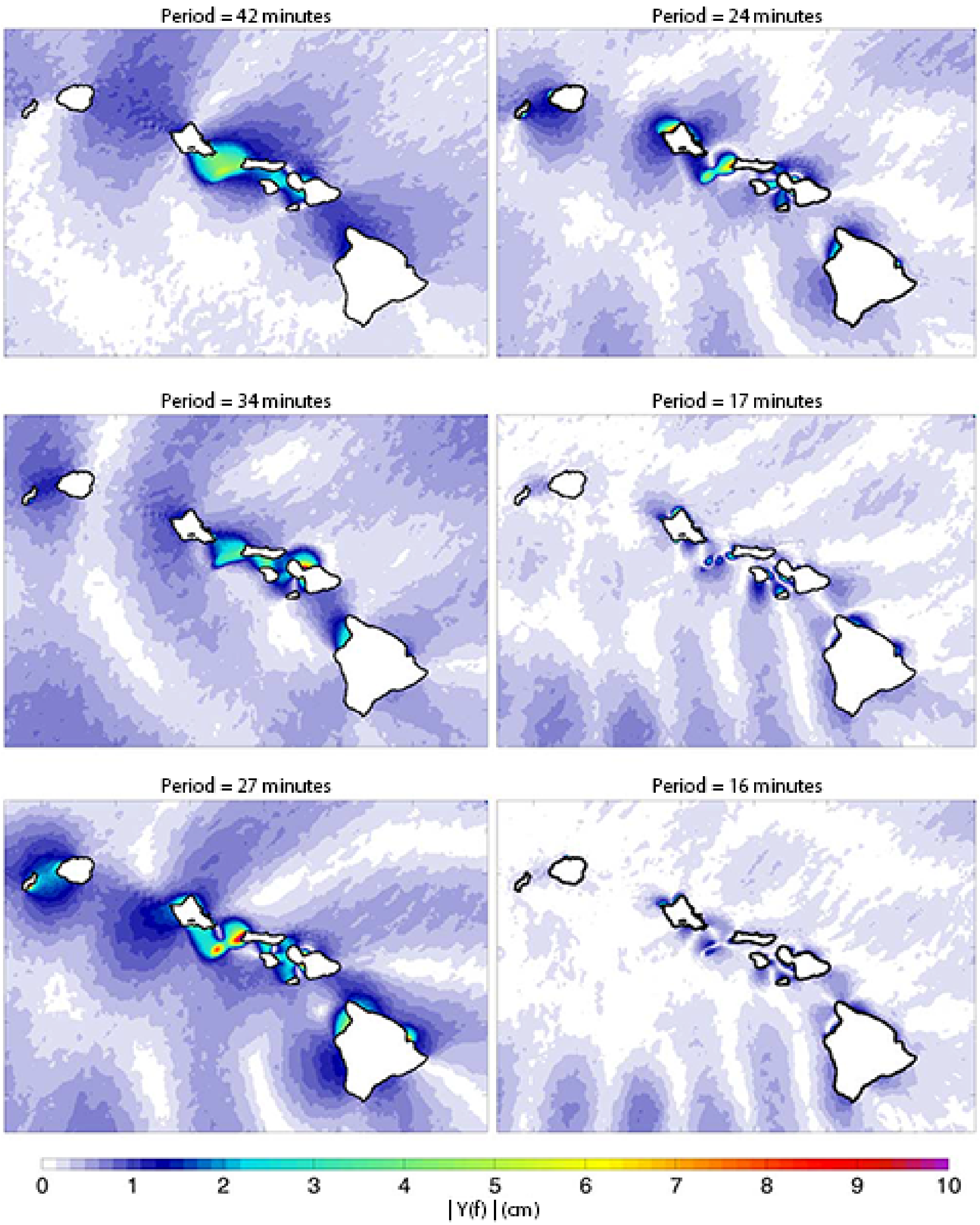

Figure 2.48: Oscillation modes around the Hawaiian Islands. Taken from *Munger and Cheung* (2008).

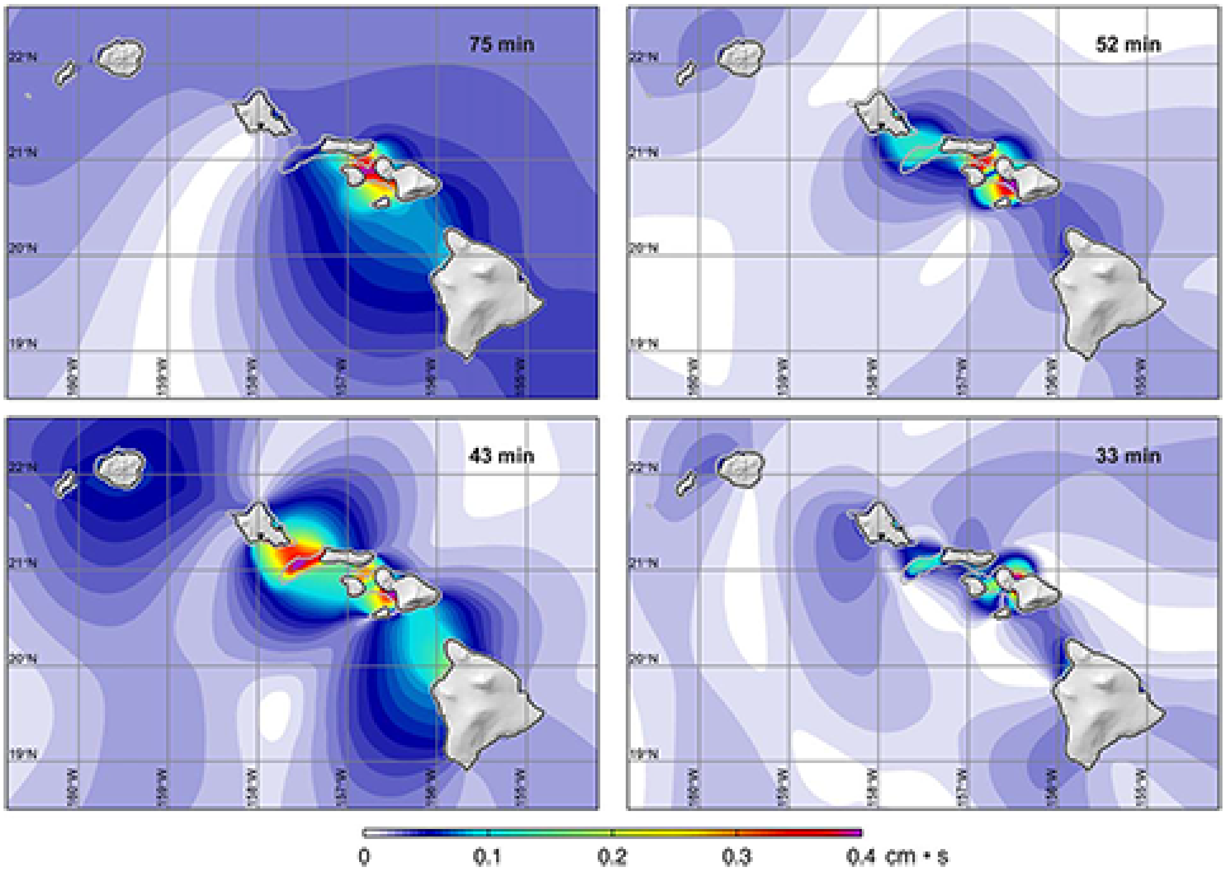

Figure 2.49: Oscillation modes around the Hawaiian Islands. Taken from *Cheung et al.* (2013).

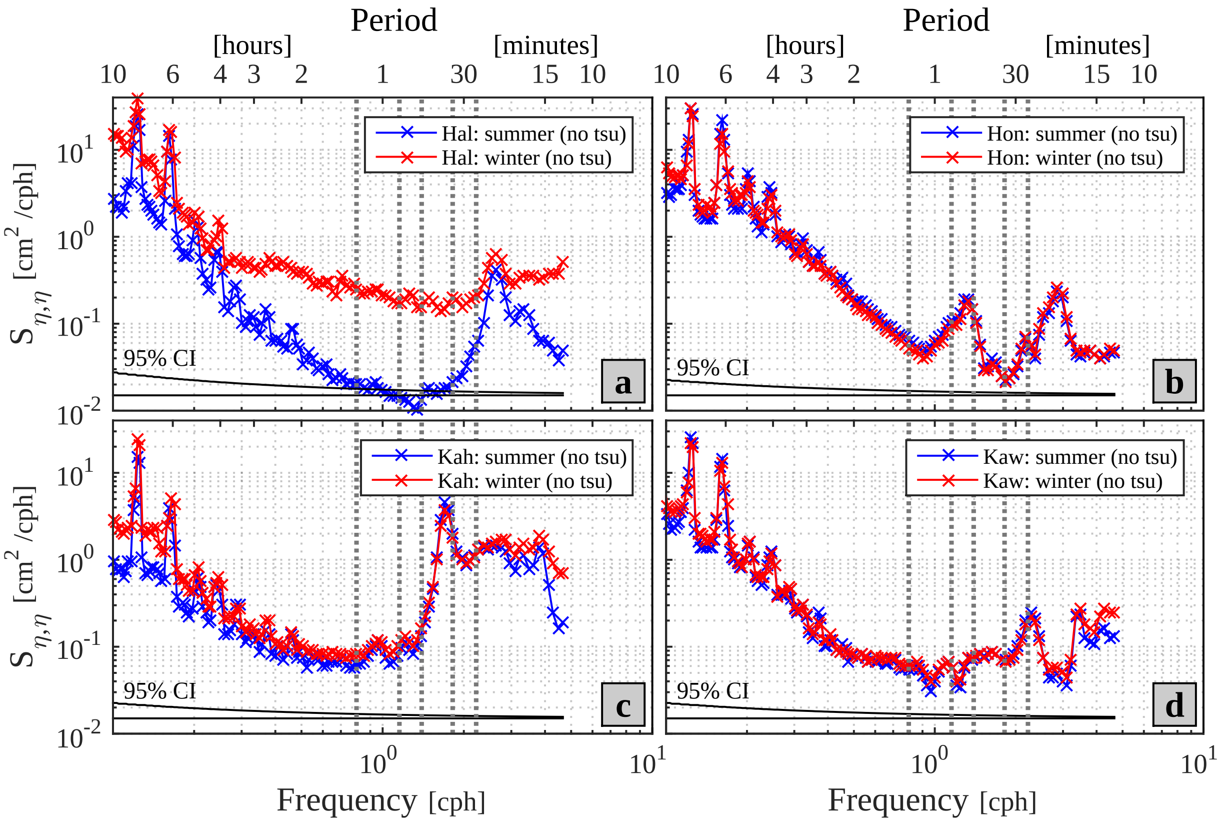

Figure 2.50: Sea level PSD at (a) site 1, Hale'iwa Hbr.; (b) site 13, Honolulu Hbr.; (c) site 14, Kahului Hbr.; and, (d) site 15, Kawaihae Hbr. Blue curves were generated using multiple 3-month long datasets during summertime (Jun, Jul, Aug; 5 seasons for Hale'iwa, and 13 for the other harbors), and red curves were generated using multiple 3-month long datasets during wintertime (Nov, Dec, Jan; 5 seasons for Hale'iwa, and 11 for the other harbors). All tsunami events during these time periods were removed (2 from summertime and four from wintertime). The 95% confidence interval for each independent spectrum estimate is shown at the bottom. The large-scale modes from the model results of *Munger and Cheung* (2008) and *Cheung et al.* (2013), are marked with vertical dashed lines (27, 33, 43, 52, and 75 min).

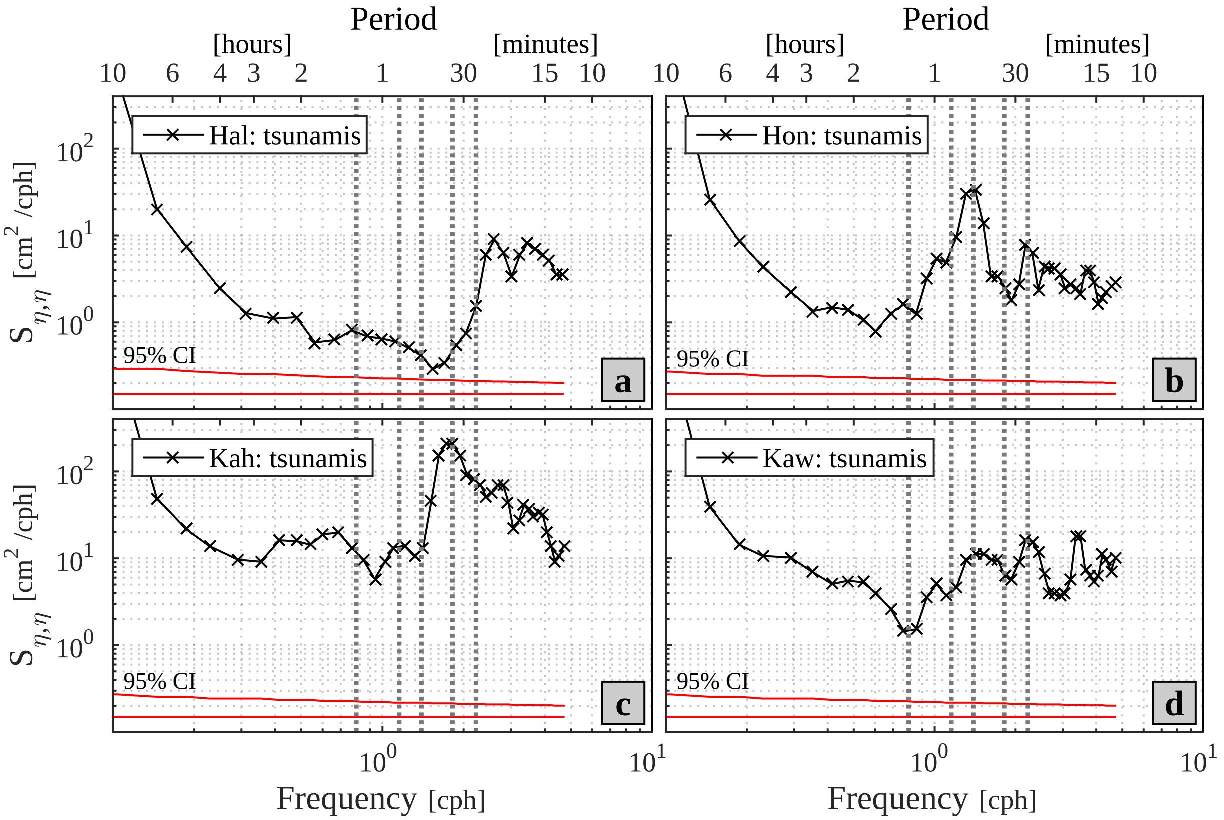

Figure 2.51: Sea level PSD at (a) site 1, Hale'iwa Hbr.; (b) site 13, Honolulu Hbr.; (c) site 14, Kahului Hbr.; and, (d) site 15, Kawaihae Hbr, during multiple tsunami events. At each site we average multiple two-day long sea level data segments that each includes a tsunami event. 7 events were included in the analysis for Hale'iwa Harbor (panel a, start times: 06/25/01, 09/25/03, 11/17/03, 05/06/06, 11/15/06, 01/13/07, and 09/29/09), and 11 in Honolulu, Kahului, and Kawaihae Harbors (panels b-d, the same tsunami events used for Hale'iwa Harbor, including events having start times: 12/05/97, 08/15/07, 02/27/10, and 03/11/11). The 95% confidence interval for each independent spectrum estimate is shown at the bottom. The large-scale modes from the model results of *Munger and Cheung* (2008) and *Cheung et al.* (2013), are marked with vertical dashed lines (27, 33, 43, 52, and 75 min).

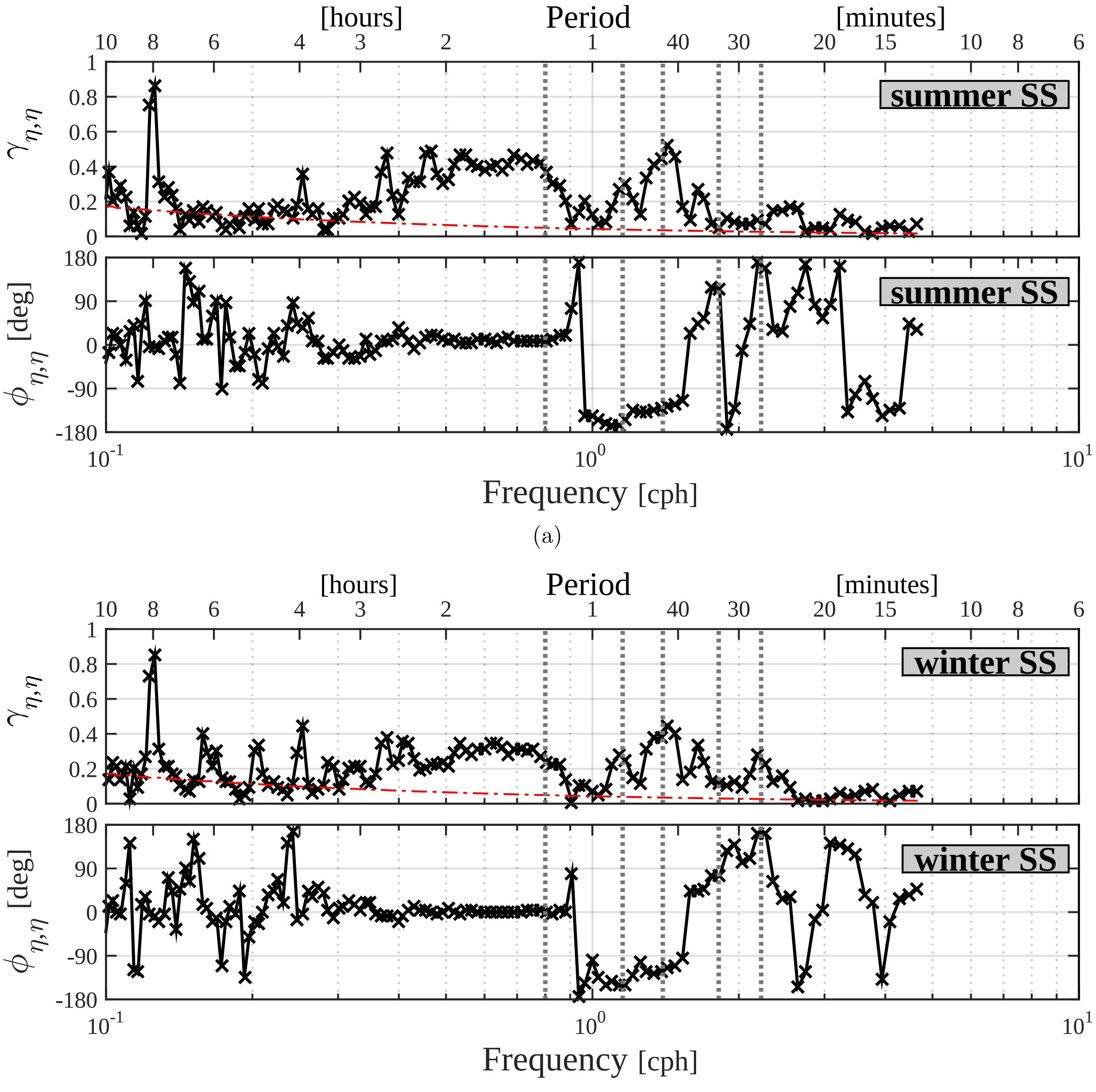

(a)

(b)

Figure 2.52: Coherence amplitude (upper panels of a, b) and coherence phase (lower panels of a, b) for Honolulu vs. Kawaihae sites using multiple 3-month long sea level records during: (a) summertime (same data as in Fig. 2.50), and; (b) wintertime (same data as in Fig. 2.50). The red-dashed line in the coherence amplitude plots is the 95% level of no significance. The large-scale modes from the model results of *Munger and Cheung* (2008) and *Cheung et al.* (2013), are marked with vertical dashed lines (27, 33, 43, 52, and 75 min).

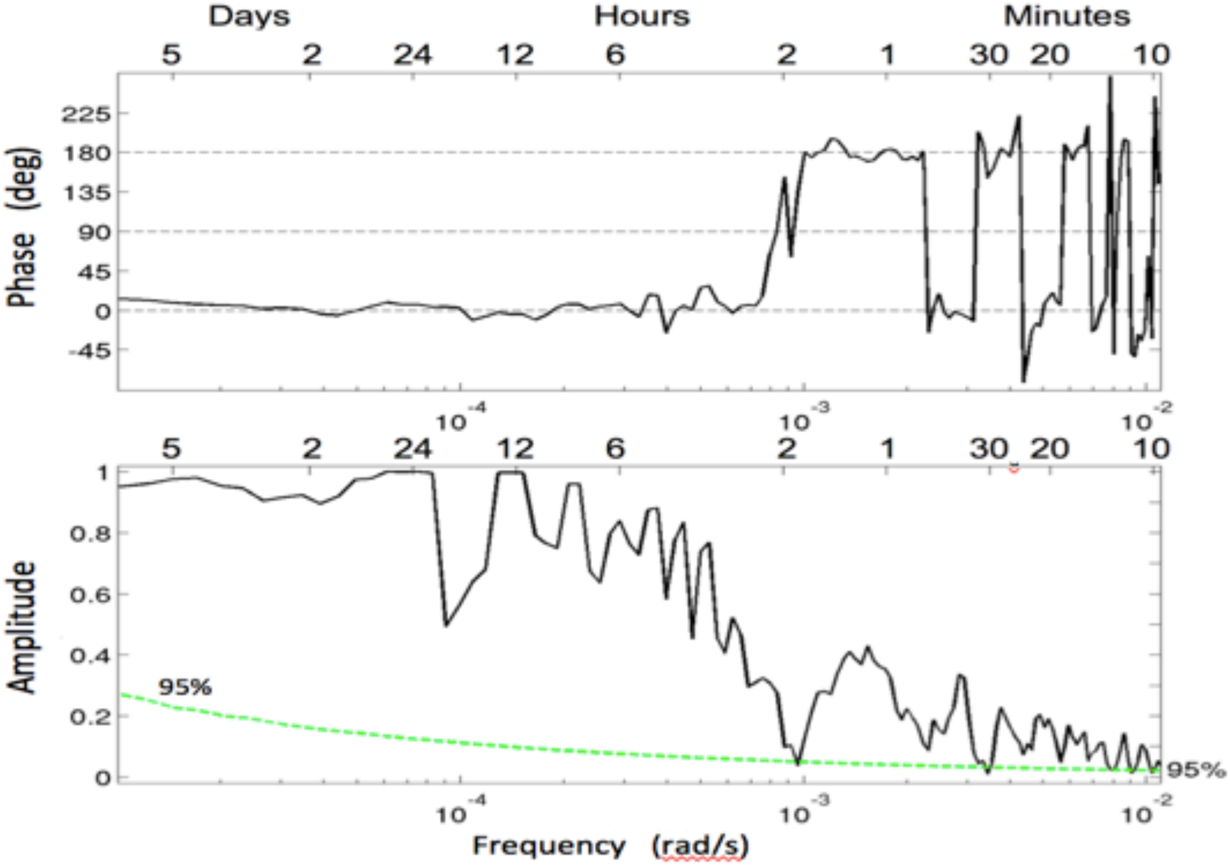

Figure 2.53: Coherence amplitude and phase between two bottom pressure sensors collected during the HOME experiment. The 95% confidence interval for each independent spectrum estimate is shown at the bottom. Figure taken from *Luther et al.* (2014).

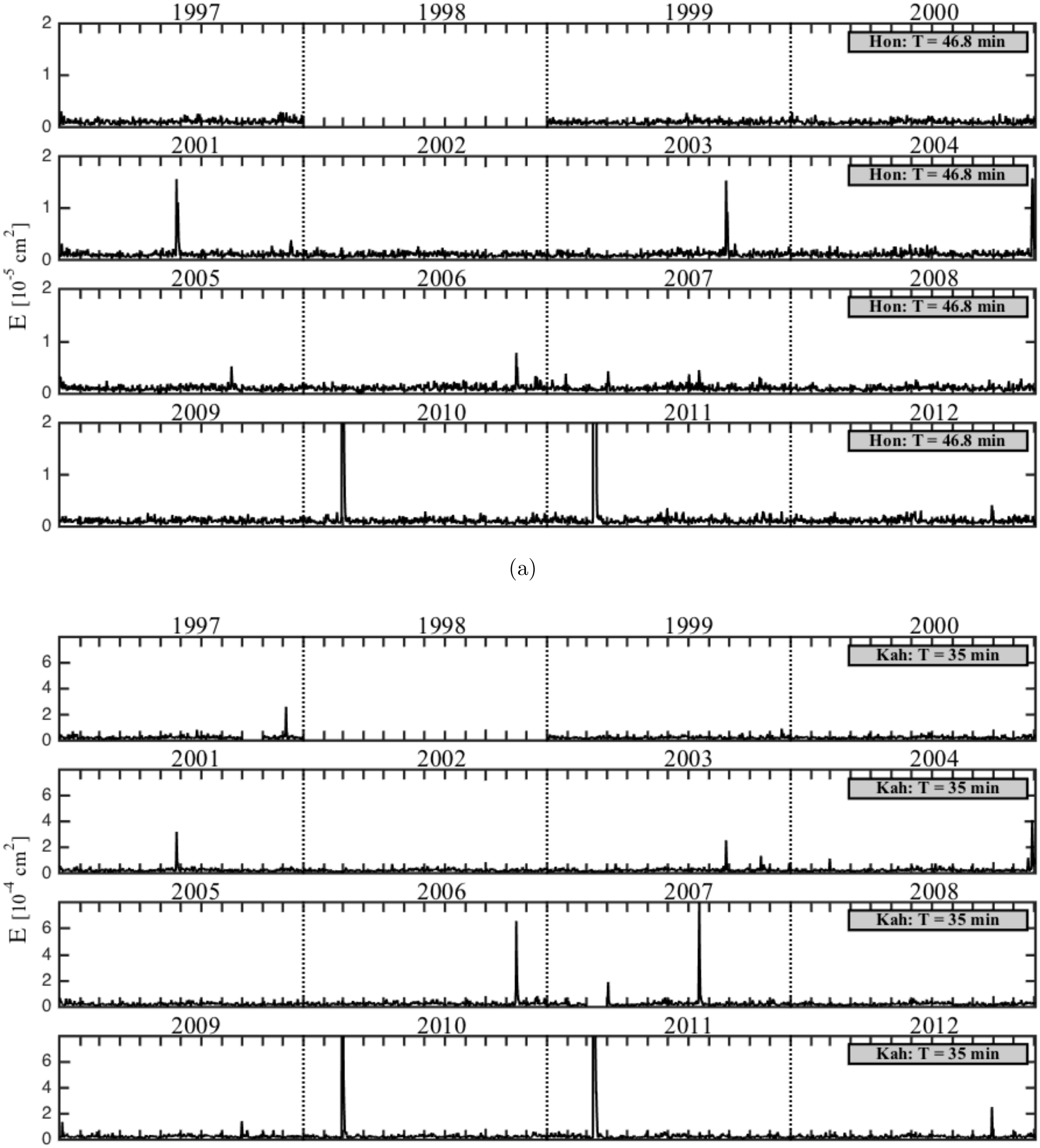

(a)

(b)

Figure 2.54: Energy vs. time for oscillation periods: (a) 44.8 min in Honolulu Harbor, and (b) 35.3 min in Kahului Harbor. Calculations were done using the complex demodulation method.

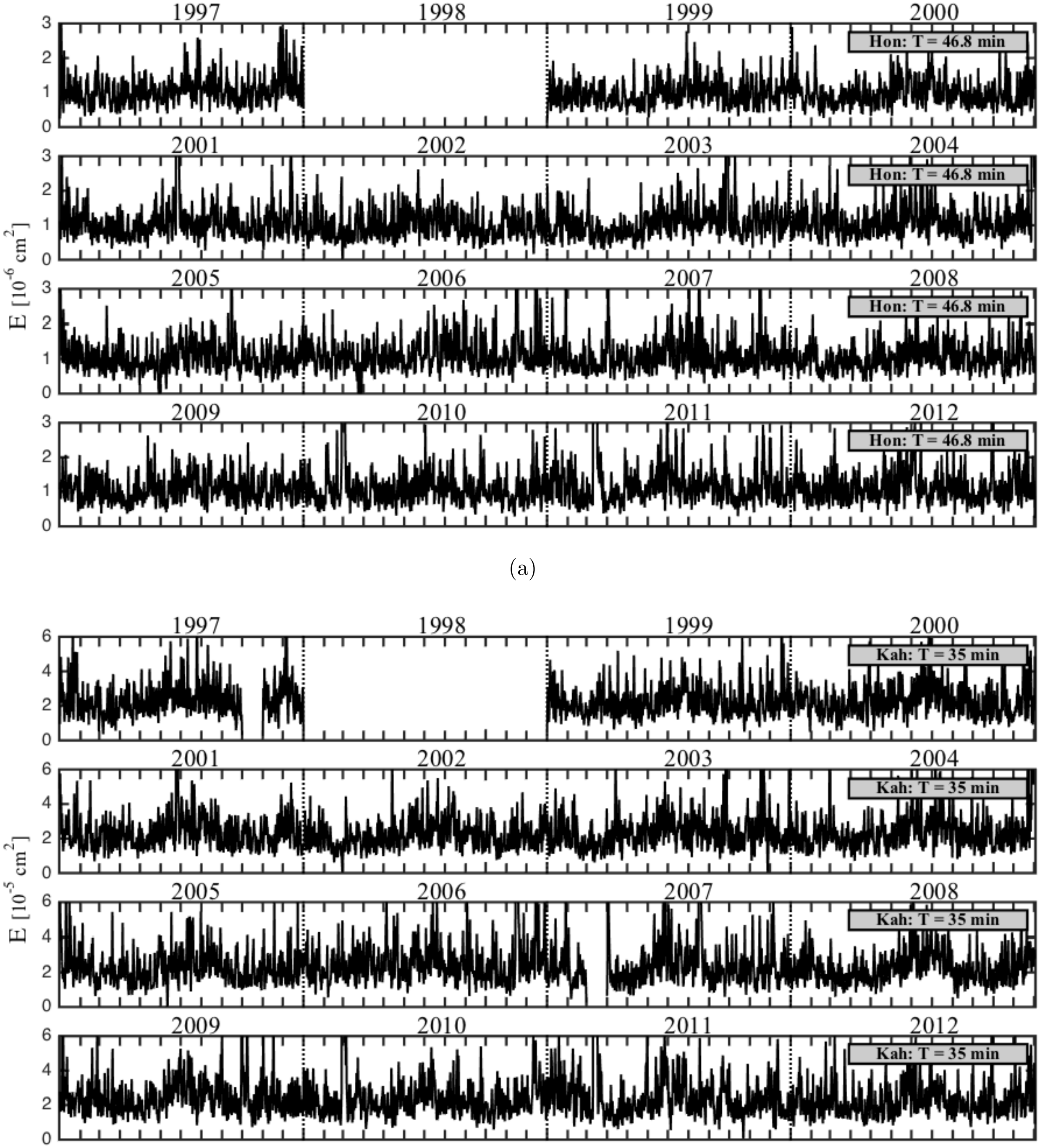

(a)

(b)

Figure 2.55: Same as Fig. 2.54, except zooming-in on the y axis.

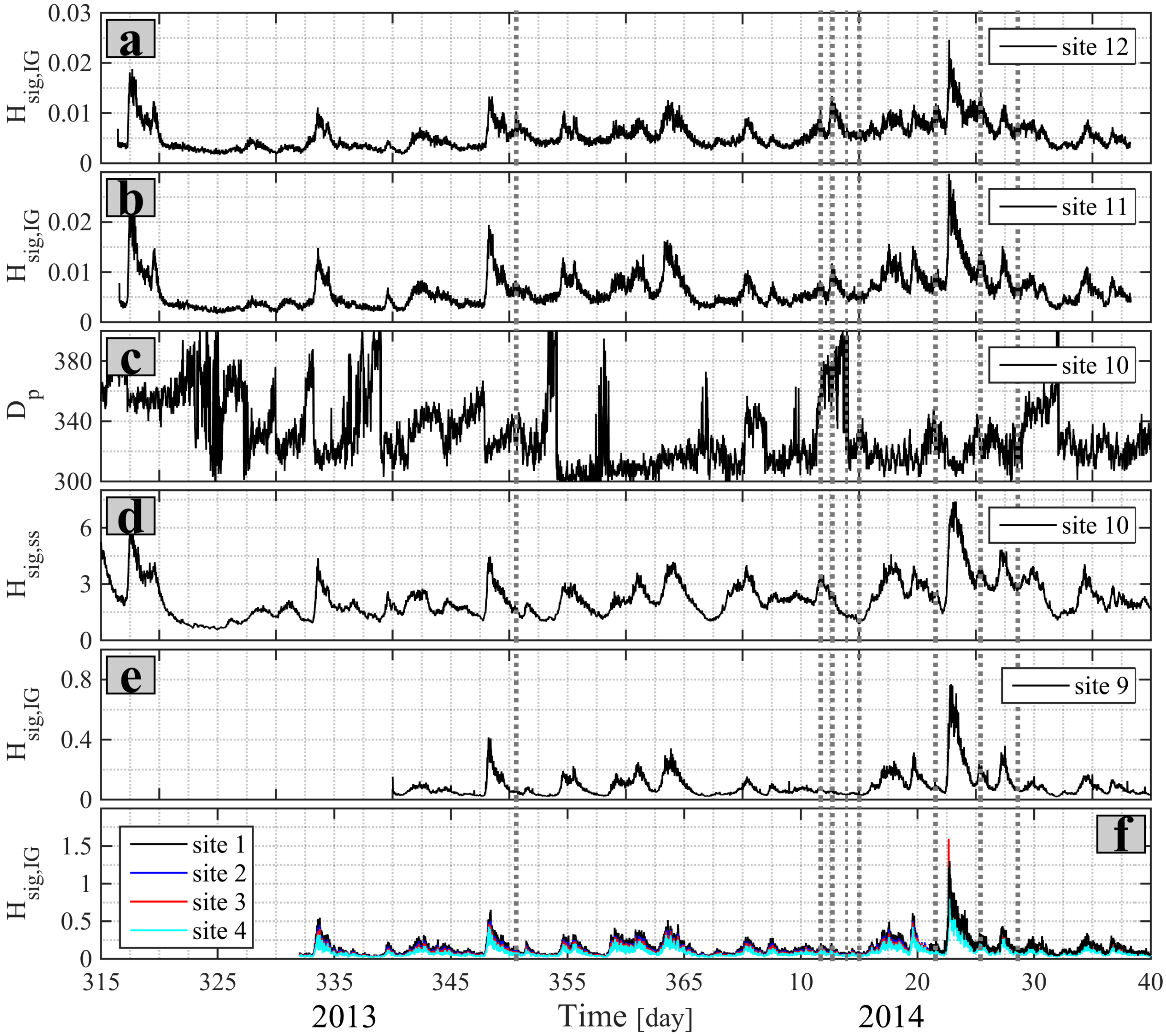

Figure 2.56: Time series of significant wave height (H_{sig}) in the 1-20 min IG band at sites 12, 11, 9, and 1-4 (panels a, b, e, and f, respectively), peak period (D_p) at site 10 (panel c), and H_{sig} at SS periods ($H_{sig,ss}$, panel d). All units are meters, except D_p which has units of degrees. Dates are number of days from the beginning of the years 2013/2014. Vertical dotted lines indicate times where $H_{sig,IG}$ was greater at site 12 than site 11.

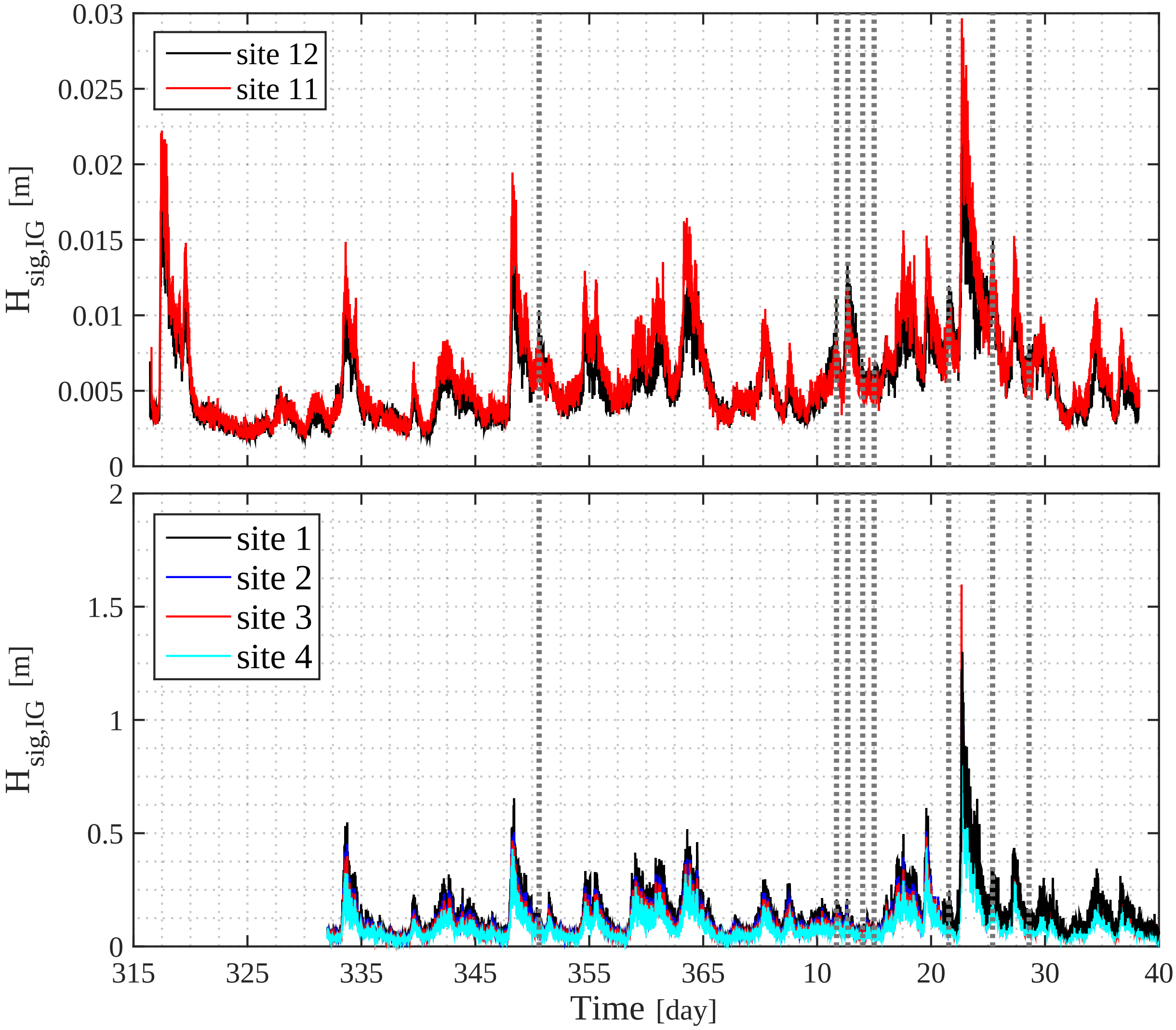

Figure 2.57: Time series of deep-water offshore and harbor $H_{sig,IG}$ in the 1-20 min IG band (all units are meters) at sites 1-4, 11, and 12. Dates are number of days from the beginning of each year (2013/2014). Vertical dotted lines indicate times where $H_{sig,IG}$ was greater at site 12 than site 11.

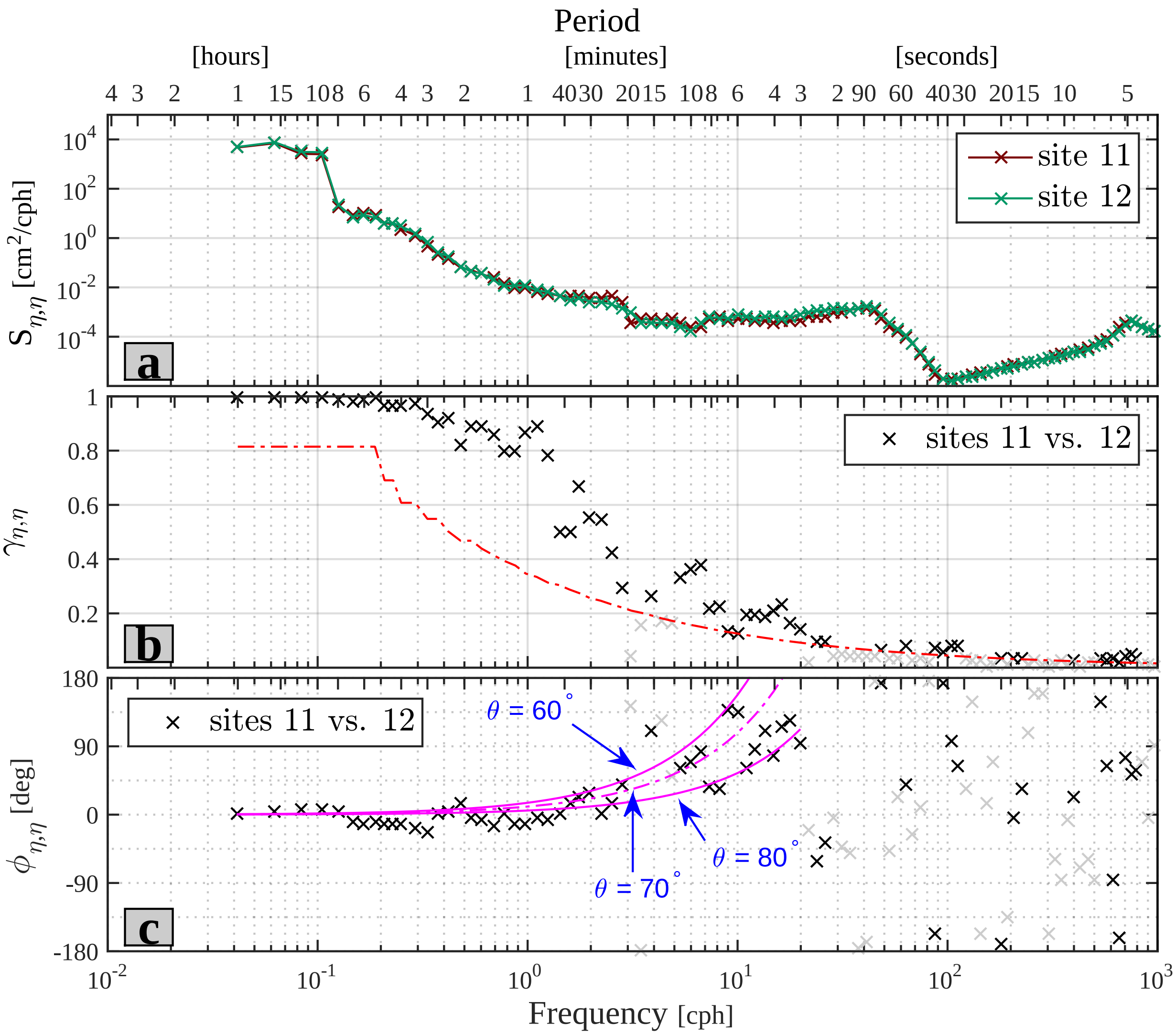

Figure 2.58: (a) PSD at site 11 (brown curve, 2016m), and site 12 (green curve, 2016m); (b) coherence amplitude, and (c) coherence phase, between sites 11 and 12. The red-dashed line in the coherence amplitude plots is the 95% level of no significance, and insignificant coherence amplitude and phase values were marked with gray crosses. Positive phase difference implies propagation where site 12 leads site 11. The magenta curves in panel c correspond to the coherence phase values of waves arriving from angles of $\theta = 60°, 70°$, and $80°$, relative to the line connecting sites 12 and 11.

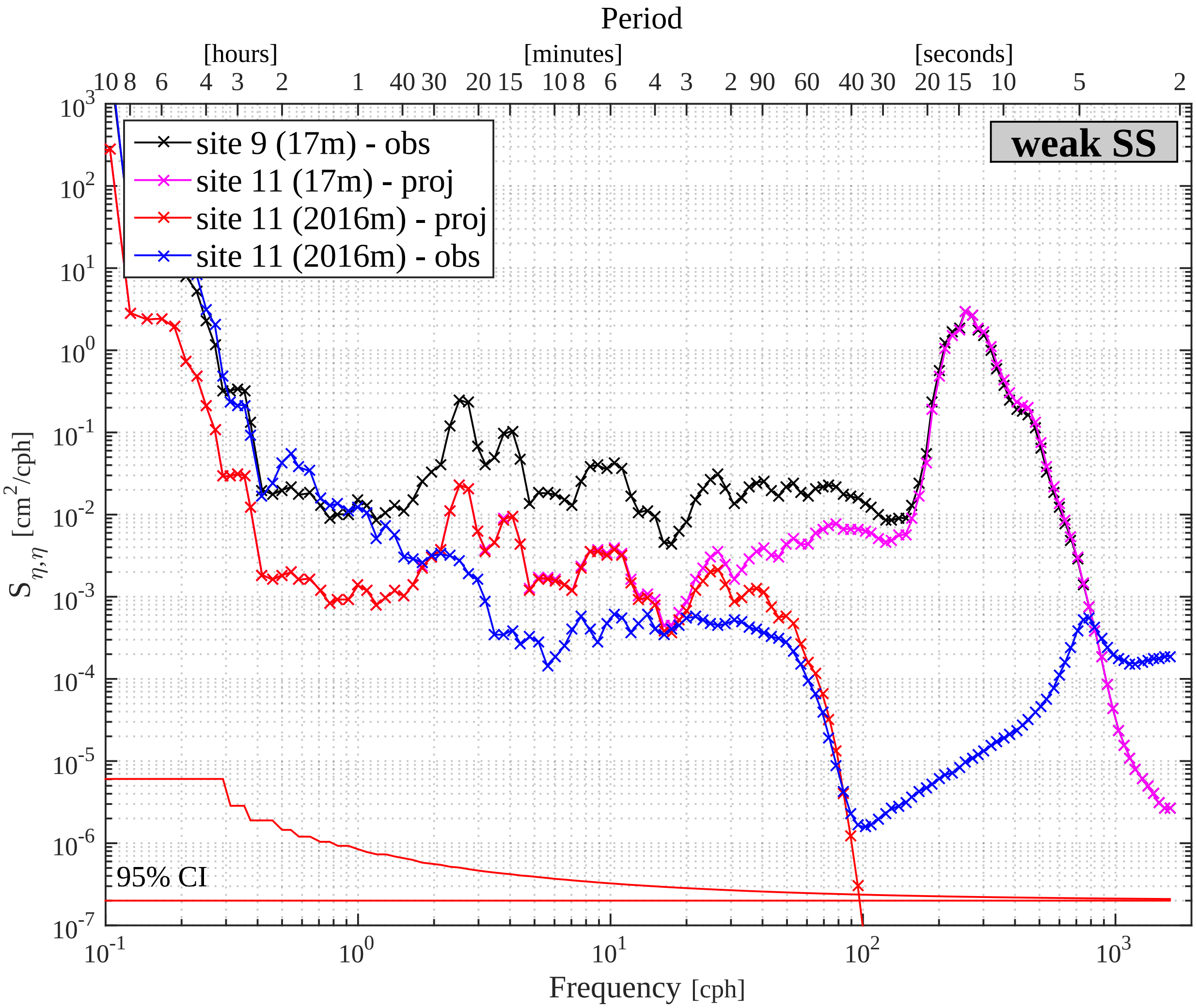

Figure 2.59: Projected PSDs from sites 9 to 11 during a time period of weak SS. (i) Black curve: PSD at site 9 (17m depth). (ii) Magenta curve: PSD at site 9 (17m depth) projected to PSD at 17m depth on site 11. (iii) Red curve: PSD at site 9 (17m depth) projected to PSD at 2016m depth on site 11. (i) Blue curve: PSD at site 11 (2016m depth).

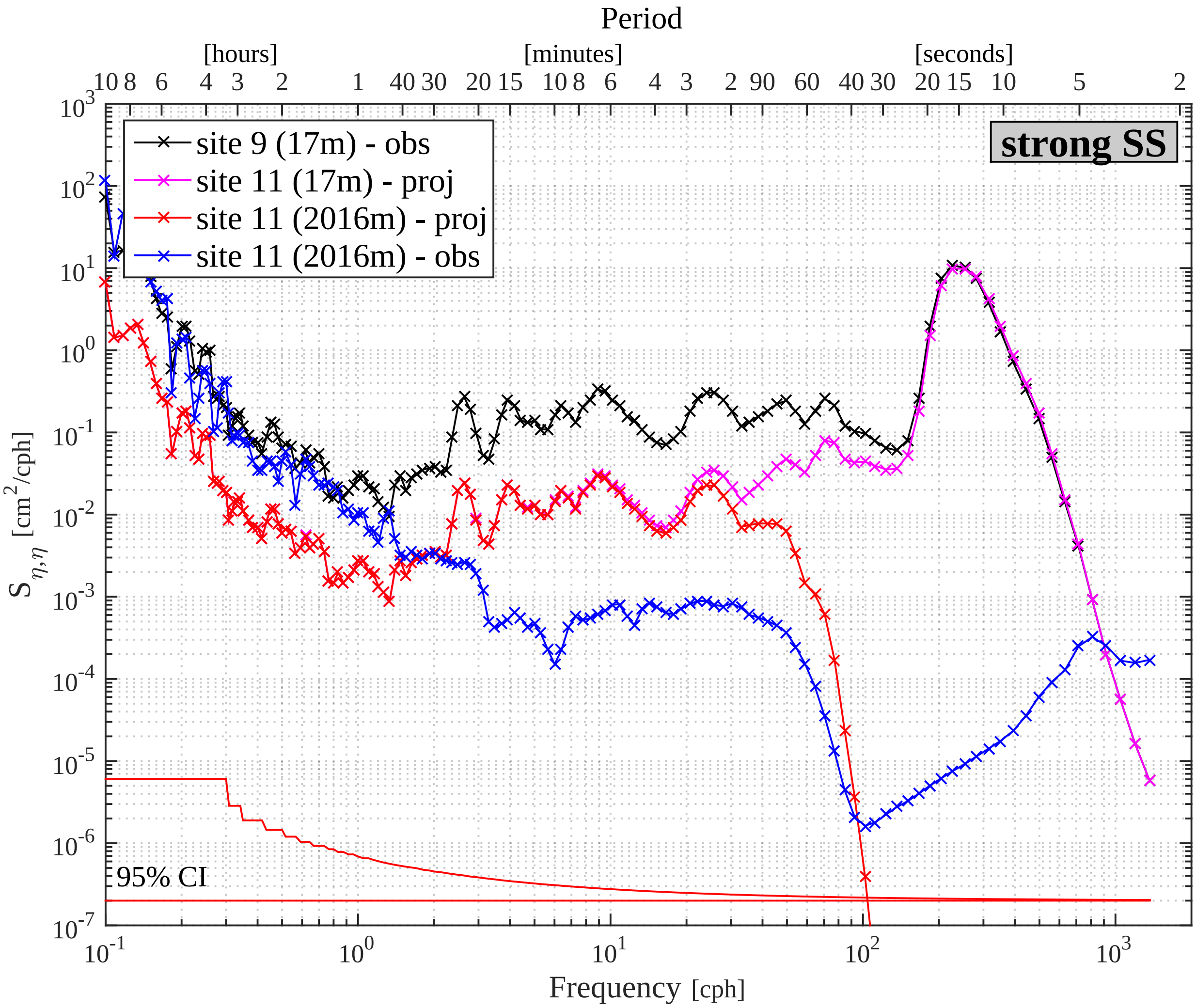

Figure 2.60: Projected PSDs from sites 9 to 11 during a time period of strong SS. (i) Black curve: PSD at site 9 (17m depth). (ii) Magenta curve: PSD at site 9 (17m depth) projected to PSD at 17m depth on site 11. (iii) Red curve: PSD at site 9 (17m depth) projected to PSD at 2016m depth on site 11. (i) Blue curve: PSD at site 11 (2016m depth).

CHAPTER 3
FORECAST OF CURRENT-DRIVEN HARBOR SURGES IN HALE'IWA HARBOR, HAWAI'I

3.1 Introduction

Earliest observations of waves oscillating at long infrgravity (IG) periods were made at the coast by *Munk* (1949), who also called them "*surf-beat*", and *Tucker* (1950). Observations of deep-ocean IG oscillations done by *Webb et al.* (1991) revealed very small amplitudes of the order of < 1 cm, that could be slightly exceeded at certain locations according to *Aucan and Ardhuin* (2013). At the coast, as IG waves propagate into shallow depths they become shallow water waves and their amplitudes may reach variances of the order of 1 m (*Wright et al.* 1982). Such oscillations may result from free waves (*Eckart* 1951), or forced (also known as bound) waves (*Longuet-Higgins and Stewart* 1962; *Hasselmann* 1962), both of which have gravity as the restoring force. The free waves can be further categorized into *edge-waves* that are trapped to the coastline between the shoreline and an offshore turning point by reflection and refraction processes, exponentially decay offshore of the turning point, and progressively propagate in the alongshore; and, *leaky-waves* that do not return to the shoreline by refraction and therefore escape to deep water.

Various observational studies have shown that the energy levels of both free and forced waves increase with increasing sea/swell (SS) energy and decreasing water depth, but their relative contributions to the total IG energy varies depending on the SS energy levels (*Okihiro et al.* 1992; *Elgar et al.* 1992, among others). In the surf zone, in most cases it was found that free wave energy dominates forced wave energy when SS conditions are weak to moderate (*Okihiro et al.* 1992; *Bowers* 1992; *Herbers et al.* 1992, 1994, 1995b, among others), but outside of the surf zone, forced wave energy levels were found to be comparable or higher under strong SS conditions (*Okihiro et al.* 1992; *Elgar et al.* 1992). Observations made by *Huntley and Kim* (1984) outside the surf zone in a relatively steep beach showed that low frequency motions in the 30-300 sec period band were dominated by forced waves. In the case of the freely propagating edge and leaky waves, the relative contribution to the total IG energy depends on the geometry of a given coastline (*Munk et al.* 1964; *Huntley* 1976).

Another source of nearshore IG oscillations is known as *shear waves* (also called *vorticity waves*). First observed by *Oltman-Shay et al.* (1989), these waves were found in the surf zone only in the presence of a mean longshore current, and have periods of 100-1000 sec. In a theoretical work by *Bowen and Holman* (1989), they identified conservation of potential vorticity as the underlying mechanism for generating these waves (hence, the restoring force is vorticity rather than gravity), and suggested that they are generated by the shear instability of the mean longshore current. Additional theoretical work by *Shrira et al.* (1997) suggested explosive instability processes as an alternative generation mechanism, and *Haller et al.* (1999) expanded the shear instability theory of *Bowen and Holman* (1989) by including a wave group forcing term in the nearshore potential vorticity balance.

When resonantly excited, standing long waves in semi-enclosed basins (commonly known as *seiches*) such as ports and harbors, may result in significant vertical displacements of the free surface, and strong horizontal currents. Such conditions could lead to delays in harbor operations, and in some cases could even result in significant damage to moored ships and harbor infrastructure (*Morison and Imberger* 1992; *Lopez et al.* 2014). *Morison and Imberger* (1992), *Okihiro et al.* (1993), *Okihiro and Guza* (1996), *Bellotti and Franco* (2011), *Thotagamuwage and Pattiaratchi* (2014a), have all observed SS (generated by non-local atmospheric disturbances) exciting harbor seiches. *Okihiro et al.* (1993), and *Okihiro and Guza* (1996) also show that the resonant response of the harbors is frequency dependent, with the strongest amplification occurring at the gravest normal modes of the harbors. The harbor IG responses in these studies were shown to be triggered primarily by free waves; however, it was theoretically shown that the mismatch of bound-wave-induced set-down across a harbor mouth introduces free long waves inside the harbor that can excite harbor resonances (*Bowers* 1977). Other processes that were shown to excite harbor seiches include: local atmospheric disturbances (*Okihiro et al.* 1993; *De Jong et al.* 2003; *De Jong and Battjes*

2004), internal tides (*Giese et al.* 1990; *Chapman and Giese* 1990; *Grimshaw and Chapman* 1992; *Giese et al.* 1998), and tsunamis (*Wilson* 1971; *Heath* 1974; *Okihiro and Guza* 1996). For instance, in a recent study, *Park et al.* (2016) used tide gauge sea level data from several harbors in the Pacific Ocean to study large-scale seiches of bays that persist continuously in time. Using spectral techniques they were able to provide some evidence supporting their hypothesis that the continuous source of forcing could potentially be driven by tidal waves that force a shelf to resonate.

Although the response of harbors to long period oscillations was addressed in many studies (as outlined above), the focus was primarily on the response of sea level rather than horizontal currents at IG periods inside the harbor. In this study we process various datasets of sea level and currents, in order to generate a forecast for surge currents at IG periods in Hale'iwa Harbor, Island of O'ahu, Hawai'i, given a forecast of SS forcing at an offshore location.

The study area and datasets are described in Section 2, the methods used in this study are outlined in Section 3, the analysis and results are presented in Section 4, and the final surge forecast and its validation are presented in Section 5. We then provide a short discussion in Section 6.

3.2 Study area and datasets

Due to the long history of damaging surge events in Hale'iwa Harbor and the lengthy sea level records that were available to us inside the harbor and at the offshore location of Waimea Buoy, we chose to focus on this harbor for our study. It is a small recreational boat harbor located in Waialua Bay on the North Shore of O'ahu Island, Hawai'i (see Figs. 2.1 and 2.2). The harbor is facing 315° (counterclockwise from north), a direction that exposes it to the very strong northern hemisphere winter swells that hit the island from October through April (*Caldwell and Aucan* 2007). In addition, about once a year on average, tsunami waves originating from remote locations across the pacific reach that part of the island.

The bathymetry along this stretch of coast is composed of an uneven volcanic reef with a relatively steep slope and multiple channels that cross the reef at several locations along the coast. The contour of the coastline is highly tortuous and contains numerous small-scale embayments that, depending on the local bathymetry, could potentially trap and amplify oscillations at particular IG periods.

At the early stages of this study we were limited to use sea level datasets from existing monitoring systems (see square symbols in Figs. 2.1 and 2.2):

1. A stilling-well tide gauge inside the Hale'iwa Harbor operated and maintained by the Pacific Tsunami Warning Center (PTWC), providing 2 min data (data points are not averaged) since 1997 to present (site 1 in Fig. 2.1).

2. A Datawell directional wave buoy located at a depth of 200 m, $\sim$ 6.5 km WNW of Waimea Bay and $\sim$ 8.5 km N of Hale'iwa Harbor (also known as *Waimea Buoy*), operated and maintained by the Coastal Data Information Program (CDIP) in Scripps Institution of Oceanography (SIO). Operating since 2001 to date, the buoy samples at 1.28 Hz and every 30 min analyzes $\sim$ 27 min of data to provide SS spectral products such as wave energy density and mean direction (site 10 in Fig. 2.2).

Although the available datasets inside the harbor were found to be very useful to this research, the 2 min sampling frequency is too low, preventing detection of high frequency IG oscillations, and horizontal currents data were not available. We therefore executed a small scale six-month long experiment where we deployed two pressure sensors and one current meter inside the harbor, and two pressure sensors at offshore sites. The deployment was done during the northern hemisphere winter swell season months, between 11/2011-05/2012 (sites 1, and 5 in Fig. 2.1 and sites 6 and 9 in Fig. 2.2).

Since the spatial coverage inside the harbor was limited to one particular location, and additional datasets of horizontal currents were needed, we executed a larger scale six-month long experiment during 11/2013-05/2014 where we deployed four pressure sensors and current meters at four locations inside the harbor, and three pressure sensors and two current meters at three offshore sites (sites 1-4 in Figs. 2.1 and sites 7 and 9 in Fig. 2.2; one of the offshore instruments containing a pressure sensor and current meter is not shown on the map since it was lost.)

3.3 Methods

Creating a surge forecast for Hale'iwa Harbor involved the following four stages (see four columns in Fig. 3.1):

1. ***Observations***: obtain observations of sea level offshore and inside the harbor, and currents inside the harbor.
2. ***Analyses***: analyze the observed datasets to generate a transfer function between offshore and harbor sea level, and another transfer function between harbor sea level and harbor currents.
3. ***Tools/Forecast***: use a forecast of offshore swell conditions as an input to the two transfer functions. The resulting output is the current-driven surge forecast.
4. ***Testing/Validation***: use observations of ongoing swell events, as well as a visual assessment of their impact on the harbor infrastructure and boats, in order to test and validate the forecast.

3.3.1 Observations: sea level and currents

For offshore sea level we used 30 min SS energy products from Waimea Buoy for the year 2002. These were obtained from CDIP (Coastal Data Information Program). For harbor sea level we used the 2 min tide gauge dataset for the year 2002, and a four month long pressure sensor dataset (10 sec sampling, 5 sec averaged) from the 11/2011-05/2012 deployment. For the harbor currents we used a four month long dataset (10 sec sampling, 5 sec averaged) from the 11/2011-05/2012 deployment. As was done in Chapter 2, all pressure records were converted to sea level using linear wave theory.

3.3.2 Analyses: transfer functions

Before generating the necessary transfer functions we tested several SS parameters in order to find one that yields a statistically optimal relationship between offshore SS forcing and harbor IG response. These parameters involve the statistical SS quantities: peak period, mean direction, and energy, and are defined below:

1. **Sea level energy density ($\boldsymbol{E_{ss}}$)**: potential energy density. This parameter was used extensively by other groups studying harbor seiches, e.g., *Okihiro et al.* (1993), *Okihiro and Guza* (1996), *Elgar et al.* (1992), among others.

2. **Sea level power spectral density ($\boldsymbol{P_{ss}} = E_{ss}/\Delta f$)**: potential energy density divided by the frequency bandwidth. This parameter emphasizes the energy that is contained in the longer period waves. It was shown by *Middleton et al.* (1987) that longer period swell waves are more important than the shorter period waves in the process of IG wave generation.

3. **Cosine-filtered sea level power spectral density ($\boldsymbol{P_{ss,cf}}$)**: sea level power spectral density propagating towards shore.

4. **Sea level energy flux ($\boldsymbol{F_{ss,cf}} = P_{ss,cf} \times T$)**: cosine-filtered sea level power spectral density multiplied by the wave period, emphasizing the longer periods even more than the previous two parameters.

For each of these SS parameters the mean standard deviation is calculated in several IG period bands. The SS parameter resulting in the smallest error will be the one we use in relating offshore SS to harbor IG.

Ideally, in order to determine the relationship between the offshore SS forcing and the IG response of harbor currents we need lengthy datasets of sea level offshore of the harbor and currents inside the harbor, for the same time period. However, the only lengthy datasets available to us inside the harbor are sea level from the tide gauge. Datasets of currents and sea level sampled at high frequencies were obtained only later during the 11/2011-05/2012 deployment, but the record length was only several months long. As a result of these limitations, we used the lengthy tide gauge sea level datasets to generate a transfer function between offshore sea level SS and harbor sea level IG (hereafter will be called: $TF1$), and the high frequency, but shorter records, of currents and sea level to generate a second transfer function between harbor sea level IG and harbor currents IG (hereafter will be called: $TF2$).

For a given pair of variables, these transfer functions are determined by generating a scatter plot, bin-average the cloud of data, and then fit a curve. That curve is the transfer function for that particular pair.

3.3.3 Tools/Forecast

The forecast of surge currents inside the harbor is generated by applying the two transfer functions $TF1$ and $TF2$ to an input of SS forecast. The SS forecast is obtained from Kwok Fai Cheung's group in the Department of Ocean and Resources Engineering (ORE) at the University of Hawai'i at Manoa (UHM), and provides a 7.5 day long forecast of SS conditions at the location of Waimea Buoy (site 10 in Fig. 2.2). This forecast of SS is being converted to our statistically-optimal SS parameter and used as an input to the transfer functions to yield the forecast of IG currents inside the harbor. We express the final forecast as a Surge Current Index (SCI), which is simply the root-mean-square (RMS) of the harbor currents IG power spectral density.

As a final step before reporting the surge forecast, we determine a SCI threshold level above which surges driven by IG currents inside the harbor are likely to cause damage to boats and/or harbor infrastructure. We do this by analyzing historical records of all tsunami events and two strongest SS events per year during the years 1997-2010, and one strong SS event during 2014.

3.3.4 Testing/Validation

During ongoing large SS events we drive to the north shore and document the impact these events have on the harbor infrastructure and boats inside Hale'iwa Harbor as well as at selected locations along the coast. For a given SS event, by using observations of its energy density, period, and direction at Waimea Buoy, convert them to our SS parameter, and then use this as an input to our two transfer functions, we are able to calculate the SCI value that corresponds to this particular event. This is then used as another data point in our SCI database resulting from strong SS events. Depending on the particular SCI value and the impact each swell event has on the harbor operations, infrastructure, and the boats, the SCI threshold level may be modified accordingly.

3.4 Analysis and results

3.4.1 Dominant IG bands in Hale'iwa Harbor

To obtain a visual look at the relationship between the offshore SS forcing and harbor IG response, we generate monthly spectrogram plots. The spectrograms are calculated following the same methodology that is described in Chapter 2, Section 2.4.

Figures 2.17 and 2.18 clearly show a one-to-one correspondence between the offshore SS forcing and the IG response in Hale'iwa Harbor. This correspondence was seen for all times when both offshore and harbor data were available between 2001-2010.

Spectral analysis of sea level and currents inside the harbor has helped us identify the harbor's IG band response that is most relevant for our surge forecast. We generate PSD plots using nearly two months of data, and follow the same methodology described in Chapter 2, Section 2.4.

Sea level PSD plots at four different locations inside the harbor are seen in Fig. 3.2. Note that the IG band of interest seems to be approximately within 4-40 min. At periods shorter than 4 min additional spectral peaks appear at $\sim$ 90 sec, $\sim$ 70 sec, and $\sim$ 50 sec; however, for the purpose of generating a forecast of surges driven by IG currents, we also need to examine the spectrum of currents at the same four locations inside the harbor. Spectra of the currents that are aligned along the major ellipse axes of sites 1-4 are shown in Fig. 3.3, and suggest that the approximate 2-10 min period band is the most energetic and all oscillations shorter than ~ 2 min are very weak and seem to be unimportant for our current-driven surge forecast. As a result, we chose the 2-40 min period band as the relevant one for our study at this particular harbor.

To get a feel for the sea level versus currents variability, Fig. 3.4 shows a two-hour long time series around the peak of a large SS event that occurred on 02/08/12 - 02/09/12. It can be seen that the dominant periodicity approximately varies around $\sim 6-9$ min for the sea level signal, and $\sim 3-5$ min for the u and v currents, consistent with our findings from the sea level and currents spectra.

Since our PSDs and all of our monthly spectrogram plots show distinct modal peaks inside the harbor at the periods of 6 min, 8 min, 12.5 min, and 23 min (particularly under none-weak SS forcing conditions, e.g., Figs. 2.7, 2.9, 2.19, and 2.20), we decided to divide the 2-40 min period band into four narrower bands: IG_a, IG_b, IG_c, IG_d as follows: (a) $2 < T_{IG_a} < 4$ min; (b) $4 < T_{IG_b} < 10$ min; (c) $10 < T_{IG_c} < 15$ min, and; (d) $15 < T_{IG_d} < 40$ min. Although at first the choice of these IG period bands seemed to be somewhat arbitrary, it will be later justified by showing how differently each of these IG period bands responds to offshore forcing.

3.4.2 Searching for appropriate sea/swell parameter and generating a surge forecast

In search of an optimal relationship between offshore SS and harbor IG, we tested four different SS parameters and used scatter plots to analyze their relationships with IG power spectral density (IG-PSD) inside the harbor. In this analysis we used year long sea level datasets. To calculate the SS parameters, we use CDIP's 9-band energy and direction datasets, and interpolate over data gaps of up to 2 hours (4 data points). For a given energy band, we vector average (smooth x and y components separately) the energy arrays by convolving the dataset with a 12-hour wide Hanning window, and then decimate the resulting dataset to 6-hour interval. The resulting smoothed energy is obtained by calculating the magnitude of the x and y energy components. The smoothed array of mean direction is obtained from the arc-tangent of the smoothed energy array. E_{ss} is obtained by summing the smoothed energy arrays from all nine bands. To calculate P_{ss}, we divide the smoothed energy of each period band by the corresponding frequency difference, and then sum the arrays from all nine bands. $P_{ss,cf}$ is calculated by applying a cosine filter to each of the smoothed energy arrays between 225° and 405° (where the angles are measured clockwise relative to the true north), divide each of the smoothed energy arrays by the corresponding frequency difference, and sum the arrays from all nine bands. $F_{ss,cf}$ is calculated as $P_{ss,cf}$, except that before summing all nine bands we multiply each one by the mid-period that corresponds to each particular band.

To calculate the IG-PSD ($IG_a - IG_d$) we use the 2 min sea level dataset from site 1 (see Fig. 2.1), and interpolate over short gaps in the data. This dataset is converted to PSD following the same approach used in the spectrogram plots, and then converted to $IG_a - IG_d$ by summing the frequency bands of interest. These are then smoothed in the time domain using a 12-hour wide running mean, and decimated from three-hour to six-hour time intervals.

Figure 3.5 shows the response of the different IG bands to each of the SS parameters that we examine. The relationships between a given IG band and a SS parameter can be seen more clearly after averaging the IG response in SS bins that contain a fixed number of data points (see Fig. 3.6). This last step results in a clear relationship between offshore SS and harbor IG. This figure also supports our choice of dividing the IG band into the aforementioned four bands. By comparing the fitted curves for a given SS parameter (looking at a given column, comparing $IG_a - IG_d$) we clearly see that each IG sub-band has a different response characteristic to SS forcing. The initial increase above the spectral noise levels in the IG_a period band occurs at very weak SS levels, whereas that initial increase appears to gradually shift to stronger SS forcing levels as we go from IG_a to IG_d.

To find the SS parameter that results in the best relationship with harbor IG we plotted the IG standard error for each of the SS parameters. The result is shown in Fig. 3.7, which clearly suggests that in each of the four IG period bands, the standard error decreases going from the energy parameter (E_{ss}) to the energy flux ($F_{ss,cf}$). Note that the most significant reduction in standard error is obtained simply by going from E_{ss} to P_{ss}. We therefore chose $F_{ss,cf}$ as our SS parameter.

Now with a SS parameter in hand, our transfer function will simply be the fitted curves from the last column of Fig. 3.6. Using these, together with a SS forecast we can now generate a forecast of the SCI.

3.4.3 Determine SCI threshold levels

The next step is to determine a threshold level for the SCI. We do this by calculating the SCI of all tsunami events and two strongest SS events per year during 1997-2010, and one strong SS event during 2014. The result can be seen in Fig. 3.8. This figure shows that the SS-driven SCIs are consistently higher than most of the tsunami events; nevertheless, a review of historical media reports reveals that tsunamis more frequently pose a threat to Hawaiian Harbors than large SS events. Since 1997, the 11/15/2006 Kuril Islands tsunami posed danger to Hawaiian Harbors and boats (*Gordon* 2006; *Leone* 2006), and the 03/11/2011 Tohoku tsunami event caused extensive damage to Hawaiian harbors and boats (*Pang and Nakaso* 2011; *Nakaso and Vorsino* 2011), including Hale'iwa Harbor in particular. We therefore use SCI values from these particular tsunami events to define the threshold levels. We set a SCI value right around the Tohoku tsunami SCI level to be the threshold above which there is a high likelihood that surge currents within the harbor will cause damage to the harbor infrastructure and boats, as well as unsafe conditions for navigation. We set the range of SCIs between the Kuril Islands tsunami SCI value and the abovementioned SCI value that corresponds to the Tohoku tsunami, to be the SCI range where surge currents within the harbor may potentially cause damage to the harbor infrastructure and boats, as well as challenging conditions for navigation.

3.4.4 Harbor's response versus phase relationships of IG waves

Following these findings, we decided to examine more carefully the differences between the characteristics of tsunamis and SS sea level records. We high-pass filtered all of our time series (excluding all periods longer than 2 hours) and noted that for a given SCI value, the tsunami event has a larger maximum sea level swing (SL_{max}) than the SS event with corresponding SCI value (e.g., compare panels a and b of Fig. 3.9).

We believe that the reason for that is the phase relationships among the different frequency components of tsunami versus SS waves. The frequency components of a tsunami wave group are typically in phase, resulting in large sea level swings, whereas for a group of SS waves the phase relationships are much more random, resulting in smaller sea level swings.

In quantifying the relationships between the SCI and SL_{max} for tsunami versus SS events, we used the maximum of the sea level RMS ($SL_{rms,max}$) instead of SL_{max}, since it is statistically more reliable. We calculated $SL_{rms,max}$ by de-tiding the sea level time series, applying a high-pass filter (2 hour cutoff), calculating the rms for 40-minute long bins with 50% overlap, and finally selecting the maximum SL_{rms} for each bin. We then fitted straight lines to the tsunami and SS trends and forced them to pass through the origin as can be seen in Fig. 3.10.

Note that the slope is smaller for the case of tsunami waves, in agreement with our initial observation that for a given SCI value SL_{max} (or, $SL_{rms,max}$) is greater for tsunamis than for SS. Since we chose to determine the SCI threshold levels based on data from historical tsunami events (SCI_{tsu}) and the goal of this study is to generate a forecast of SCI triggered by SS events (SCI_{ss}), the above results imply that our forecast of SCI_{ss} will be overestimated and should be scaled down to match the corresponding SCI_{tsu} value. A relationship between the tsunami and SS SCIs is obtained by looking at their corresponding SCI values at a fixed $SL_{max,rms}$, which translates into:

$$SCI_{tsu} = \frac{slope_{tsu}}{slope_{ss}} \times SCI_{ss}, \tag{3.1}$$

where $slope_{tsu}$ and $slope_{ss}$ are the slopes of SCI vs. tsunami events, and SCI vs. two strongest SS events per year, respectively; and,

$$\frac{slope_{tsu}}{slope_{ss}} = 0.61. \tag{3.2}$$

Therefore, we take our forecast value of SCI_{ss} and scale it down by 0.61. The resulting SCI value is the one we report in our surge forecast.

3.5 Surge forecast and forecast validation

A particular example from our final surge forecast product is shown in Fig. 3.11. Plots on the left column are the total SCI in the 2-40 min period band, and on the right column we have the SCI contribution of four different IG period bands: 2-4, 4-10, 10-15, and 15-40 min. Note that SCI values within the shaded pink region indicate that surge currents within the harbor may potentially cause damage to the harbor infrastructure and boats, as well as challenging conditions for navigation (based on the aftermath of the 11/15/2006 Kuril Islands tsunami). SCI levels exceeding the red threshold line imply that there is a high likelihood that surge currents within the harbor will cause damage to the harbor infrastructure and boats, as well as unsafe conditions for navigation (based on the aftermath of the 03/11/2011 Tohoku tsunami).

These figures provide an example of our surge forecast product for the particular swell event of 02/22/16 (local Hawai'i time), as seen on the PacIOOS website. A forecast on 02/18/16 (panels a and b) suggested that on 02/22/16 the SCI of a large swell event will slightly exceed the upper threshold (red line), an indication of potentially damaging and dangerous currents in the harbor. Closer to the time of the event, an updated forecast on 02/21/16 (panels c and d) suggested that the SCI levels are still expected to be very high. A nowcast during the peak of that event (panels e and f) revealed good agreement between the forecast and observations, with a slight over-prediction at some time during the peak of the event. A hindcast on 02/23/16 (panels g and h) revealed that during the peak of the event the SCI was indeed at, or very close, to the upper threshold line for most of 02/22/16.

In order to validate the harbor surge forecast we arrive to Hale'iwa Harbor site during the peak of several large SS events and document any unusual IG oscillations and the impact of each SS event on the harbor infrastructure and boats. In the particular example of Fig. 3.11, we collected evidence that large portions of the harbor were flooded during much of the day on 02/22/16 (local Hawai'i time).

It should be pointed out that although the SCI has units of speed, it should not be interpreted as the actual speed of IG currents in the harbor. The sole intent of this index is to validate potential boat movement inside the harbor by comparing the index value to the threshold line.

Although no measurements were taken during the peak of the 02/22/16 SS event, we were able to be on the harbor site during the event and document its impact. The various pictures and video footages we collected provided proof of very strong surge currents at all parts of the harbor, having IG periods ranging between 4-6 min. Several docks were periodically flooded for several hours, and large portions of a low-lying parking lot were also flooded. In Fig. 3.12 we see several pictures that demonstrate the impact of this large SS event on the harbor. All pictures were taken at the southern-most extension of the harbor. Times of low/high sea level are seen on the left/right columns. Note the high range of sea level change between the left and right columns. In panels a and b we can see the sea level change by looking at the water level at the PTWC tide gauge. In panels c and d we see an example of a fixed dock of the harbor that was completely flooded when the surge currents were filling in. On the opposite side, a boat ramp was completely underwater every several minutes. Panels e and f are pictures that were taken from the parking lot at the southern side of the harbor. Note how far the water reaches on the road during times of high surge. The water was flowing on the road where vehicles were driving.

3.6 Discussion

Lengthy historical sea level records were used to examine the 2-40 min IG response of Hale'iwa Harbor to offshore SS forcing. Datasets of sea level and near-surface horizontal currents from two new six-month long deployments provided new details regarding the spatial distribution of the IG response of sea level and horizontal currents inside the harbor. With these datasets we tested several SS parameters in order to identify one that results in a statistically optimal relationship between the offshore forcing and harbor response in four IG period bands: 2-4 min, 4-10 min, 10-15 min, and 15-40 min. For each of these IG period bands, we determined two transfer functions relating the (statistically optimal) SS parameter to the horizontal currents inside the harbor in that particular IG band. These transfer functions, together with a forecast of offshore SS conditions (i.e., peak period, mean direction, and energy) as an input, were used to predict harbor IG response that was expressed in terms of a SCI. A threshold of SCI was determined, indicating the level above which surge current inside the harbor may lead to disruption in harbor operations or even cause damage to harbor infrastructure and boats.

The SCI levels generated by our surge forecast are showing good agreement with observed SCI levels, even with high SCI levels such as the ones observed during the large SS event of 02/22/2016. The SCI threshold level that we determined based on Hale'iwa Harbor's IG response during various SS and tsunami events, seems to adequately represent the potential risks in that particular Harbor as a result of very strong SS events. As part of our ongoing efforts, we keep monitoring all significant SS events in order to validate the forecast and potentially add additional improvements in order to improve its reliability. Our plans for future projects involve developing a similar forecast for other Hawaiian Harbors such as Barbers Point, Kahului, Kaumalapau, Hilo, and possibly others.

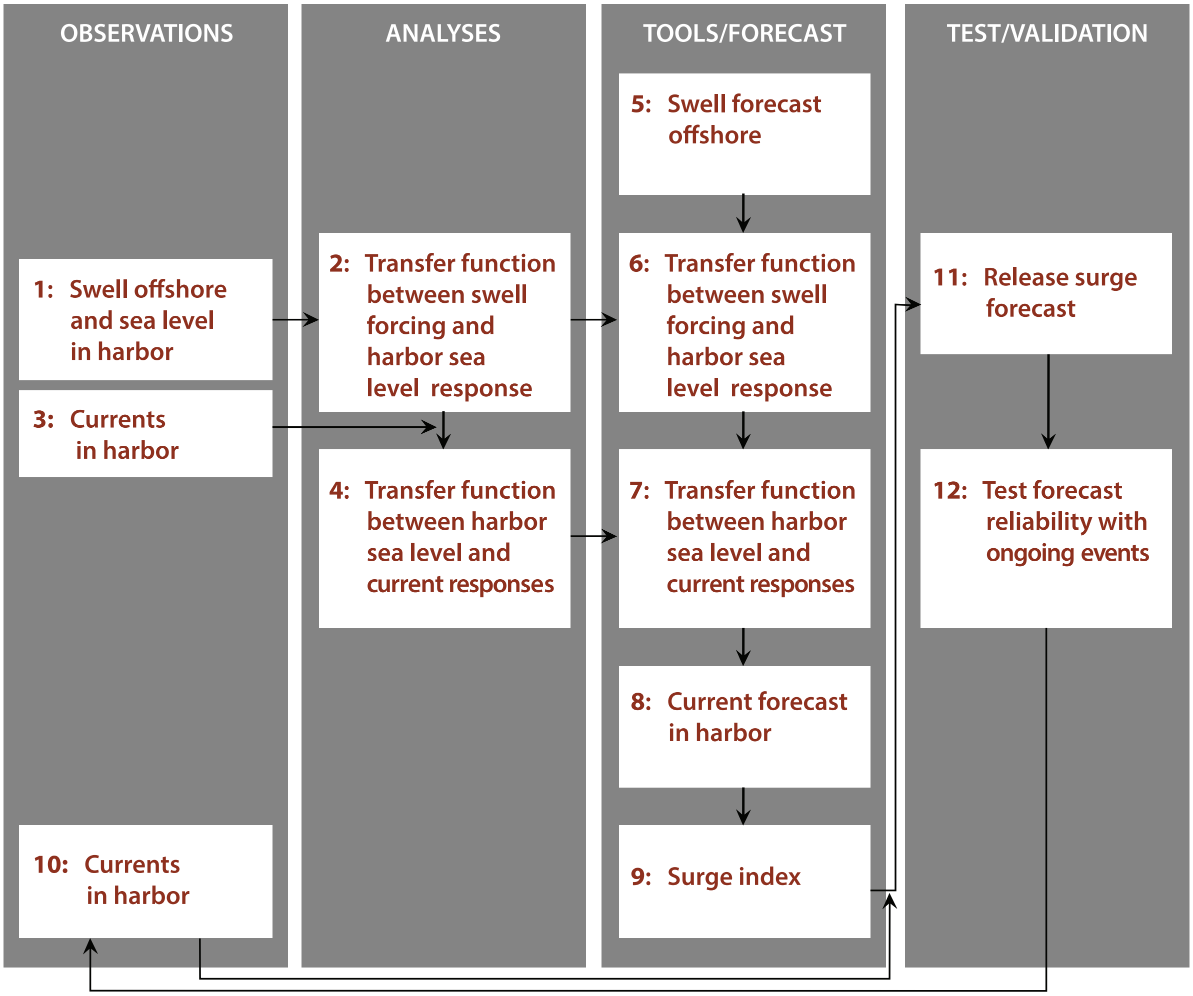

Figure 3.1: The building blocks of forecasting surge currents for Hale'iwa Harbor.

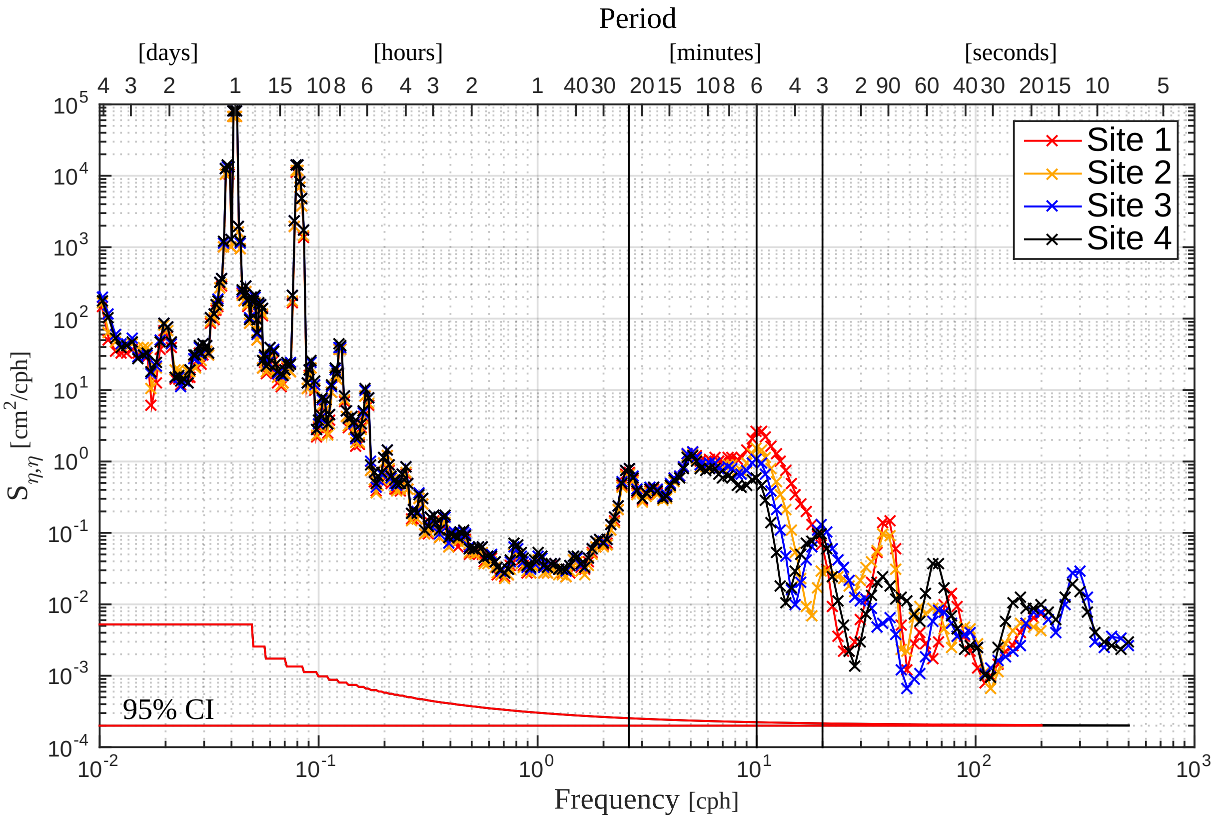

Figure 3.2: Power spectral density of observed sea level at the locations of the four sensors inside Hale'iwa Harbor during 11/28/13 - 01/20/14. The 95% confidence interval for each independent spectrum estimate is shown at the bottom.

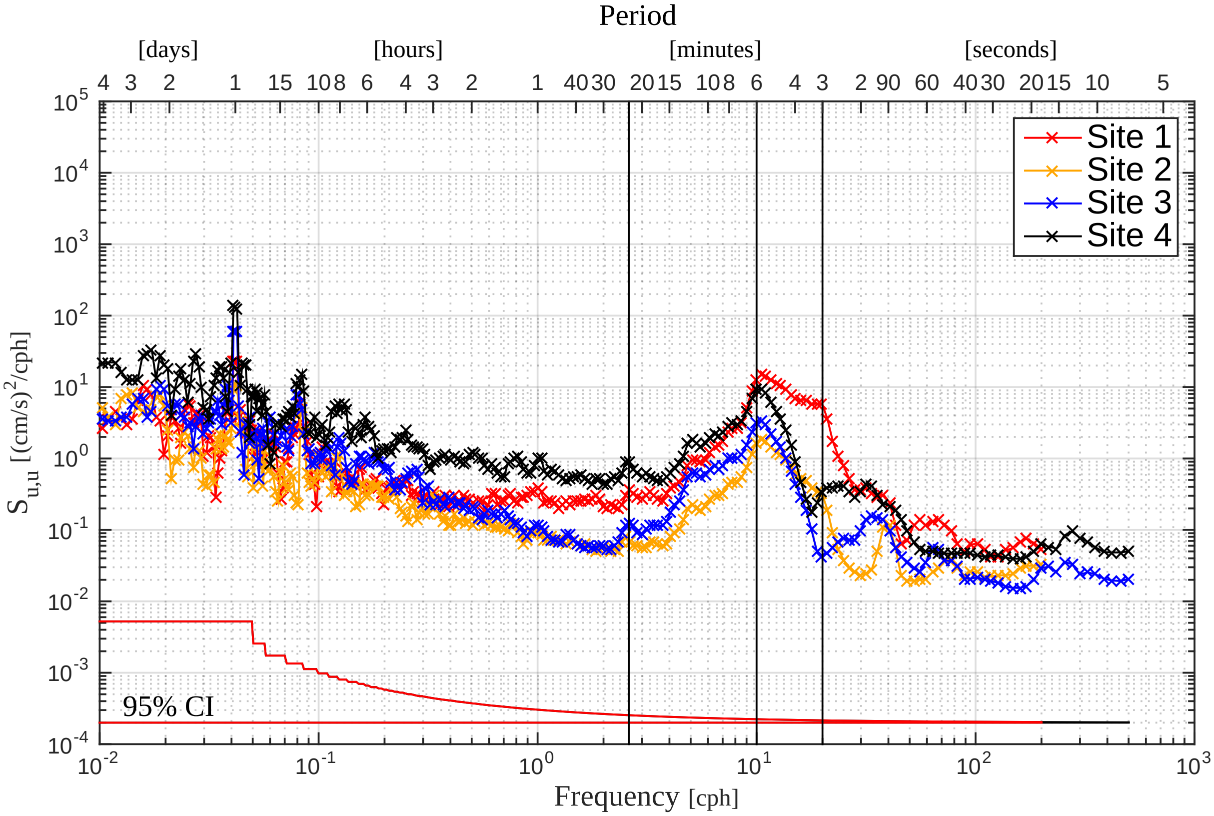

Figure 3.3: Power spectral density of observed current (aligned along major ellipse axis) at the locations of the four sensors inside Hale'iwa Harbor during 11/28/13 - 01/20/14. The 95% confidence interval for each independent spectrum estimate is shown at the bottom.

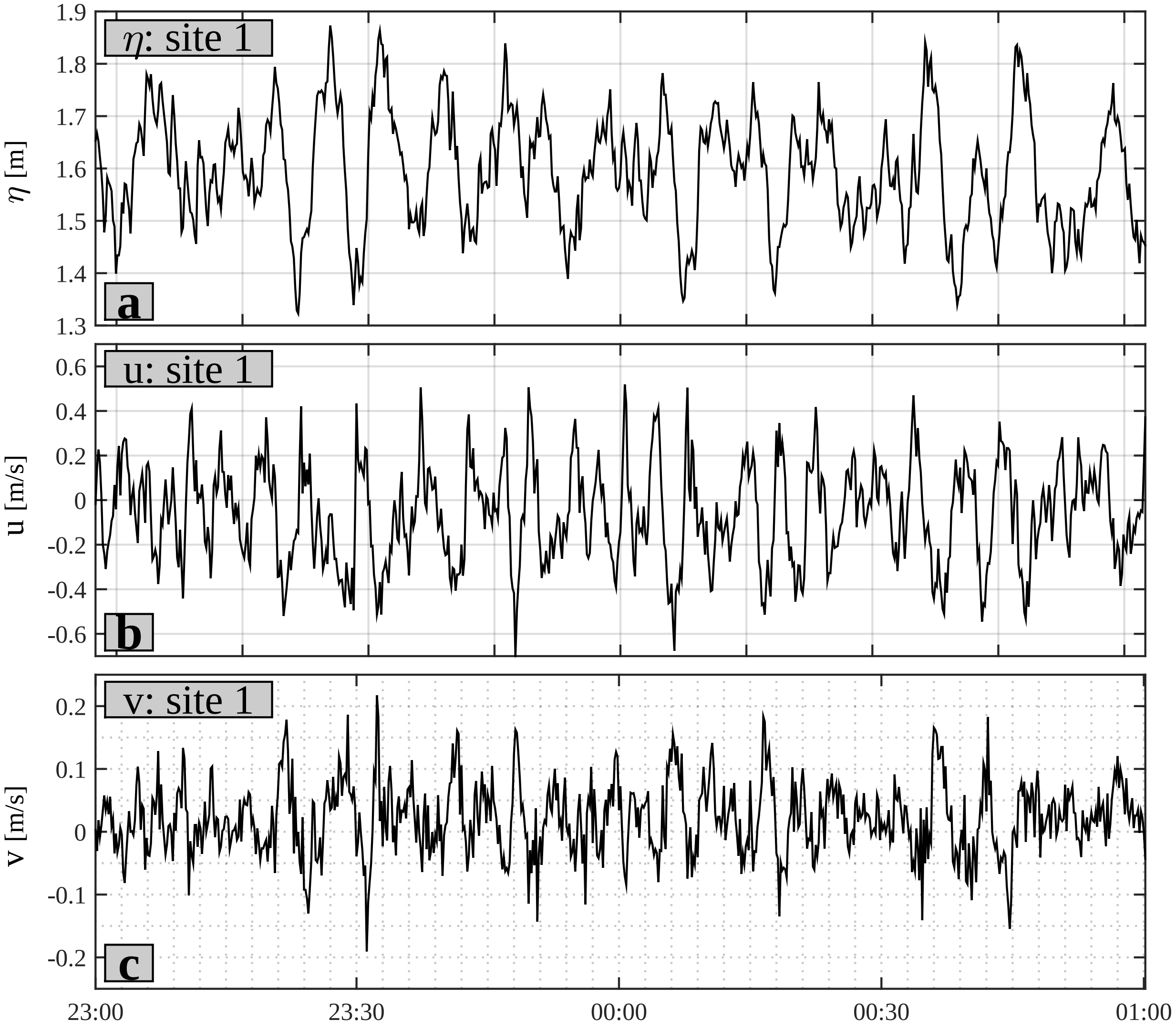

Figure 3.4: Two-hour long times series of (a) sea level; (b) u; and, (c) v, currents at site 1 inside Hale'wa Harbor, during a large SS event on 02/08/12 - 02/09/12. Note the longer period character of sea level variability as compared to the uv currents.

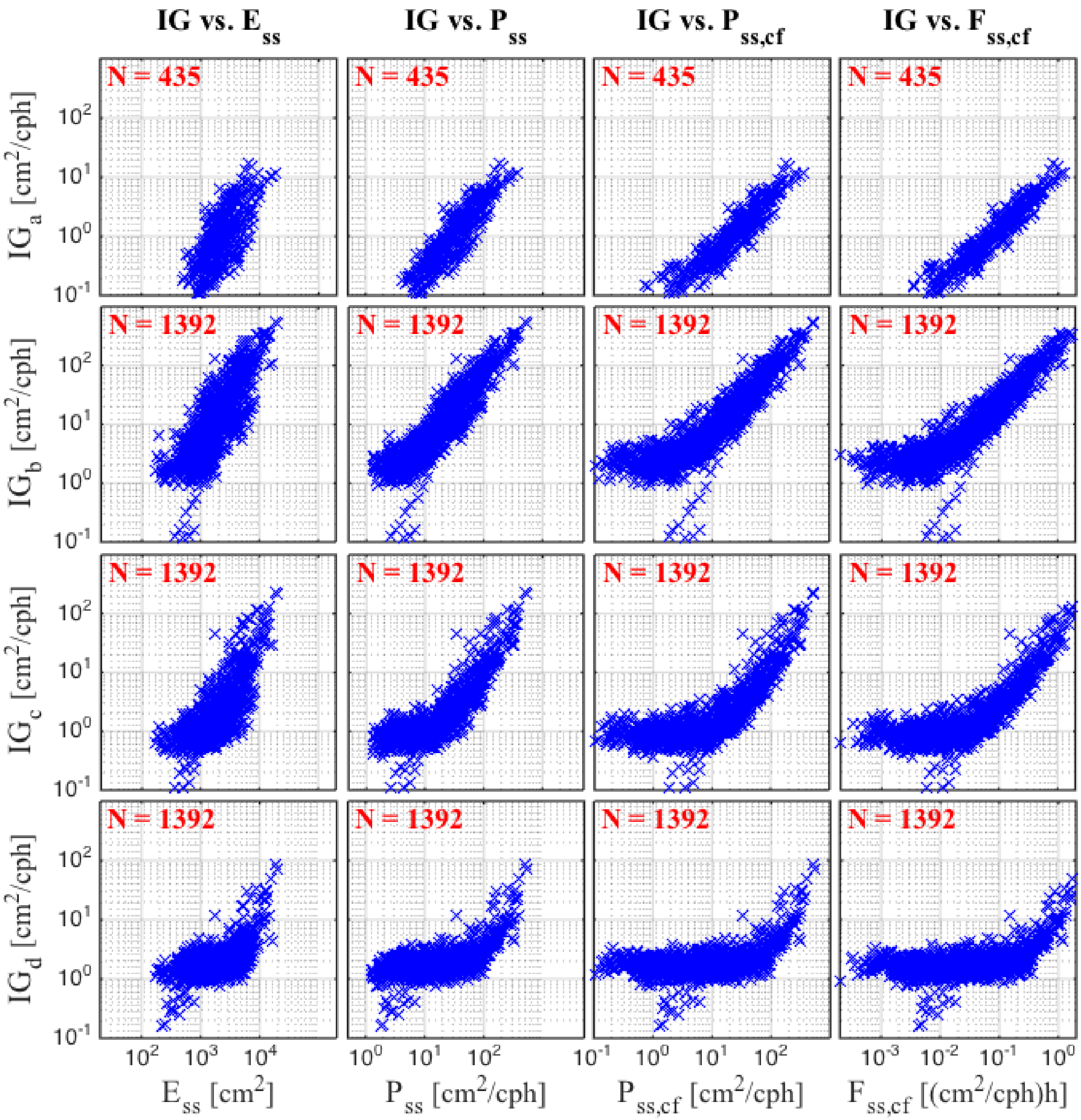

Figure 3.5: Scatter of IG-PSD vs. various sea/swell parameters. The number of data points plotted is shown at the top of each figure. The figure in the first row were generated using a four month long dataset, and the figures in rows 2-4 were generated using a year-long dataset from 2002.

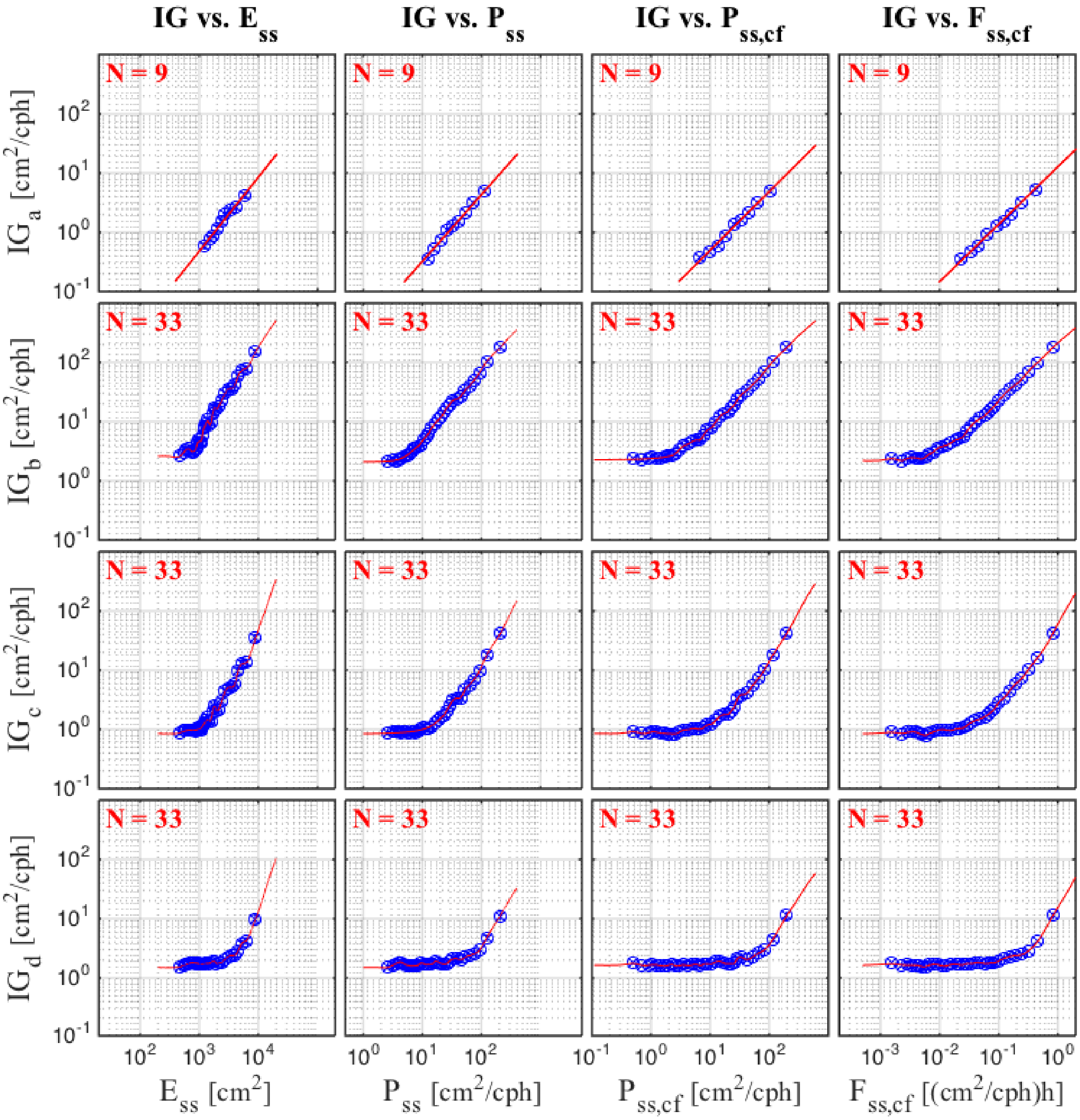

Figure 3.6: Scatter plots of IG-PSD vs. sea/swell parameters. The red curve was fitted to the data using piecewise interpolation technique. The figure in the first row were generated using a four month long dataset, and the figures in rows 2-4 were generated using a year-long dataset from 2002.

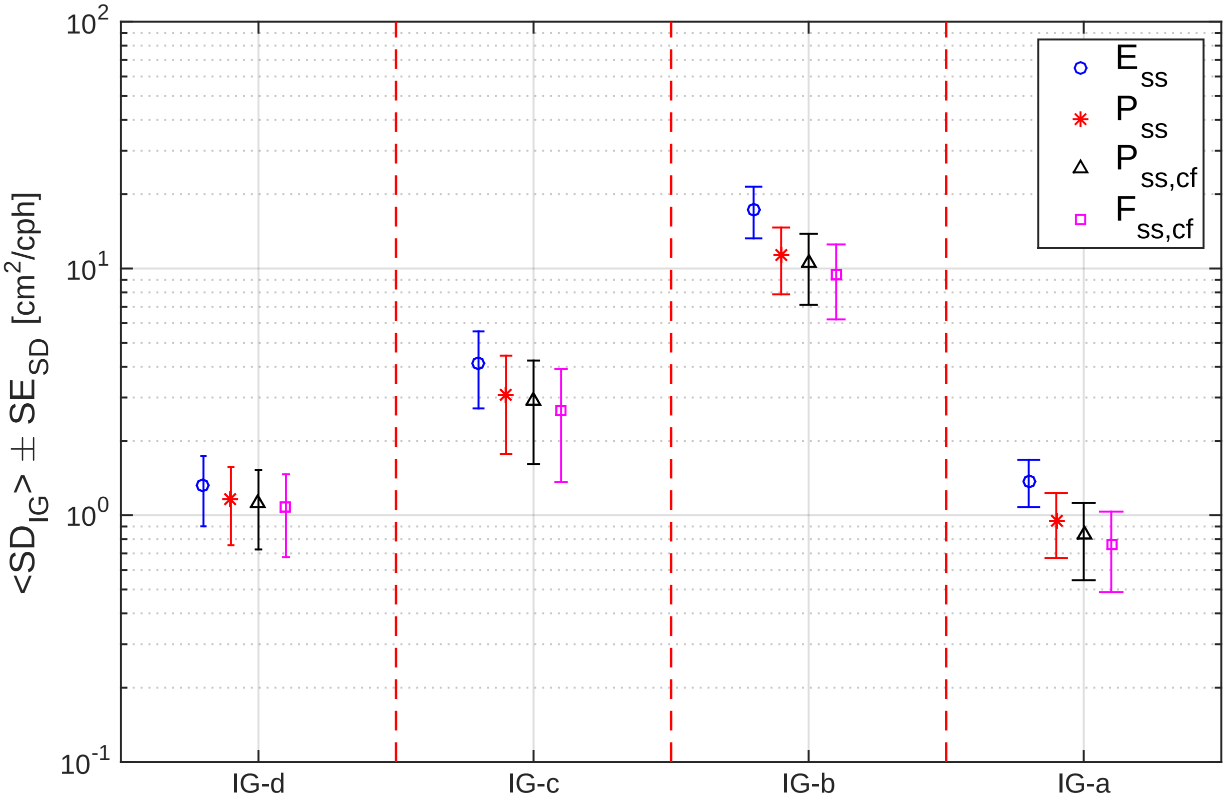

Figure 3.7: Mean IG standard deviation for each of the SS parameters.

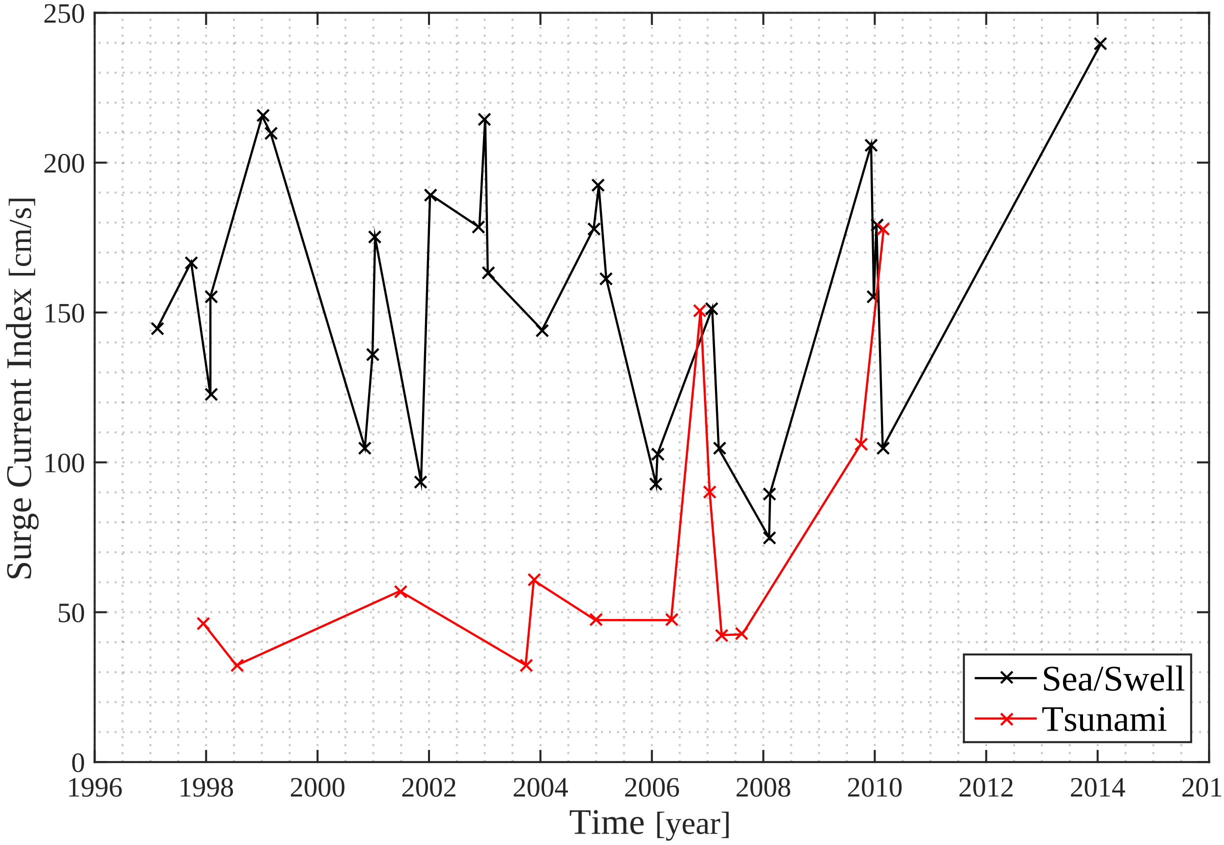

Figure 3.8: SCI of all tsunamis and two strongest SS events per year during 1997-2010, and one strong SS event during 2014.

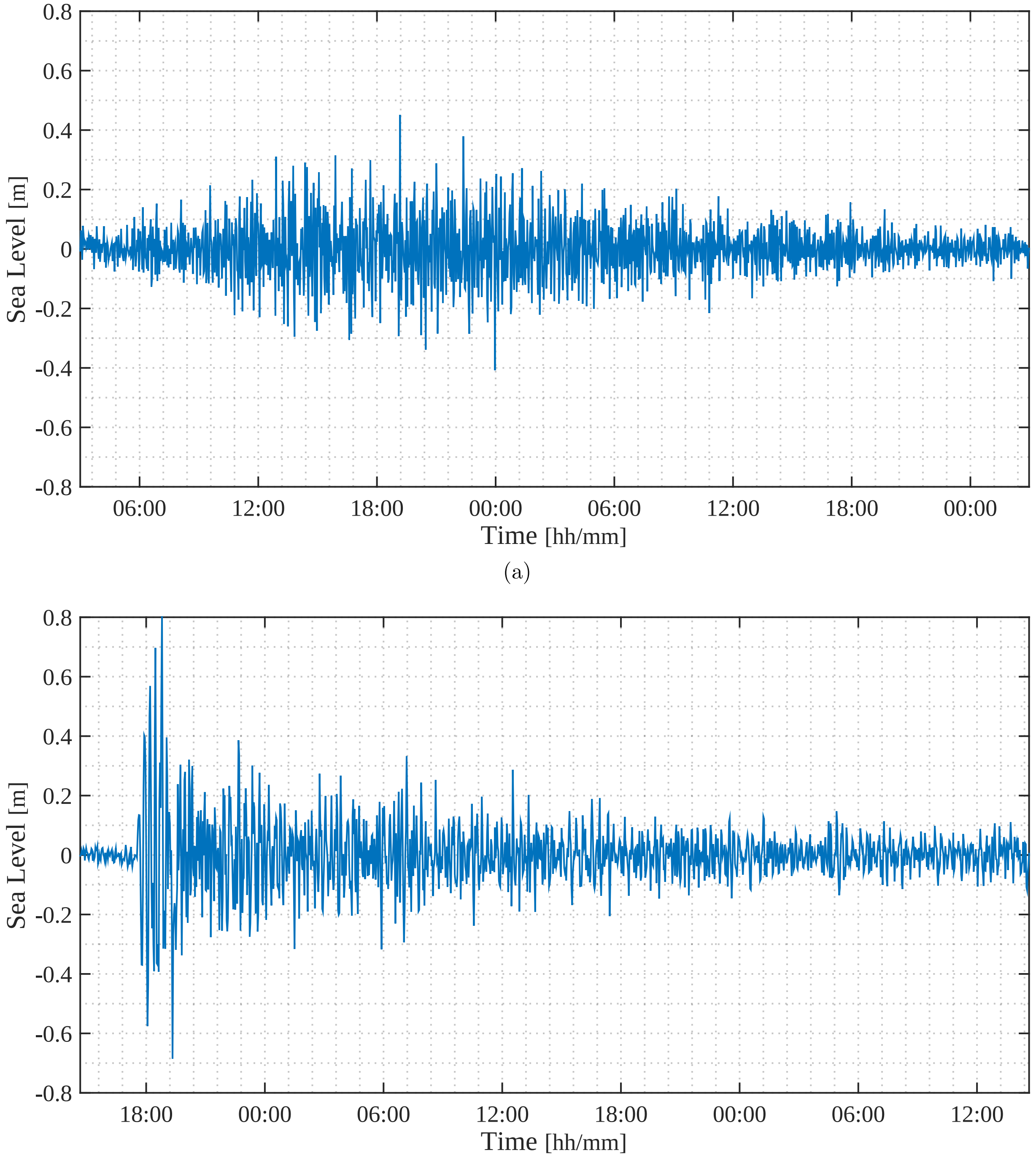

(a)

(b)

Figure 3.9: High-pass filtered sea level time series on the western side of Hale'iwa Harbor during (a) 12/25/2009 SS event; and, (b) 11/15/06 tsunami event. The maximum sea level swings nearly reaching 0.75 m. SCI = 155 cm/s for the SS event, and 1.2 m. SCI = 151 cm/s. for the tsunami event.

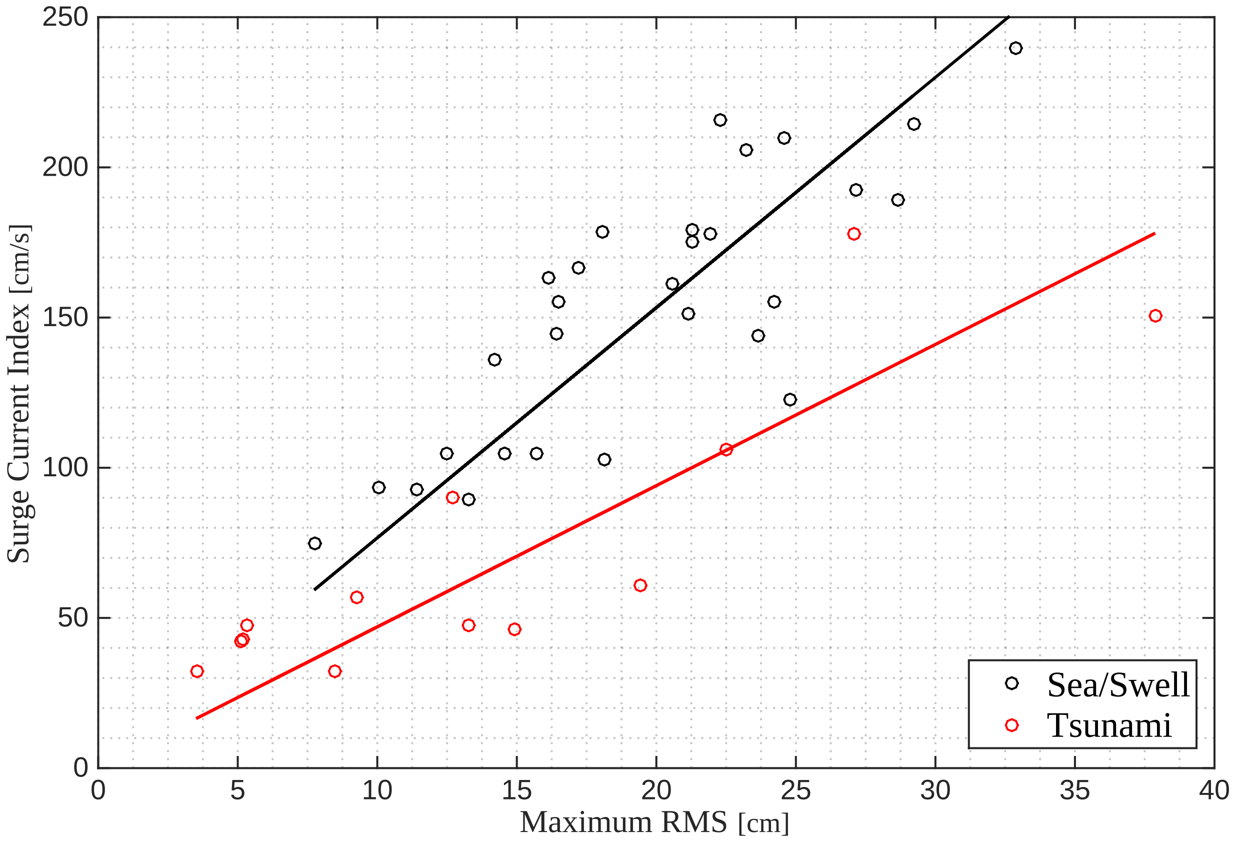

Figure 3.10: SCI versus maximum root-mean-square of all tsunamis and two strongest SS events per year during 1997-2010, and one strong SS event during 2014. The correlations of the line fits are: 0.86, and 0.79, for the tsunami and SS cases, respectively. The slopes of the fitted lines are: 4.70 ± 0.89 s^{-1}, and 7.70 ± 0.54 s^{-1}, for the tsunami and SS cases, respectively. The ratio of tsunami to SS slopes is: 0.61.

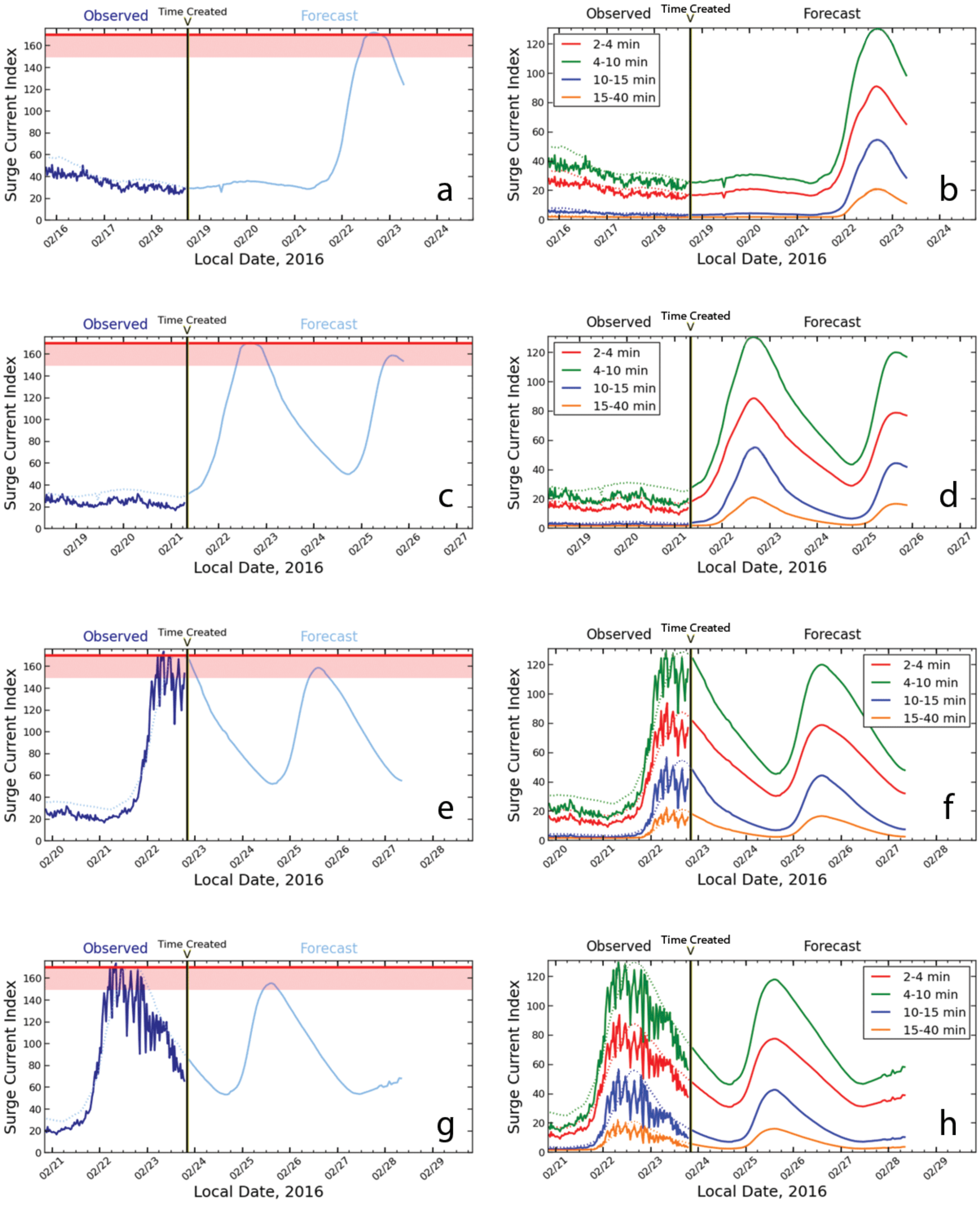

Figure 3.11: Forecast (rows 1 and 2), nowcast (row 3), and hindcast (row 4) of Hale'iwa Harbor SCI for the 02/22/2016 (local date) swell event. Left column: SCI in 2-40 min period band. Right column: SCI in 2-4, 4-10, 10-15, and 15-40 min period bands.

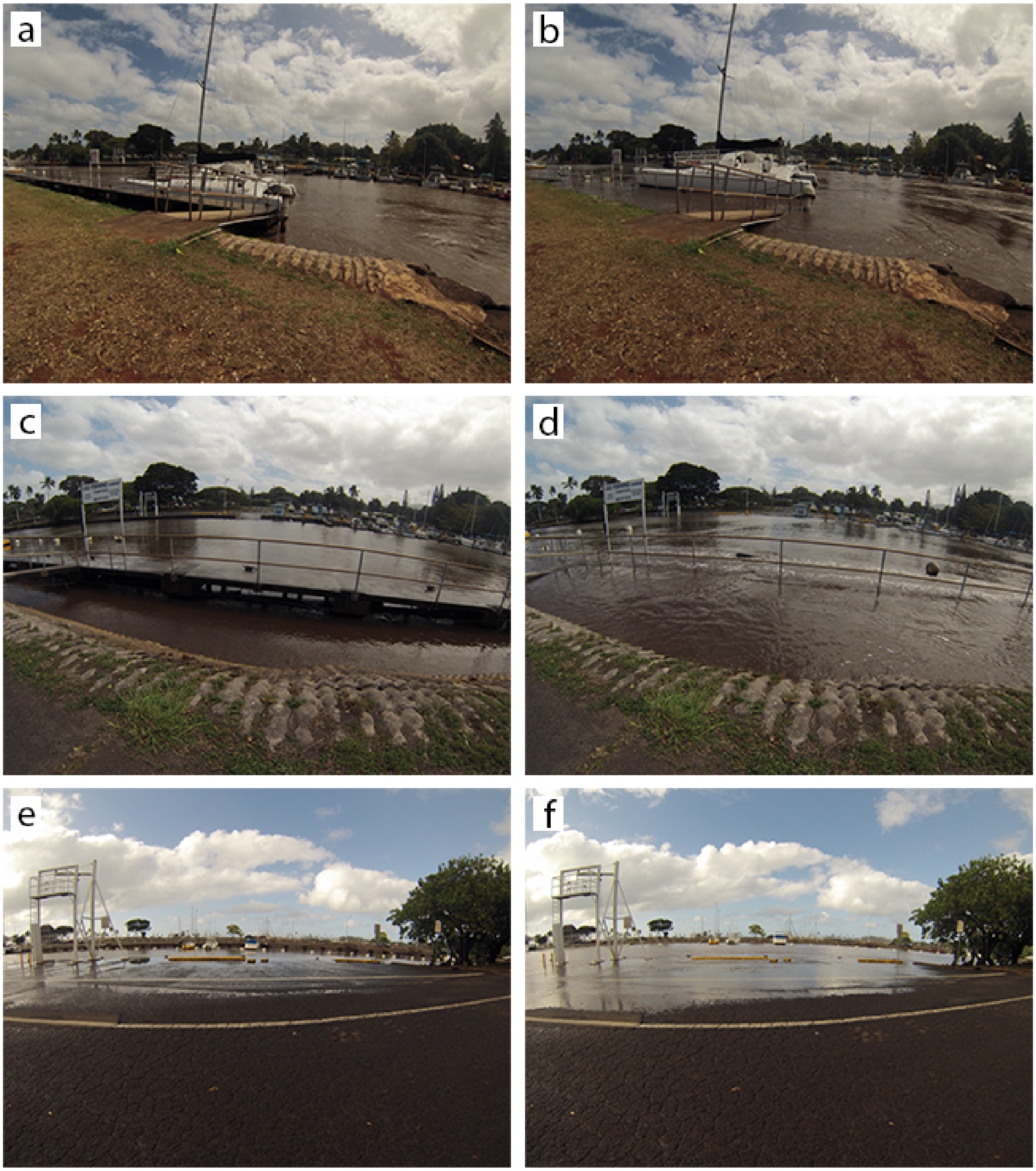

Figure 3.12: Impact of surges in Hale'iwa Harbor during the 02/22/16 SS event. All pictures were taken at the southern-most extension of the harbor. Times of low/high sea level are seen on the left/right column.

CHAPTER 4
INFRAGRAVITY OSCILLATIONS IN HALE'IWA HARBOR REGION, HAWAI'I. PART II: NUMERICAL MODELING

4.1 Introduction

The important role that infragravity (IG) waves play in nearshore coastal processes have attracted many researchers to apply various observational and laboratory studies. Nevertheless, the role of numerical modeling has become increasingly important as it allows for high spatial and temporal resolution that in many cases may not be feasible or even possible using observations or laboratory settings. Certain numerical models can also be used to identify the mechanisms by which IG waves are generated at particular coastal sites.

Numerical model studies of long waves are typically done using linear or non-linear models. The linear models generate solutions relatively fast, but a major disadvantage of such models is that they involve various assumptions and they cannot account for long wave generation by non-linear interactions. These models require the direction and period of a long wave as an input. Non-linear Boussinesq-type models contain information regarding the physics of the waves and are computationally more expensive than linear models. Taking wave dispersion into account, these models propagate the short waves throughout the computational domain and long waves are generated by non-linear wave-wave interactions. They require a short-period wave field as an input. What follows is a literature summary of various studies that have applied numerical modeling to learn about IG waves in harbors and along coastlines.

Linear models were employed in several studies. *Briggs et al.* (1994) have used HARBD, a linear, steady-state finite-element model, that solves a generalized Helmholtz equation in the frequency domain. They used the model to identify the modes of oscillations of Barbers Point Harbor (O'ahu, Hawai'i), and tested several proposed modifications that can potentially reduce the amplifications inside the harbor. *Thompson et al.* (1996) employed the same model for a similar study at Kahului Harbor (Maui, Hawai'i). This model was also used by *Okihiro et al.* (1993) to study harbor oscillations in Barbers Point Harbor, Hawai'i. When compared to observations inside the harbor, they found that the model was successful in reproducing the general spectral structure at different sites inside the harbor; however, the energy amplification factors between the different harbor sites and an offshore site were over-predicted at the gravest modes of oscillations. *Bellotti* (2007) added a source term to the Helmholtz equation of this linear model and attempted to quantify the transient response of harbor basins to modal IG oscillations. *Bellotti and Franco* (2011) used the same model together with field observations, in order to study the long wave field in a harbor.

Non-linear models have also been used in various harbor and coastal studies. The numerical models in the following studies are solved in the time-domain and are based on different variations of the Boussinesq equations, which account for wave non-linearity and dispersion. *Van Giffen* (2003) used Delft 3D's Surf Beat model to study IG motions in two harbors. He applied this model to Barbers Point Harbor, Hawai'i, and a bay in South Africa, but most of the work focused on studying Barbers Point Harbor. Using the model he determined the dominant oscillation periods in Barbers Point Harbor, and tested the effects of several suggested alterations to the harbor. *Douyere* (2003) used COULWAVE model to determine the resonant IG modes in Barbers Point Harbor (O'ahu, Hawai'i) and Kahului Harbor (Maui, Hawai'i). For Barbers Point, his results were found to be in good agreement with results from previous studies, but a large discrepancy was found when comparing with previous results from Kahului Harbor. This discrepancy is likely due to the fact that the previous studies involved linear models that treat the harbor boundaries as vertical walls, whereas COULWAVE model involves a swashing mechanism that allows for a moving boundary. Since $\sim 50\%$ of the boundary inside Kahului Harbor contains beaches, a proper modeling of the waterline inside the harbor could be critical. *Woo and Liu* (2004) studied the IG oscillations in harbors of different configurations. Comparison of the model results with experimental data showed good agreement, and when compared with another nonlinear model and a linear model, it appeared to perform better. *Dong et al.* (2013) used FUNWAVE2D model to study IG modal oscillations in a long rectangular harbor. They developed a simple analytical formulation to separate the IG wave field into bound and free waves, and used the numerical model to examine the proportion of these waves as a function of the periods of the incoming short waves. Using FUNWAVE, *McComb et al.* (2009) studied the IG wave field in Port Geraldton, Western Australia. They found that, once generated over the reef, refraction, diffraction, and reflection processes allow these IG waves to enter the harbor. The numerical model was also used to examine the effectiveness of a breakwater extension to reduce the IG wave energy entering the harbor. Their results suggested an optimal breakwater length that could reduce the IG wave penetration into the harbor by $\sim 30\%$.

González-Marco et al. (2008) modeled how a combination of short and long waves affects the harbor. They found that the harbor is quite efficient in preventing short waves from entering the harbor, but when the incident short wave trains were superimposed with long waves, significant IG activity entered the harbor, especially when the wavelength of the long waves was close to the harbor's natural modes. *Thotagamuwage and Pattiaratchi* (2014b) have used MIKE 21 model to study how the offshore topography influences IG oscillations in Two Rock Marina, Western Australia, under four different forcing conditions. As the waves propagated shoreward, the model results along a transect indicated that the short-wave energy decreased and IG energy increased. They attributed this result to the energy transfer from the short period to the long period waves.

In a coastal numerical study, *List* (1992) compared the relative importance between the bound wave release and the time-varying breakpoint mechanisms. He found that the amplitude of IG waves generated by the former mechanism are greater than the ones generated by the latter mechanism. *Breaker et al.* (2010) used ROMS model to study the natural oscillations of Monterrey Bay, California. The large model domain, high resolution grid spacing, and 3 hour long model runs in the study of *Thotagamuwage and Pattiaratchi* (2014b), allowed them also to look at the spatial distribution of IG waves at the coast in the 25-300 min period band. The solution revealed that most of the IG energy is located at the primary reef, $\sim$ 5 km offshore of the marina, distributed along the contour of the reef parallel to the coast.

In recent years, various studies attempted to learn about the response of coastal zones and harbors under tsunami forcing. *Munger and Cheung* (2008) used a nonlinear shallow-water model to examine the resonant response of the Hawaiian Islands to the 2006 Kuril Islands tsunami. The model results revealed the resonant coastal modes for O'ahu Island (in the 6-24 min period band), as well as several large scale inter-island oscillations (in the 27-42 min period band). *Cheung et al.* (2013) used NEOWAVE (Non-hydrostatic Evolution of Ocean Waves), a nonlinear shallow-water model that also accounts for weakly dispersive waves and flow discontinuities (*Yamazaki et al.* 2009). Under the forcing of the 2011 Tohoku tsunami, they found some of the resonant coastal modes that *Munger and Cheung* (2008) have found earlier for O'ahu Island, as well as inter-island modes in the 33-75 min period band. They also looked at the response inside and in the vicinity of several Hawaiian Harbors. *Roeber et al.* (2010) also used NEOWAVE and identified resonant coastal and shelf oscillations around Samoa Island, in response to the 2009 Samoa tsunami.

In this study we use the Boussinesq model BOSZ (*Roeber and Cheung* 2012) to better understand the spatial variability of IG waves in Hale'iwa Harbor and at the North Shore coast in the vicinity of the harbor. We will start by presenting results from several sensitivity tests, and results from additional runs will be presented and validated with some of the observational data that was presented in Chapter 2.

4.2 Model Description

The numerical model used in this study is called BOSZ, which stands for Boussinesq Ocean and Surf Zone model (*Roeber and Cheung* 2012). It is a phase-resolving model that models the flow of a nearshore wave field over highly irregular bathymetry. The model solves Boussinesq-type equations expressed in a conserved form in terms of the conserved variables: H, Hu, and Hv (where $H = h + \eta$ is the total water depth), instead of η, u, and v. This formulation handles non-linear processes, frequency dispersion, and shock-capturing (i.e., breaking waves). Discretized into rectangular cells with variables η, u, and v at the center of each cell, the governing equations are being solved using two methods: (i) finite-volume scheme: treats discontinuous processes such as wave breaking; and, (ii) finite-difference scheme: calculates dispersion and source terms. A bottom shear stress that is a function of the Manning roughness coefficient (n), is used to represent frictional drag with respect to the surface property of a material. A constant Manning roughness coefficient value is used in each of the model runs throughout this study. At the open ocean boundaries a $\sim$50 cell wide sponge layer is applied in order to damp out short waves that may potentially reflect from the domain boundaries. The resulting width of the sponge layer at each boundary is of the order of several hundred meters, which can effectively reduce potential reflection from outgoing short SS waves, but not long period IG waves.

4.3 Methods

4.3.1 Sensitivity tests

The sensitivity tests are done using simple spectral methods. Power spectral density (PSD) plots are used to test the sensitivity of the model results to the domain boundaries and run time. Maps of integrated energy and phase angle are used to show the spatial distribution of these quantities at the coast within the computational domain, for selected period bands. These IG period bands are determined based on spectral analysis from observations inside and outside Hale'iwa Harbor (see Chapter 2 for details). The 1-2 min, 2-4 min, 4-8 min, and 8-17 min period bands are centered on the periods that were observed in all of our sea level spectra inside the harbor (e.g., see Figs. 2.7, 2.19, and 2.20). The 0.5-1 min period band was included for completeness, and is not shown here in the sensitivity tests. For a given period band, the effect of the friction term on the model solutions is quantified by integrating the spectral energy over small bands of isobaths. The energy density and PSD calculations are done following the same procedures that were described in Chapter 2, Section 2.4.

4.3.2 Observations vs. model comparison

Comparisons between the numerical model and observational results are carried out by generating PSD, coherence amplitude, and coherence phase plots using BOSZ gauge outputs at selected sites at the coast and inside Hale'iwa Harbor. The PSD and coherence analyses are done following the same techniques that were described in Chapter 2, Section 2.4.

4.3.3 Hypotheses testing

The hypotheses that were formulated in Chapter 2 are tested here using PSD and coherence tools, as well as several other methods that are described in this section. A detailed description of the hypotheses is given in Chapter 2. The PSD and coherence analyses are done following the same techniques that were described in Chapter 2, Section 2.4.

4.3.3.1 Excitation of Linear Coastal or Harbor Modes (Hypotheses A1, B1, C1, A2, B2, & C2)

Following the observational analyses of Chapter 2 we identified 3 min (or, potentially ∼6 min) as a possible cutoff between harbor and coastal oscillations. Here, we use BOSZ to isolate Hale'iwa Harbor from the coastal region, and attempt to determine its normal modes. In addition, the model results are also used to provide us a look at the spatial distribution of the modes inside the harbor, something that is not possible to obtain with the limited number of observations we have. To do that, we use a small computational domain of 3m x 3m grid resolution that encloses the harbor and a small portion outside the harbor where the bathymetry is set to a constant value. A TMA directional spectra (*Hughes* 1984) with $H_{sig} = 2$ m and $T_p = 15$ sec, is used as an input to the wavemaker. The forcing will be acting over the domain for an hour, and propagate perpendicular to the outer entrance to the harbor. Various domain sizes are tested in order to assure us that any oscillations outside the harbor do not interfere with oscillations that originate from inside the harbor. The model runs with long and short extensions outside the harbor turned out to yield nearly identical results inside the harbor, suggesting that the solutions inside the harbor are not affected by these short segments outside of the harbor.

BOSZ is also used to look at the IG response of Hale'iwa Harbor and the coast to weak, moderate, and strong SS forcing, in order to see if it can reproduce some of the observed response. This, however, only allows us to look at oscillations at periods shorter than 2 hr, since the longest model run time used in this study is four hours. Increasing the model run time will allow to resolve longer period oscillations, but it will be at the expense of longer computational time. Taking these factors into account, a four-hour run time limit was decided following the sensitivity testing stage. In addition, the model domain sizes used in this study further restrict the validity of the solutions to periods shorter than ∼15-20 min, since the sponge layer is not efficient in attenuating long-waves at the boundaries; as a result, such long waves may potentially reflect from the boundaries and potentially resonate at periods that match the normal modes of the rectangular domain.

4.3.3.2 Bound Wave Impacts; Generation of Leaky and Edge Waves (Hypotheses B3, C3, C4, & C5)

To learn about the dynamics of the IG wave field on the North Shore, the dominant type of IG waves, and the dominant generation mechanisms, under strong SS forcing conditions, we force a BOSZ domain with strong SS forcing event. Using the model results we generate maps of energy, coherence amplitude squared (γ^2), and coherence phase ($\phi_{x,y}$). γ^2 and $\phi_{x,y}$ are calculated relative to a fixed reference point inside Hale'iwa Harbor.

In addition, spatial maps of energy flux are used to indicate the magnitude and direction of energy flow at the coast, in particular IG period bands. Following *Sheremet et al.* (2002), the net cross-shore energy flux is calculated using the sea level and cross-shore velocity data. In a similar way, the net alongshore energy flux is calculated using the sea level and alongshore velocity data. The resulting two-dimensional energy flux vector ($\vec{F}$) is:

$$\vec{F}(\xi) = (F_x(\xi), F_y(\xi)) = h \int_{f_1}^{f_2} df \big(Co(g\eta, u), Co(g\eta, v) \big), \tag{4.1}$$

where ξ is the geographical coordinate, h is the water depth, f_1 and f_2 are the low and high frequencies of the IG band of interest, respectively; g is the gravitational acceleration, Co is the one-sided co-spectral density, η is the sea level elevation, u is the cross-shore velocity (positive offshore), and v is the alongshore velocity (positive to the left of offshore).

We also separate the cross-shore energy flux into incoming and outgoing components to identify the portion of incoming flux that is radiated back offshore. Here we again follow the methods described in *Sheremet et al.* (2002). The incoming (+) and outgoing (-) energy fluxes integrated over a given period band ($F^{\pm}$), are calculated as follows:

$$F^{\pm} = \frac{\sqrt{gh}}{4} \int_{f_1}^{f_2} df \big[Co(\eta, \eta) + \frac{h}{g} Co(u, u) \pm 2\sqrt{\frac{h}{h}} Co(\eta, u) \big]. \tag{4.2}$$

The possible existence of IG edge waves is examined using BOSZ gauge data from carefully designed alongshore arrays (following the methodology described in *Davis and Regier* (1977)): one at Mokuleia, where observational data from a cross-shore array is available, and the other at Pua'ena Point, where the coastline is relatively straight and the bathymetric contours are relatively parallel to the coast. These alongshore arrays have a short alongshore extent relative to the the wavelengths of the IG waves of interest. To increase the spatial resolutions of these arrays, we employ the high resolution statistical method called the Maximum Likelihood Estimate (MLE), following the methodology that was described by *Oltman-Shay and Guza* (1987). The MLE of the variance ($\hat{E}$) as a function of wavenumber is:

$$\hat{E}(\omega, k) = \left\{ \sum_{i,j=1}^{n} \hat{M}_{i,j}^{-1} e^{ik|y_i - y_j|} \right\}^{-1}, \tag{4.3}$$

with the complex cross-spectral data matrix:

$$\hat{M}_{i,j} = \mathcal{F}\left\{ v(x, y_i, t) \right\} \mathcal{F}^{*}\left\{ v(x, y_j, t) \right\}, \tag{4.4}$$

where $\hat{E}$ is the MLE of the variance, ω is the radial frequency, k is the wavenumber, $\mathcal{F}$ is the Fourier transform operator and an asterisk denotes its complex conjugate, v is the alongshore velocity component, x is the distance from shore, and y_i is the i^{th} alongshore location. We compare the results with curves from the discrete edge wave dispersion relation that was theoretically derived by *Ursell* (1952) for a plane beach of slope β:

$$\omega^2 = gksin[(2n+1)\beta], \tag{4.5}$$

with the constraint:

$$(2n+1)\beta < \pi/2, \tag{4.6}$$

where $n = 0, 1, ...$ For a given site, Eq.(4.6) is being used to determine the highest possible edge wave mode n, given a slope β.

To identify bound waves and free IG waves that were released by bound waves, we look at the coherence amplitude and phase between the SS envelope and sea level at a given location. This analysis is done for a cross-shore array that is located at Waialua Bay, very close to Hale'iwa Harbor, in order to identify whether in the vicinity of the harbor the bound waves are released as free waves seaward, shoreward, or at, the breakpoint.

To find additional evidence of bound and free waves, a coherence analysis is applied between the SS sea-level envelope (η_{env}) and the sea-level (η), at single locations aligned in the cross-shore. We use model data from five BOSZ gauges located along a cross-shore line in Waialua Bay, located about 1.5 km west from the entrance to Hale'iwa Harbor.

4.3.3.3 The Role of Time-Varying, SS-Driven "Setup" (Hypothesis C6)

To setup hypothesis is tested using BOSZ the same way it was done with observations, except using high-frequency model output from multiple BOSZ gauges along the cross-shore line at Waialua Bay. A coherence analysis is applied between different pairs of these BOSZ gauges, and the possibility of a setup at the coast is examined using the coherence phase relationships. Due to the limited run time of the model (4 hours), the frequency resolution is limited and allows to resolve waves having periods as long as 2 hrs. However, as was mentioned earlier, the finite size of the domain along the North Shore of O'ahu likely limits the longest waves to 15-20 min (*Munger and Cheung* (2008) found the 24 min mode of oscillation to nearly cover the entire North Shore coast). The above suggest that BOSZ will allow us to address only a setup mechanism with periods shorter than $\sim$15-20 min. This means that here, hypothesis C6 ($T < 30$ min) can only be partially addressed using BOSZ, and hypothesis D1 ($T > 30$ min) cannot be addressed using BOSZ.

4.3.3.4 Large-Scale Modes of the Hawaiian Islands (Hypothesis D2)

This hypotheses cannot be addressed using the model runs in this study due to the restrictions mentioned above regarding the model run time and domain sizes used. These will confine the validity of the solutions to periods shorter than $\sim$15-20 min.

4.4 Analysis and Results

4.4.1 Sensitivity tests

4.4.1.1 Model setup and input

The numerical model requires the following inputs: (i) bathymetry and topography, (ii) directional spectra for the wavemaker, and (iii) model parameters. The bathymetry used in all model runs was synthesized by blending three different datasets of different grid resolutions. For the offshore region of the domain we used Multibeam Bathymetry dataset that was obtained from the Hawai'i Mapping Research Group (HMRG) at SOEST. The nearshore bathymetry dataset was obtained from the Scanning Hydrographic Operational Airborne Lidar Survey (SHOALS) that was conducted by the USACE on 2000. Although the Lidar bathymetry covers the bathymetry of Hale'iwa Harbor, the resolution inside the harbor is poor and the outline of the harbor is inexact. As a result, we obtained a high resolution bathymetry dataset from a survey done by the USACE on May 2009.

Unless indicated differently, in all of the following sensitivity test (ST) runs we used a given directional spectra taken from the peak of the strong 01/23/14 SS forcing event (at 06:55), at site 10 (see Fig. 2.2). The waves in all of these runs are allowed to propagate for 4 hours, and the first 20 min are ignored in order to exclude the time during which the model spins up until equilibrium has been reached. Hence, we are left with 3 hr 40 min of data to analyze.

Table 4.1 provides a summary of the specifications of all sensitivity test runs, excluding the first, preliminary, sensitivity test run (labeled: ST1). The different domains used for all model runs in this study are seen in Fig. 4.1. The domains with small, intermediate, and large alongshore extent are also labeled: ST2, ST3, and ST4, respectively (see continuous lines forming green, blue, and red rectangles in Fig. 4.1). The intermediate & narrow (labeled: ST5) domain has the same alongshore extent of the intermediate domain, except that it is shorter in the cross-shore (in Fig. 4.1, continuous lines forming blue rectangle with shorter cross-shore extent). Within each of these domains in Fig. 4.1 there are dotted lines forming rectangles, indicating a distance of 50 cells ($\sim$ 350 m for a 7m x 7m grid resolution) from the respective domain boundaries. For a given domain, the rectangular gap formed between the continuous and dotted line boundaries represent the region where model results are affected by the sponge layer. The large domain size is used to test scenarios of strong SS forcing with very weak (ST6; see Table 4.1) and very strong (ST7; see Table 4.1) friction coefficients, respectively.

In order to make quantitative comparisons among the outputs from the different model runs, as well as comparing model results with observations, we also sample the model output at higher frequencies at particular sites of interest. Hereafter we refer to these as *BOSZ gauge* sites. Red circle symbols in Fig. 4.1 indicate BOSZ gauge sites. Red square symbols indicate sites where observational data was available (sites 1-7, 8a-8c, 9, and 10), and BOSZ gauge data was also collected (sites 1-7 and 8a-8c).

Figs. 4.2-4.5 provide a closer look on the different regions from Fig. 4.1, showing more clearly the exact locations where high frequency model output was collected. From west to east, Fig. 4.2 shows the BOSZ gauges along the Mokuleia stretch of coast, Fig. 4.3 shows the BOSZ gauges in the vicinity of Kaiaka Bay, Fig. 4.4 shows the BOSZ gauges in Waialua Bay, including Hale'iwa Harbor sites, and Fig. 4.5 shows the BOSZ gauges from Pua'ena Point eastward. The black square symbols indicate sites where observational data was available (see Chapter 2 for more details).

4.4.1.2 Effect of varying computational time

In order to obtain good spectral resolution in the infragravity (IG) period bands of greatest interest (from sea level and currents data, it is the ∼3-8 min period band, according to Fig. 1.2), the model runs should be as long as possible. However, increasing the computation time may unintentionally develop artificial long-period oscillations that may potentially be amplified over time if these match the normal modes of the rectangular computational domain.

We examine such effects using the sea level model outputs at particular BOSZ gauge sites inside Hale'iwa Harbor and outside in its vicinity at the coast, and calculate the spectra from the first hour (1 hr, head), last hour (1 hr, tail), first two hours (2 hr, head), last two hours (2 hr, tail), and the entire record length (3 hr 40 min; excluding first 20 min of the 4 hr runs to avoid the model spinup time period), and compare them. For the purpose of evaluating the effects of various domain sizes on the model solution, the above is calculated for the large, intermediate, small, and intermediate & narrow runs (ST2 - ST5; see Table 4.1). Analysis of that aspect is examined in subsection 4.4.1.3.

The analyses for the different BOSZ gauges are seen in Fig. 4.6 for site 1, Fig. 4.7 for site 3, Fig. 4.8 for site W14, and Fig. 4.9 for site 7. The five panels in each figure are: (a) the first hour out of the 3 hr 40 min runs (1 hr, head); (b) the last hour out of the 3 hr 40 min runs (1 hr, tail); (c) the first two hours out of the 3 hr 40 min runs (2 hr, head); (d) the last two hours out of the 3 hr 40 min runs (2 hr, tail); and, (e) 3 hr 40 min model runs.

The PSD curves in panels a and b of Figs. 4.6- 4.9 can be used to compare the spectral content of the heads and tails of the 1 hr model runs. Qualitatively, we see that the main spectral features are the same at periods shorter than ∼1-2 min. In the case of the 2 hr model runs (see panels c and d), we see that the qualitative similarity between the heads and tails of the datasets is up to slightly longer periods of ∼3-5 min. This results from the fact that longer time series (2hr vs. 1hr in this case) will always have higher spectral resolution. The 3 hr 40 min runs (panels e) show that the longer run time indeed improves the spectral resolution and allows to resolve features up to longer periods. Nevertheless, it should be kept in mind that modal oscillations around ∼15-20 min and longer are most likely the result of model artifacts, since the wavelength of these long period waves are potentially on the order of the domain size, or longer. The model solutions from *Munger and Cheung* (2008) support this, showing that the mode structure of the 24 min oscillation has an alongshore scale greater than our large domain. Following what we have learned from these results we decided to use the 3 hr 40 min run time for the remaining analyses.

4.4.1.3 Effect of artificial oscillations from the domain boundaries

In all panels of Figs. 4.6-4.9 we see that the PSD curves of the different domain sizes appear to overlap each other at periods up to several minutes, with several exceptions. One exception is the PSD curve of the small domain, which tends to deviate from the curves of the remaining domains in many cases. This is possibly the result of the small alongshore extent that presents an alongshore limit on long wavelength/period waves. Waves having wavelengths longer than the alongshore distance between these boundaries will not be strongly amplified. Another exception arises from the effect of shortening the cross-shore extent, which is seen by comparing the curves of the intermediate and intermediate & narrow domains. We note some deviations between the two curves, several spectral peaks that are seen in the curve of intermediate domain but not in the curve of the other domain. These suggest that the model results are sensitive to the offshore location of the wavemaker.

We integrate the potential energy in the 1-2, 2-4, 4-8, and 8-17 min period bands and plot them as two-dimensional maps. The coherence phase (with a reference point located in the middle basin of the harbor) was averaged over these period bands and also plotted as maps. These maps provide a look at the spatial distribution of potential energy and coherence phase for the cases of model runs having small (ST2), intermediate (ST3), large (ST4), and intermediate & narrow (ST5) domains.

The spatial distribution and magnitude of the energy in the 1-2 min period band (Fig. 4.10) is nearly identical in all test runs. We also note that in all of these runs the energy levels are weakening in the sponge layers near the northeastern and southwestern boundaries. The corresponding coherence phase in Fig. 4.11 reveals complex patterns that are qualitatively consistent across all runs. In the inner portion of the domain near Hale'iwa Harbor, only the intermediate & narrow domain shows minor differences around Kaiaka Bay. Similar results are obtained for the 2-4 min period band (Figs. 4.12 and 4.13). The larger scale of the patterns is the result of the longer wavelengths in this period band. There are, however, various regions where the energy levels of the large domain appear to be smaller than the ones seen in the smaller domains. One plausible explanation for such an outcome is that in the smaller domains the smaller alongshore (and cross-shore, in the intermediate & narrow domain) distance between the boundaries results in less attenuation of reflected wave energy at the inner portions of the domain. The result is higher energy levels at particular locations within the inner portion of the domain. In the 4-8 min (Figs. 4.14 and 4.15), and 8-17 min (Figs. 4.16 and 4.17) period band cases, the larger scale energy patterns and corresponding coherence phases are qualitatively similar for all domain sizes, except the weaker energy levels in Waialua Bay in the small domain (see Fig. 4.16c), and higher energy levels in Kaiaka Bay in the intermediate & narrow domain (see Fig. 4.16d).

The analyses of these maps suggest that, overall, the potential energies and corresponding coherence phases are qualitatively consistent across all domains. This is seen for all four period bands in question here. Nevertheless, the smaller sizes of the intermediate, small, and intermediate & narrow domains, appear to be affecting the energy levels at the coastal regions near Hale'iwa Harbor (Waialua Bay and Kaiaka Bay). Furthermore, the energy levels near the northeastern and southwestern sides of all domains are greatly affected by the sponge layers. Naturally, the inner region of the coastal domain in the vicinity of Hale'iwa

Harbor is least affected by these sponge layers in the large domain. All of these results point to the large domain as the best candidate for further numerical model analyses.

4.4.1.4 Sensitivity to variation of the friction coefficient

In the following analysis the large domain is used with a Manning friction coefficient that is typical for the coral-reef/rock bottom in the Hawaiian Islands. Two additional model runs are carried out using the large domain, except with different Manning friction coefficients in order to test sensitivity of the model solutions to friction.

In Fig. 4.18 we have three panels showing the spatial distribution of potential energy in the 1-2 min period band for the cases of: (a) low friction ($n = 0.01$, ST6); (b) typical friction ($n = 0.035$, ST4); and, (c) high friction ($n = 0.1$, ST7) scenarios. For each of these scenarios of friction coefficients, the bottom right panel shows the potential energy integrated along the coast between adjacent isobaths separated by 1 m. What we will be referring hereafter as a "typical" Manning roughness coefficient ($n = 0.035$) was obtained by *Bretschneider et al.* (1986) who measured wind profiles over lava and coral reef surface types that are covered with vegetation. This Manning roughness coefficient value was used and found to yield realistic results in other studies in the Hawaiian Islands (e.g., *Roeber and Cheung* (2012)). Setting the friction to a very low value clearly adds a lot of energy at the coast, but the spatial distribution of energy at the coast have barely changed compared to the typical friction case (compare panels a and b). A similar comparison can be done between the typical and high friction cases (panels b and c, respectively). The energy levels in the strong friction case are very low, making it difficult to make a good comparison, but still many of the main features seen in the typical friction case can be identified in the high friction case. Comparing it with the maps of the 2-4 min (Fig. 4.19), 4-8 min (Fig. 4.20), and 8-17 min (Fig. 4.21) period bands, we arrive at the same conclusions.

The plots of energy vs. depth in Figs. 4.18-4.21 (bottom right panels) provide a quantitative way to compare the effect of friction in the cross-shore. In the 1-2 and 2-4 min period bands (bottom right panel in Figs. 4.18 and 4.19, respectively) we see that the energy levels with low and typical friction cases are very similar at all depths (compare black and blue curves). Differences in energy levels are seen in the high friction case near the coast and offshore (in Figs. 4.18 and 4.19, compare red curve to remaining curves). In the 4-8 min band (bottom right panel in Fig. 4.20), the energy vs. depth is weaker for all friction cases, but the relative differences between them did not change significantly. One exception is the energy level of the low friction case around 35 m depth, as it is the same as the level in the 2-4 min case. In the 8-17 min case (bottom right panel in Fig. 4.21), the energy level of the low friction case has increased offshore of the reef, between depths of $\sim 30-60$ m. This increase in energy is likely the result of the great amount of energy that is reflected at the coastline and radiated back offshore via the channels, especially through the channel offshore of Hale'iwa Harbor (as will be shown using energy flux analyses in subsection 4.4.3.2). For the typical and high friction cases, the energy levels in this period band have lowered, likely since the higher friction limits the offshore flow via the channels. Closest to the coast, a comparison of the different period bands shows that the relative energy levels among the three friction cases remains nearly constant at depths shallower than ~5 m.

4.4.2 Observations vs. model vs. comparison

4.4.2.1 Model setup and input

The sensitivity test results show that the best choice for the domain is the large one (ST4), as its boundaries are far enough from the middle part of the domain, therefore barely affecting the model solution in the vicinity of Hale'iwa Harbor. Nevertheless, at a relatively late stage of this study the importance of the observations from Mokuleia stretch of coast became more apparent, which eventually led us to slightly increase the large domain in order to include alongshore and cross-shore arrays of BOSZ gauges that overlap with the three observation sites at Mokuleia. This new domain is a westward-shifted version of the large domain and is longer in the alongshore and cross-shore directions. This is the purple domain seen in Fig. 4.1, and it will be used in the remainder of the analyses in this chapter, unless specified otherwise. Hereafter, it will be referred to as the largest domain. When compared to the sensitivity test results of the small, intermediate, large, and intermediate & narrow domains (not shown here), results from the largest domain were found to be most consistent with the ones of the large domain. In the following comparison of observations and model data, we use the directional spectra of the strong 01/23/14 SS event that was obtained from CDIP's Waimea Buoy (site 10 in Fig. 2.2), and is being applied as an input to the wavemaker. A 7m x 7m resolution computational grid is being used in the following comparisons.

4.4.2.2 Comparison with observations

Several comparisons are made between the model output data and observations, at several sites. This step is very important as it is used to calibrate and validate the model results with respect to the observations.

To calibrate the model results we selected several sites where observations were available and compared the PSD levels of the observed sea level (η) data with the corresponding model data for the three scenarios of friction coefficients (low, typical, and high). Under very strong SS conditions, Figs. 4.22 and 4.23 show such comparison for observational sites 3 and 4 inside the harbor. Aside from the clear difference seen between the spectral levels of the curves under low ($n = 0.01$), typical ($n = 0.035$), and high ($n = 0.1$) friction (n is the Manning roughness coefficient), we note that the best qualitative overlap between observations (green curve) and the model PSDs is obtained for the case of typical friction (blue curve, $n = 0.035$). The same comparison at site 7 on the coast is seen in Fig. 4.24. Here it appears as if the PSD of the typical ($n = 0.035$) and strong ($n = 0.1$) friction cases could be used to represent the observed PSD levels, but a closer look at the PSDs suggests that the general trend in the case of typical friction with $n = 0.035$ is more similar to the observed PSD.

The above comparisons show that running the BOSZ model with a Manning roughness coefficient of $n = 0.035$ reproduced spectral levels that are comparable to the ones observed in the harbor and at the coast (although at the coast there appears to be some model over-prediction). We therefore use a Manning roughness coefficient value of $n = 0.035$ for the remainder of the analysis in this chapter.

We now compare the model (with $n = 0.035$) and observed spectra of η at various observational sites to see whether the model is capable of reproducing the spectral details that we observe. A comparison of the model and observed PSDs of η at sites 1, 2, 4, 5, 6, and 7, during strong SS events, is seen in Fig. 4.25. Inside the harbor (panels a-d), the model seems to capture the main spectral structure of the observed spectra, especially at sites 2, 4, and 5 (except for some over-prediction at site 5). At the coast (panels e, f), the model is successful in reproducing the main spectral peak of the SS forcing (i.e., around 15 sec), and the general spectral levels are in good agreement (except for some over-prediction at site 7). At IG periods at the coast, both the observed and modeled spectra appear to be noisy and contain features that are mostly statistically insignificant. Overall, the model tends to slightly over-predict the spectra levels, with greatest discrepancies seen at sites 5 and 7.

A coherence analysis was carried out between sea level (η) datasets of several pairs of sites. In Fig. 4.26 we see the coherence amplitude and coherence phase inside the harbor for the pairs of sites 1 vs. 2 (panels a and b), and 1 vs. 4 (panels c and d). In both cases, the model captures very well the observed peaks and valleys in coherence amplitude. From long to short periods, it also captures very well the initial phase change in the observed coherence phase (around a period of 4-5 min). The subsequent phase changes in the model follow the trends seen in the observations. In Fig. 4.27 we see very good agreement between the model and observed coherence for sites 1 vs. 5. The agreement appears to deteriorate as we look at the coherence between harbor site 1 and coastal site 6 (Fig. 4.27), likely because of the greater distance between the two sites.

4.4.3 Hypotheses testing

In this section, BOSZ is used to address the hypotheses from Chapter 2, in order to clarify and improve on the results that were obtained using observations. The model setup and input used here are the same as the ones from the previous section (comparisons of model vs. observations).

4.4.3.1 Excitation of Linear Coastal or Harbor Modes (Hypotheses A1, B1, C1, A2, B2, & C2)

The observational results of Chapter 2 provided evidence that Hale'iwa Harbor and the coast have their own sets of normal modes, and the approximate period of ∼3 min (or, potentially ∼6 min) likely separating the two systems. In this section, we use BOSZ to further explore these observational results by isolating the domain of the harbor from the coast, and force it in an attempt to excite and identify the normal modes of the harbor. We also use the model to provide a look at the spatial distribution of the modes inside the harbor. Using sea level model output we look at the spatial distribution of the potential energy ($E_{\eta,\eta}$), coherence amplitude squared (γ^2), and coherence phase (ϕ_{η,η_r}, where the subscript "r" refers to a reference point), and search for any signatures of standing oscillations inside the harbor. We identify a mode structure by looking for regions of sharp transitions between high and low $E_{\eta,\eta}$ and/or γ^2, accompanied by sharp 180° transitions in the corresponding ϕ_{η,η_r}.

We isolate a small domain that contains Hale'iwa Harbor and a small portion outside the harbor (extending ∼300 m north of the harbor's outer entrance, in order to allow proper setting to the wavemaker), and force it with a TMA wave spectrum having $H_{sig} = 2$ m, and $T_p = 15$ s, and arriving from straight north, perpendicular to the harbor entrance (run R7 in Table 4.1). In Fig. 4.28 we see maps of energy, coherence amplitude squared (γ^2), and coherence phase (ϕ_{η,η_r}), in the 0.5-1, 1-2, 2-4, 4-8, and 8-17 min period bands. A complex structure of modes consisting of nodes and antinodes is clearly seen at periods shorter than 4 minutes. We identify a node where γ^2 is near zero, and the corresponding values of ϕ_{η,η_r} jump by 180°. In the 4-8 min period band, nearly the entire harbor (inner and middle basins, and part of the outer basin) is in phase and it seems like there is a relatively sharp 180° change in ϕ_{η,η_r} around the middle of the outer basin. At this location, γ^2 also has a relatively strong minimum suggesting that there may be a node in that basin. In the 8-17 min period band, the harbor appears to be highly coherent with the region outside the harbor, and the phase is uniform all across the domain. This suggests that there are no harbor modes in this period band. These numerical modeling results seen in Fig. 4.28 lead to the conclusion that the gravest mode of Hale'iwa Harbor potentially lies within the 4-8 min period band. The spatial structure of this gravest harbor mode is the one of a quarter-wave Helmholtz mode, where the node (that would normally be found at the entrance of a harbor of simple shape) occupies much of the outer basin of the harbor. This grave harbor mode is followed by a three-quarter wave rocking mode in the 2-4 min period band. In the observational study (Chapter 2), the PSDs inside the harbor (e.g., Fig. 2.9), and the coherence analysis between a site inside the harbor and another one at the coast (e.g., Fig. 2.23), provided evidence that the gravest mode of the harbor is likely around 3 min. However, the coherence analysis between observations at two sites inside the harbor (sites 1 vs. 5 in Fig. 2.41) suggested that the gravest mode of the harbor could potentially be around ∼6 min, in agreement with the present numerical modeling result of Fig. 4.28 that reveals a harbor mode in the 4-8 min period band.

It is possible to obtain a crude estimate of the gravest mode of a basin with dimensions similar to the ones of Hale'iwa Harbor. If we consider that the harbor is a rectangular basin of constant depth, we can estimate the period of the gravest mode using the following analytical expression (*Rabinovich* 2009):

$$T_{n,m} = \frac{2}{\sqrt{gH\left[\left(\frac{n}{L_x}\right)^2+\left(\frac{m}{L_y}\right)^2\right]}}, \tag{4.7}$$

where g is the gravitational acceleration, H is a constant water depth, L_x, L_y are the lengths of the basin in the x and y directions, respectively, and $n, m = 0, 1, 2, 3 \ldots$. Using Eq.(4.7) with a constant water depth of $h = 4$m, $L_x = 250$m, $L_y = 450$m, and setting $n, m = 0, 1$ to obtain the gravest mode of oscillation, we obtain $T_{0,1} = 144$ sec, which is much shorter than the potentially ∼6 min mode. One problem with Eq.(4.7) is that it does not take into account the fact that the harbor is not an entirely closed basin, it is open on the ocean side. We therefore try another estimate where we assume that the harbor is a long and narrow open-ended channel. An analytical expression for this case is (*Rabinovich* 2009):

$$T_n = \frac{4L}{2n + 1\sqrt{gH}}, \tag{4.8}$$

where L is the length of the channel. Using Eq.(4.8) with a constant water depth of $h = 4$m, we obtain for the gravest mode $T_0 = 287$ sec, for a channel length of $L = 450$m, and $T_0 = 319$ sec, for a channel length of $L = 500$m. These estimated grave mode periods are within the 4-8 min band and are consistent with the mode that was observed around ∼6 min.

We would also like to address whether BOSZ is able to reproduce the spectral content and relative spectral levels that we observe inside and outside Hale'iwa Harbor under weak, moderate, and strong SS forcing conditions (e.g., Fig. 2.7). In Fig. 4.29 we see such a comparison inside and outside the harbor, using results from 4-hour long model runs (generated by forcing the largest domain) that were forced with weak (03/28/14, blue curves), moderate (12/22/13, green curves), and strong (01/23/14, red curve) SS events. Inside Hale'iwa Harbor, we see that the model is able to capture the main observed spectral peaks (e.g., 6 min, ∼1.5-2 min, and ∼1 min), with remarkably similar spectral levels under all three SS forcing scenarios. Outside the harbor, the model agrees with the observations as it shows lack of spectral peaks; however, under strong SS forcing conditions the model overestimates the spectral levels by a factor of ∼2-4, suggesting that at these greater depths of the reef, slightly different friction parameter values should be used. Both inside and outside the harbor the relative spectral levels of the model under weak, moderate, and strong SS forcing, are in good agreement with the observations.

Results from the above auto- and cross-spectral analyses, provided evidence that Hale'iwa Harbor has its own set of normal modes that are independent of the coast. We find that the gravest (quarter wave) harbor mode potentially lies in the 4-8 min period band, a result that is also supported by an observational result inside the harbor that points out to the ∼6 min as potentially being the band where the gravest harbor mode lies.

Forcing the model with weak, moderate, and strong SS forcing conditions at a site inside the harbor and another site outside, resulted in relative spectral levels that are very similar to the observed ones, with a slight tendency of the model to over-predict. Inside the harbor, the model was able to capture all of the dominant spectral peaks that were observed. At the coast, the spectra generated by the model appears to be noisy and it does not reveal any statistically significant features. This result is also consistent with the observations.

4.4.3.2 Bound Wave Impacts; Generation of Leaky and Edge Waves (Hypotheses B3, C3, C4, & C5)

The observations used in the analyses of Chapter 2 were obtained from a small number of sites and from locations that are not ideal for the purpose of fully addressing the hypotheses in this study. In this section, we use numerical model results of BOSZ to generate energy and coherence maps of our North Shore domain, in order to improve our understanding of the IG generation mechanisms, the IG wave dynamics, and the types of IG waves that dominate in this coastal region. The potential energy and coherence analyses will allow us to identify spatial patterns in different IG period bands. Maps of net energy flux will help us determine the direction and magnitude of energy flow at the coast and inside the harbor. Breaking down the energy flux into the incoming and outgoing components will help us identify regions over the reef where reflection is strong. Applying the Maximum Likelihood Estimate (MLE) method to two different alongshore arrays along the coast we also try to obtain evidence for the existence of edge waves. If the MLE in a certain region provides weak evidence for the existence of edge waves, and the energy flux indicates a net flow that is predominantly perpendicular to the coast and is also reflective, it would suggest that the free IG wave field may be predominantly in the form of leaky waves.

In the following analyses, the largest model domain is being forced with observed directional spectra of the strong SS forcing event from 01/23/14 (R2 in Table 4.1). Results from additional SS events representing weak, moderate, and strong forcing, are shown towards the end of this section. The details of all model runs are summarized in Table 4.1. The directional spectra of the different SS forcing events are plotted in Fig. 4.30 (see panels a, b, c). The outputs from these model runs are being used to generate plots of energy (potential, $E_{\eta,\eta}$, and total, E_{tot}), coherence amplitude squared (γ^2), coherence phase (relative to a reference point, ϕ_{η,η_r}) and energy fluxes (net, $\vec{F}$, and incoming/outgoing $F^{\pm}$). After examining several possible reference points for the coherence analysis (two inside and one outside Hale'iwa Harbor), we chose our reference point to be inside the harbor, in the middle of the main basin, away from nodes. The exact location of the reference point is indicated with a gray circle on all γ^2 and ϕ_{η,η_r} plots.

In Fig. 4.31 we see $E_{\eta,\eta}$, γ^2, and ϕ_{η,η_r}, in the 5-30 sec SS period band. The greatest energy is found offshore and it rapidly dissipates as these short waves shoal and break. Due to the very short wavelengths in this period band, the corresponding γ^2 and ϕ_{η,η_r} do not reveal any interesting relationships. ϕ_{η,η_r} is simply showing a pattern of propagating waves.

Fig. 4.32 shows $E_{\eta,\eta}$, γ^2 and ϕ_{η,η_r}, in the 0.5-1 min period band. An interesting feature that can be identified in $E_{\eta,\eta}$ is a sharp band of minimum energy that stretches along the entire coastline, but is more clearly seen along the Mokuleia stretch of coast (west of Kaiaka Bay). In the cross-shore direction it is bounded by a narrow energy maximum on the land side and in the offshore it is followed by several energy highs and lows. This alternating pattern appears to extend several hundred meters offshore (see ϕ_{η,η_r} in Fig. 4.32).

The same plot for the 1-2 min period band is seen in Fig. 4.33. Here we also see the same pattern of highs and lows, extending away from the coast all the way to where the slope of the bathymetry increases drastically, $\sim$1 km from the coast (see Fig. 2.46). The pattern is most apparent in Pua'ena Point region, the corner just north of Hale'iwa Harbor.

One possible explanation for these alternating cross-shore patterns is that these are low-mode edge waves, since these have a maximum in sea level at the coast, as can be seen here in $E_{\eta,\eta}$. Another possibility is that there is a strong reflection of IG waves at the coast, creating standing wave patterns in the cross-shore. This can be generated by leaky waves, as these are known to be reflected back offshore but are not trapped to a cross-shore band along the coastline as edge waves. Looking at the plot of γ^2, around Hale'iwa Harbor we see an alternating pattern of highs and lows with an alongshore symmetry. The signal is strongest inside the harbor since the reference point for the coherence analyses was chosen to be in the middle basin. Looking at ϕ_{η,η_r}, we see that the alongshore symmetry extends along the entire coastline in the domain. We also note that the lows that appear in $E_{\eta,\eta}$ and γ^2 inside and outside the harbor coincide with rapid $\sim 180°$ changes in ϕ_{η,η_r}, suggesting that these regions are most likely the nodes of standing IG waves. We also see that the rapid $\sim 180°$ change in ϕ_{η,η_r} appears along the coastline at a distance from shore that matches the long band of $E_{\eta,\eta}$ minimum near the coast, supporting our belief that it is part of a modal structure.

Very similar conclusions can be drawn from the corresponding plots of the 2-4 min period band (see Fig. 4.34), except that the cross-shore scale of these alongshore features of highs and lows is larger, since the wavelengths in this period band are longer.

The same results for the 4-8 min period band show much larger scale features (see Fig. 4.35), and the highs in $E_{\eta,\eta}$ are now broader (in the offshore direction) at the coast, and there is only one more low in $E_{\eta,\eta}$ between the coastal high and another high at the fore-reef zone. γ^2, and ϕ_{η,η_r} also show that a large section of the coast is coherent and in phase, extending from the channel outside Kaiaka Bay to slightly up the coast from Pua'ena Point. At these two boundaries there is a rapid $\sim 180°$ phase change.

In the 8-17 min band (see Fig. 4.36) we see high levels of $E_{\eta,\eta}$ at the coast, that gradually decrease going offshore. γ^2 and ϕ_{η,η_r} also reveal an interesting large-scale modal structure, with two clear nodes that are located at the channel offshore of Mokuleia, and the channel just west of Kaiaka Bay. $E_{\eta,\eta}$ and γ^2 at these channels reach minimal values, and ϕ_{η,η_r} changes rapidly by $\sim 180°$, an indication of nodes.

To get a more detailed look on what happens inside Hale'iwa Harbor and whether the IG oscillations are connected to the coast at the short period bands: 0.5-1, 1-2, and 2-4 min, we generated zoomed-in versions of the above plots. Fig. 4.37 is such a plot for the 0.5-1 min period band. Right outside the harbor we see a complex pattern of nodes and antinodes with an alongshore symmetry. A similar pattern can be seen in the 1-2 min period band, in Fig. 4.38. The node at the outer basin of the harbor (between the ends of the two breakwaters), and the one just south of the inner harbor entrance, appear to be extensions of nodes that stretch along the coast outside the harbor. This innermost node also extends to the eastern basin of the harbor where Anahulu River empties into the ocean.

For the 2-4 min period band, Fig. 4.39 (bottom two panels) reveals a clear node right at the inner-most part of the harbor (southernmost corner), at the exact same location where we found it in the harbor mode analysis in subsection 4.4.3.1 (see second column in Fig. 4.28). The middle panel of Fig. 4.39 also shows that γ^2 has minimal values outside the harbor, suggesting that this mode is purely a harbor mode.

In Figs. 4.37-4.39 we see that the energy right outside the harbor (on the seaward part of the breakwater) is higher than the energy anywhere inside the harbor. Furthermore, we see that right outside the harbor γ^2 has minimal levels in the 0.5-1 min period band (Fig. 4.37), and 2-4 min period band (Fig. 4.39). However, in the 1-2 min period band (Fig. 4.38), γ^2 remain relatively high at ∼0.4-0.5. Since the energy in the 1-2 min period band is so much higher outside than inside the harbor, and γ^2 implies that $\sim 50-60\%$ of the variance is explained by a different source than the one inside the harbor, we believe that the harbor and the coast may have modes in this period band that are independent of each other but are centered on very similar periods, and the coastal mode oscillations are overwhelming the ones of the harbor.

We further looked into that possibility and plotted γ^2 using different reference points: two inside the harbor, and one outside. The results are seen in Fig. 4.40. The middle panel of this Figure is the same one as the middle panel of Fig. 4.38. The top panel of Fig. 4.40 has a reference point just outside the harbor, adjacent to the main breakwater. Here, γ^2 has dropped from 1 at the reference point to %50 or less everywhere inside the harbor. When the reference point is further down inside the harbor (bottom panel of Fig. 4.40), γ^2 outside the harbor is 0.4 or less. These results suggest that there is some connection between the harbor and the coast in the 1-2 min period band, but the reduced levels of variance explained could result from a partial coupling between a harbor and a coastal mode that have slightly different periods in the 1-2 min band. These results are relevant for the hypotheses in the previous subsection.

In the observational study we looked at the coherence amplitude and phase, amplification, and gain between harbor site 1 and coastal site 6 (see Fig. 2.23 in Chapter 2). The amplification shows that the harbor dominates the coastal oscillations near the 90 sec period. The cross-spectral gain between the two sites near the 90 sec period, suggests that there is some relationship between the signal at the coast and inside the harbor, but the gain is less than 1, meaning that there is something else that causes these two systems to be only partially coupled. One thing, however, that we need to keep in mind here, is that site 6 is located quite far offshore from the reference point outside the harbor, at a site where oscillations at the 90 sec period appear to be non-modal under such strong SS forcing conditions (see Chapter 2, Figs. 2.25 and 2.26). This means that the greater amplification that is observed inside the harbor is not in conflict with our assumption (following the model results described above) that the 90 sec mode inside the harbor is dominated by a corresponding mode outside the harbor.

Since we had available sea level observations from a cross-shore array at Mokuleia during the winter swell season of 2007/2008, we ran BOSZ model for the case of the strong SS forcing event on 01/13/08 (R6; see Table 4.1), and looked at the integrated potential energy in a line passing through this array. This was done for each IG period band and was plotted vs. distance from shore. We then overlayed the corresponding observed energies from the sensors at 2m, 6m, and 12m (sites 8c, 8b, and 8a, respectively). The result is seen in Fig. 4.41, where the cross-shore energy variation is calculated for 21 different lines separated in the alongshore by $\sim$ 11 m, spanning $\sim$ 220 m in the alongshore. The thicker black line is the average of all lines. As seen from the different curves in this figure, there is some alongshore variation of the energy in the short period bands, and a smaller alongshore variation in the longer period bands. The reason for that is likely that the shorter period band waves have shorter wavelengths, and are therefore affected by local bathymetric variation, whereas the large-scale waves of the long period bands result in a more uniform distribution of energy at the coast (e.g., compare $E_{\eta,\eta}$ in Figs. 4.33 and 4.36). These results reveal good agreement between the model and observations for the 0.5-1 min, 4-8 min, and 8-17 min bands, and partial agreement for the 2-4 min band. The worst agreement is obtained for the 1-2 min band. The choice of the shoreline for calculating the energy using model datasets was subjective, which could result in a shoreward or offshore shift of the energy curves.

We now look at the total energy (potential + kinetic) along the coast, in order to see whether or not the cross-shore patterns of highs and lows in the potential energy disappear once we account for the energy contribution from the horizontal velocity components u and v. Fig 4.42 shows the results for the (a) 5-30 sec; (b) 0.5-1 min; (c) 1-2 min; (d) 2-4 min; (e) 4-8 min; and, (f) 8-17 min period bands, using the model output from run R2 (the largest domain). For the most part, the high and low patterns indeed seem to disappear once we add the kinetic energy to the potential energy, meaning that this could potentially indicate a signature of standing waves. Such oscillations were observed by (*Péquignet et al.* 2009) during a fringing reef study. Nevertheless, in the 0.5-1, 1-2, and 2-4 min period bands we can still see the some of the patterns of highs and lows, except that these were also smoothed out and appear to be weaker than the ones seen on the potential energy plots.

As was previously mentioned, these standing wave patterns could be generated by: (i) edge waves that are trapped between the shoreline and the edge of the fore-reef, (ii) leaky waves, or, a combination of these two types of waves.

At the long period bands, 4-8 min and 8-17 min (and in the 2-4 min band to some extent), in the channel outside of Hale'iwa Harbor, we observe a striking large-scale feature that extends several kilometers offshore from the channel. A similar tendency for such a response can be also identified in the adjacent channel to the west. At first, we suspected that this large-scale feature is a result of statistical noise, since the frequency resolution decreases going from the higher to lower frequency bands. However, the shape of that feature resembles the structure of a turbulent flow. Since we use an exceptionally large SS forcing event for this model run, we believe that some of the IG energy that was generated at the coast propagated offshore as rip currents through the channels, extending offshore, where we see features that resemble small eddies. The results from this study are insufficient to test and validate this hypothesis, and additional research would be required to adequately address it.

Another important quantity that we examine is the energy flux in the SS band and the different IG period bands. In Fig. 4.43 we see the energy flux in the (a) 5-30 sec; (b) 0.5-1 min; (c) 1-2 min; (d) 2-4 min; (e) 4-8 min; and, (f) 8-17 min period bands, using the model output from run R2. In the SS band (panel a), we see that the energy flux is greatest offshore and decreases over a very short distance on the fore-reef (located $\sim 1-1.5$ km offshore). The energy flux in the 0.5-1, 1-2, and 2-4 min period bands also appears to be strongly affected by the sharp bathymetry gradient at the fore-reef. This strong contrast between the spatial distribution of energy flux in the SS and IG bands is not surprising, since most coastal IG wave generation takes place in the region where the SS waves shoal and break. Since this particular SS event was very large, SS wave breaking is expected to take place relatively far offshore on the reef.

Along the coastal section that extends upcoast from Pua'ena Point, the offshore flow of energy flux becomes more parallel to the coast as we go from shorter to longer period bands. West from Hale'iwa Harbor towards Mokuleia, the energy flux is oriented more perpendicular to the coast, and west from Mokuleia the flow is predominantly parallel to the coast in all IG periods bands, mainly since the SS arrives at an angle of $\sim 45°$ relative to that stretch of coast. The length and magnitude of the arrows also indicate that overall, the flow of energy flux over the reef is greatest in the 0.5-1 and 1-2 min period bands.

In the 8-17 min period band (and to a lesser extent, in the 4-8 min band) we notice that offshore of the reef there are strong energy fluxes that point in different directions. A quick comparison with the total energy shows that these appear in the region of the turbulent flow that was described earlier. Away from the coast, in the channel offshore of Hale'iwa Harbor, there are arrows pointing in the offshore direction, supporting our hypothesis that these are strong rip currents.

Fig. 4.44 provides a detailed look at the region of Hale'iwa Harbor and its immediate vicinity. The energy flux in the SS band is strong within the channel offshore of Hale'iwa Harbor, and dies outside of that channel. For all IG period bands, the energy flux on the reef seems to be strongest in the channel. Inside the harbor, the energy flux is minimal at periods shorter than 2 min, and increases at the longer IG period bands. Only in the 4-8 and 8-17 min bands the energy flux appears to be significant in the inner basin (relative to the energy flux outside the harbor). In these bands a return flow is also seen in the southern extension of the harbor.

In a similar study of a harbor, *Guedes et al.* (2015) used observations from two cross-shore sections of the reef outside the harbor and found that the energy flux at periods shorter than 1 min was always greater than the energy flux at periods longer than 1 min, except for a small region very close to shore. In Fig. 4.44, the energy flux outside the harbor in the 0.5-1 min band seems to be weaker than the energy flux in the 1-2 min band. In fact, in Fig. 4.43 we see that this is not the case everywhere along the coast, as there are regions like Pua'ena Point and Mokuleia where the opposite is the case. Further study would be required in order to determine the reason for such differences along the coast.

Another thing that we see here is related to an earlier result from this section, where we found evidence that points to the possibility of independent coastal and harbor modes in the 1-2 min period band, with the coastal mode being much more energetic than the harbor mode (e.g., Fig. 4.38). Here in Fig. 4.44 we see that at the coast in the vicinity of the harbor, the strongest energy flux lies in the 1-2 min period band, supporting the possibility that a coastal mode in this period band will overwhelm a harbor mode having a similar period.

To obtain a better idea of how much of the incoming energy flux is radiated offshore, we plot the incoming and outgoing energy fluxes at Mokuleia site, for each of the IG period bands (Fig. 4.45). We immediately see that the outgoing flux is small in the short period bands, and increases going to the longer period bands. For the 8-17 min period band nearly all incoming flux is radiated back offshore. At a fixed point, these results are consistent with a study on a reef done by *Péquignet et al.* (2014). The same analysis was applied to Pua'ena Point site, as can be seen in Fig. 4.46. Qualitatively, the results here are the same with the longer period IG waves being more reflective than the shorter period waves.

These results suggest that for the short period bands (say, T<4 min) the divergence of energy flux within the surf zone is mostly dissipated by friction on the reef, with very little reflection (Fig. 4.43). For the long period bands (say, T>4 min), the opposite appears to be true, as friction seems to play an insignificant role and reflection is very high. It is important, however, to keep in mind that this analysis is based on the assumption that the incoming wave field propagates perpendicular to shore. In reality, of course, the incoming SS wave field does not approach all parts of the coast exactly perpendicular; a SS event arriving from $\sim 315°$ will be propagating approximately perpendicular to the stretch of coast extending from Kaiaka Bay to Waimea Bay (and includes Hale'iwa Harbor), but at an oblique angle of $\sim 45°$ from the line perpendicular to Mokuleia stretch of coast (although the the energy flux in the vicinity of Mokuleia stretch of coast approaches the shore at a slightly more perpendicular angle).

An interesting thing we noted in nearly all the numerical modeling plots is high frequency patterns of alternating highs and lows at certain regions near the coast. This is most strongly seen in the close-up plots of $E_{\eta,\eta}$ and γ^2: Fig. 4.37- 4.39. The wavelengths of these oscillations have the same dimensions in all of the IG period bands examined in this study (the separation distance is on the order of tens of meters). Panel a of Fig 4.42 also reveals the regions of strongest SS energy near the coast, and these in fact match the locations where we see these high-frequency patterns. Following these results we feel confident that these high-frequency oscillations are the result of numerical noise. The energy levels of these high-frequency patterns decrease in the longer period bands (the corresponding close-up figures for the 4-8 min and 8-17 min bands are not shown here, but are consistent with the findings described here). This type of numerical noise is possibly common in swell-driven gravity wave models, as it was seen in other studies using a different numerical model (*McComb et al.* 2009;

Johnson et al. 2011).

To look for edge wave signatures, we use BOSZ gauges from alongshore arrays at Mokuleia and Pua'ena point (see Figs. 4.2 and 4.5), and employ the MLE method. The results are presented in two dimensional frequency-wavenumber PSD plots. Fig. 4.47 shows the results using the alongshore and cross-shore velocity components at the Mokuleia alongshore array site, and Fig. 4.48 shows the same using the alongshore array site in Pua'ena Point. Theoretical dispersion curves of several modes for the case of a plane beach slope (calculated using Eq.(4.5)), are superimposed with their corresponding mode numbers labeled on each of these plots. Using estimated slopes values of 0.0138 and 0.0125 for Mokuleia and Pua'ena Point sites, respectively, and plugging them into Eq.(4.6), we also estimate that the highest possible edge wave modes are: $n = 55$ for Mokuleia site, and $n = 61$ for Pua'ena Point site. However, it is not plausible to observe such high mode numbers. For the Mokuleia case, we note that the greatest PSD levels of the alongshore velocity component (Fig. 4.47a) are concentrated at high mode numbers. A similar result is seen in the PSD plot of the cross-shore velocity component (Fig. 4.47b). For the Pua'ena Point case, we note that the greatest PSD levels of the alongshore velocity component are concentrated near low modes (Fig. 4.48a), and the PSD levels of the cross-shore velocity component are concentrated at high mode numbers (Fig. 4.48b), as was seen in the Mokuleia site.

Qualitatively, the PSD levels of the cross-shore and alongshore velocity components at Pua'ena Point site are quite similar to the results obtained by *Oltman-Shay and Guza* (1987). That is, however, not the case in the Mokuleia site. Observations by *Oltman-Shay and Guza* (1987) showed that the variance of the alongshore velocity component was in good agreement with the low-mode edge wave dispersion curves, and the variance of the cross-shore velocity component showed good agreement with the dispersion curves of high-mode edge waves (or, leaky waves). The cross-shore bathymetry profiles at Mokuleia and Pua'ena Point sites are qualitatively similar (see Fig. 4.49a,b), with slightly greater alongshore variation and milder slope at Pua'ena Point site; however, the coastlines in our study are not quite straight as the ones in the study of *Oltman-Shay and Guza* (1987).

In the energy flux analysis (Fig. 4.43) we saw that although the flow over much of the reef in the domain is in the cross-shore direction, there are some regions where the flow has a significant alongshore component. Although the alongshore component of energy flux appears to be quite strong around Mokuleia site in the 0.5∼8 min period band, the frequency-wavenumber analysis did not reveal the signature of low-mode edge-waves. At Pua'ena Point site, the energy flux maps indicate an alongshore component of energy flux in the 1∼8 min period band; however, the greatest PSD levels in the frequency-wavenumber MLE analysis are found in the $\sim 45 - 60$ sec band, although significant PSD levels are clearly seen at periods as long as ~ 2 min.

A coherence analysis between the SS sea-level envelope (η_{env}) and sea-level (η) at a relatively close distance from Hale'iwa Harbor, is applied to model data from five BOSZ gauges located at Waialua Bay along a cross-shore line formed by sites K6-K9 and 6 (Fig. 4.4). The results are seen in Fig. 4.50, together with the distance from shore and water depth at each site. From the offshore-most site (6) towards shore, the sequence of plots reveal a bound wave signature with a transition into a free wave somewhere shoreward of site K9. Going from site 6 to this transition point, the coherence amplitude in the ∼0.5-8 min period band is well above the 95% level of no significance, and the corresponding coherence phase is close to 180° and shifts towards 90°, consistent with observation of shoaling bound IG waves (*Elgar and Guza* 1985). An exception to the high coherence amplitude between η_{env} and η is site K8, which is likely because this site is within the surf zone very close to the breakpoint region where the groupiness signal may be overwhelmed by the turbulent motion due to breaking SS waves. Going from the transition point toward shore, we see that the coherence amplitude increases again since these sites are farther away from the breakpoint region. Closest to shore, the coherence phase in the ∼0.5-8 min period band consistently remains near 0°, and it even extends up to periods as long as 30 minutes at the shoreward site, K6. The distance from shore of that transition point is approximately the same as the transition between the energy flux of SS and IG waves that is seen in Fig. 4.43 (compare panel a with remaining panels).

The energy and coherence analysis results presented in this section revealed standing wave patterns in the cross-shore with a strong alongshore symmetry along the entire coast within the domain. For the short IG period bands, we are able to identify several highs and lows and the distances between these are short. From the short period to long period IG period bands, the number of highs and lows decreases and the separation distance between them increases. When considering the total energy, much of these patterns are smoothed out as the total energy becomes more uniform across the entire domain. Although these standing wave patters are harder to identify, they do not entirely disappear at certain regions within the domain.

The MLE analysis revealed patterns that resemble low-mode edge waves at Pua'ena Point site, but these appear to have greatest spectral levels at relatively short IG periods of $45-60$ sec. At Mokuleia site, the MLE analysis revealed patterns of high-mode edge waves, but these could also be leaky wave modes, as it is not easy to distinguish between these two types of waves. The net energy flux analysis revealed that the energy flow is predominantly perpendicular around Waialua Bay (where Hale'iwa Harbor lies), it has some alongshore component northeast of Pua'ena Point, and even more to the west along Mokuleia stretch of coast. Separating the energy flux into incoming and outgoing components at two different sites, showed little reflection at the short period IG bands and near total reflection at the long period IG bands (with a cutoff around 4 min). Close to the coast, reflection is high at all IG period bands. These suggest that the short period (small scale waves) IG bands are dissipative, and the long period (large scale waves) IG bands are reflective. These results suggest that under strong SS forcing conditions within the surf zone (up to ∼800m form shore), leaky waves may be a dominant form of free waves at periods longer than ∼4 min.

The coherence analysis at the BOSZ gauge sites in the cross-shore array at Waialua Bay, reveals a signature of bound waves at the offshore-most sites, with transition into free waves around the SS breakpoint region. The clear bound wave signature offshore of the SS breakpoint, that is accompanied by high variance explained ($\sim$ 50 $-$ 80%), suggests that the free IG wave field within the surf zone potentially consist of significant levels of free released-bound IG waves.

Energy and coherence analysis in the harbor and its immediate vicinity, suggest that in addition to the observed 90 sec harbor mode (see Section 2.5.1 in Chapter 2), it is likely that an independent but much more energetic mode exists at the coast in the 1-2 min period band. The decrease in γ^2 over relatively short distances suggests that the coastal mode in the 1-2 min period band is likely centered at a slightly different period than the 90 sec mode observed inside the harbor. Therefore, even though in the previous subsection we found that the gravest harbor mode seems to lie in the 4-8 min period band, the coast seems to have modes at shorter periods (e.g., in the 1-2 min period band), meaning that there is an overlap between the coastal and harbor modes.

4.4.3.3 The Role of Time-Varying, SS-Driven "Setup" (T < 30 min; Hypothesis C6)

In this section we examine the possibility that strong SS forcing induces in Hale'iwa Harbor "setup" variability at IG periods shorter than 30 min (hypothesis C6). In Chapter 2, the observations from Mokuleia cross-shore array (sites 8a-8c in Fig. 4.2) provided evidence for the existence of a SS-driven "setup", but this site is relatively far from Hale'iwa Harbor. Here we use model results from a cross-shore line located closer to the harbor ($\sim$1.5 km west of the harbor entrance), at Waialua Bay, and apply the same coherence analysis that was employed in Chapter 2 for single sites and pairs of sites.

For a setup/set-down forced by SS wave groups at the coast, we consider the following scenarios: (i) if the SS breakpoint region lies between two given sites, we are looking for high coherence between η vs. η with corresponding 180° coherence phase, since the site offshore of the breakpoint region experiences a set-down, and the site within the surf zone experiences a setup; and, we are also looking for high coherence between $\eta_{ss,env}$ at the seaward site vs.

η at the shoreward site, with corresponding coherence phase of 0°, since the site within the surf zone experiences the setup that was induced by the SS wave groups. (ii) if the SS breakpoint region lies seaward of the two sites, we are looking for high coherence of η vs. η with corresponding coherence phase of 0°, since the two sites are within the surf zone and experience a setup. Also in this case, the coherence phase between $\eta_{ss,env}$ at the seaward site vs. η at the shoreward site is expected to be 0°.

The cross-shore line formed by BOSZ gauge sites K6-K9 and 6, are used here. Since from Fig. 4.50, we learned that the SS breakpoint region is located somewhere in the vicinity of site K8, just offshore of site K8, we apply a coherence analysis of η_{env} vs. η (blue curves in Fig. 4.51) and η vs. η (black curves in Fig. 4.51), for the pairs of sites: (i) 6 vs. K8 and 6 vs. K7, where the SS breakpoint lies in between the sites; and, (ii) K7 vs. K6, that are both located shoreward of the SS breakpoint region.

For the pairs of sites: 6 vs. K8 and 6 vs. K7, the coherence amplitude levels are statistically-significant and relatively high for the blue and black curves, up to a period of 30 min. The corresponding coherence phase is qualitatively not very far from 0° for η_{env} vs. η, and 180° for η vs. η, as would be expected for a SS-driven setup. For the pairs of sites: K7 vs. K6, the coherence amplitude levels are statistically-significant and very high for η vs. η, but much lower for η_{env} vs. η (and statistically insignificant at periods longer than ~5 min). Even though the corresponding coherence phase of η_{env} vs. η is not close to zero (since their coherence amplitude is statistically insignificant), the corresponding coherence phase of η vs. η is very close to 0°. These results provide evidence supporting the mechanism of SS-driven setup in the vicinity of Hale'iwa Harbor in the $3 \sim 30$ min period band.

4.5 Discussion

In this chapter, we use results from the numerical model BOSZ in order to shed some light on unanswered questions that remained open following the observational study of Chapter 2. The high spatial resolution of the model enables us to see large-scale patterns that are not possible to capture with the few isolated observations inside and outside Hale'iwa Harbor.

1. **Excitation of linear coastal or harbor modes**: Forcing Hale'iwa Harbor when isolated from the coast resulted in excitation of several modes with complex structure. The gravest mode of the harbor appears to be similar to a quarter-wave Helmholtz mode that lies in the 4-8 min period band and has a node at outer basin of the harbor.

   Energy and coherence analyses in Hale'iwa Harbor and its immediate vicinity suggested that the coast has modes with periods shorter than the gravest mode of the harbor. In particular, a coastal mode in the 1-2 min period band seems to be much more energetic than a well defined 90 min mode that was observed inside the harbor. The results suggest that, in this period band, a slight offset could possibly exist between the periods of these harbor and coastal modes. The above suggests that although the harbor and the coast have their own sets of normal modes, there is an overlap between the coastal and harbor modes, at least down to ∼1-2 min.

2. **Bound wave impacts; generation of leaky and edge waves**: The maps of potential energy, coherence squared, and coherence phase, under strong SS forcing conditions, revealed clear standing wave patterns of highs and lows in the cross-shore direction. This was most clearly seen at periods shorter than 4 min. We examined the possibilities that these cross-shore standing wave patterns are the signature of edge-waves trapped to the reef, or leaky waves. The frequency-wavenumber spectra of the alongshore velocity component at Pua'ena Point revealed a signature of low-mode edge-waves that are most energetic at relatively short IG periods of ∼45-60 sec. The same analysis applied to the cross-shore velocity component resulted in a signature of high-mode edge waves, which could also be leaky waves. At Mokuleia site we only found a signature of high-mode edge waves, which could also be leaky waves.

   With the exception of a few regions, the energy fluxes in much of the domain in the vicinity of Hale'iwa Harbor appear to be predominantly in the cross-shore direction.

   The cross-shore component of the energy flux was separated into incoming and outgoing components, in order to see how much of the incoming flux is reflected back offshore. The results revealed that most of the energy of the short period IG waves (e.g., 0-1 min, 1-2 min, and 2-4 min period bands) is dissipated due to friction with little energy being reflected back offshore. The long period IG waves (the 4-8 min and 8-17 min period bands), on the other hand, are nearly completely reflected back offshore and are not affected by friction at all. This is also consistent with the picture obtained from the 2-D energy flux maps, where energy flux cancellation is seen in the long period bands (4-8 min and 8-17 min) along the entire coastline of the domain. In addition, we see that for all IG period bands there is nearly full reflection very close to the shoreline. The above results suggest that high-mode edge-waves or leaky waves possibly dominate the variance at IG periods longer than ∼4 min.

Coherence analysis of data from the cross-shore gauges at Waialua Bay revealed a strong signature of bound IG waves offshore of the surf zone, and free IG waves within the surf zone. Those free waves could very likely be released-bound waves (since the coherence amplitude of the bound waves outside the surf zone suggests a variance explained of $\sim 50 - 80\%$), or free IG waves generated by some other mechanism (i.e., nonlinear triad interaction, or time-varying breakpoint).

3. **The role of time-varying, SS-driven "setup"**: The coherence analysis applied to the cross-shore array at Waialua Bay (∼1.5 km west of the harbor entrance), revealed results that are qualitatively very similar to the ones observed at Mokuleia (∼5.5 km west of the harbor entrance), suggesting that such a pathway of energy could result in the elevated spectral levels that we observe in the harbor and at the coast at periods in the $3 \sim 30$ min period band.

In addition to the above, the numerical model also revealed some interesting results that were not possible to address in this study. One such example is the turbulent flow structure seen flowing offshore via Hale'iwa Harbor channel. This flow is most developed at the long period bands (periods longer than ∼4 min) and it extends over a large area outside the reef. We believe that strong rip currents are responsible for the generation of these turbulent patterns, but additional research would be required to prove this hypothesis.

Table 4.1: Specifications of all BOSZ model runs. Columns are: Run name, SS forcing level, date of SS directional spectra, alongshore domain size (y), cross-shore domain size (x), grid resolution, friction coefficient for bathymetry, friction coefficient for topography.

Run	**SS level**	**SS date**	**y (km)**	**x (km)**	**Res (m)**	α_{bathy}	α_{topo}
ST2	strong	01/23/14 06:55	5.6	9	7	0.035	0.025
ST3	strong	01/23/14 06:55	8.4	9	7	0.035	0.025
ST4	strong	01/23/14 06:55	11.2	9	7	0.035	0.025
ST5	strong	01/23/14 06:55	8.4	6.9	7	0.035	0.025
ST6	strong	01/23/14 06:55	11.2	9	7	0.01	0.01
ST7	strong	01/23/14 06:55	11.2	9	7	0.1	0.1
R2	strong	01/23/14 06:55	12.2	10.2	7	0.035	0.025
R3	moderate	12/22/13 00:25	12.2	10.2	7	0.035	0.025
R4	weak	03/28/14 14:55	12.2	10.2	7	0.035	0.025
R5	strong	02/08/12 20:28	12.2	10.2	7	0.035	0.025
R6	strong	01/13/08 22:40	12.2	10.2	7	0.035	0.025
R7	weak	N/A	0.45	1.4	3	0.035	0.025

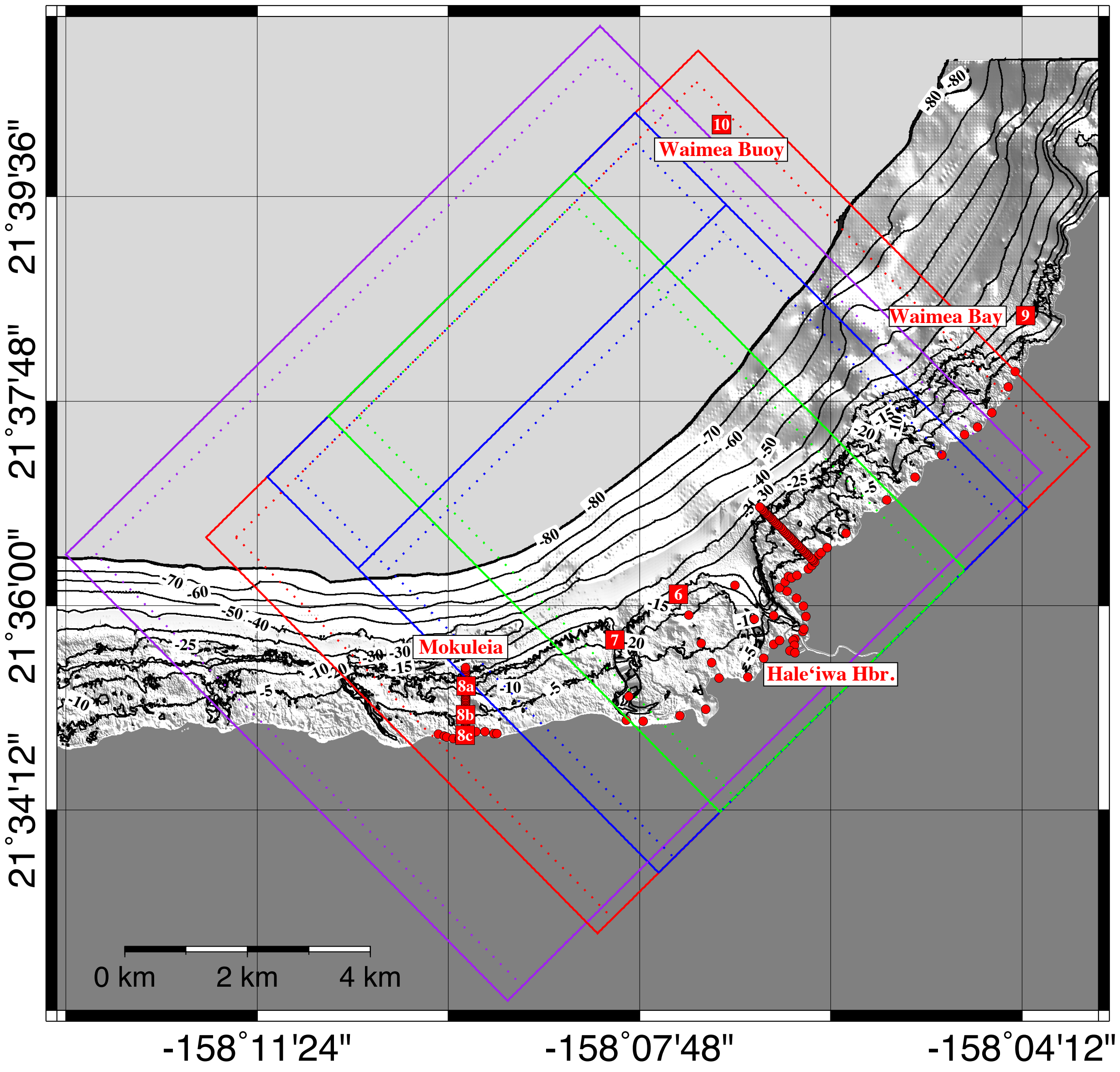

Figure 4.1: Map of model domains along the North Shore. Continuous lines forming green, blue, and red domains are called: small, intermediate, and large, respectively (test runs ST2-ST4). Continuous blue rectangle domain is called: intermediate & narrow (test run R5). Continuous purple rectangle domain is called: largest, and is used for all runs following the sensitivity testing stage (runs R2-R6). The sponge layer acts in the gaps between continuous and dotted lines. Circles indicate high frequency model data sites. Squares indicate observational data sites, with BOSZ gauges collecting data at sites 1-7 and 8a-8c.

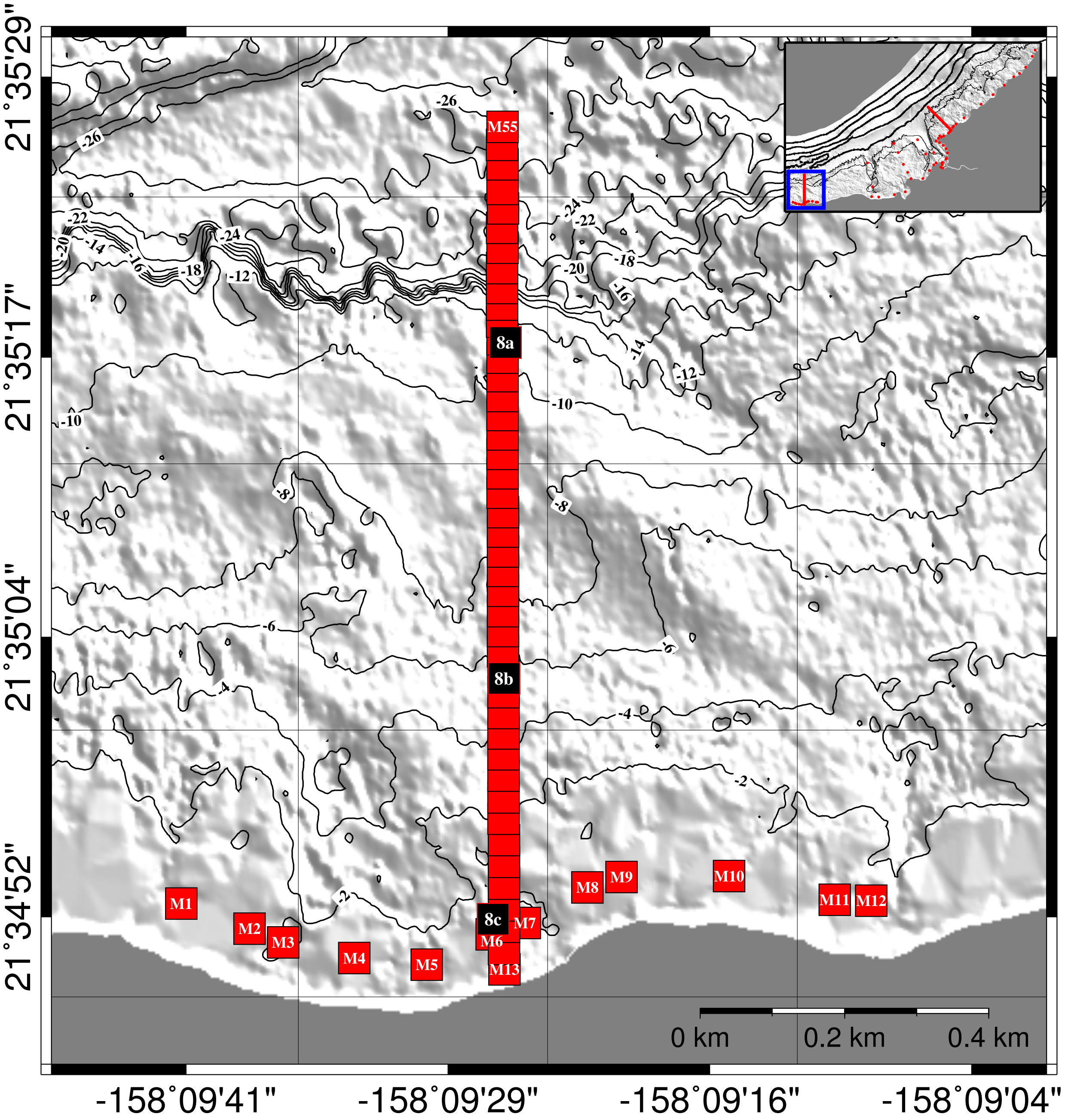

Figure 4.2: Map of BOSZ gauges along Mokuleia stretch of coast (red and black squares). Black square symbols indicate sites where observational data was also available. The location of this region along the North Shore coast is indicated by the blue rectangle on the inset.

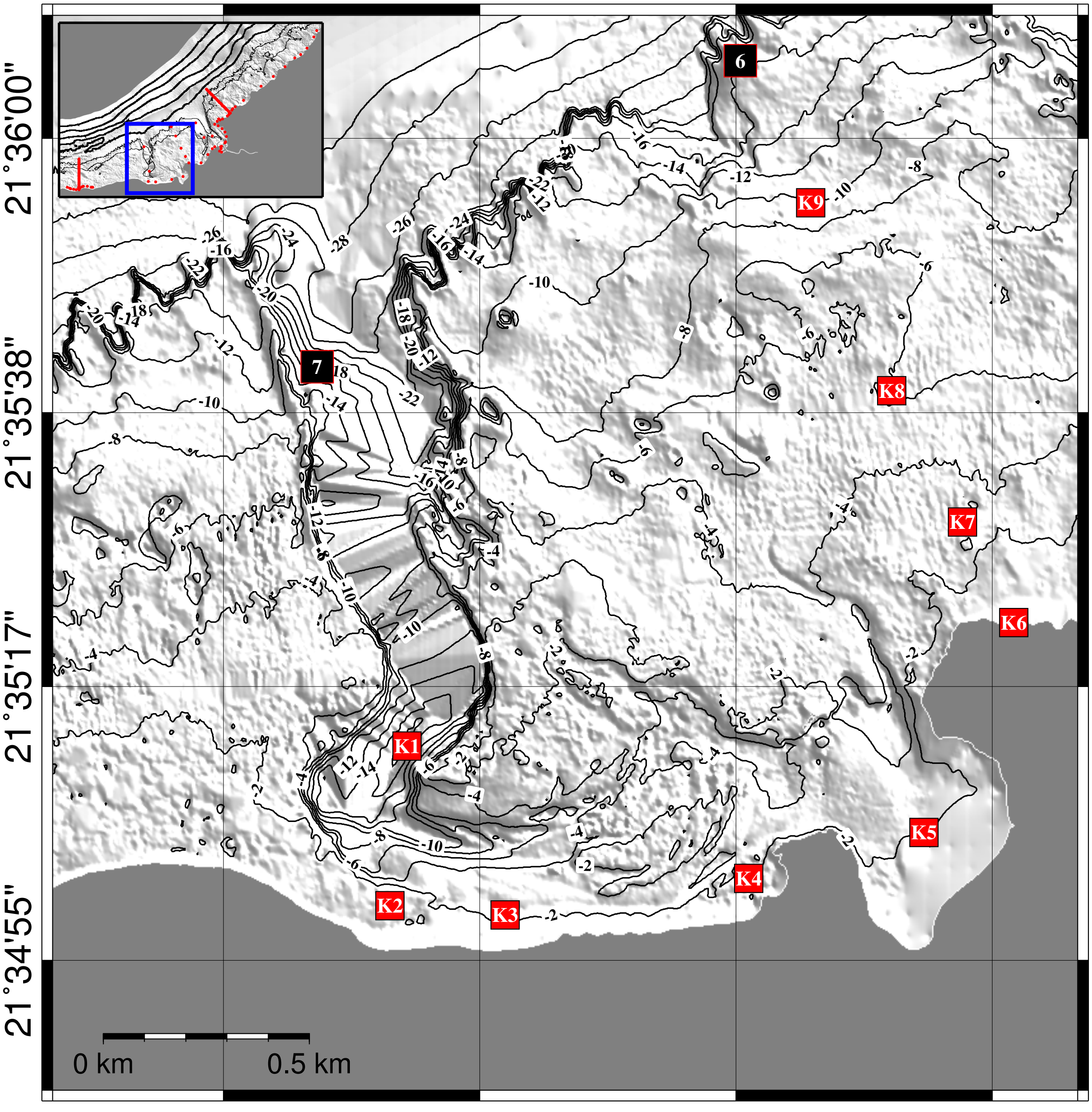

Figure 4.3: Map of BOSZ gauges in the vicinity of Kaiaka Bay (red and black squares). RBlack square symbols indicate sites where observational data was also available. The location of this region along the North Shore coast is indicated by the blue rectangle on the inset.

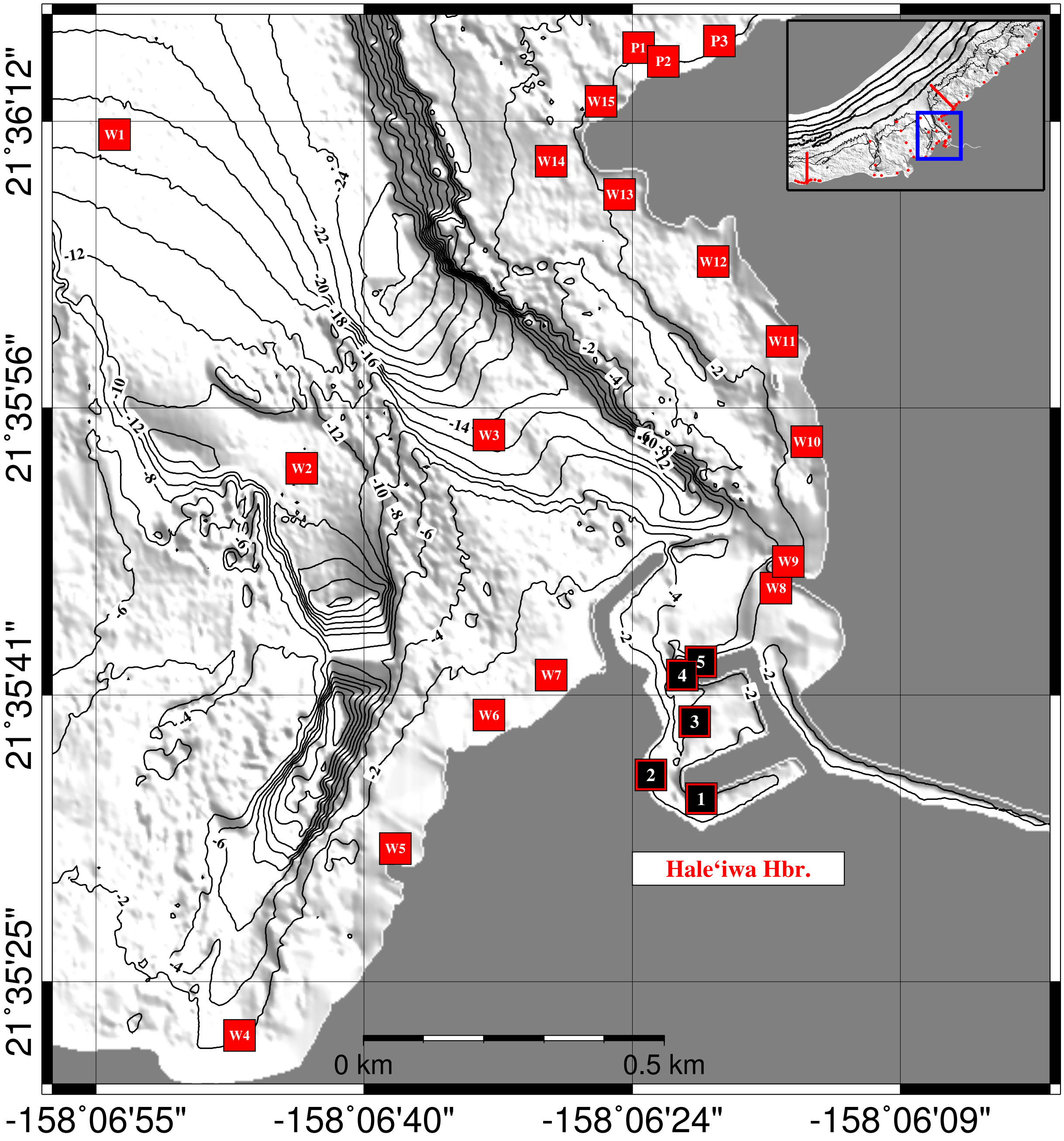

Figure 4.4: Map of BOSZ gauges in Waialua Bay, including inside Hale’iwa Harbor (red and black squares). Black square symbols indicate sites where observational data was also available. The location of this region along the North Shore coast is indicated by the blue rectangle on the inset.

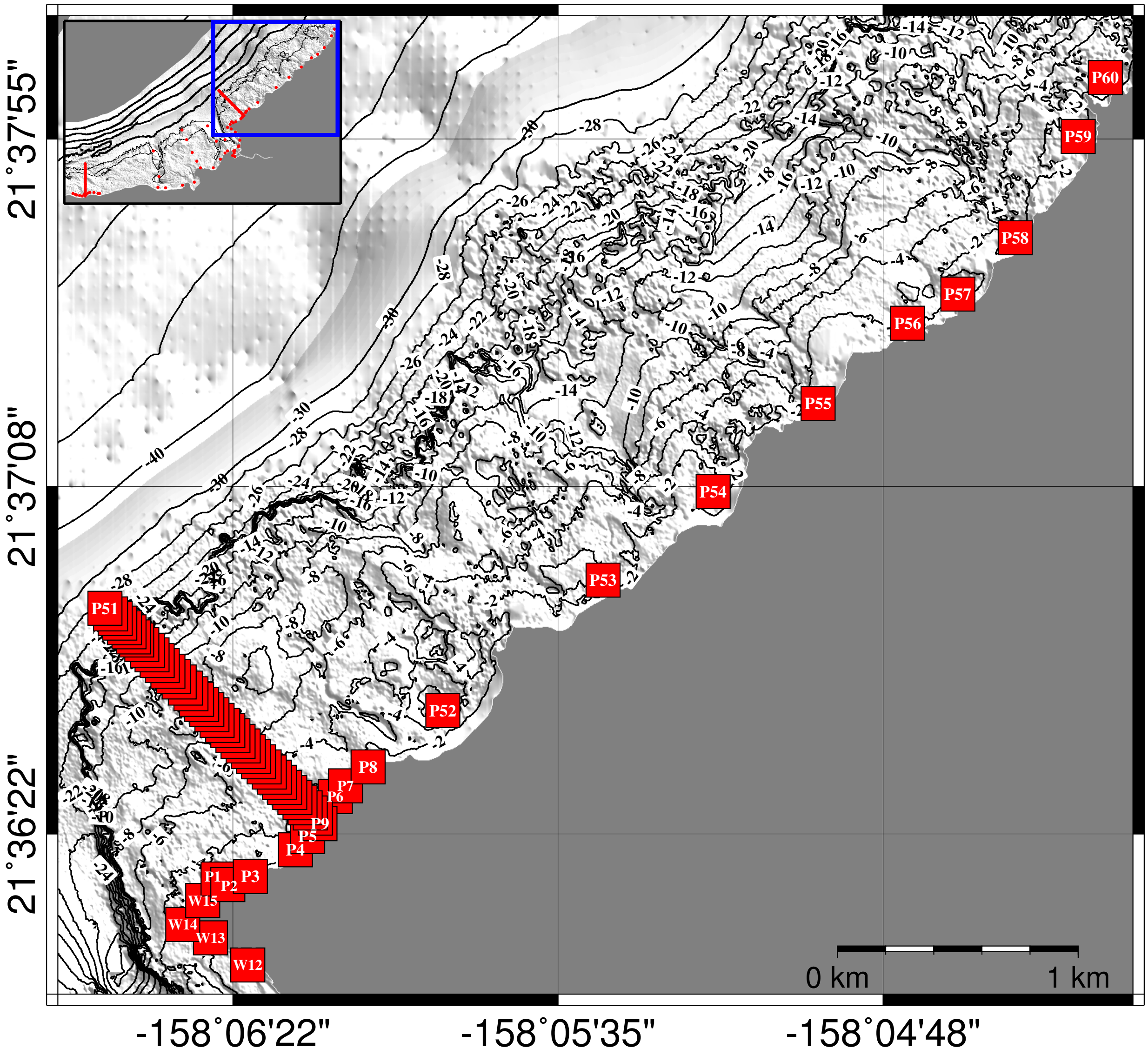

Figure 4.5: Map of BOSZ gauges stretching eastward from Pua'ena Point (red squares). The location of this region along the North Shore coast is indicated by the blue rectangle on the inset.

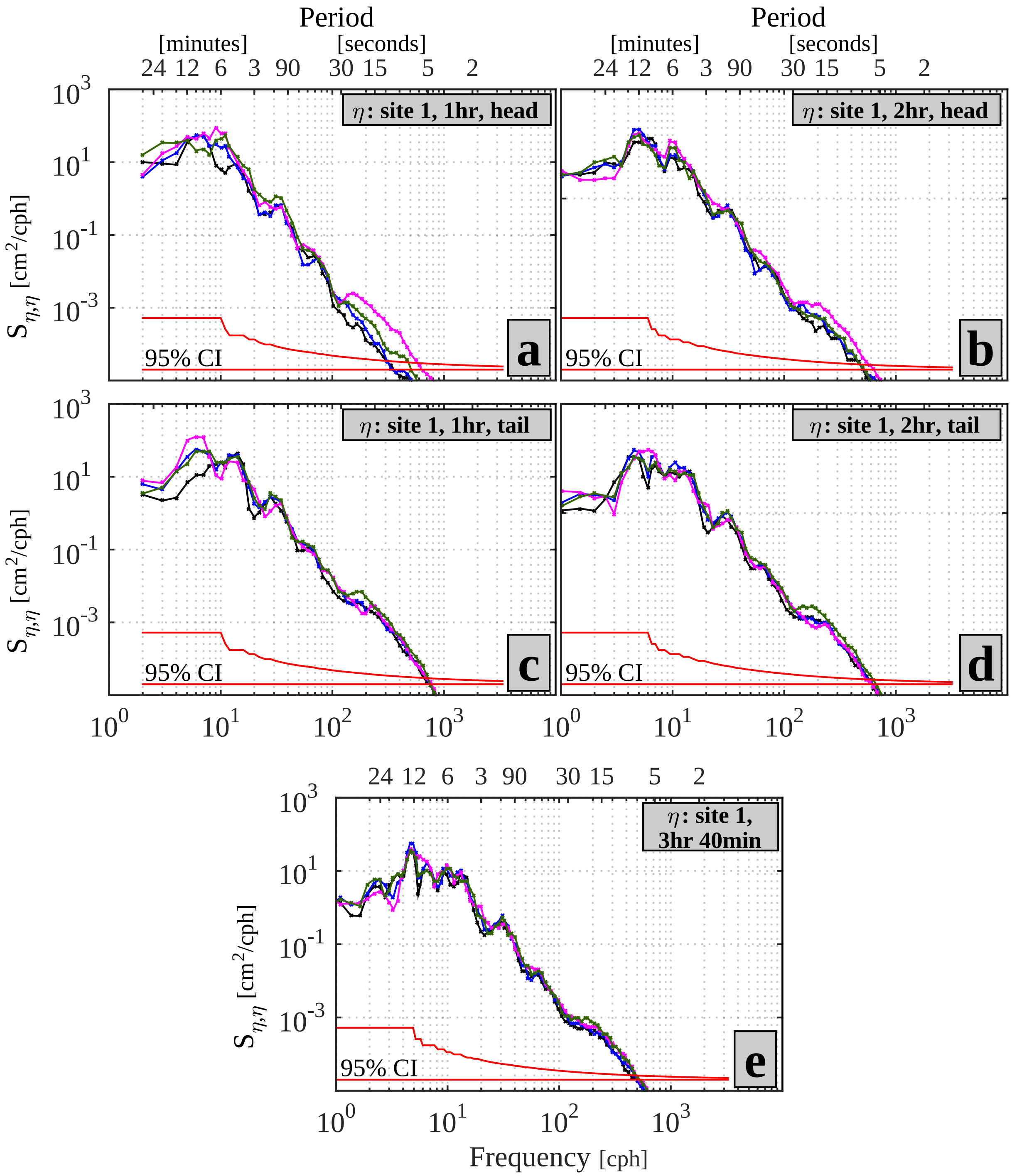

Figure 4.6: PSD of model data at site 1, for model runs having small (black), intermediate (blue), large (magenta), and intermediate & narrow (green), domains (rus ST2-ST5, respectively), under strong SS forcing. The 95% confidence interval for each independent spectrum estimate is shown at the bottom.

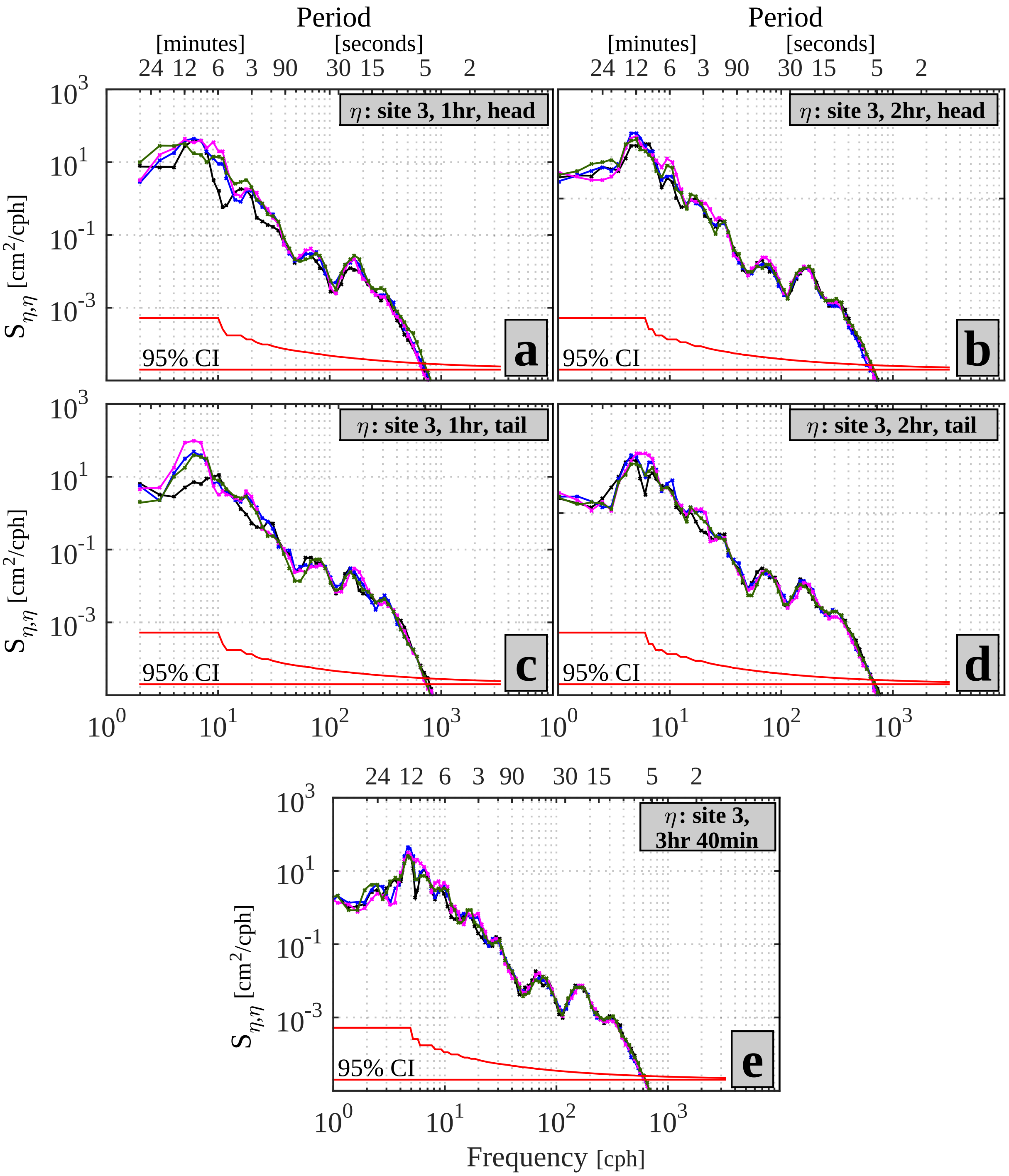

Figure 4.7: PSD of model data at site 3, for model runs having small (black), intermediate (blue), large (magenta), and intermediate & narrow (green), domains (rus ST2-ST5, respectively), under strong SS forcing. The 95% confidence interval for each independent spectrum estimate is shown at the bottom.

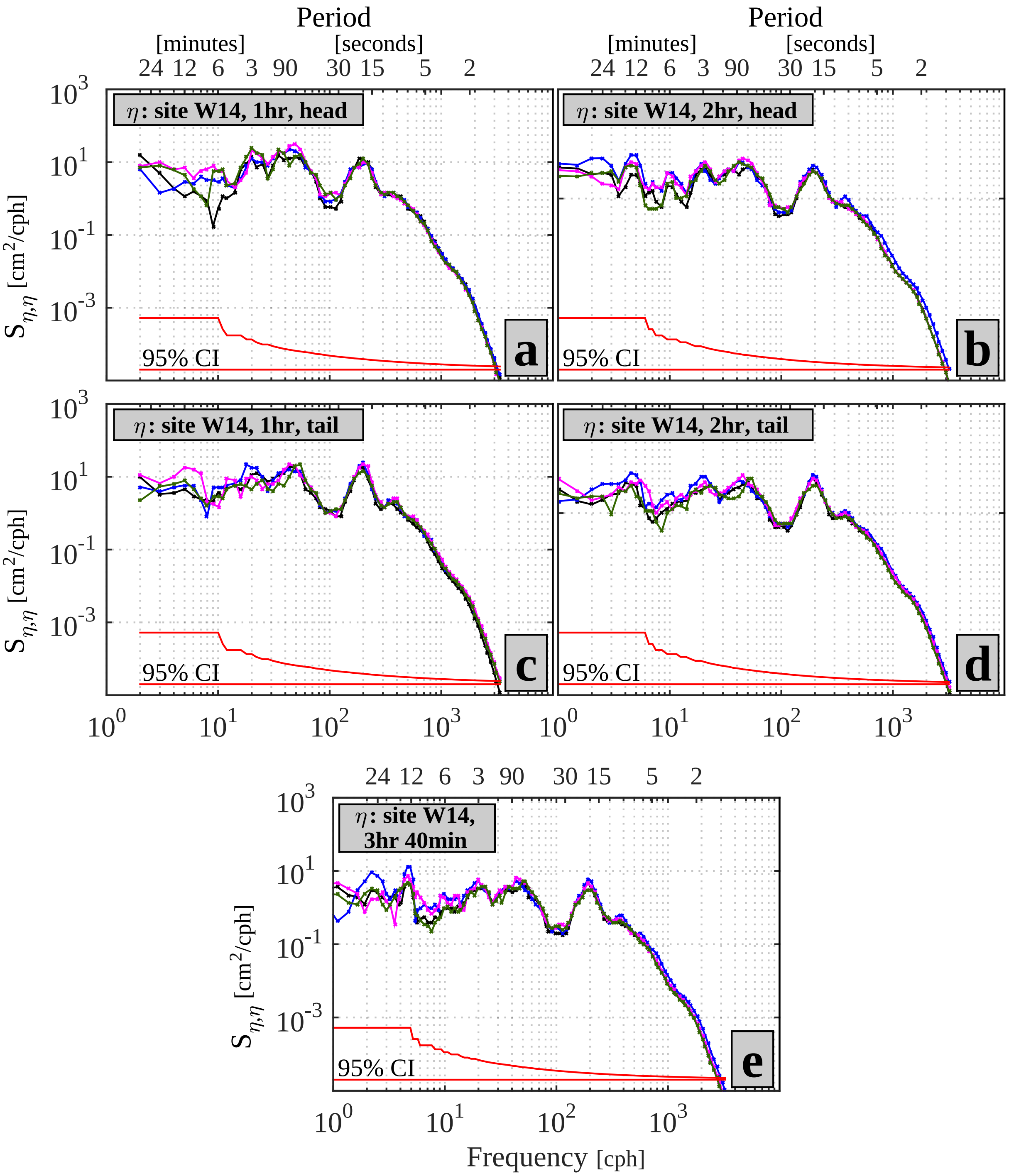

Figure 4.8: PSD of model data at site W14, for model runs having small (black), intermediate (blue), large (magenta), and intermediate & narrow (green), domains (rus ST2-ST5, respectively), under strong SS forcing. The 95% confidence interval for each independent spectrum estimate is shown at the bottom.

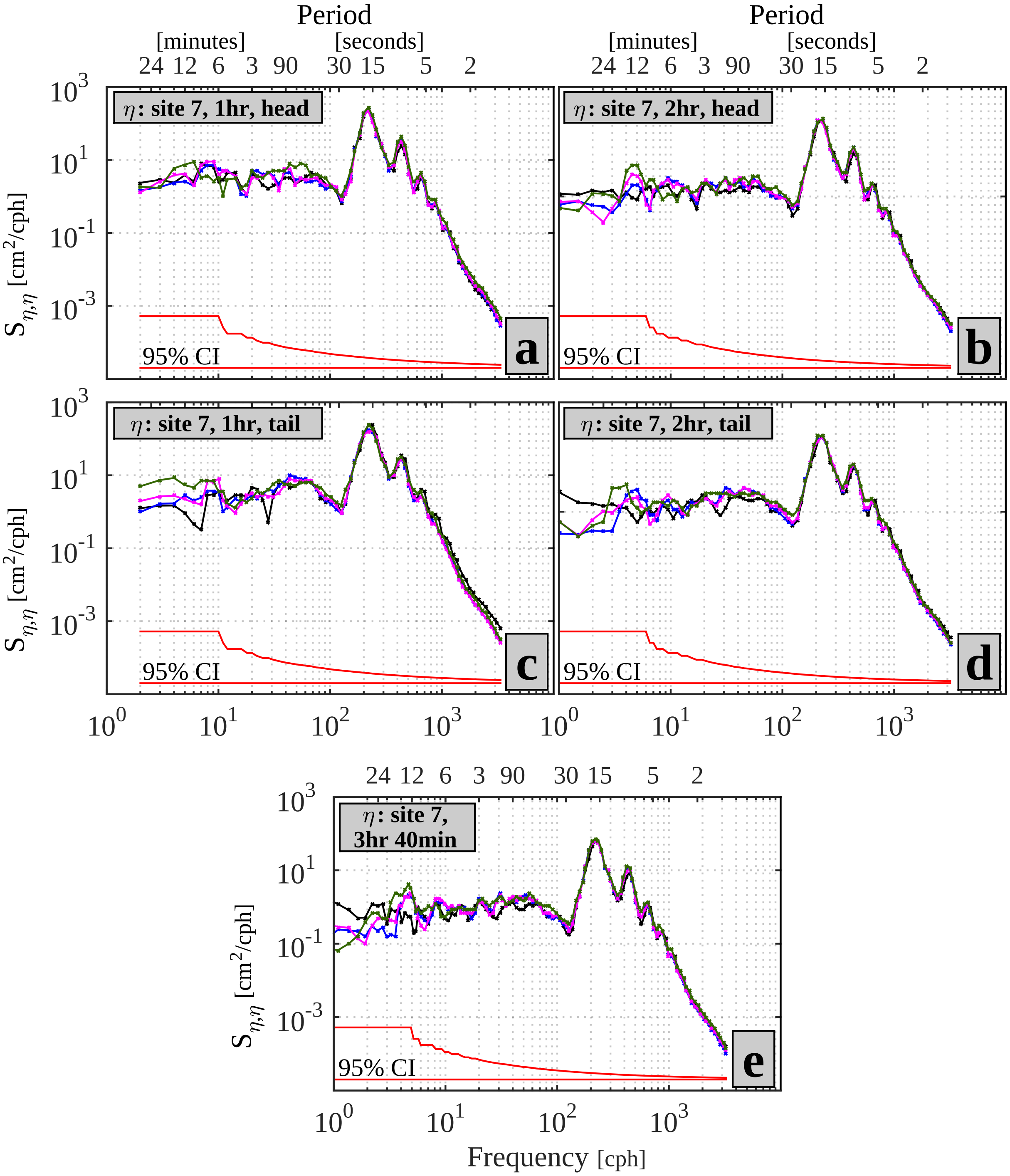

Figure 4.9: PSD of model data at site 7, for model runs having small (black), intermediate (blue), large (magenta), and intermediate & narrow (green), domains (rus ST2-ST5, respectively), under strong SS forcing. The 95% confidence interval for each independent spectrum estimate is shown at the bottom.

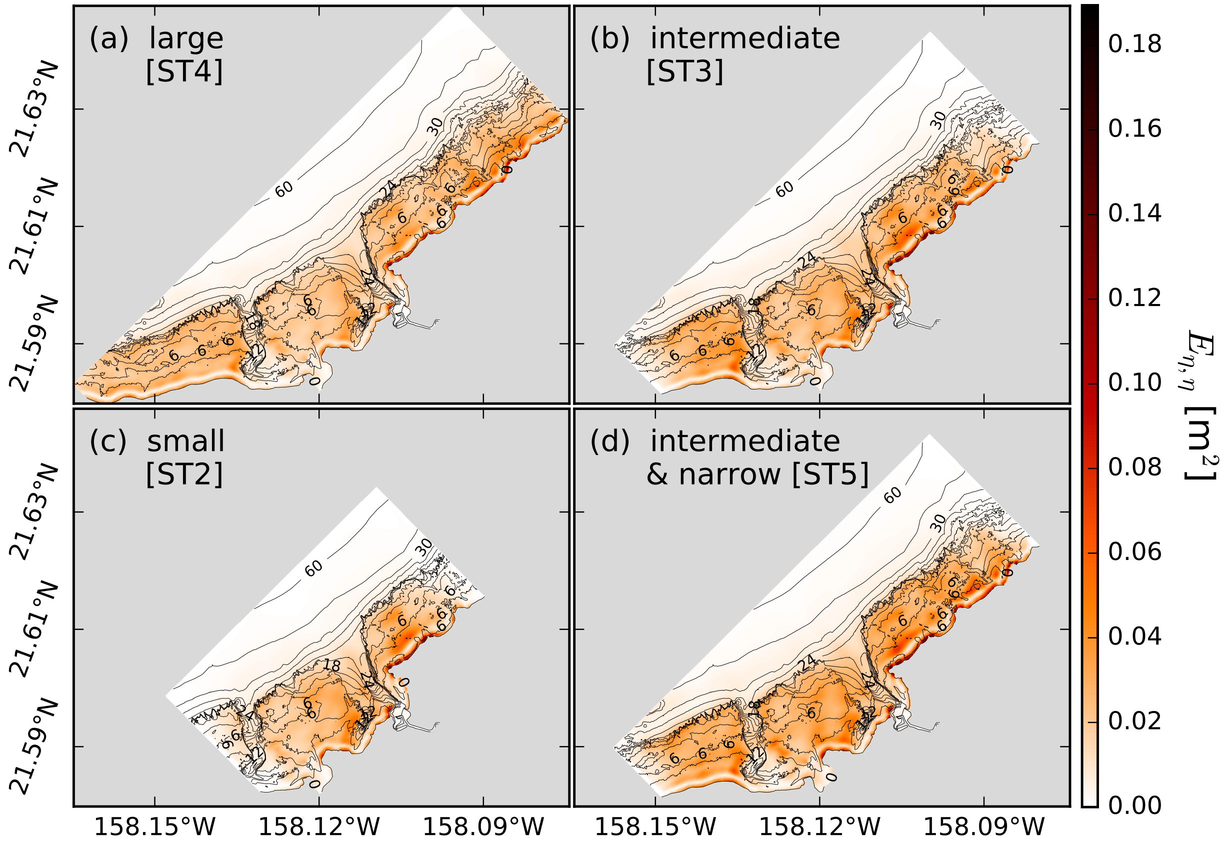

Figure 4.10: Spatial distribution of potential energy in the 1-2 min period band for the (a) large (domain ST4), (b) intermediate (domain ST3), (c) small (domain ST2), and (d) intermediate & narrow (domain ST5), domains, under strong SS forcing.

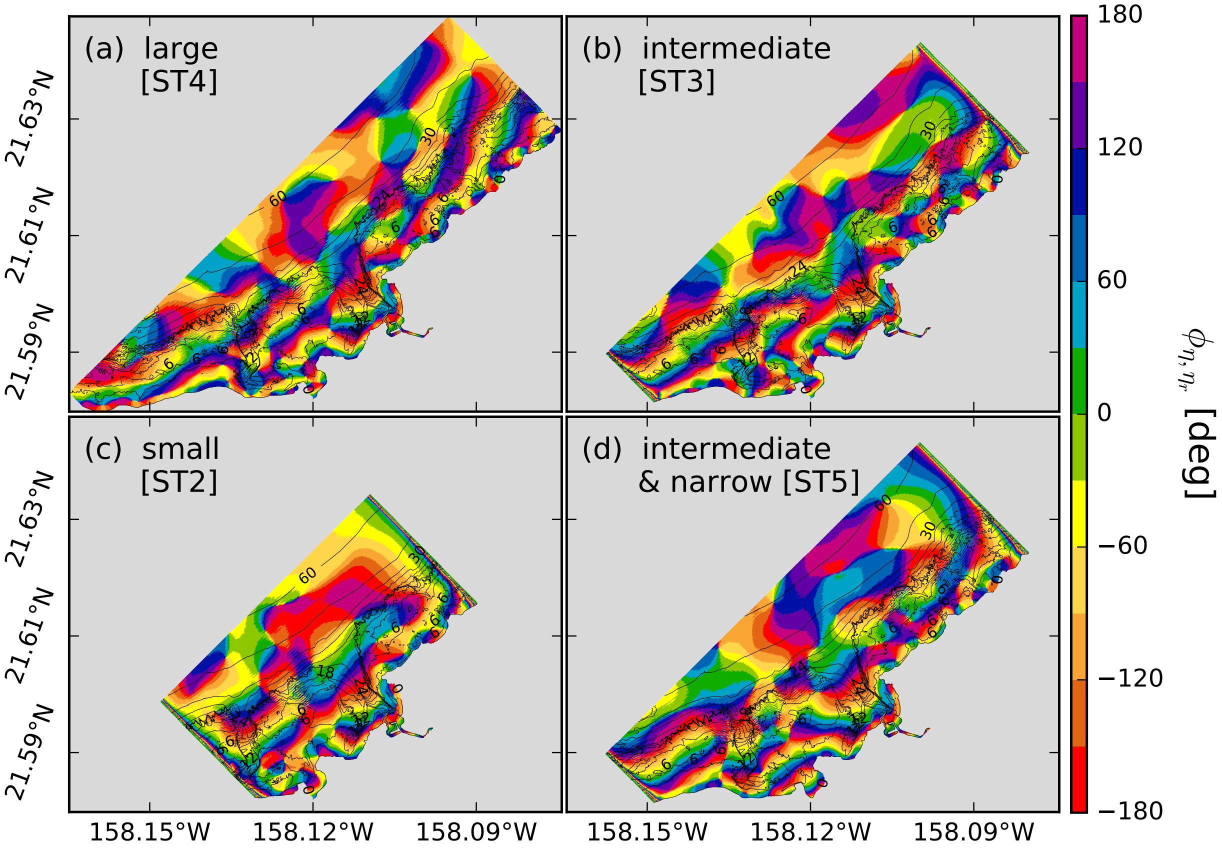

Figure 4.11: Spatial distribution of coherence phase in the 1-2 min period band for the (a) large (domain ST4), (b) intermediate (domain ST3), (c) small (domain ST2), and (d) intermediate & narrow (domain ST5), domains, under strong SS forcing.

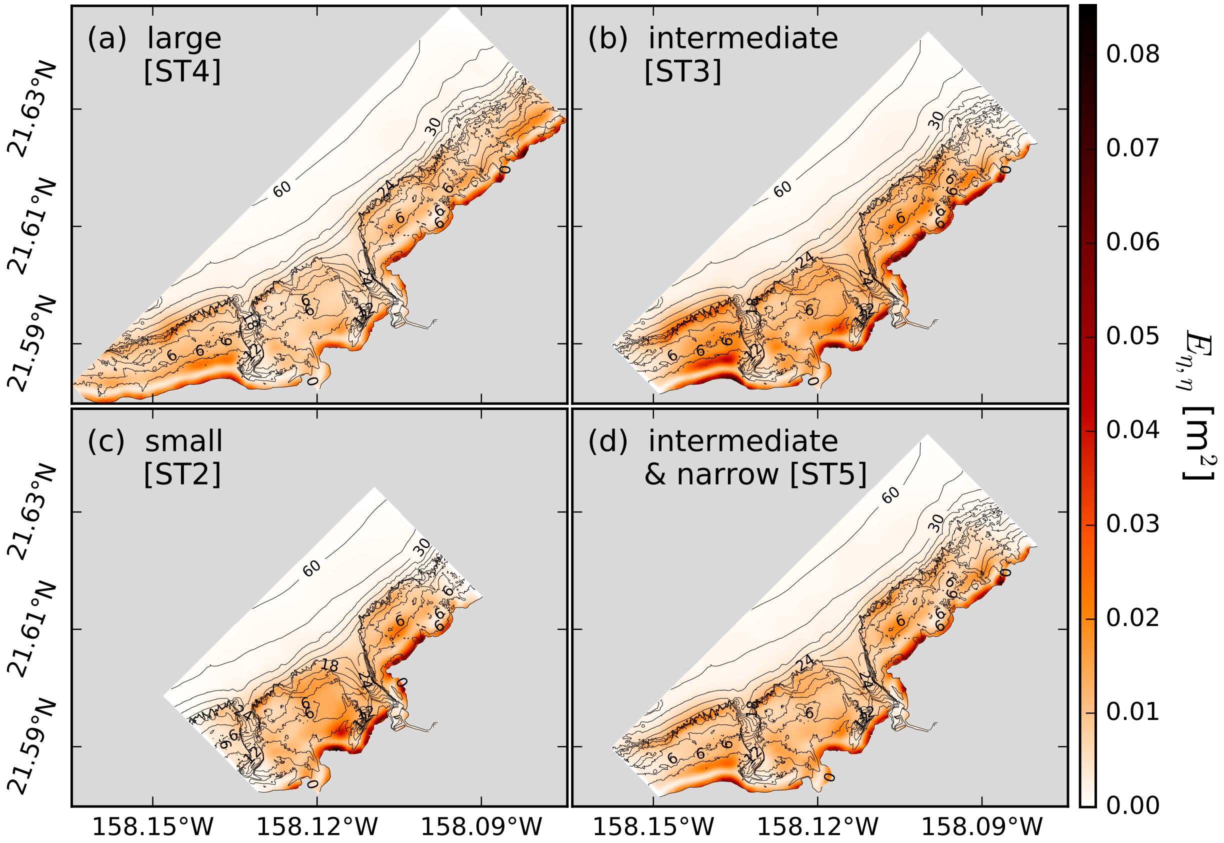

Figure 4.12: Spatial distribution of potential energy in the 2-4 min period band for the (a) large (domain ST4), (b) intermediate (domain ST3), (c) small (domain ST2), and (d) intermediate & narrow (domain ST5), domains, under strong SS forcing.

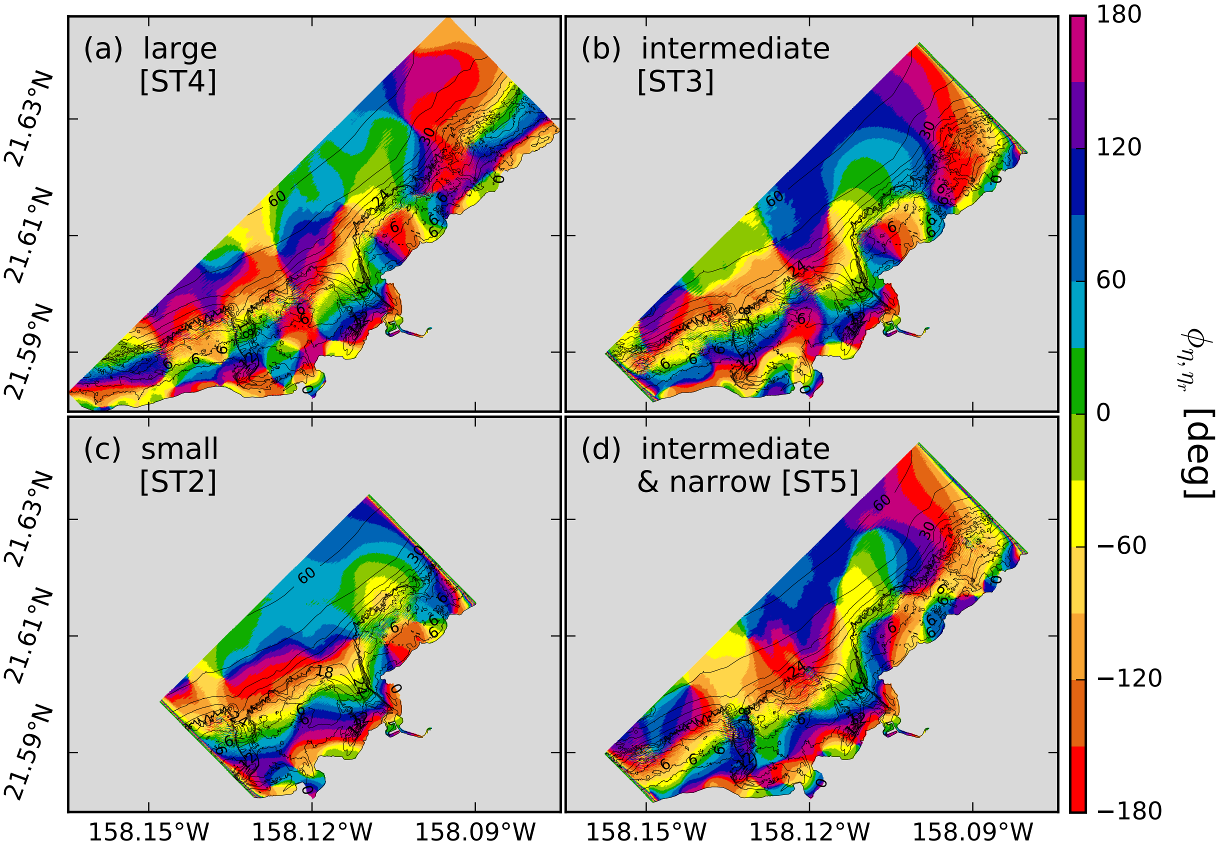

Figure 4.13: Spatial distribution of coherence phase in the 2-4 min period band for the (a) large (domain ST4), (b) intermediate (domain ST3), (c) small (domain ST2), and (d) intermediate & narrow (domain ST5), domains, under strong SS forcing.

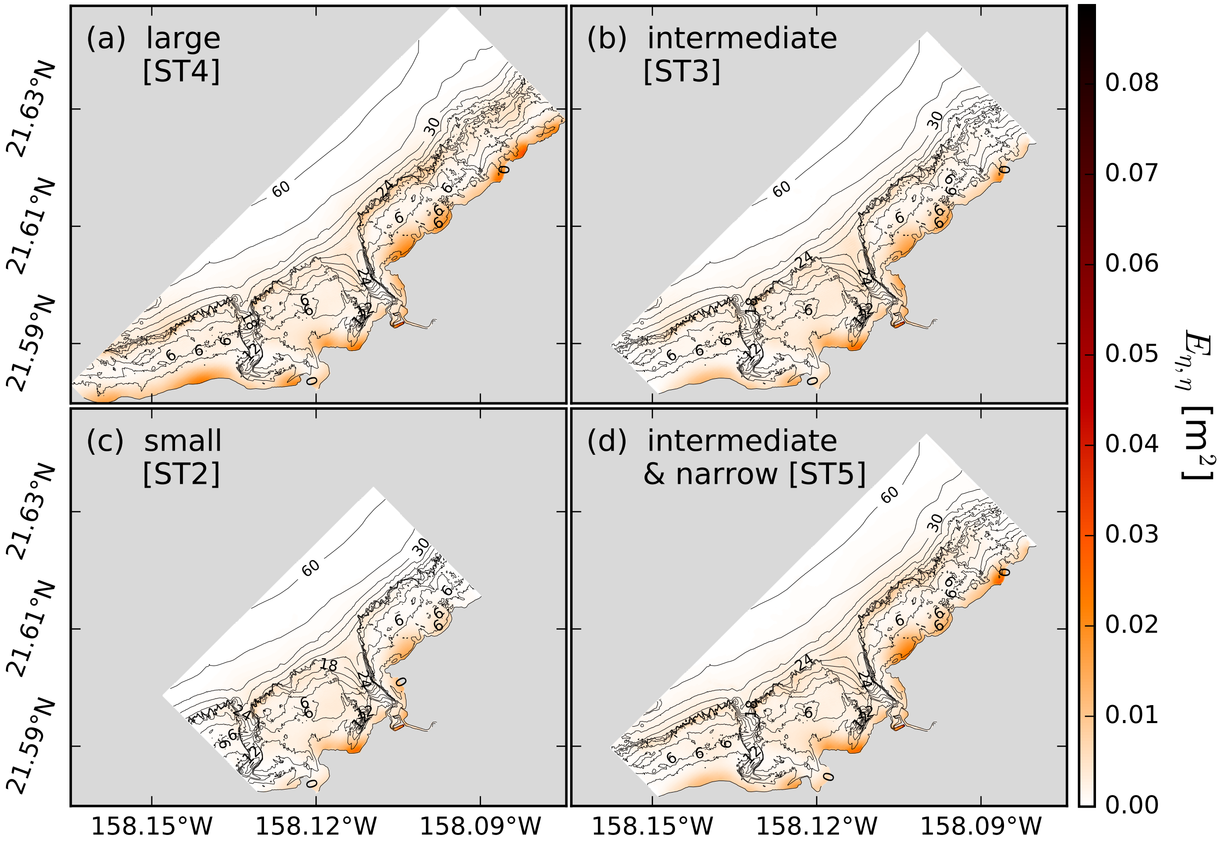

Figure 4.14: Spatial distribution of potential energy in the 4-8 min period band for the (a) large (domain ST4), (b) intermediate (domain ST3), (c) small (domain ST2), and (d) intermediate & narrow (domain ST5), domains, under strong SS forcing.

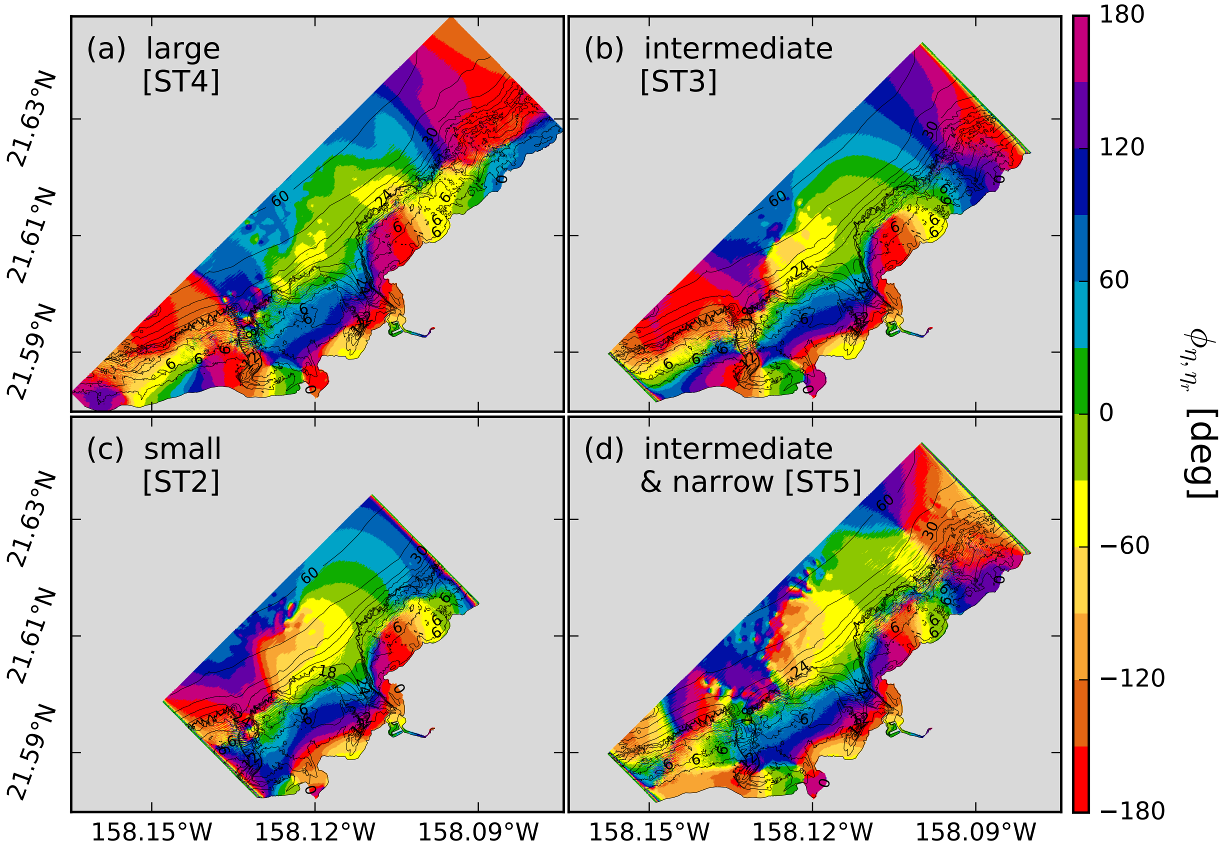

Figure 4.15: Spatial distribution of coherence phase in the 4-8 min period band for the (a) large (domain ST4), (b) intermediate (domain ST3), (c) small (domain ST2), and (d) intermediate & narrow (domain ST5), domains, under strong SS forcing.

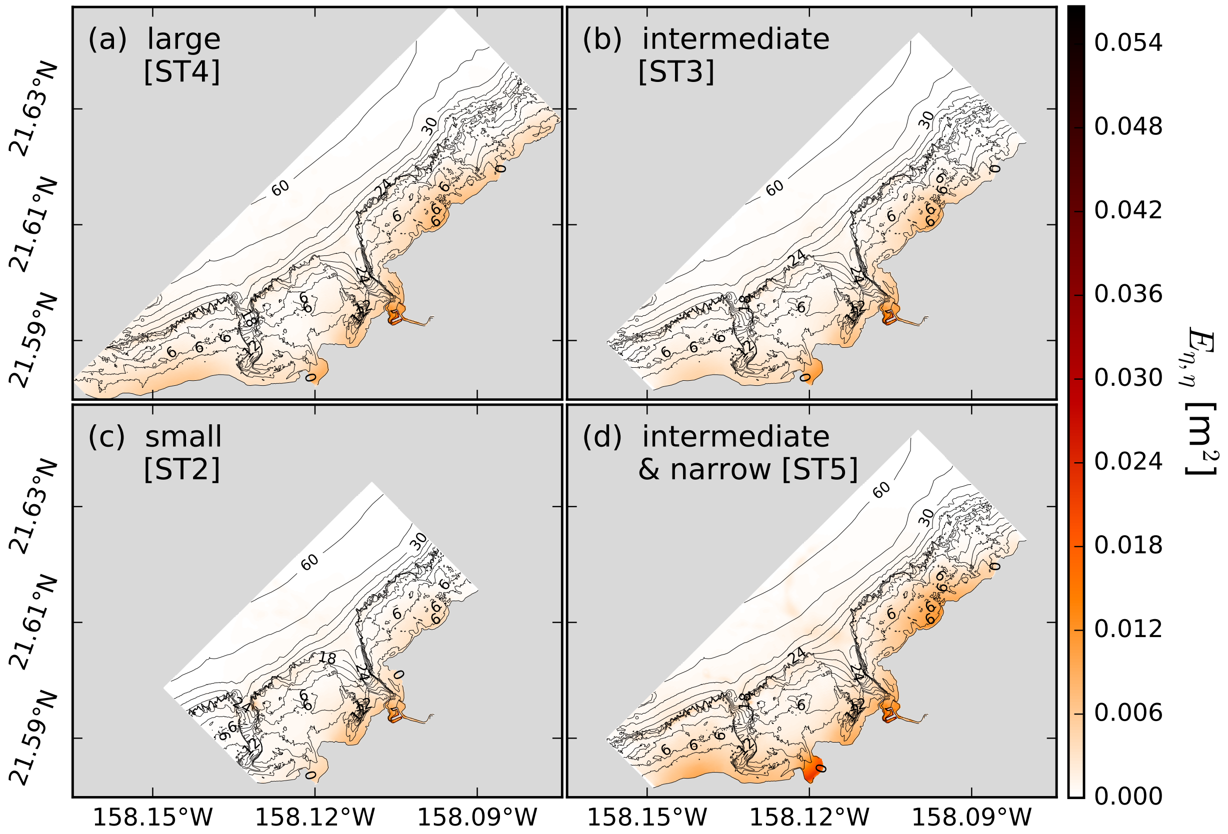

Figure 4.16: Spatial distribution of potential energy in the 8-17 min period band for the (a) large (domain ST4), (b) intermediate (domain ST3), (c) small (domain ST2), and (d) intermediate & narrow (domain ST5), domains, under strong SS forcing.

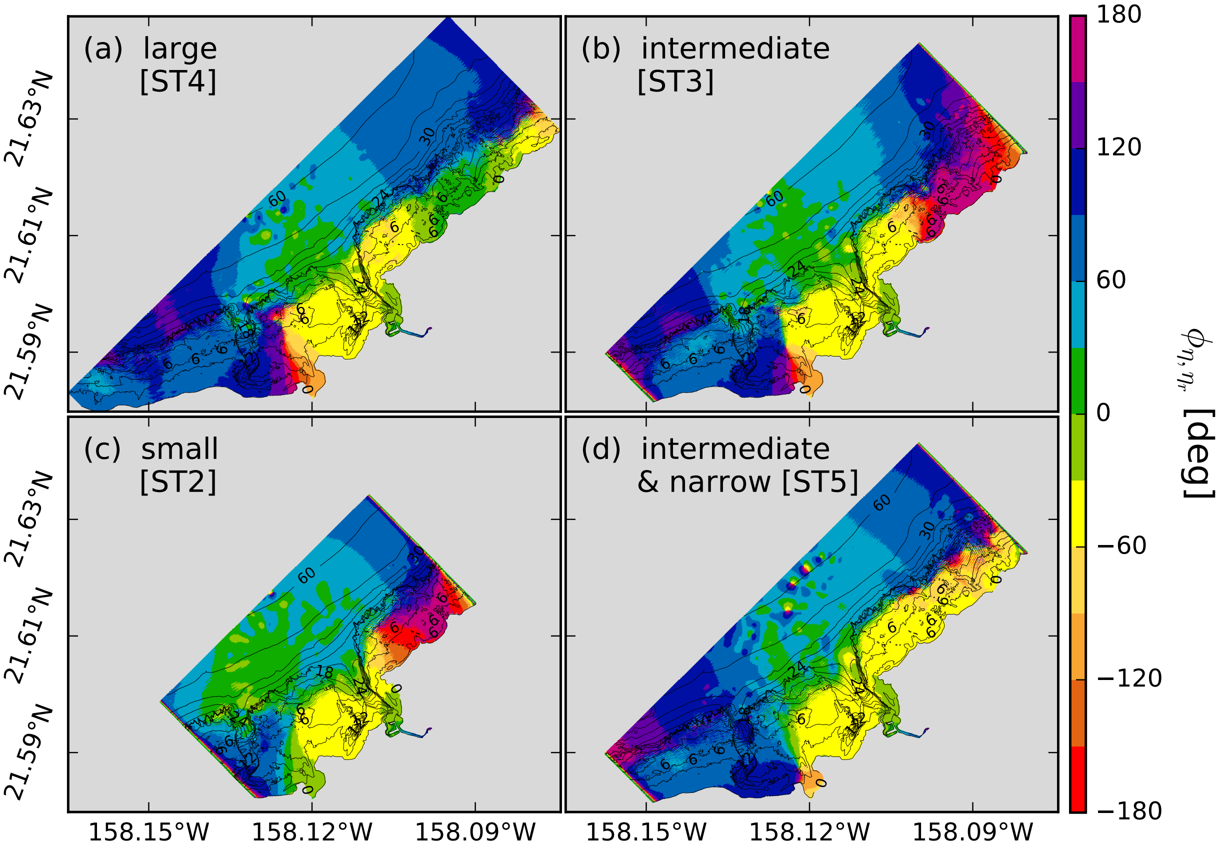

Figure 4.17: Spatial distribution of coherence phase in the 8-17 min period band for the (a) large (domain ST4), (b) intermediate (domain ST3), (c) small (domain ST2), and (d) intermediate & narrow (domain ST5), domains, under strong SS forcing.

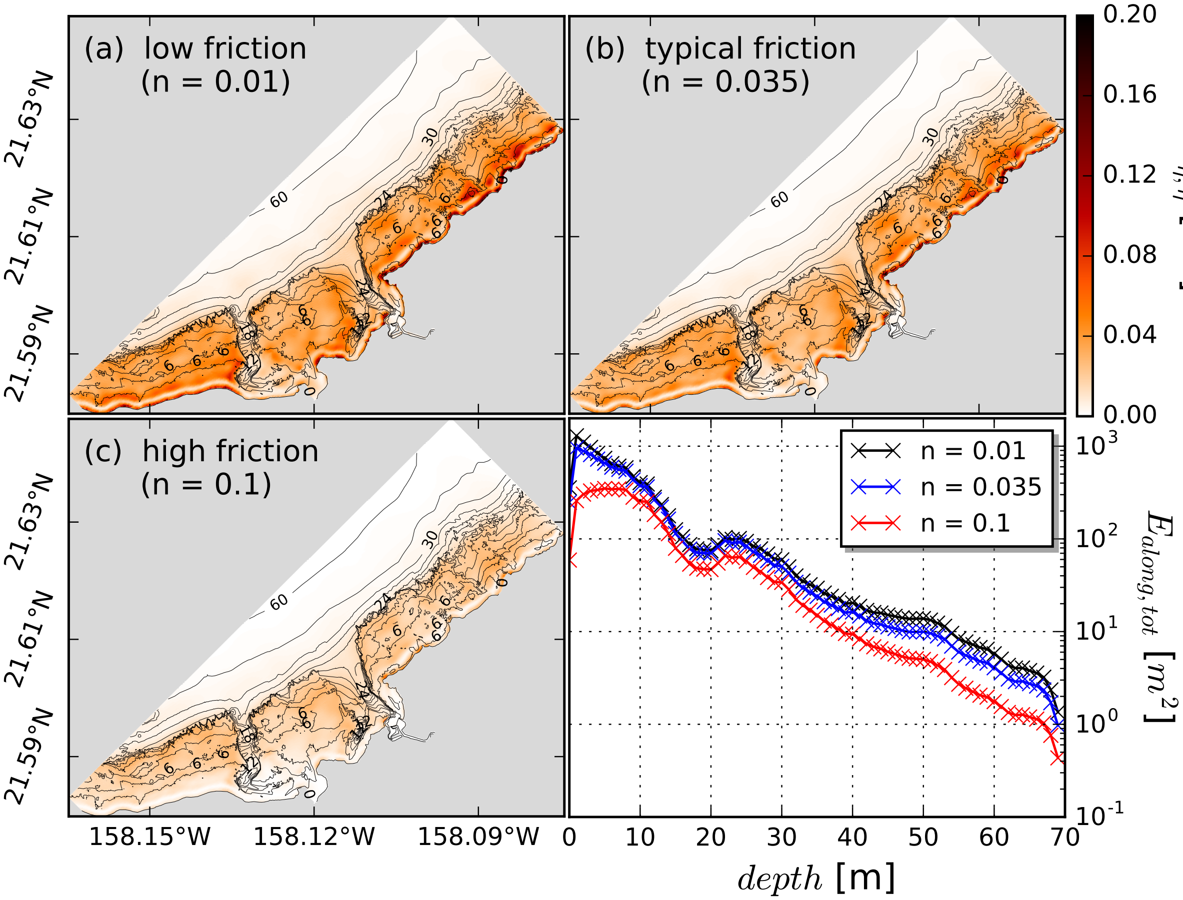

Figure 4.18: Spatial distribution of energy in the 1-2 min period band for the cases of (a) very weak (n = 0.01), (b) typical (n = 0.035), and (c) very strong (n = 0.1), friction coefficients, under strong SS forcing. For each of these friction scenarios, the bottom right panel shows the total energy along the coast between adjacent isobaths separated by 1m.

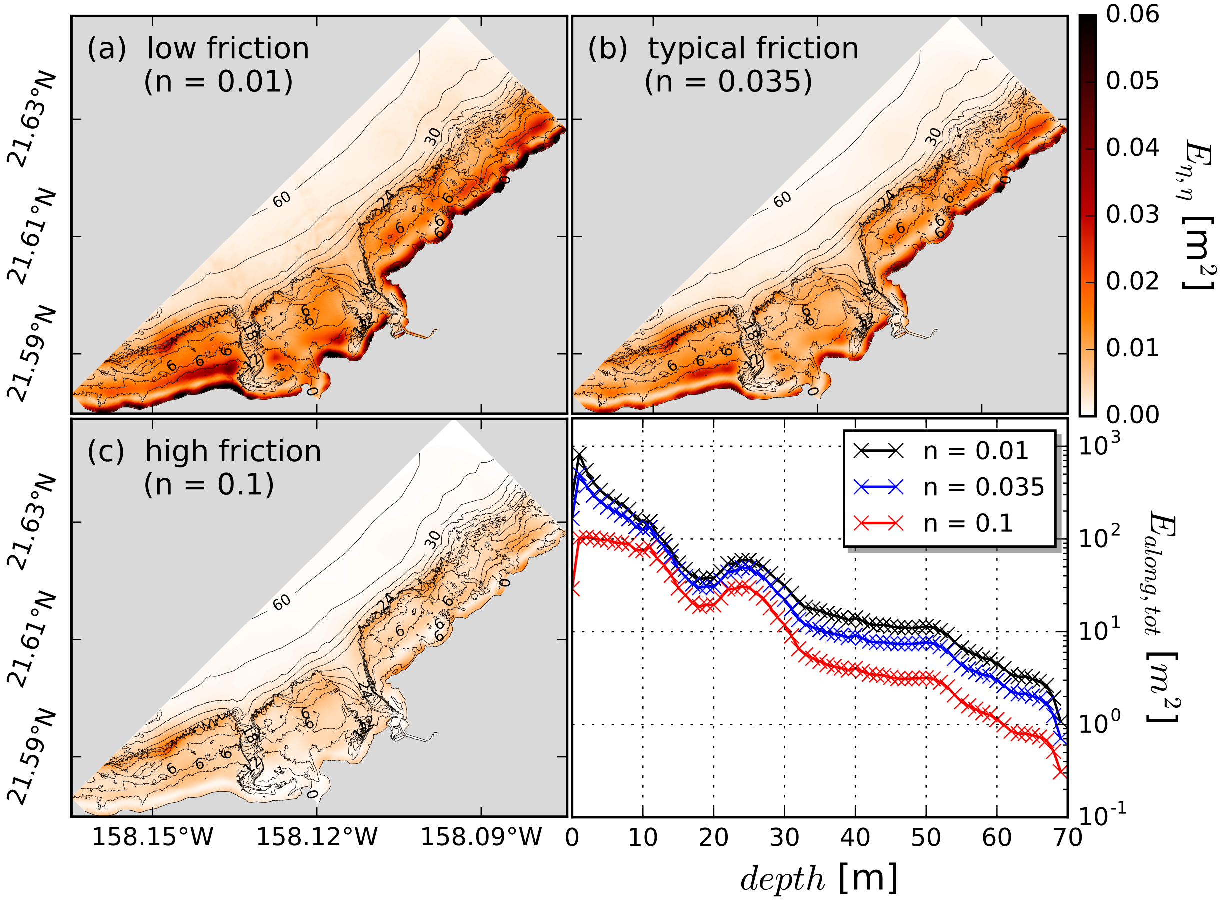

Figure 4.19: Spatial distribution of energy in the 2-4 min period band for the cases of (a) very weak (n = 0.01), (b) typical (n = 0.035), and (c) very strong (n = 0.1), friction coefficients, under strong SS forcing. For each of these friction scenarios, the bottom right panel shows the total energy along the coast between adjacent isobaths separated by 1m.

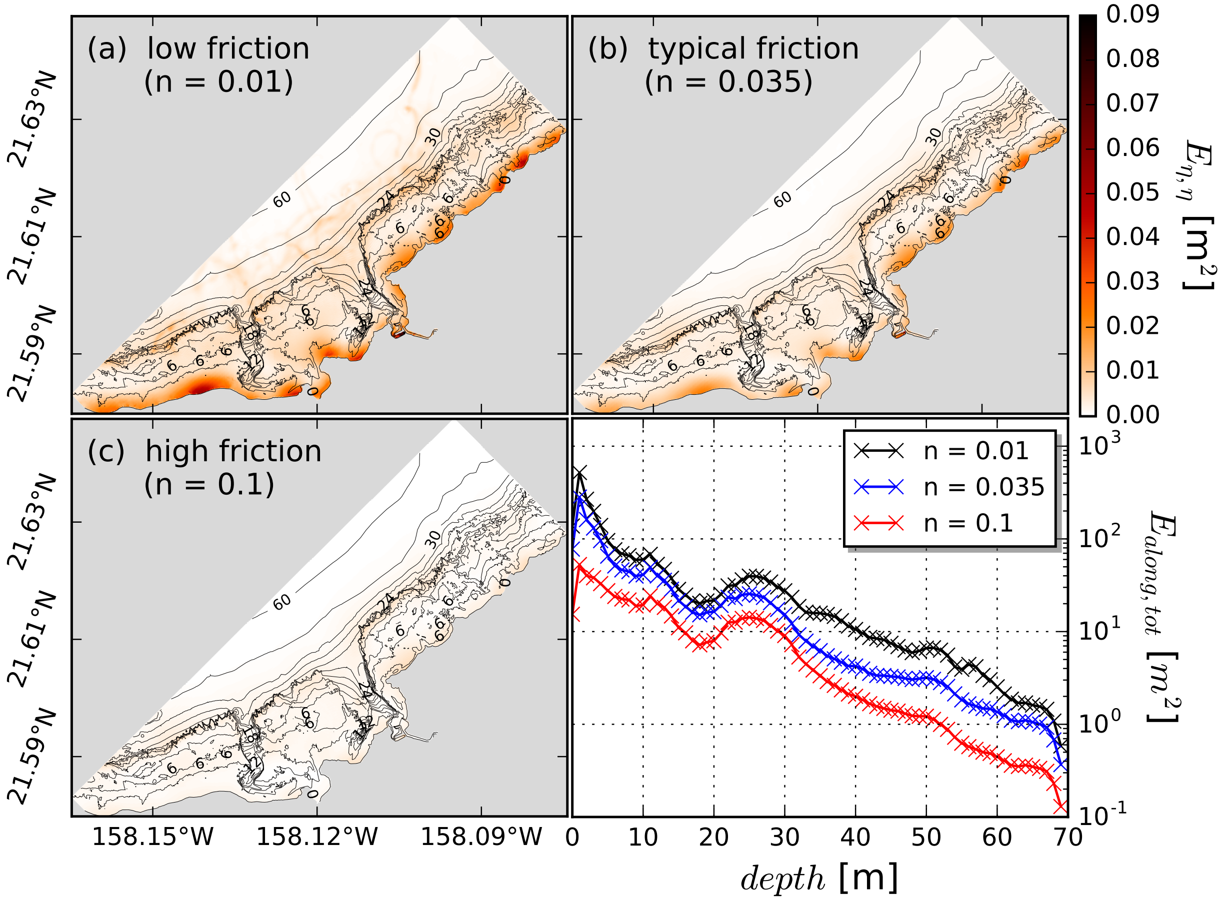

Figure 4.20: Spatial distribution of energy in the 4-8 min period band for the cases of (a) very weak (n = 0.01), (b) typical (n = 0.035), and (c) very strong (n = 0.1), friction coefficients, under strong SS forcing. For each of these friction scenarios, the bottom right panel shows the total energy along the coast between adjacent isobaths separated by 1m.

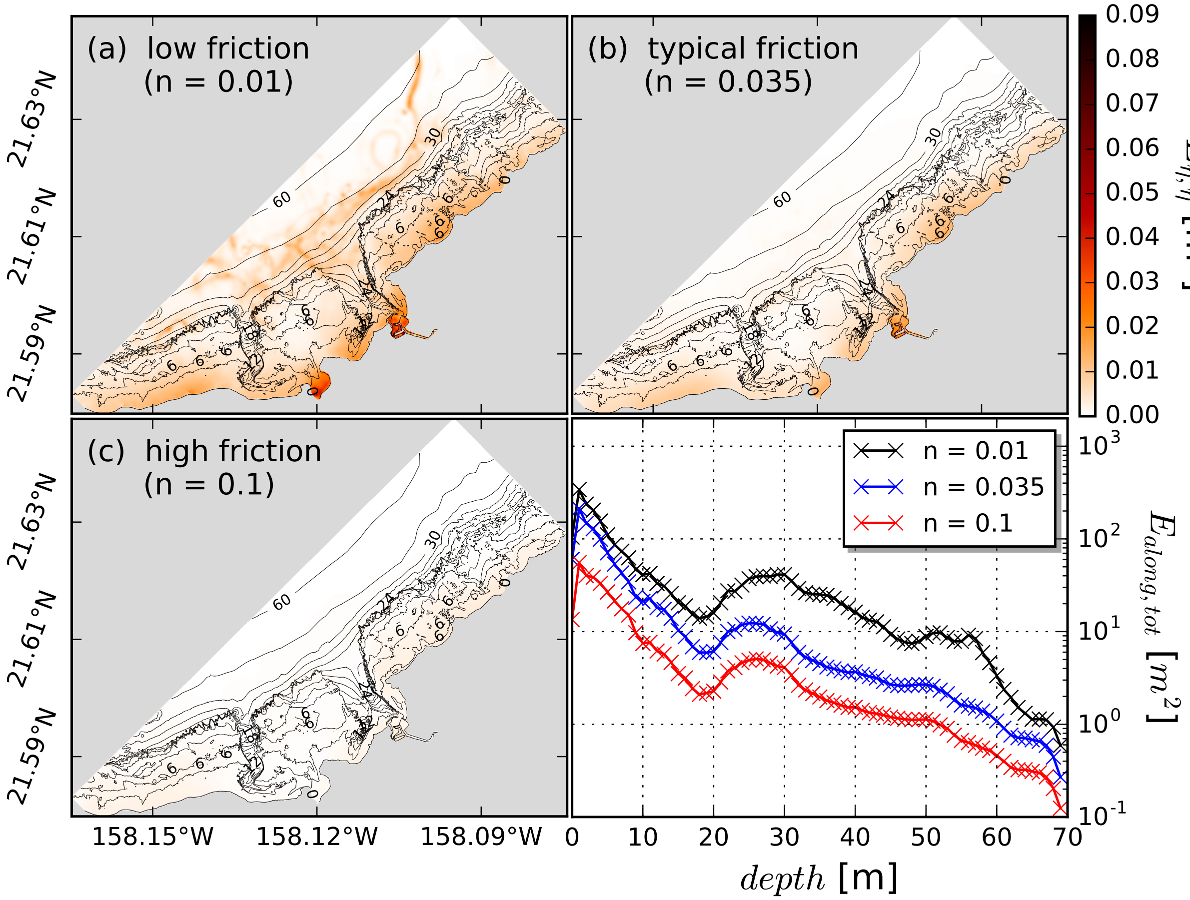

Figure 4.21: Spatial distribution of energy in the 8-17 min period band for the cases of (a) very weak (ST6), (b) typical (ST4), and (c) very strong (ST7), friction coefficients, under strong SS forcing. For each of these friction scenarios, the bottom right panel shows the total energy along the coast between adjacent isobaths separated by 1m.

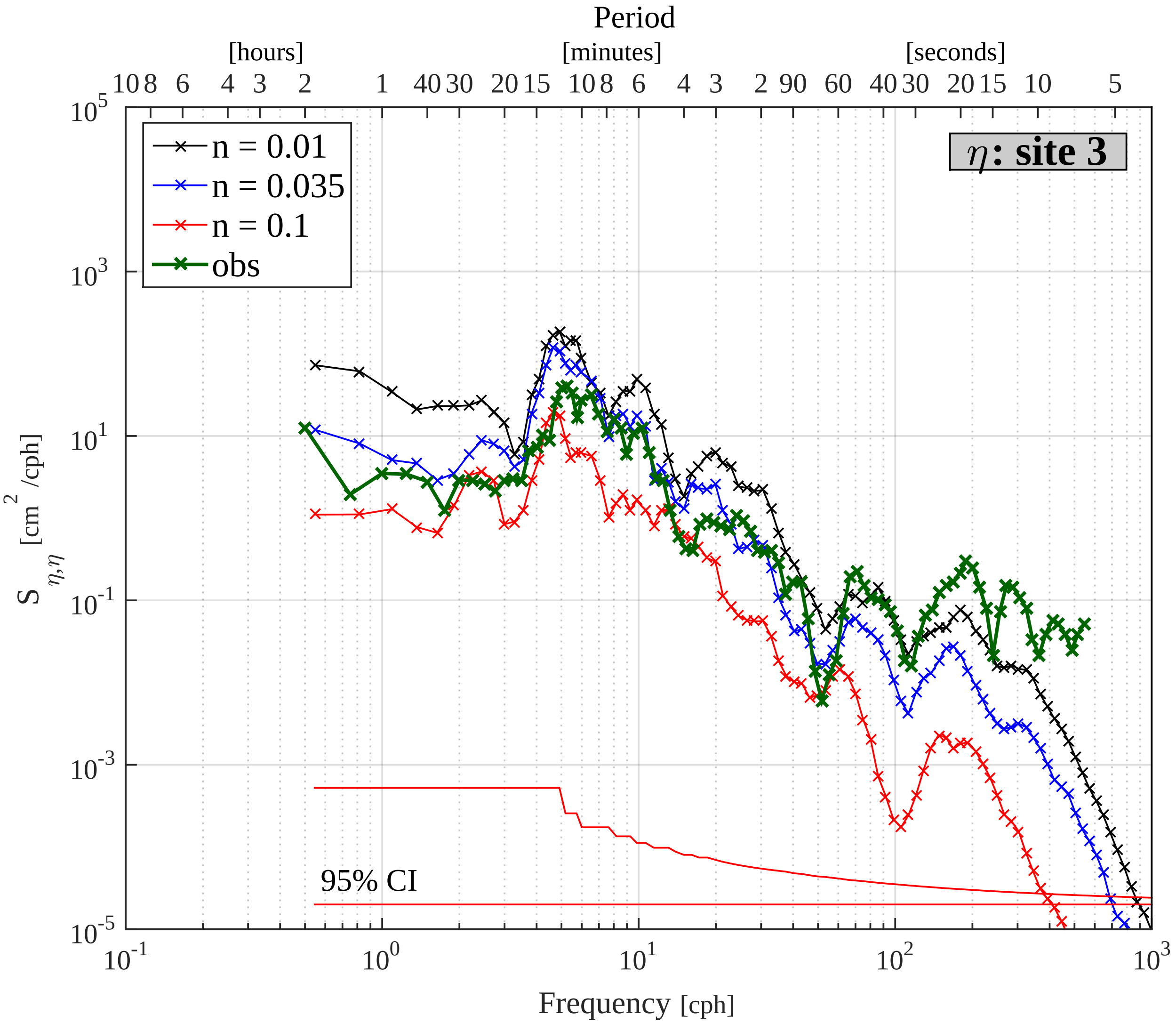

Figure 4.22: Comparison of PSDs generated using model output and observations at site 3, under very strong SS conditions (01/23/14 swell event). The model PSDs correspond to model runs with different values of Manning roughness coefficient (n): (i) little friction (black curve, $n = 0.01$); (ii) typical friction for north shore bottom (blue curve, $n = 0.035$); and, (iii) strong friction (red curve, $n = 0.1$). The green curve is the observed PSD. The 95% confidence interval for each independent spectrum estimate is shown at the bottom.

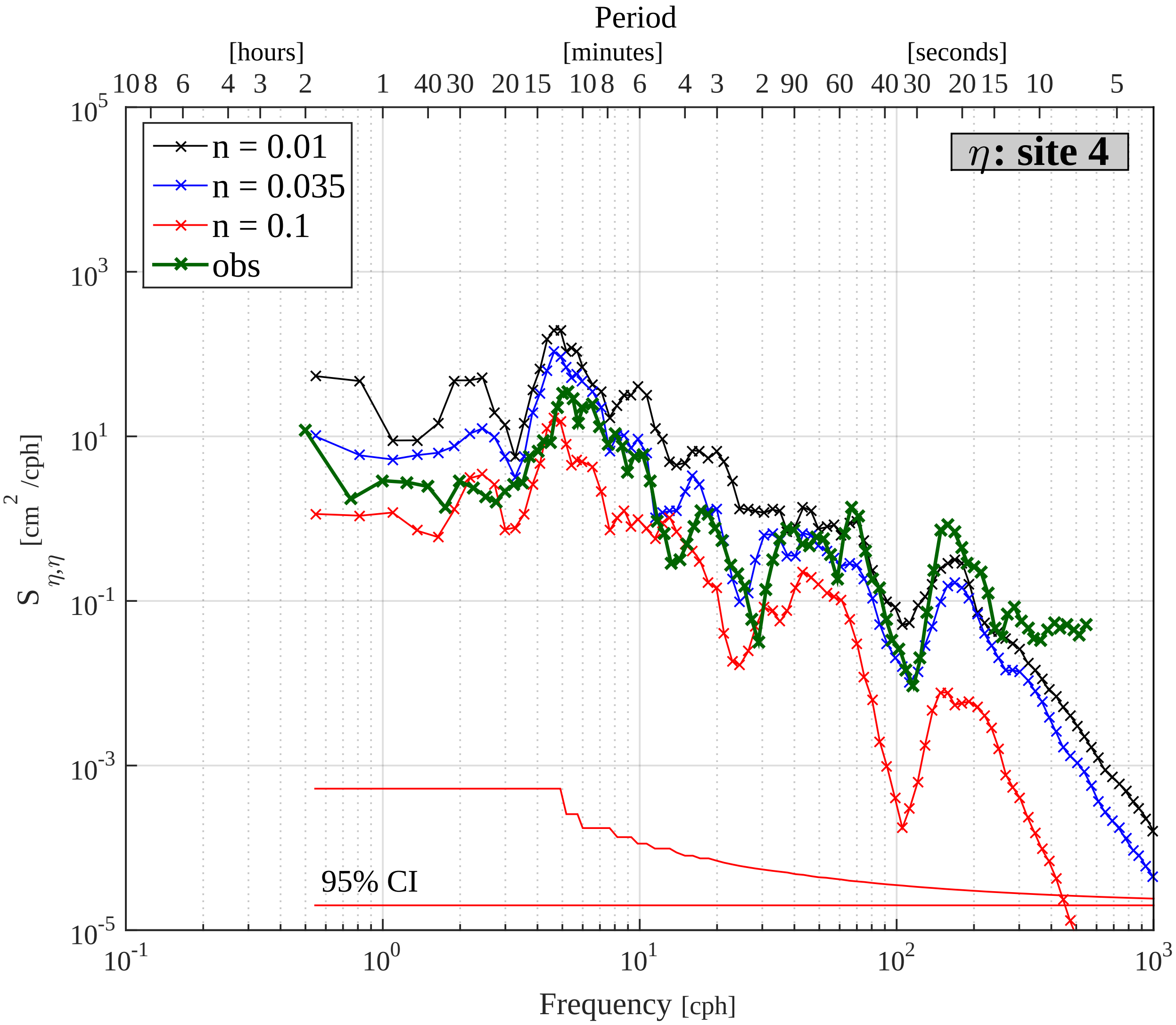

Figure 4.23: Comparison of PSDs generated using model output and observations at site 4, under very strong SS conditions (01/23/14 swell event). The model PSDs correspond to model runs with different values of Manning roughness coefficient (n): (i) little friction (black curve, $n = 0.01$); (ii) typical friction for north shore bottom (blue curve, $n = 0.035$); and, (iii) strong friction (red curve, $n = 0.1$). The green curve is the observed PSD. The 95% confidence interval for each independent spectrum estimate is shown at the bottom.

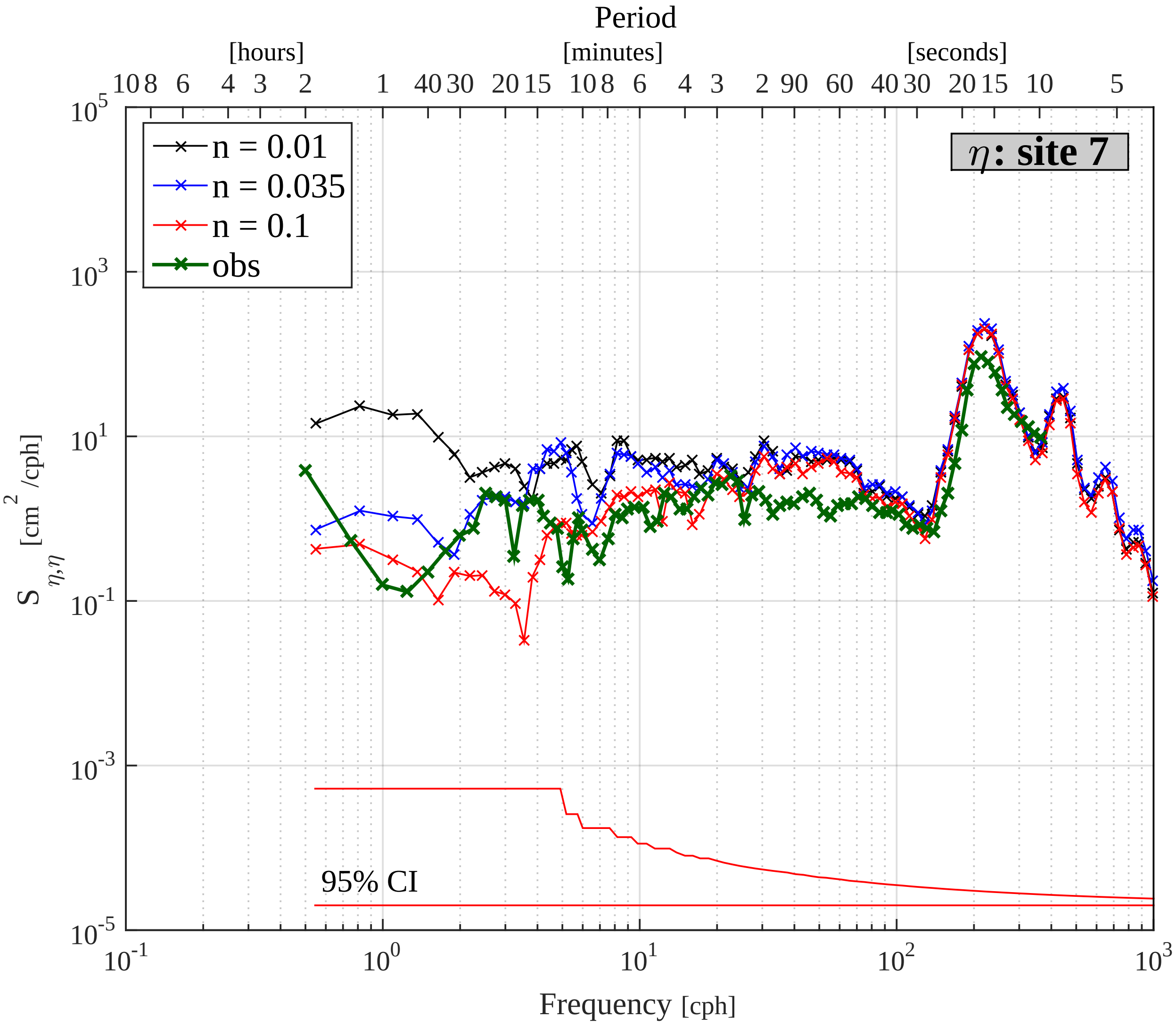

Figure 4.24: Comparison of PSDs generated using model output and observations at site 7, under very strong SS conditions (01/23/14 swell event). The model PSDs correspond to model runs with different values of Manning roughness coefficient (n): (i) little friction (black curve, $n = 0.01$); (ii) typical friction for north shore bottom (blue curve, $n = 0.035$); and, (iii) strong friction (red curve, $n = 0.1$). The green curve is the observed PSD. The 95% confidence interval for each independent spectrum estimate is shown at the bottom.

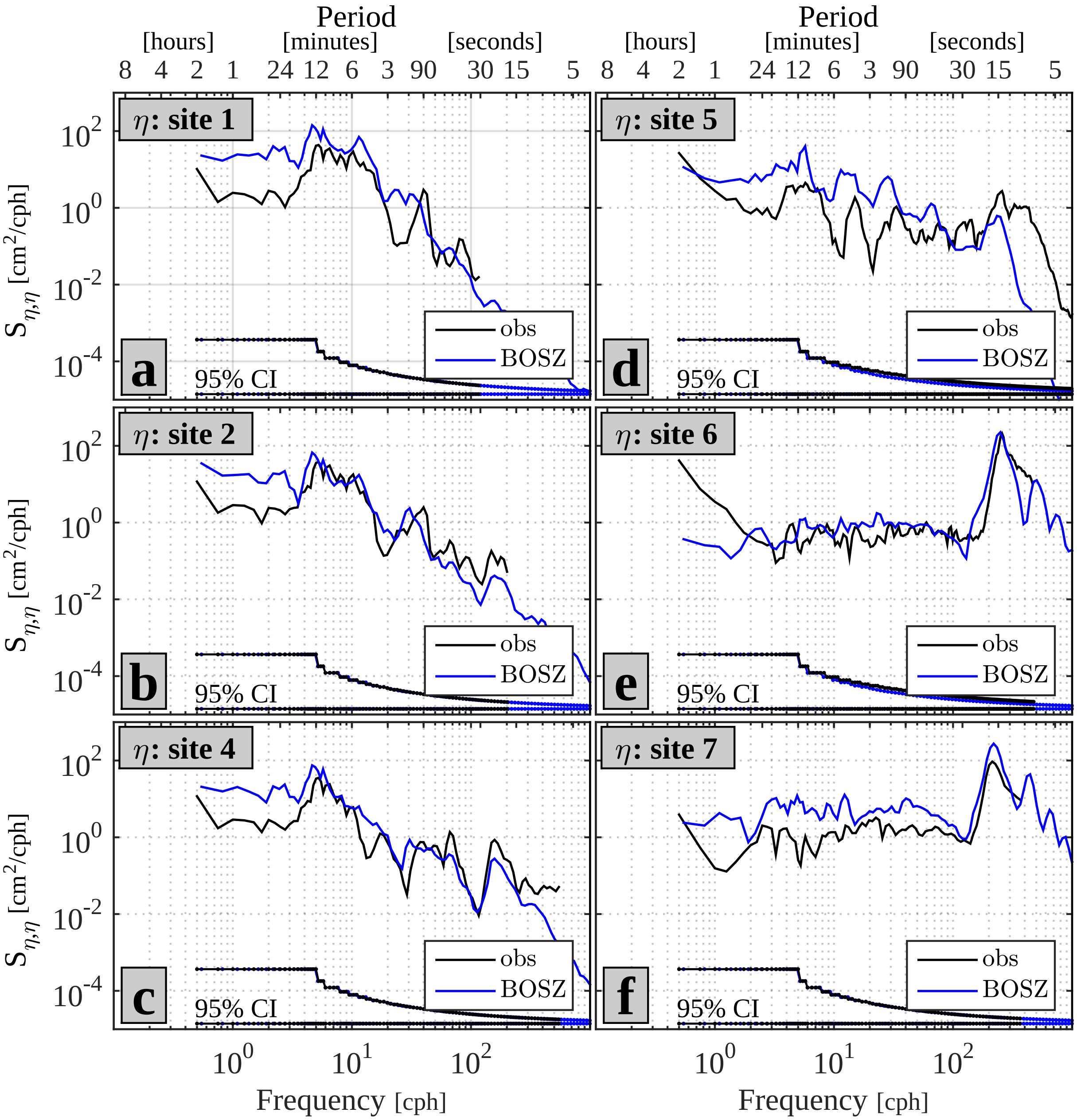

Figure 4.25: Comparison of PSDs generated under strong SS conditions using model output (blue curves) and observations (black curves) at sites (a) 1, (b) 2, (c) 4, and (d) 7, for the 01/23/14 event; and (e) 5, and (f) 6, for the 02/08/12 event. The 95% confidence interval for each independent spectrum estimate is shown at the bottom.

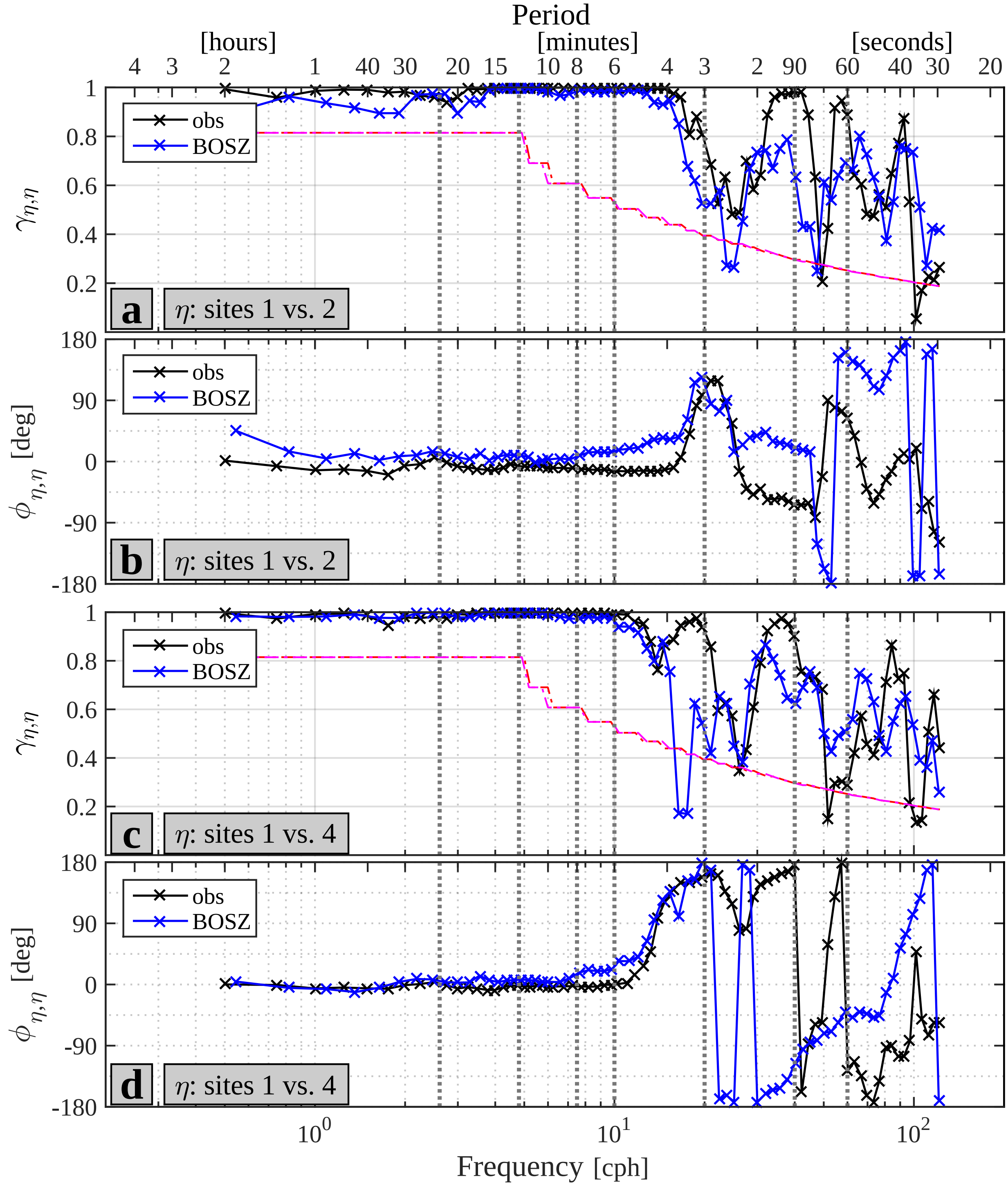

Figure 4.26: Comparison of coherences generated using model output and observations for the pairs of sites 1 vs. 2 (01/23/14 SS event, panels a&b); and, 1 vs. 4 (01/23/14 SS event, panels c&d).

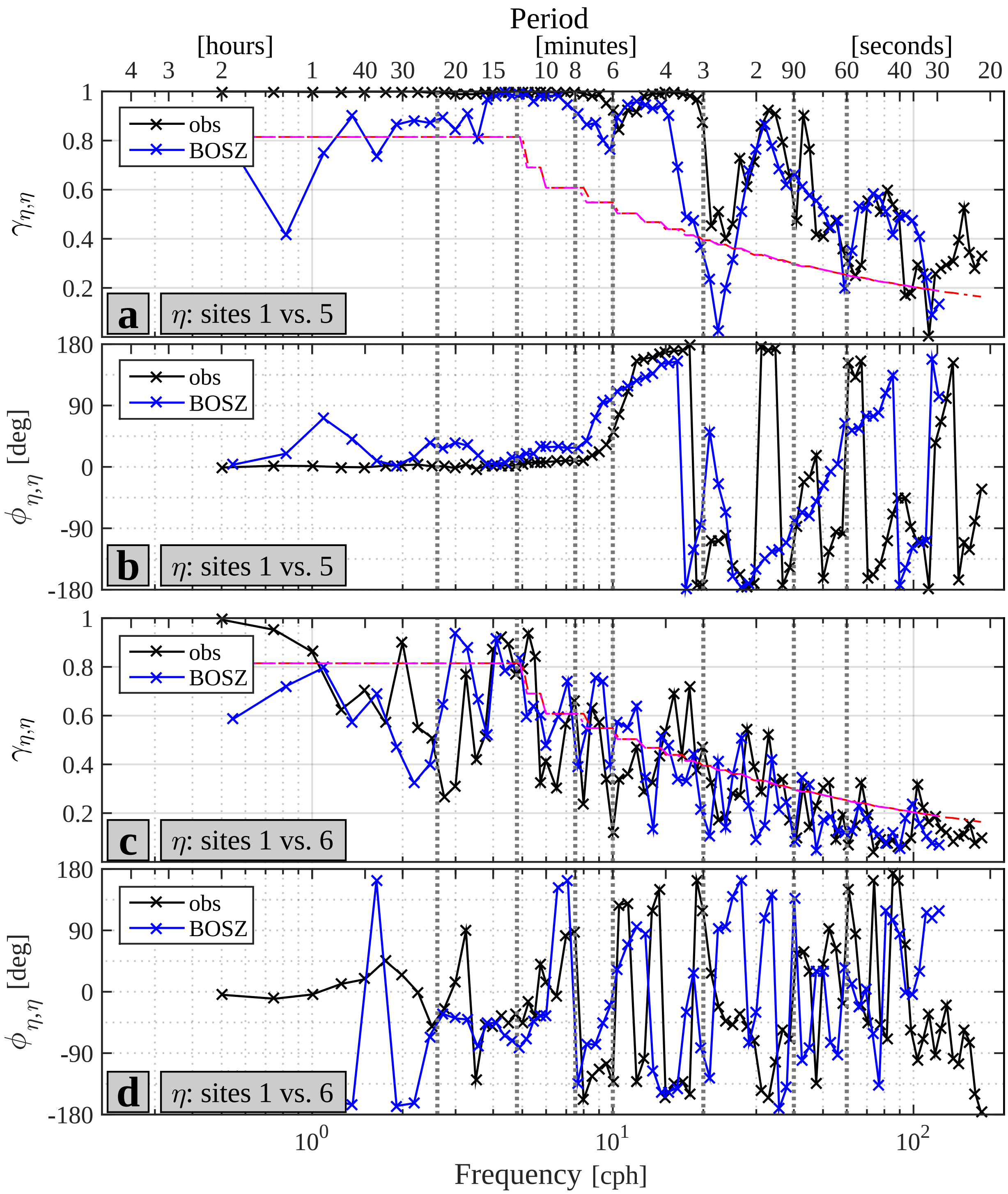

Figure 4.27: Comparison of coherences generated using model output and observations for the pairs of sites 1 vs. 5 (02/08/12 SS event, panels a&b); and, 1 vs. 6 (02/08/12 SS event, panels c&d).

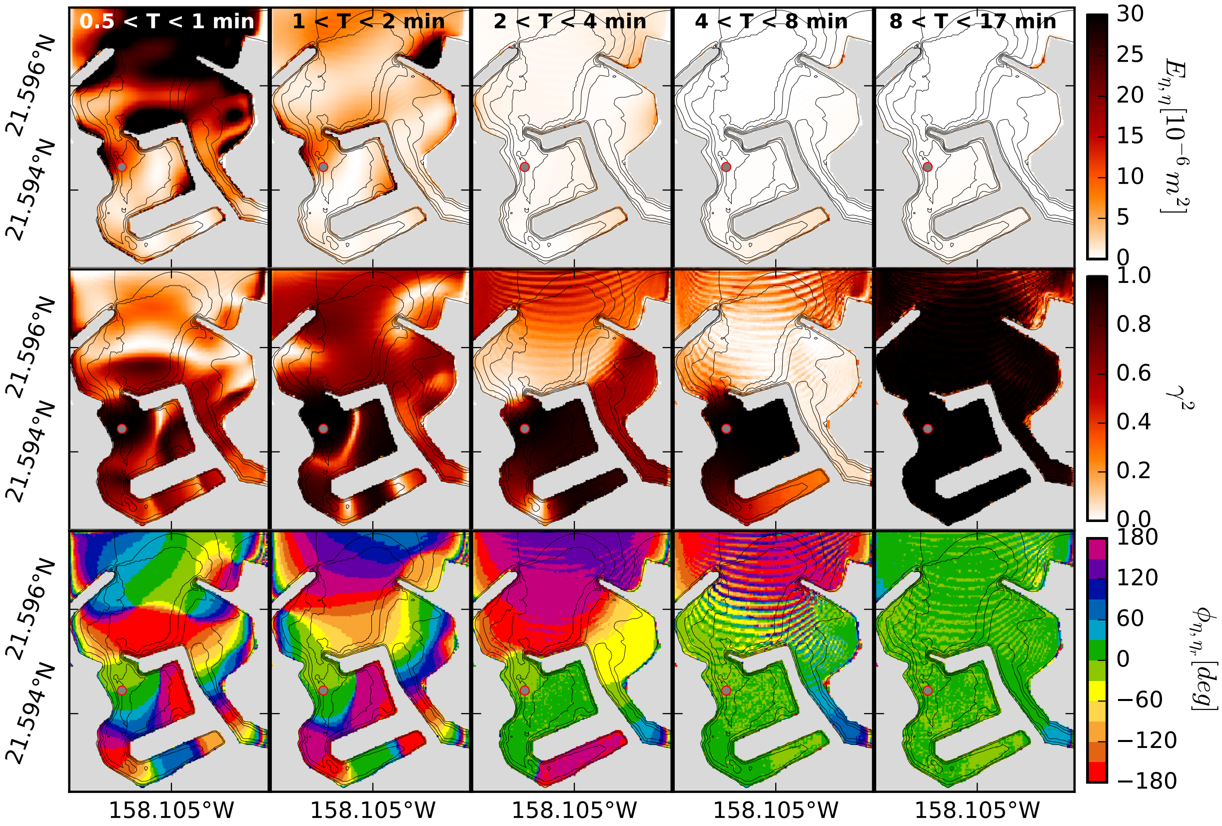

Figure 4.28: Maps of energy, coherence amplitude squared, and coherence phase, inside Hale'iwa Harbor in the 0.5-1, 1-2, 2-4, 4-8, and 8-17 min period bands using output from a model run isolating the harbor (run R7). The reference point site for the coherence analysis is indicated with gray circles.

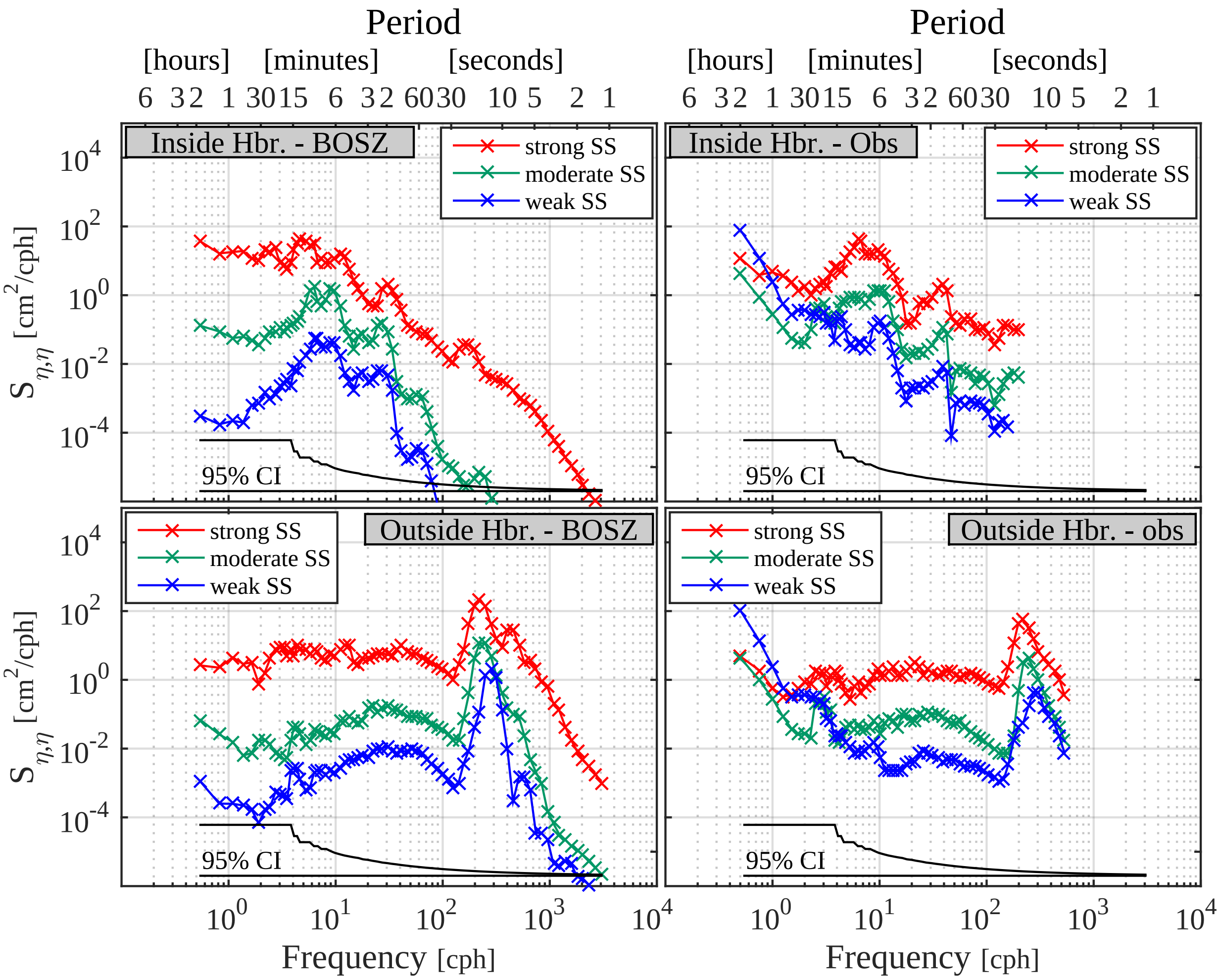

Figure 4.29: Model vs. observed PSDs under weak, moderate, and strong SS forcing conditions, inside (site 2), and outside (site 7) Hale'iwa Harbor.

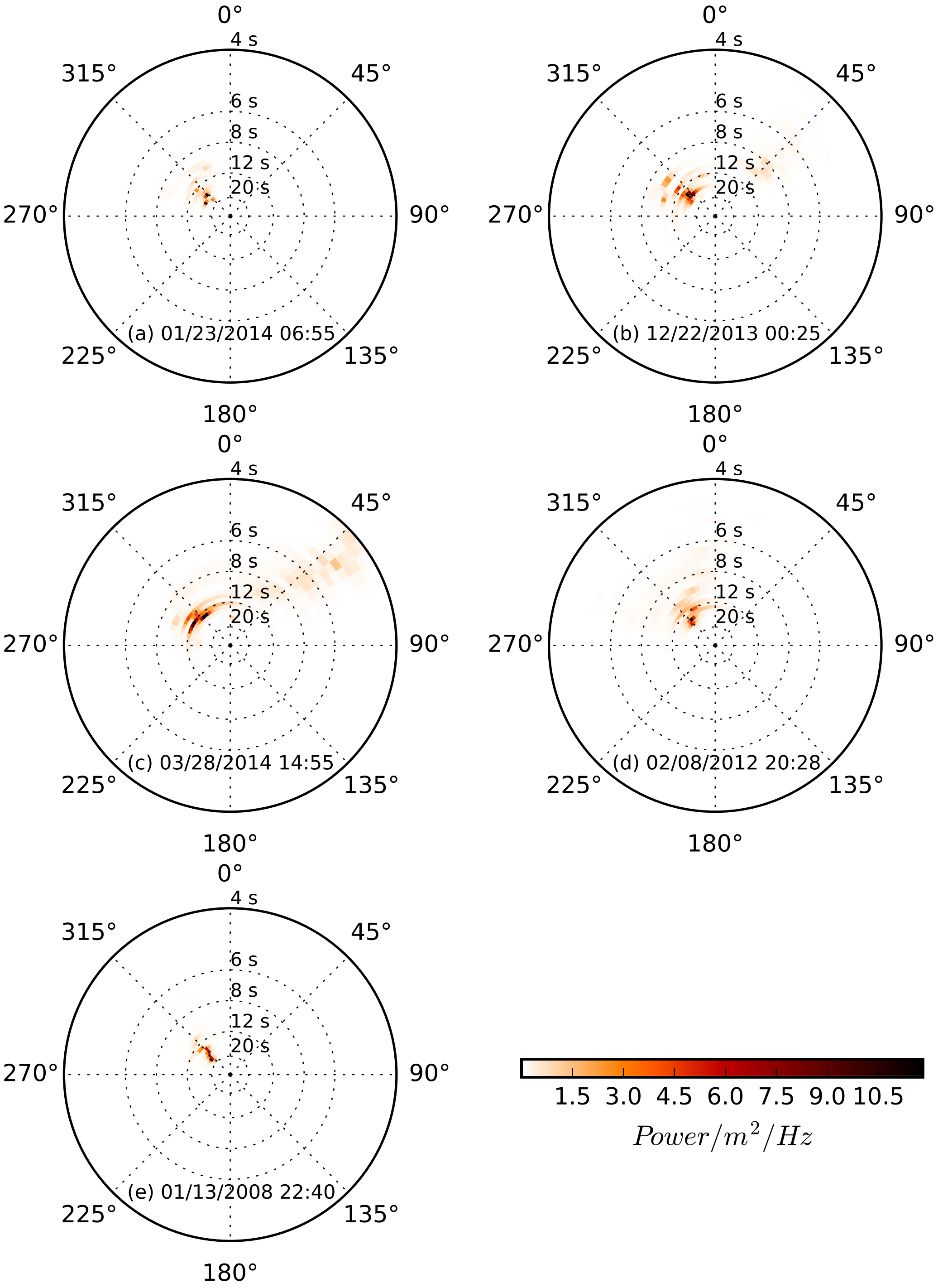

Figure 4.30: Directional spectra of all SS forcing events used in this numerical modeling study. These SS events represent cases of (a) strong, (b) moderate, (c) weak, (d) strong, and (e) strong SS forcing. UTC times are indicated near the bottom of each plot.

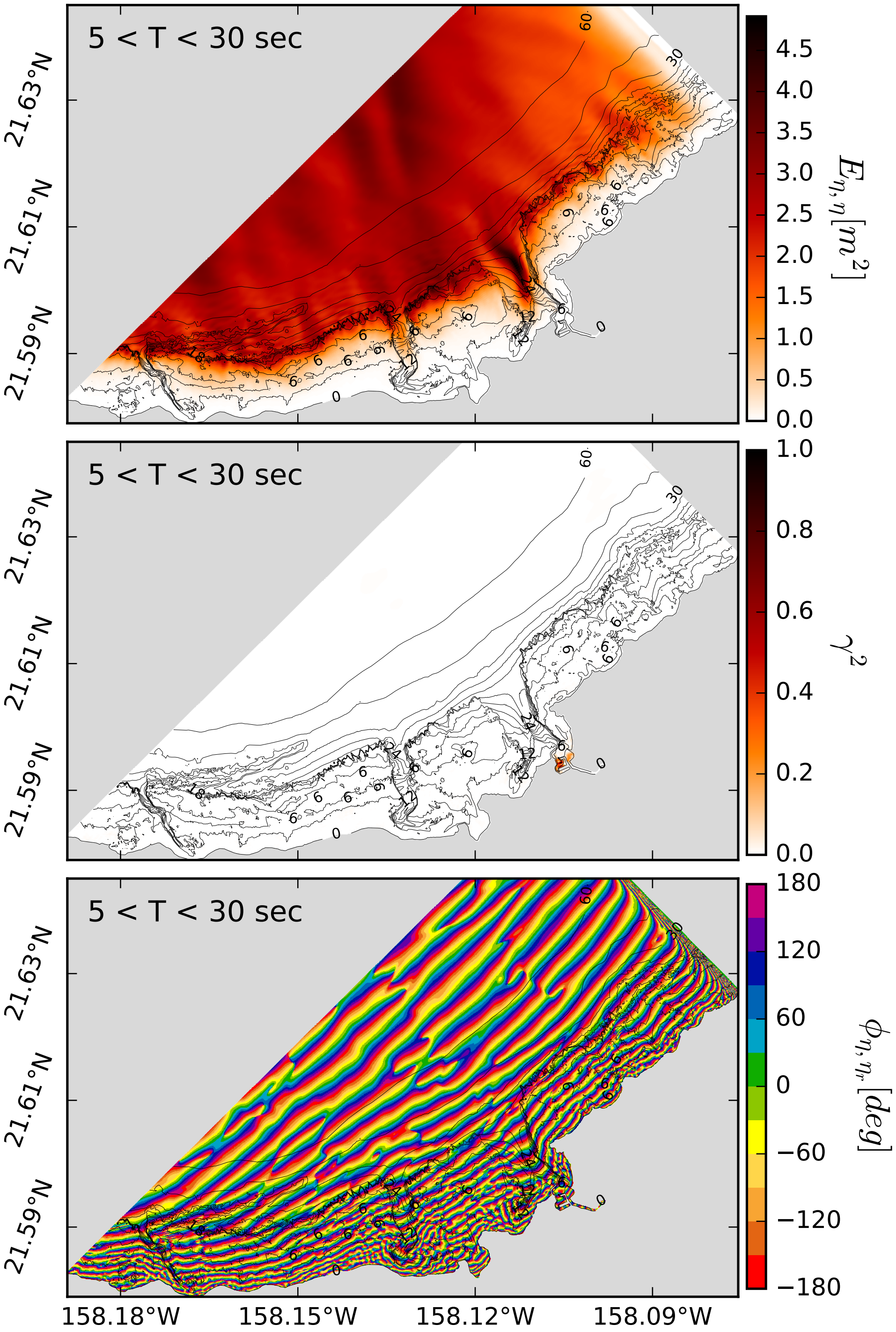

Figure 4.31: Maps of (a) potential energy, (b) coherence amplitude squared, and (c) coherence phase, in the 5-30 sec SS period band, using output from the largest model run with strong SS forcing (run R2).

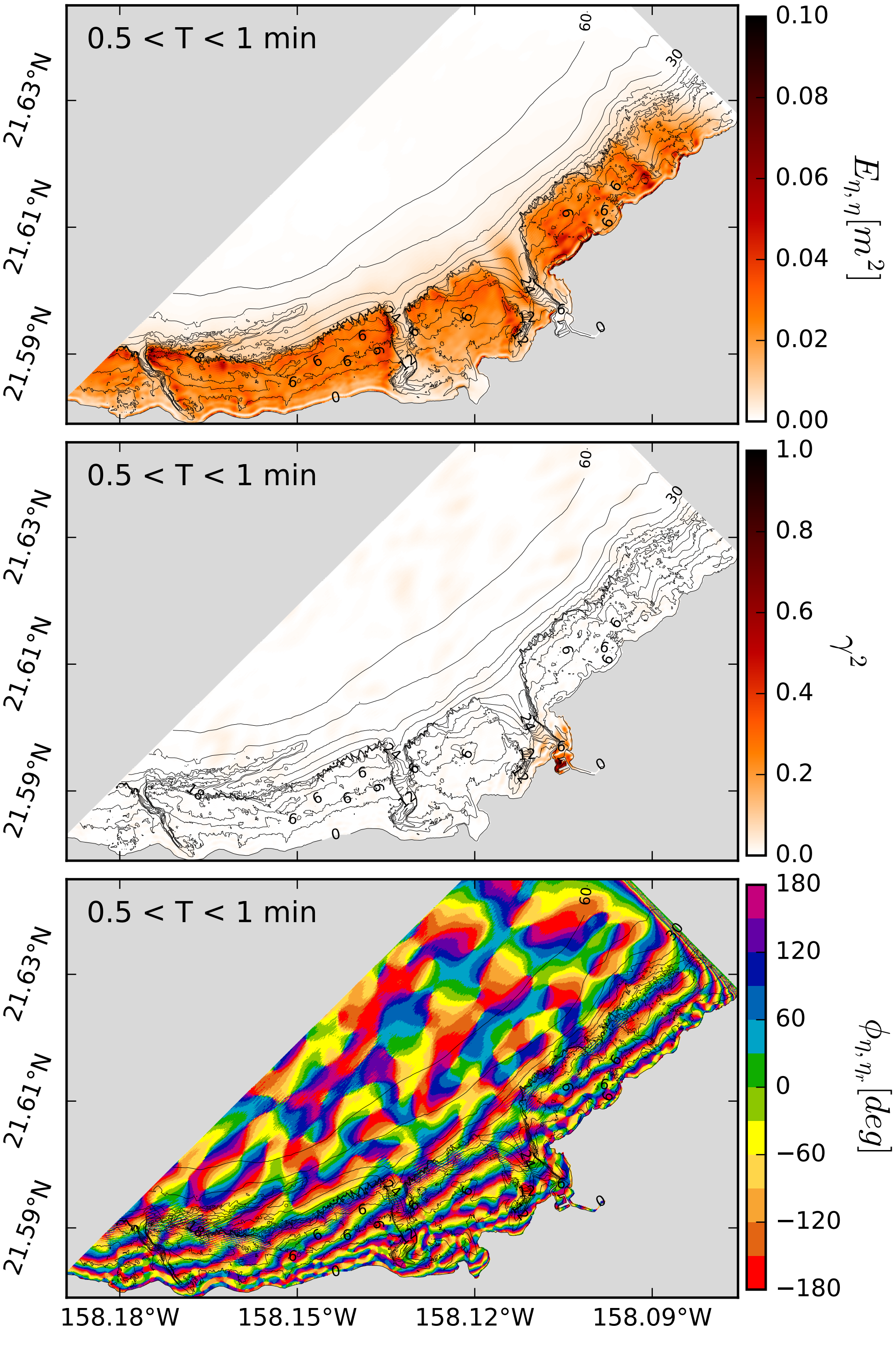

Figure 4.32: Maps of (a) potential energy, (b) coherence amplitude squared, and (c) coherence phase, in the 0.5-1 min period band, using output from the largest model run with strong SS forcing (run R2)

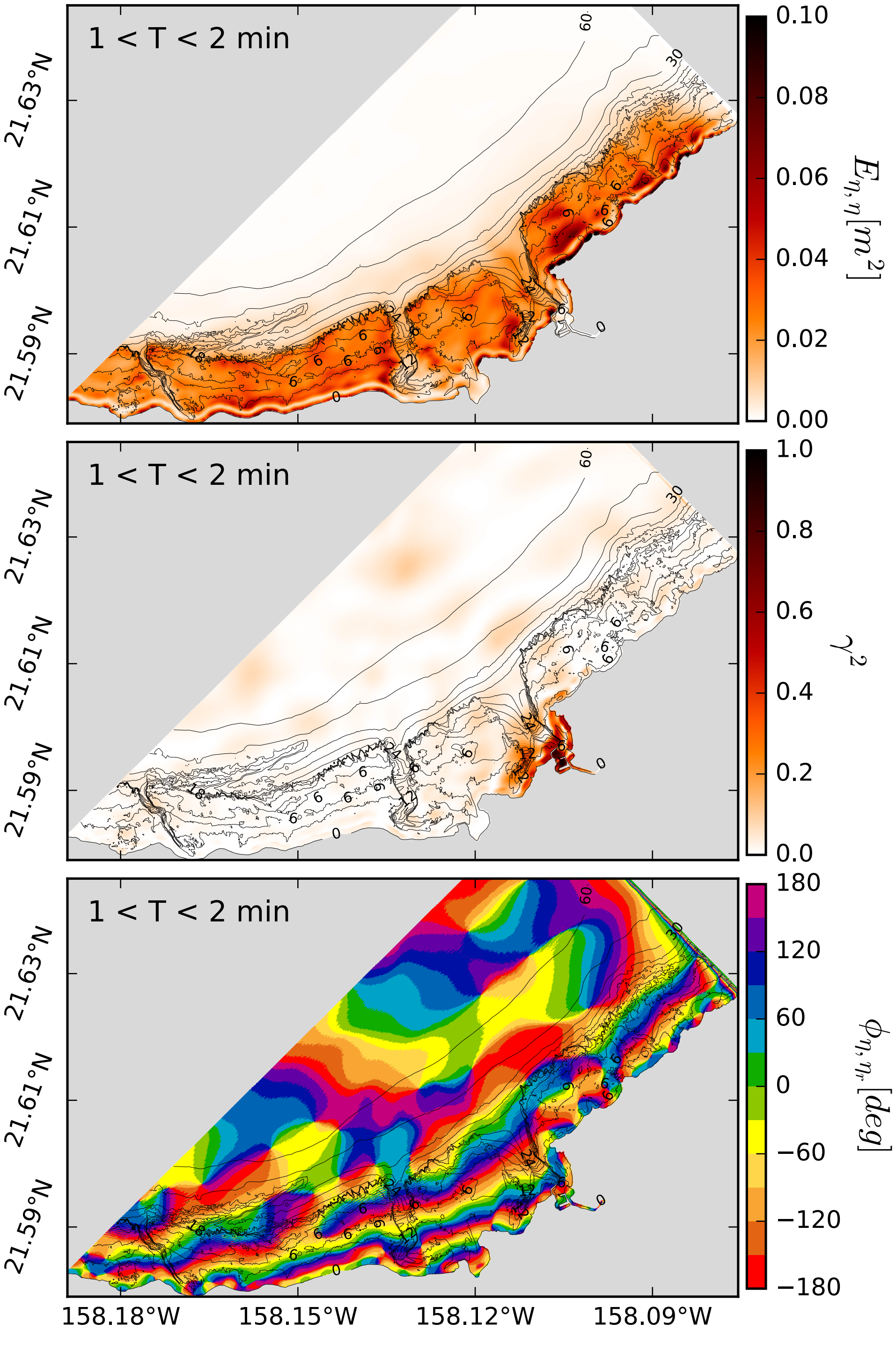

Figure 4.33: Maps of (a) potential energy, (b) coherence amplitude squared, and (c) coherence phase, in the 1-2 min period band, using output from the largest model run with strong SS forcing (domain R2).

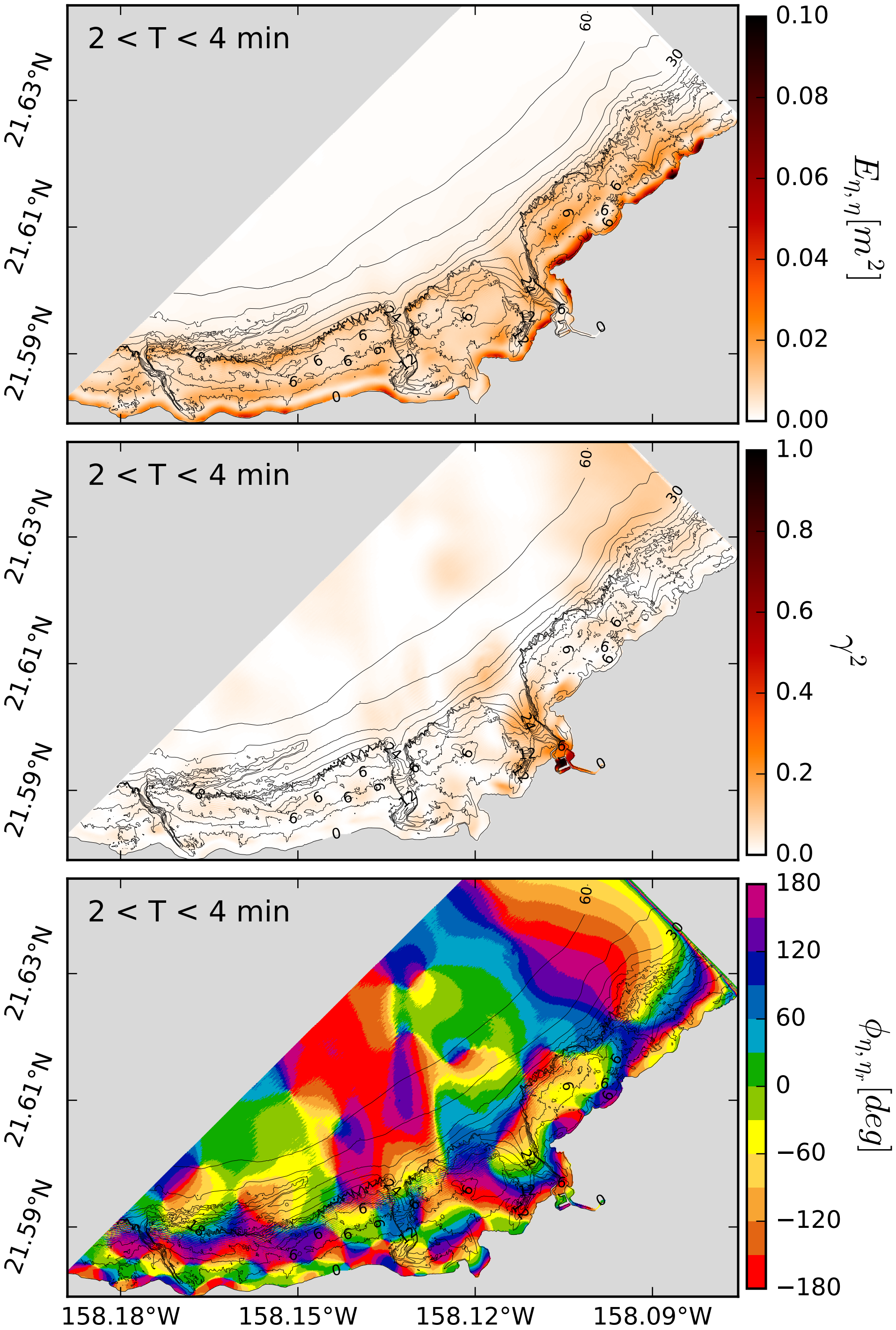

Figure 4.34: Maps of (a) potential energy, (b) coherence amplitude squared, and (c) coherence phase, in the 2-4 min period band, using output from the largest model run with strong SS forcing (run R2).

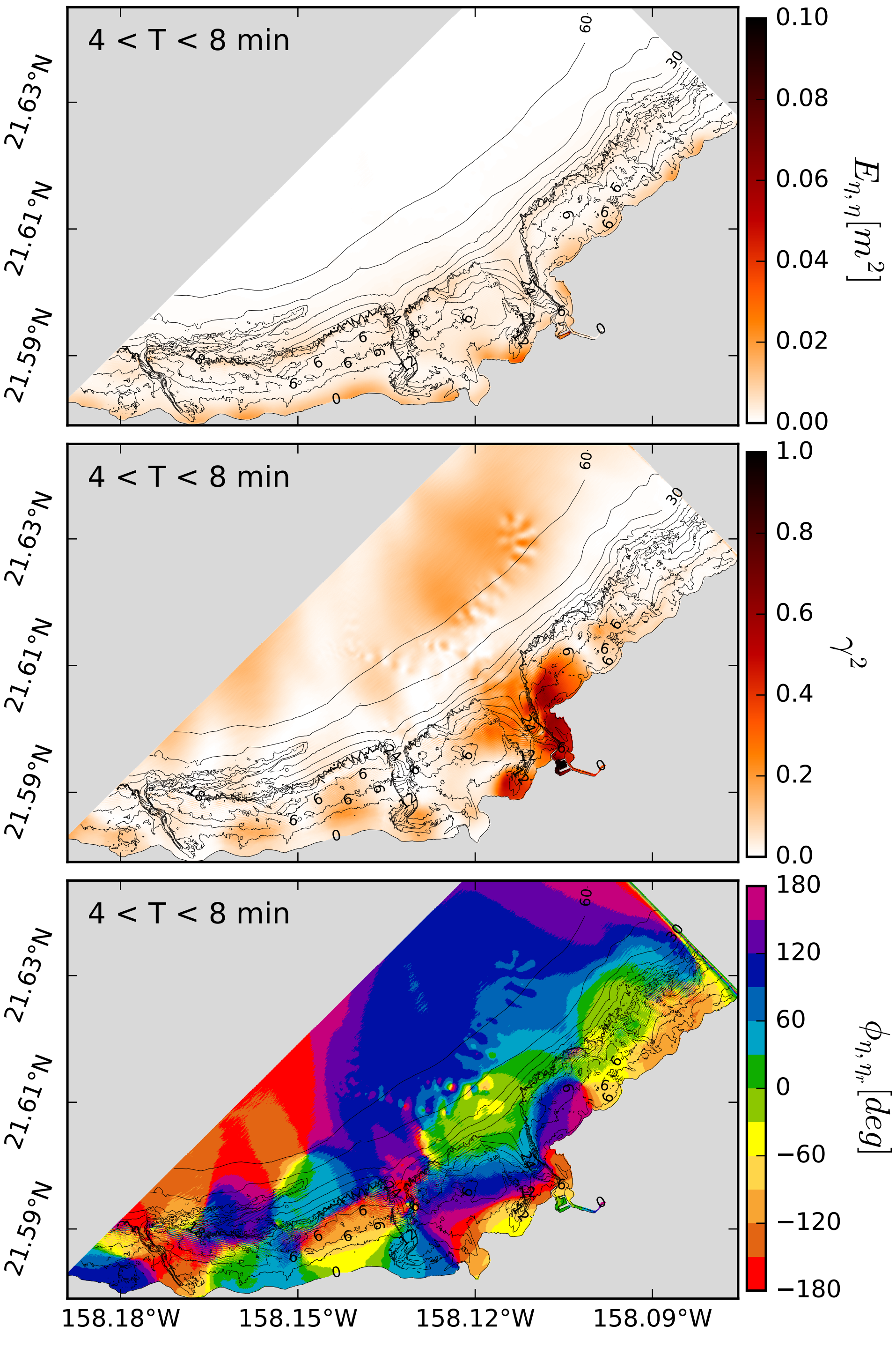

Figure 4.35: Maps of (a) potential energy, (b) coherence amplitude squared, and (c) coherence phase, in the 4-8 min period band, using output from the largest model run with strong SS forcing (run R2).

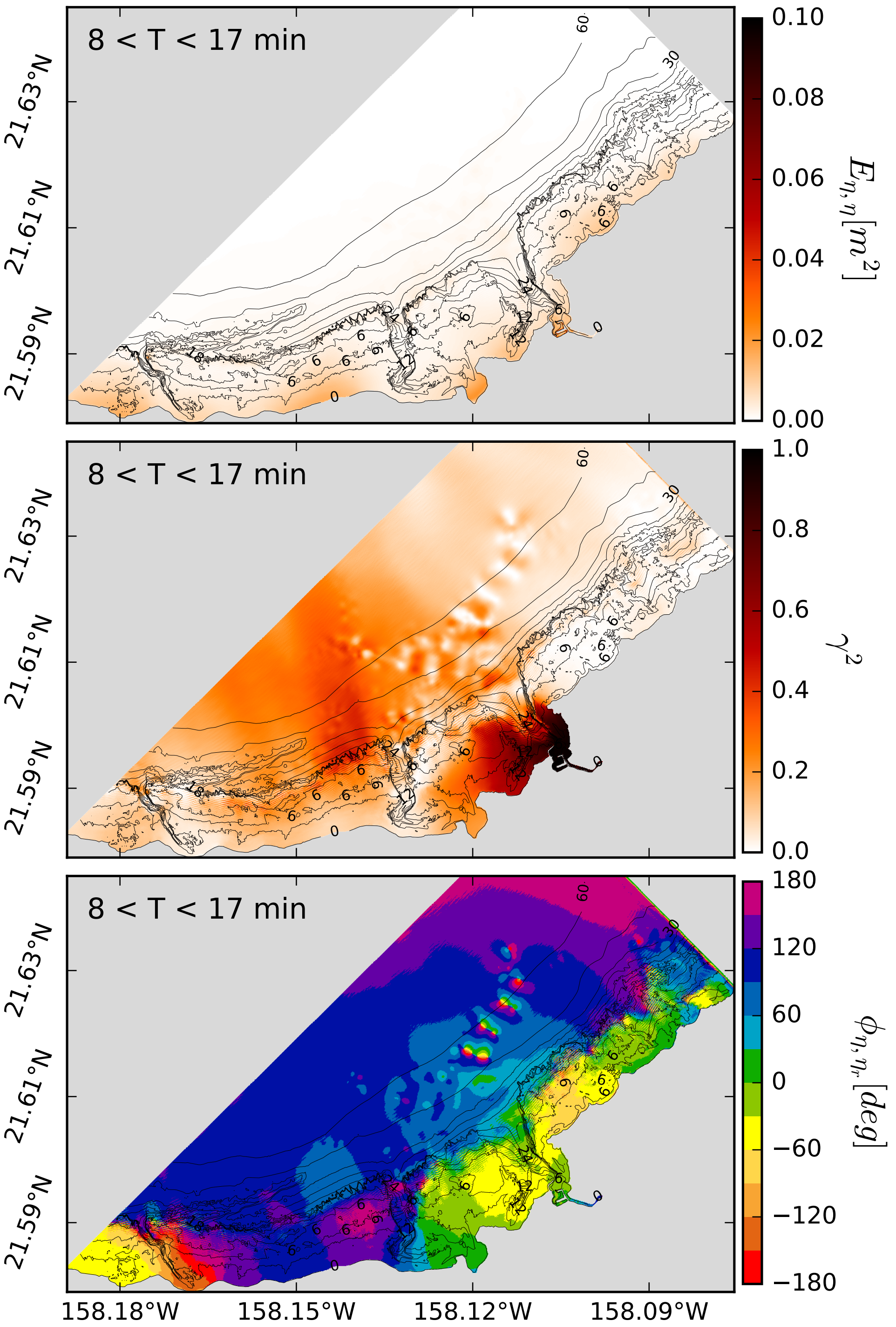

Figure 4.36: Maps of (a) potential energy, (b) coherence amplitude squared, and (c) coherence phase, in the 8-17 min period band, using output from the largest model run with strong SS forcing (run R2).

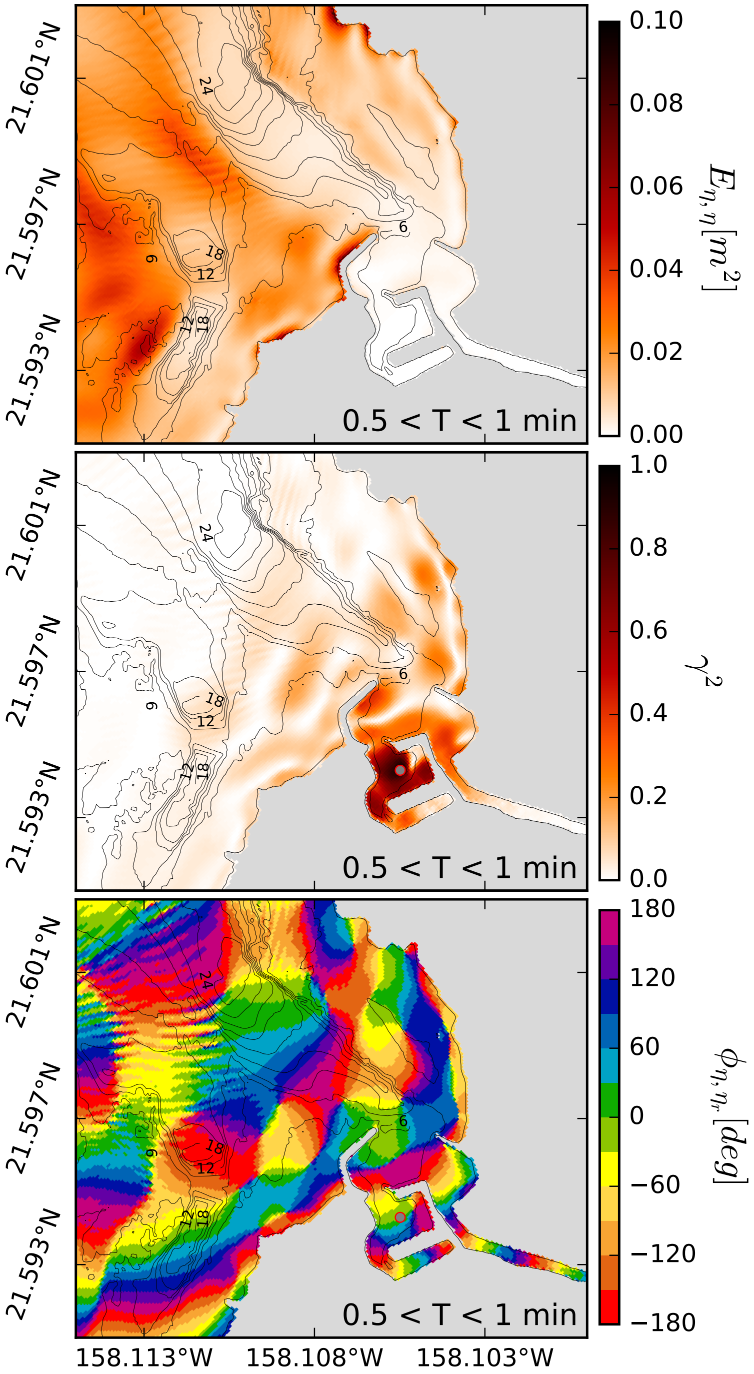

Figure 4.37: Maps of (a) potential energy, (b) coherence amplitude squared, and (c) coherence phase, in the 0.5-1 min period band, using output from the largest model run with strong SS forcing (run R2), focusing on Hale'iwa Hbr. region. Gray circles represent the reference points.

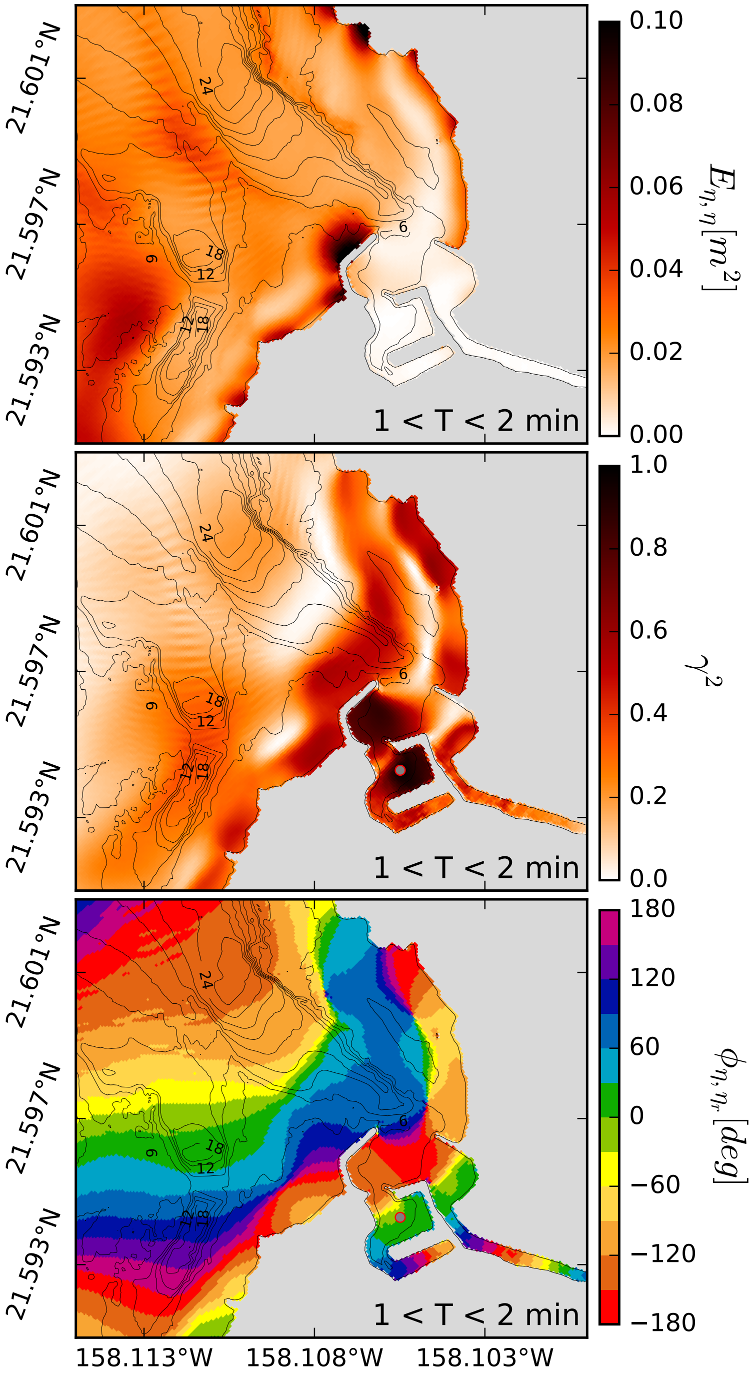

Figure 4.38: Maps of (a) potential energy, (b) coherence amplitude squared, and (c) coherence phase, in the 1-2 min period band, using output from the largest model run with strong SS forcing (run R2), focusing on Hale'iwa Hbr. region. Gray circles represent the reference points.

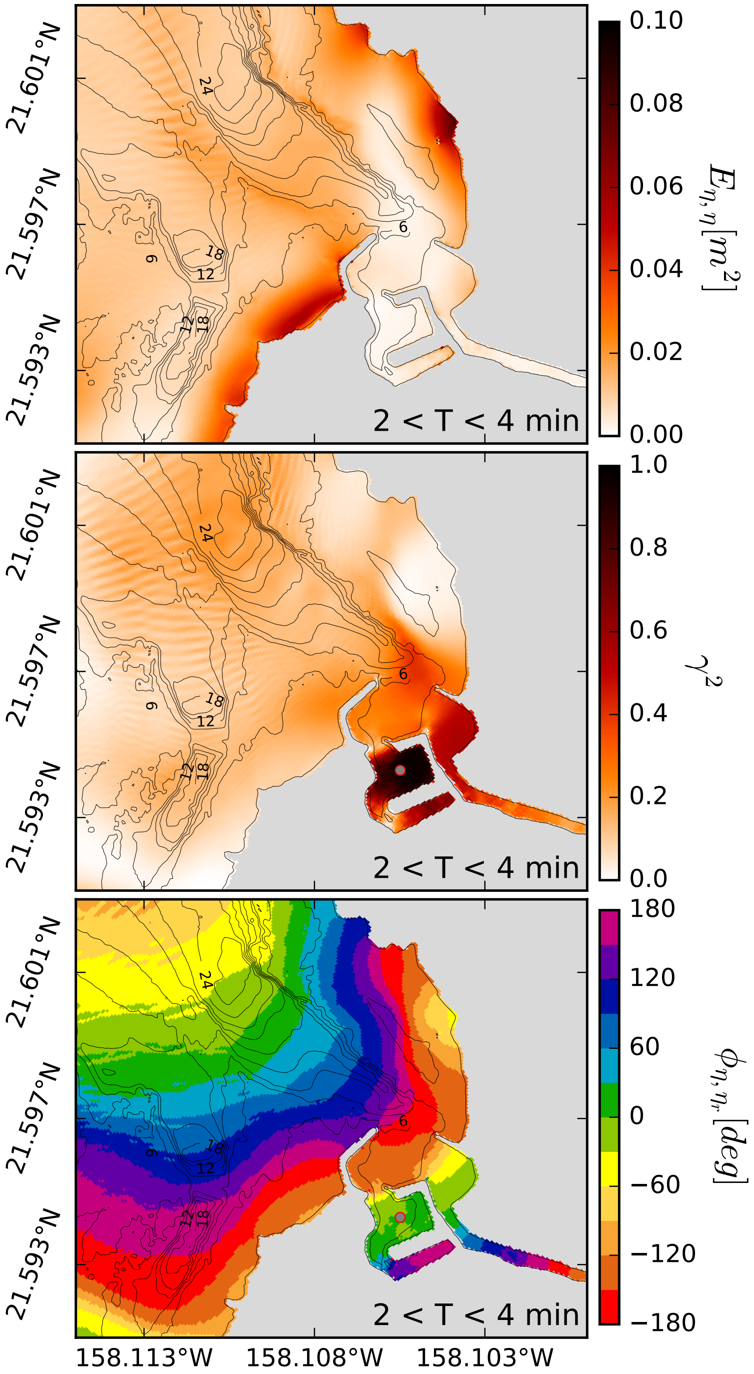

Figure 4.39: Maps of (a) potential energy, (b) coherence amplitude squared, and (c) coherence phase, in the 2-4 min period band, using output from the largest model run with strong SS forcing (run R2), focusing on Hale'iwa Hbr. region. Gray circles represent the reference points.

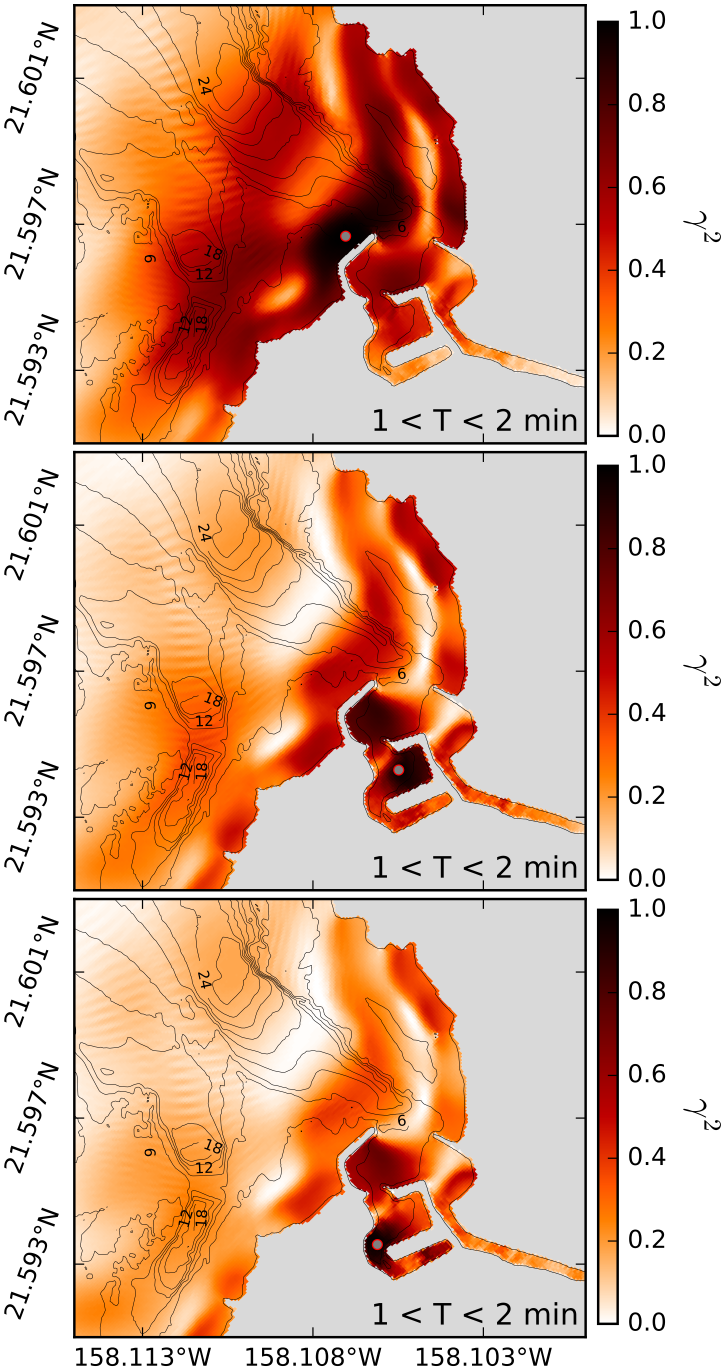

Figure 4.40: Comparison of γ^2 in the 1-2 min band, using different reference points. The reference points are located (a) right outside hbr., (b) main hbr. basin, and (c) southern portion of hbr. Model output is from the largest model run with strong SS forcing (run R2), focusing on Hale'iwa Hbr. region. Gray circles represent the reference points.

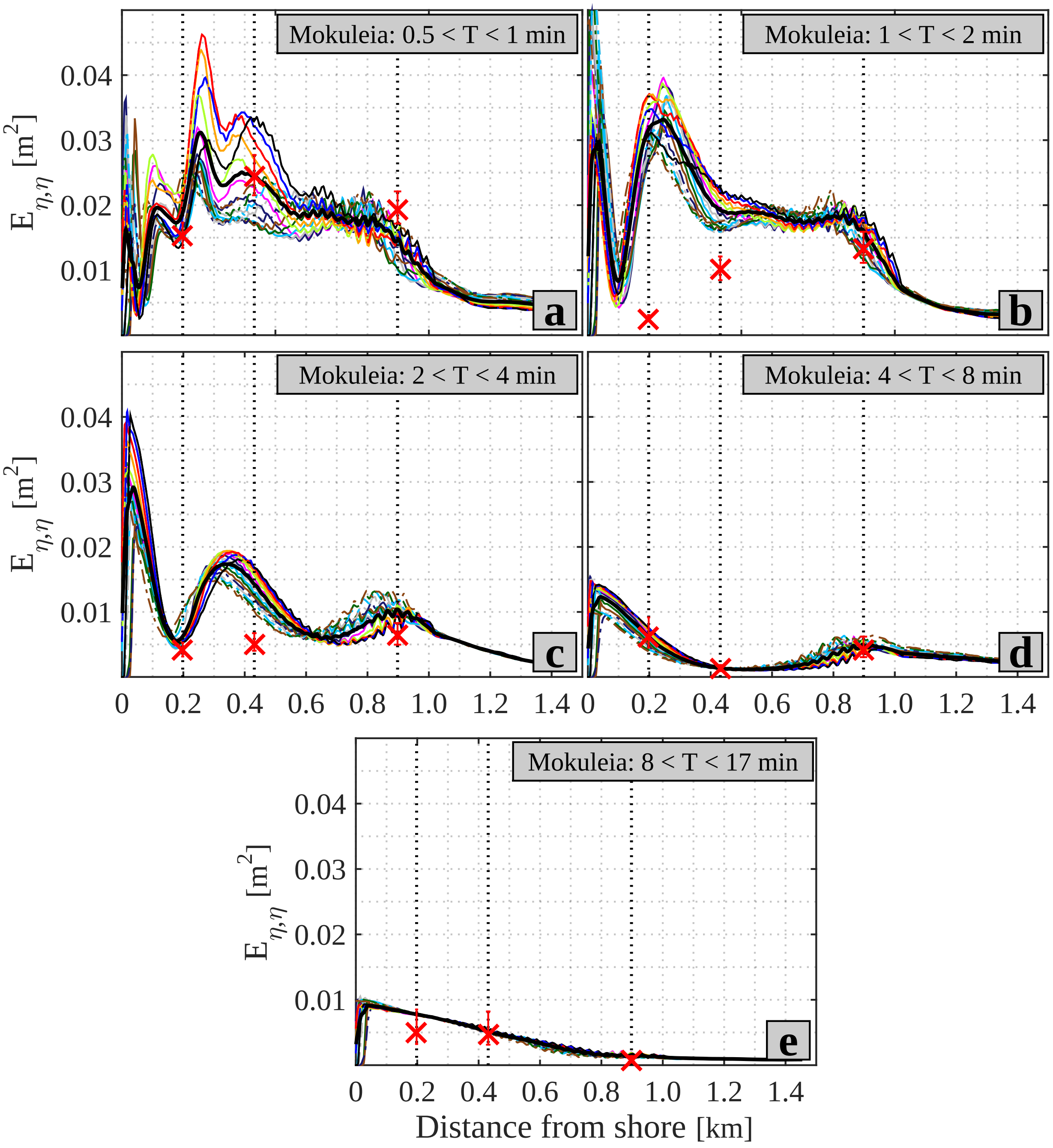

Figure 4.41: Energy vs. distance from shore for (a) 0.5-1, (b) 1-2, (c) 2-4, (d) 4-8, and (e) 8-17 min period bands, for 21 cross-shore lines separated by ∼11m. The thicker black line is the average of all 21 lines. The corresponding observations from depths 2m, 6m, and 12m, at the Mokuleia site, are shown with red crosses. The 95% confidence intervals are shown on the observed points.

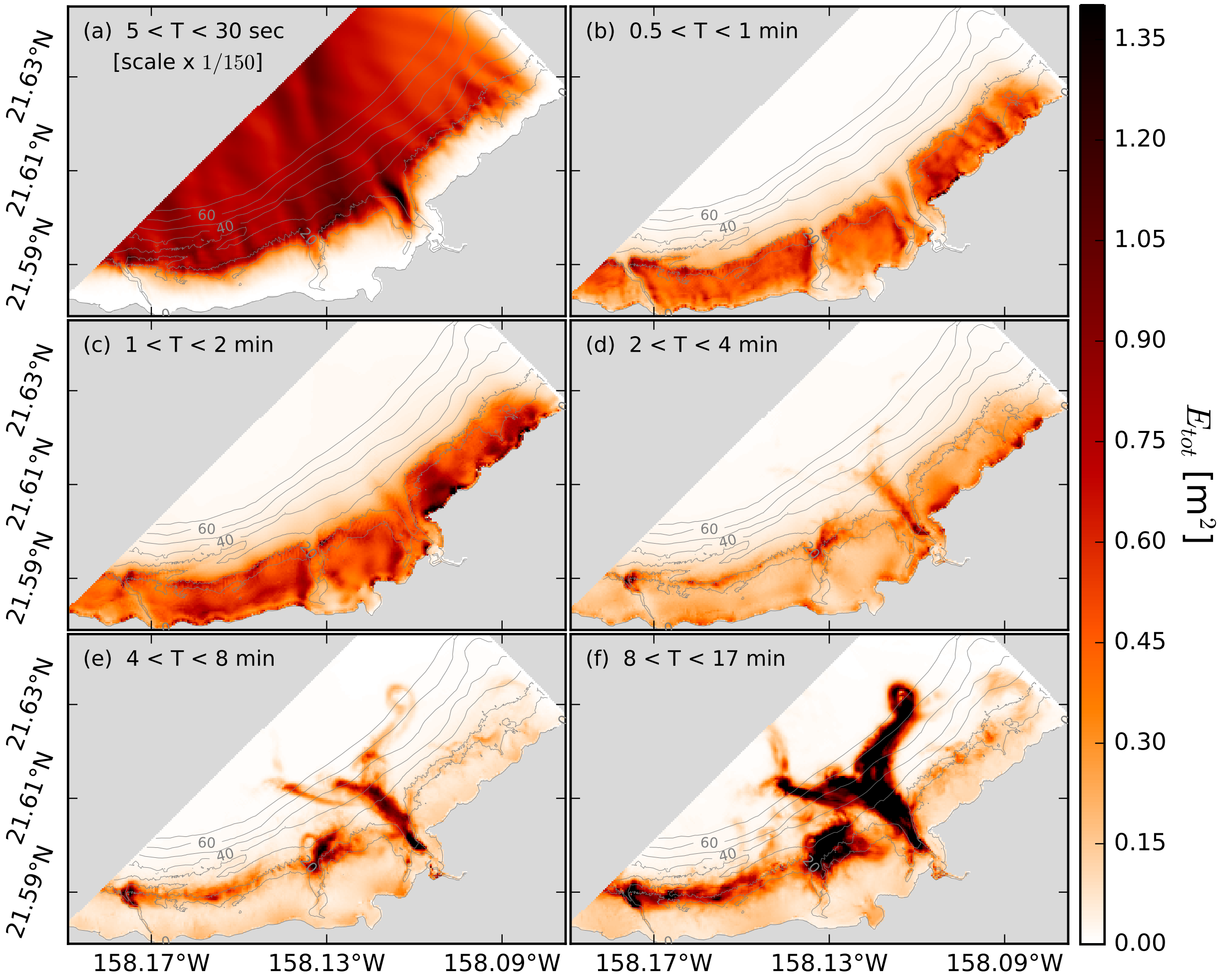

Figure 4.42: Maps of the total (potential + kinetic) energy in the 5-30 sec, 0.5-1, 1-2, 2-4, 4-8, and 8-17 min period bands, using output from the largest model run with strong SS forcing (run R2).

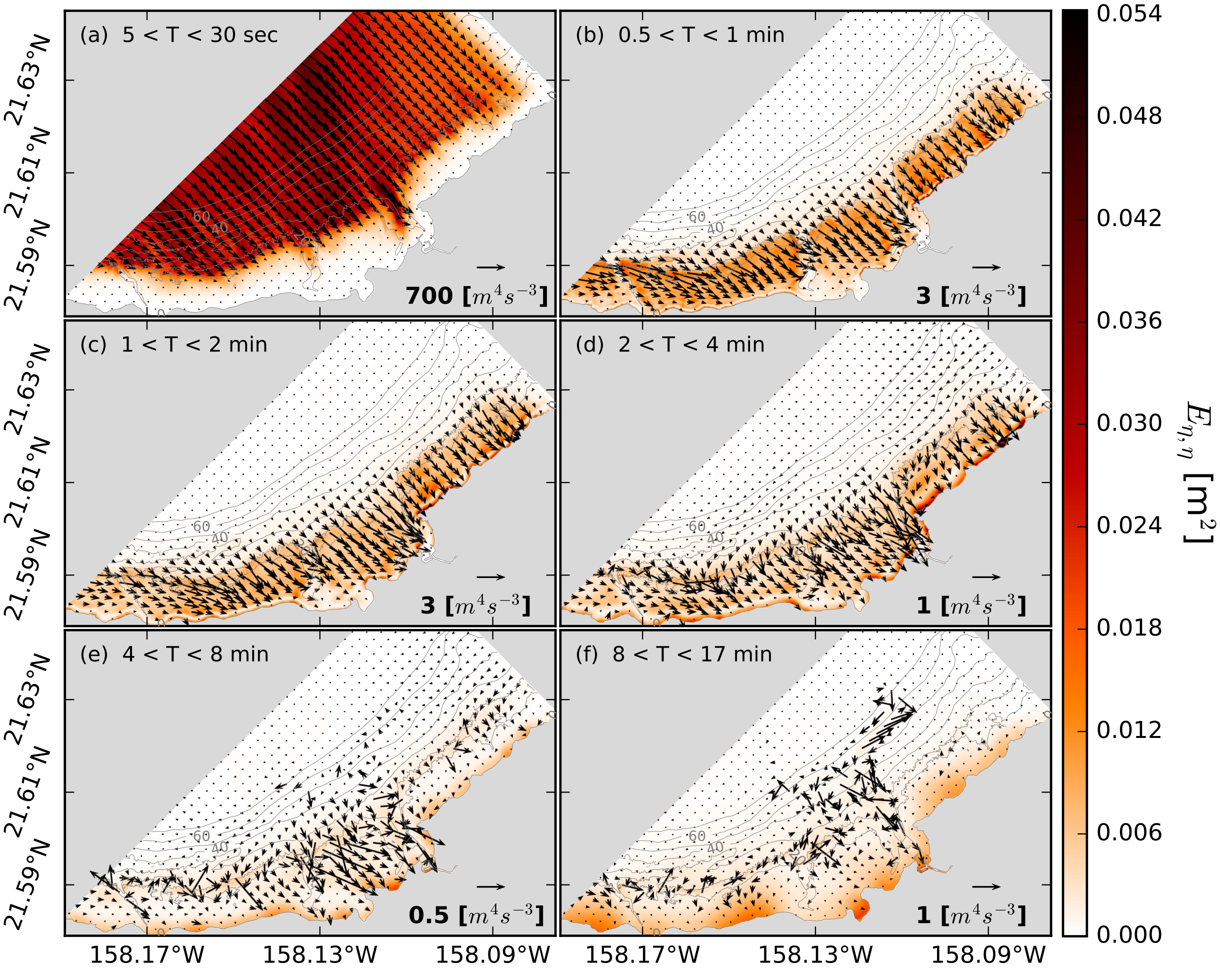

Figure 4.43: Maps of energy flux in the 5-30 sec, 0.5-1, 1-2, 2-4, 4-8, and 8-17 min period bands, using output from the largest model run with strong SS forcing (run R2).

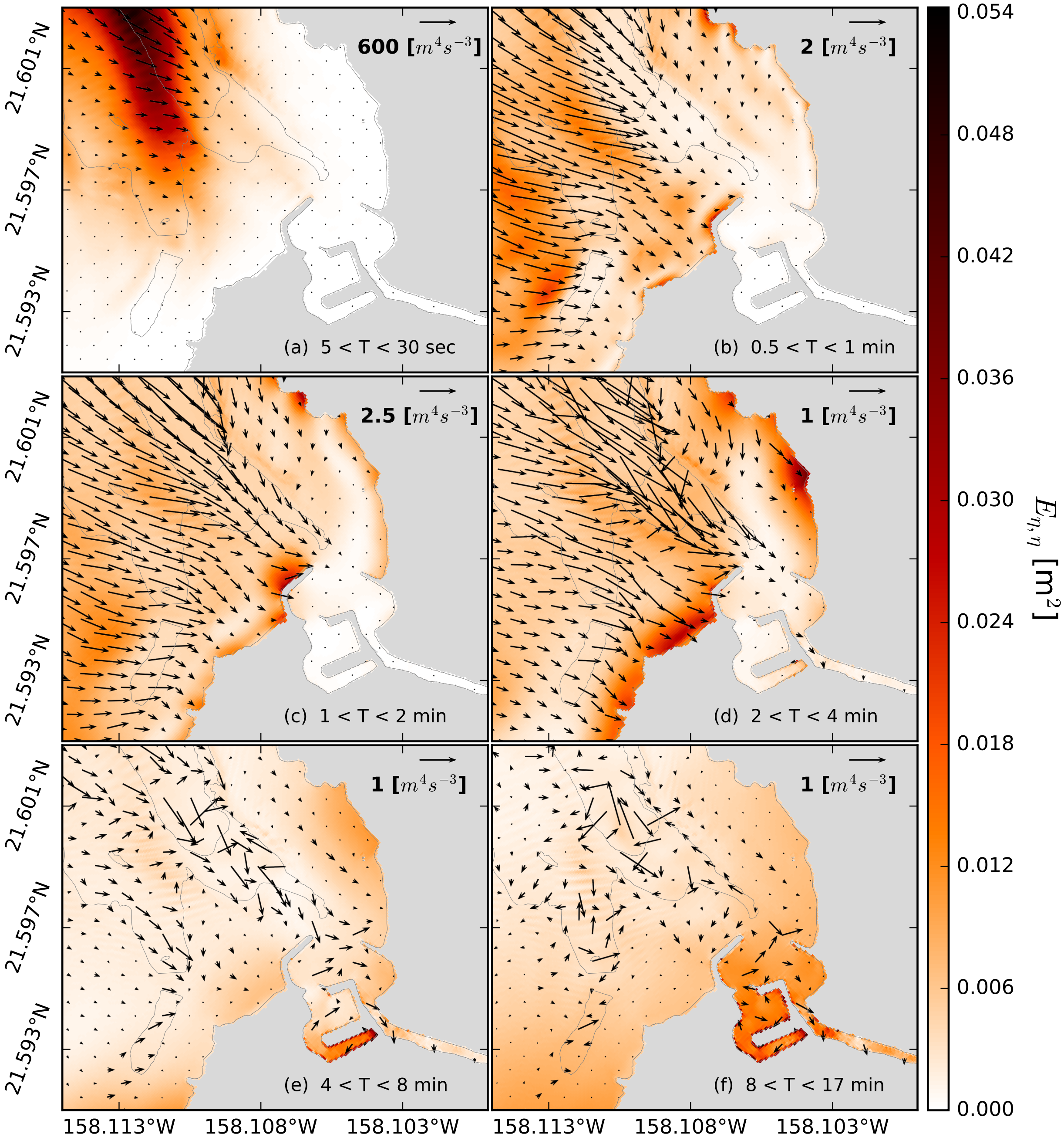

Figure 4.44: Maps of energy flux in the 5-30 sec, 0.5-1, 1-2, 2-4, 4-8, and 8-17 min period bands, using output from the largest model run with strong SS forcing (run R2), focusing on Hale'iwa Harbor and its immediate vicinity.

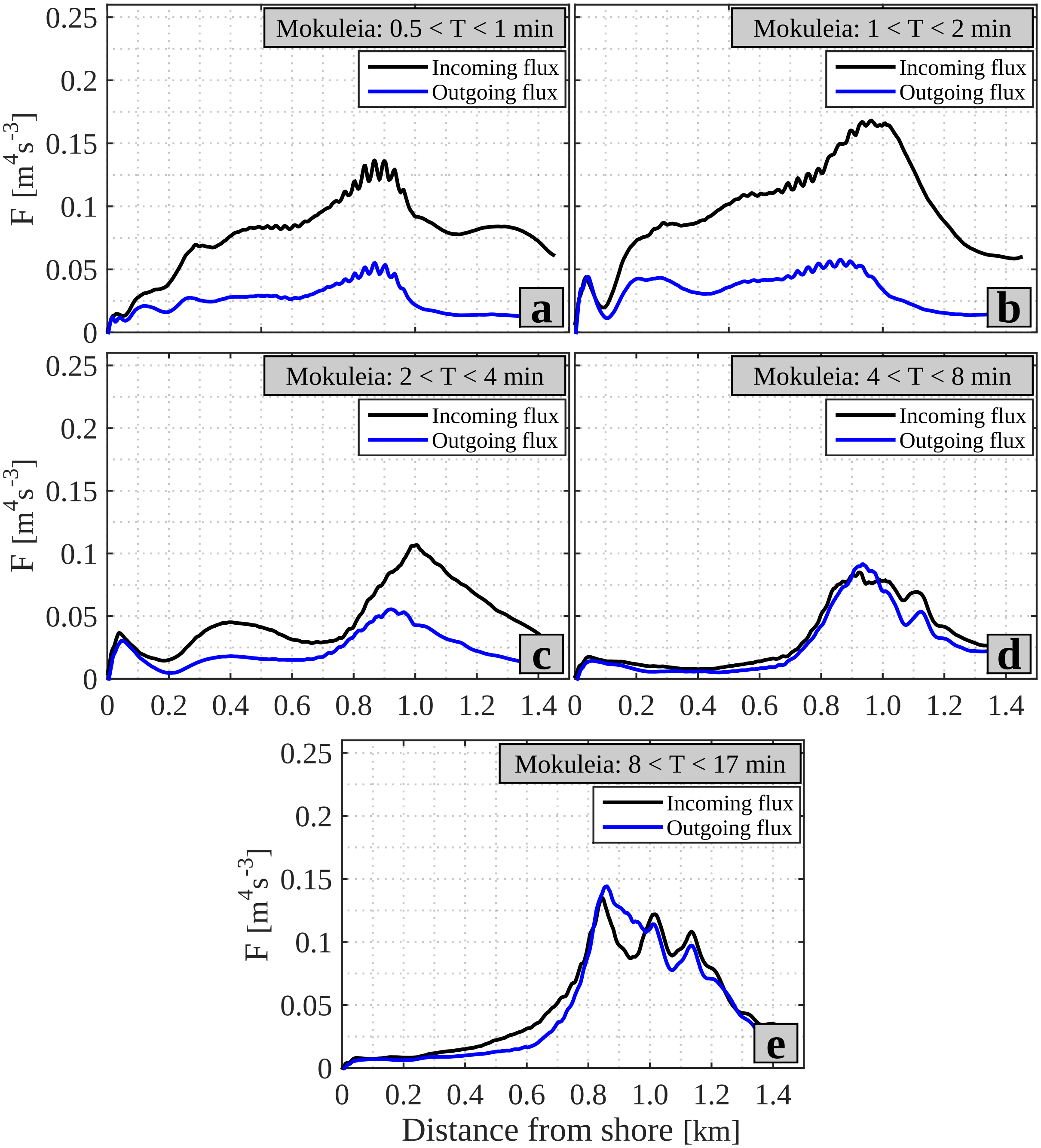

Figure 4.45: Incoming and outgoing energy flux vs. distance from shore at Mokuleia site, for (a) 0.5-1, (b) 1-2, (c) 2-4, (d) 4-8, and (e) 8-17 min period bands, using output from the largest model run with strong SS forcing (run R2).

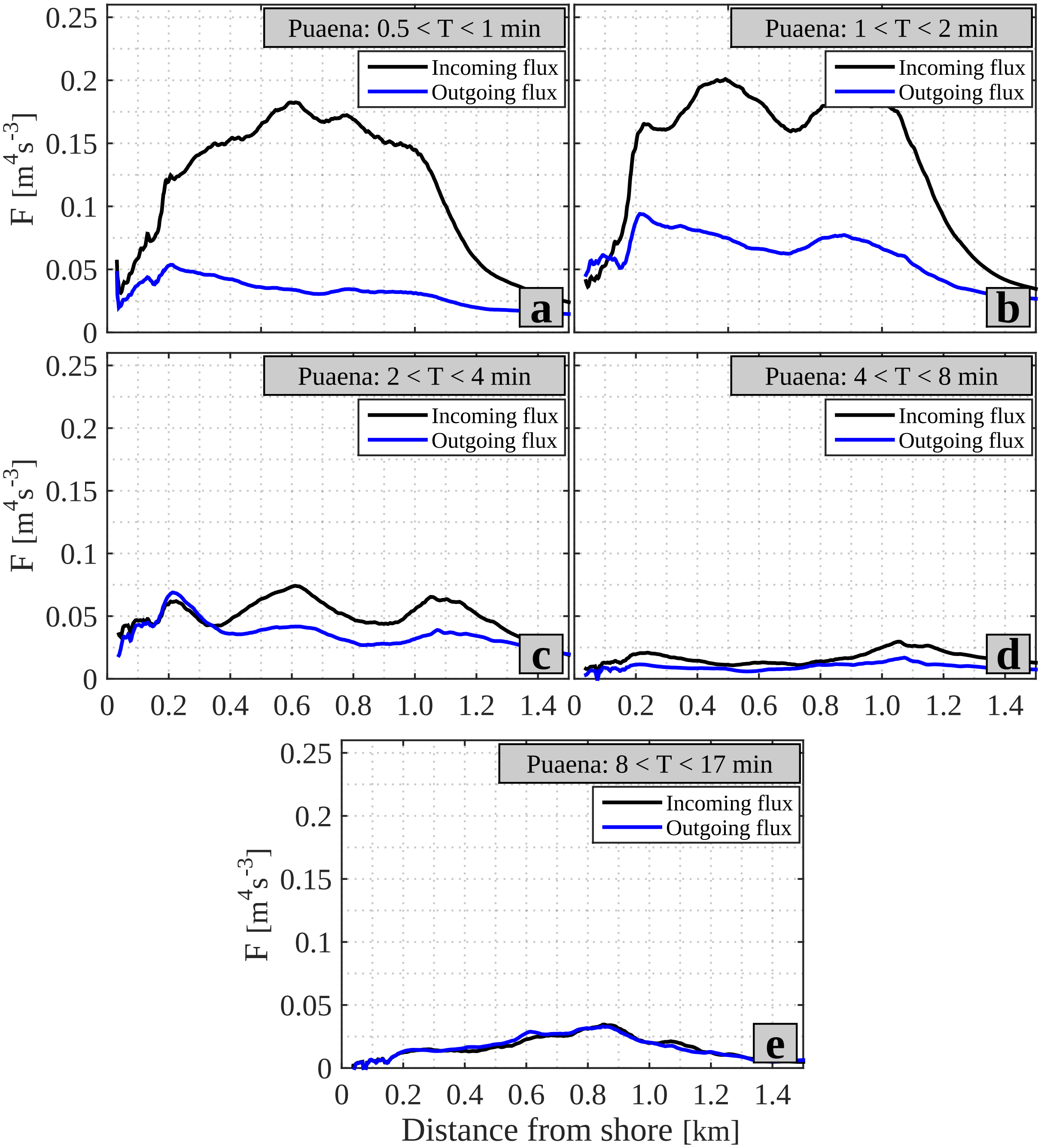

Figure 4.46: Incoming and outgoing energy flux vs. distance from shore at Pua'ena Point site, for (a) 0.5-1, (b) 1-2, (c) 2-4, (d) 4-8, and (e) 4-17 min period bands, using output from the largest model run with strong SS forcing (run R2).

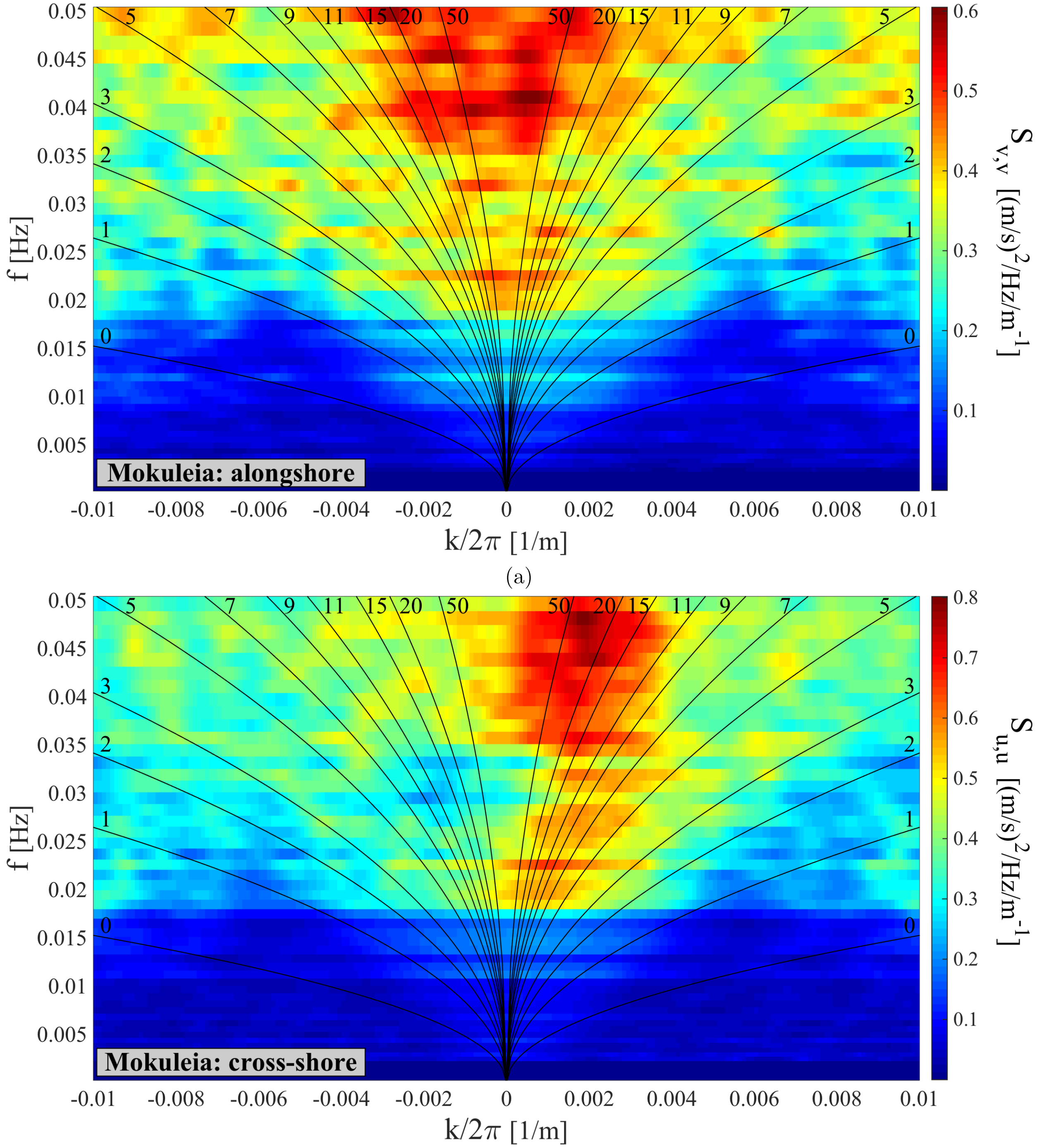

(a)

(b)

Figure 4.47: Frequency-wavenumber PSD of (a) alongshore, and (b) cross-shore, velocity components at Mokuleia alongshore array site, using the MLE method. Superimposed are the theoretical dispersion curves of several modes for the case of a plane beach.

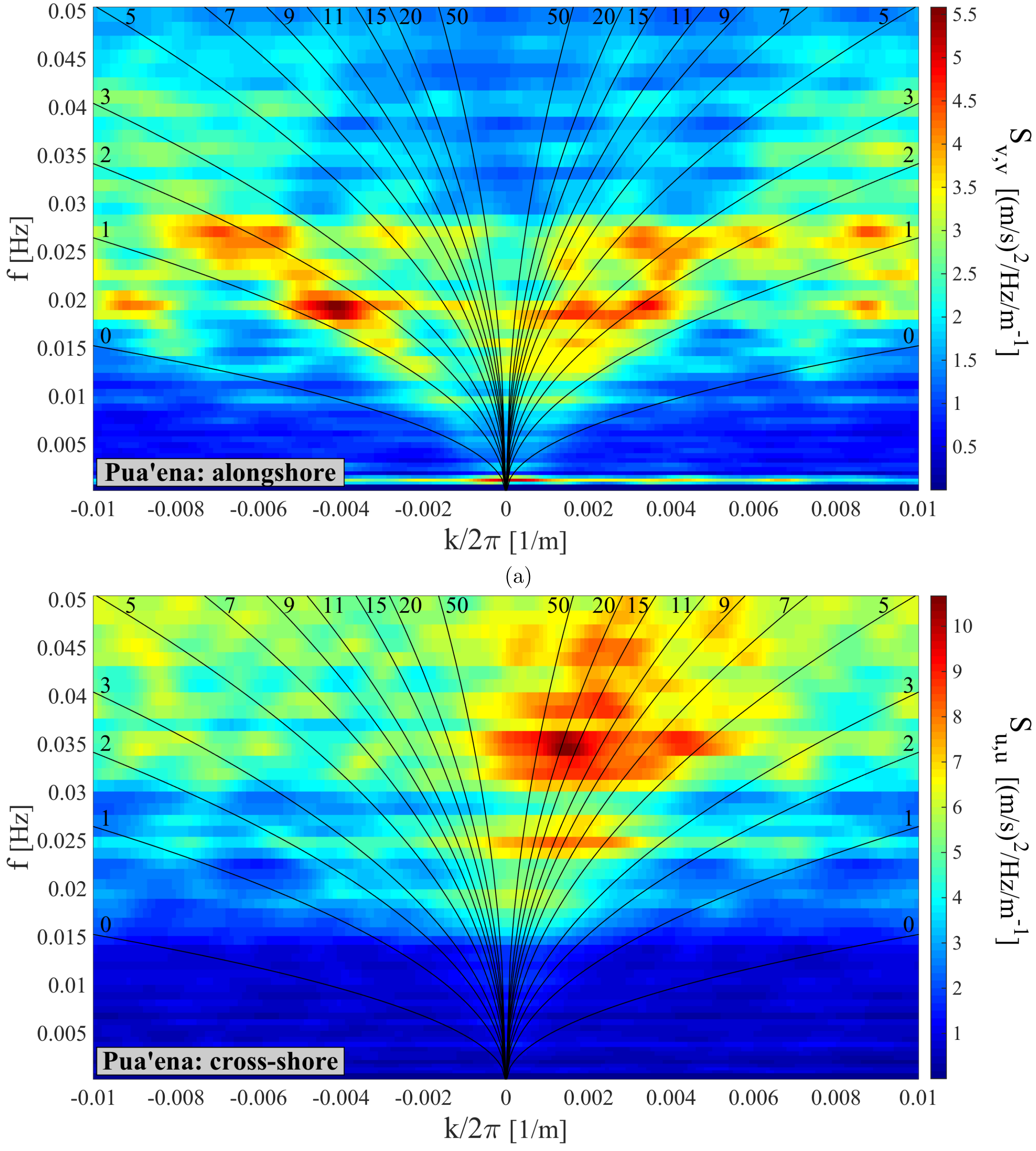

(a)

(b)

Figure 4.48: Frequency-wavenumber PSD of (a) alongshore, and (b) cross-shore, velocity components at Pua'ena Point alongshore array site, using the MLE method. Superimposed are the theoretical dispersion curves of several modes for the case of a plane beach.

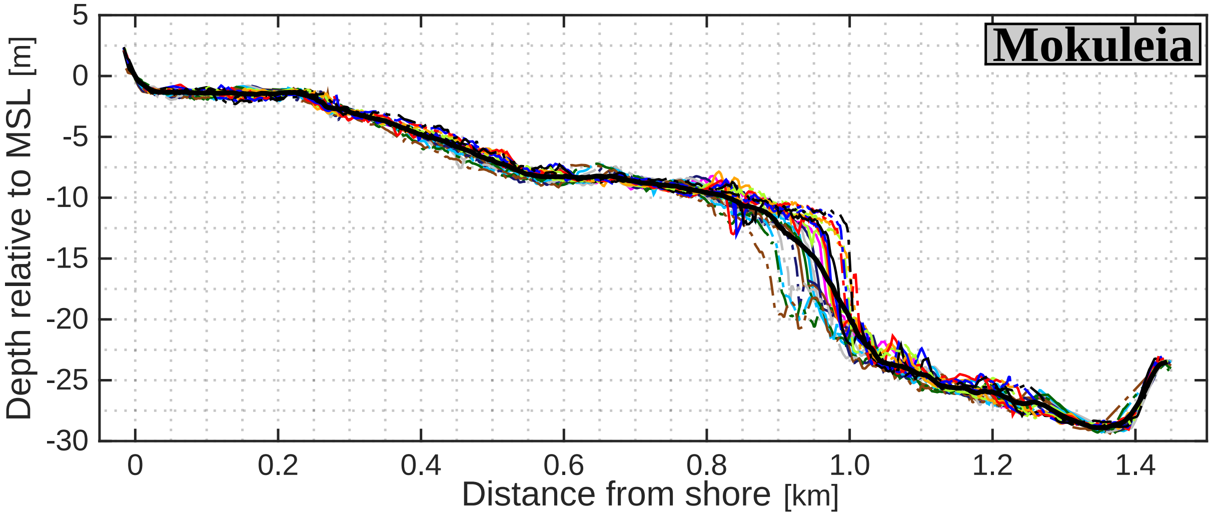

(a)

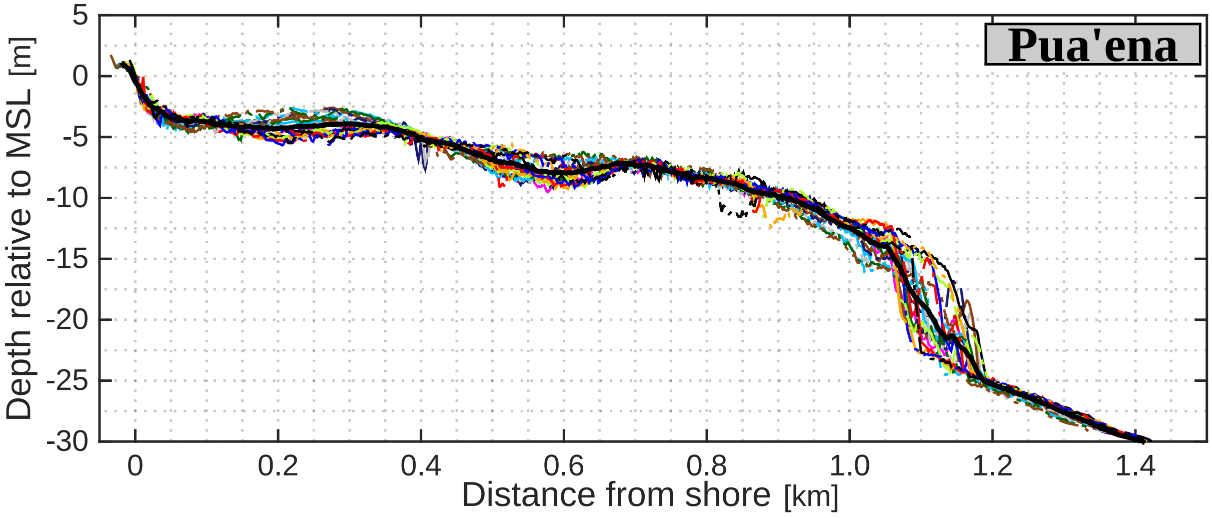

(b)

Figure 4.49: Cross-shore depth profiles relative to MSL vs. distance from the shoreline, at (a) Mokuleia, and (b) Pua'ena Point sites. At each site, there are 21 profiles separated by ~11m in the alongshore, and the thick black curve in each panel is the average profile.

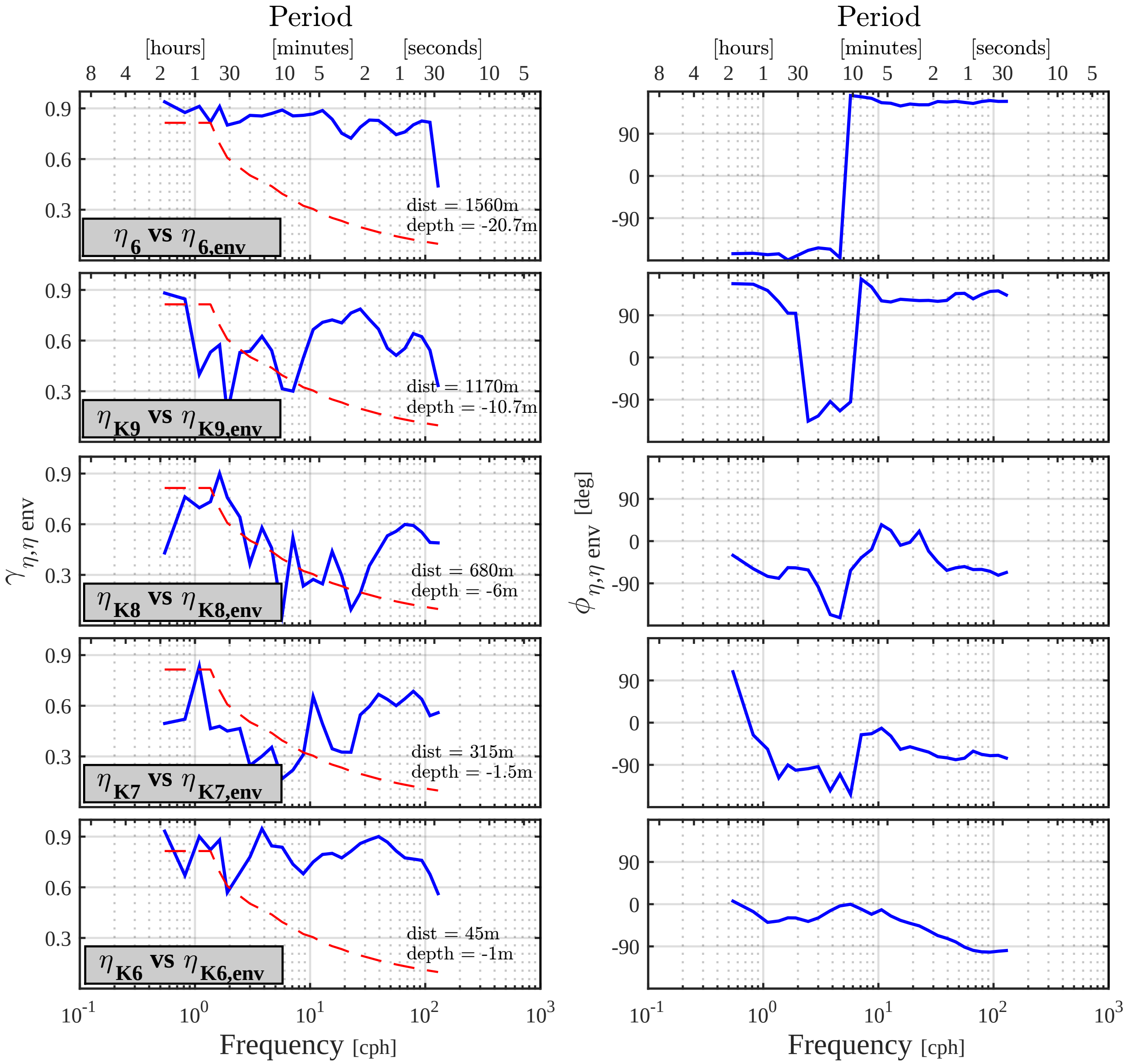

Figure 4.50: Coherence amplitude and phase between η vs. ηenv at Waialua cross-shore array at sites K6-K9 and 6. The red dotted lines in the coherence amplitude plots mark the 95% levels of no significance.

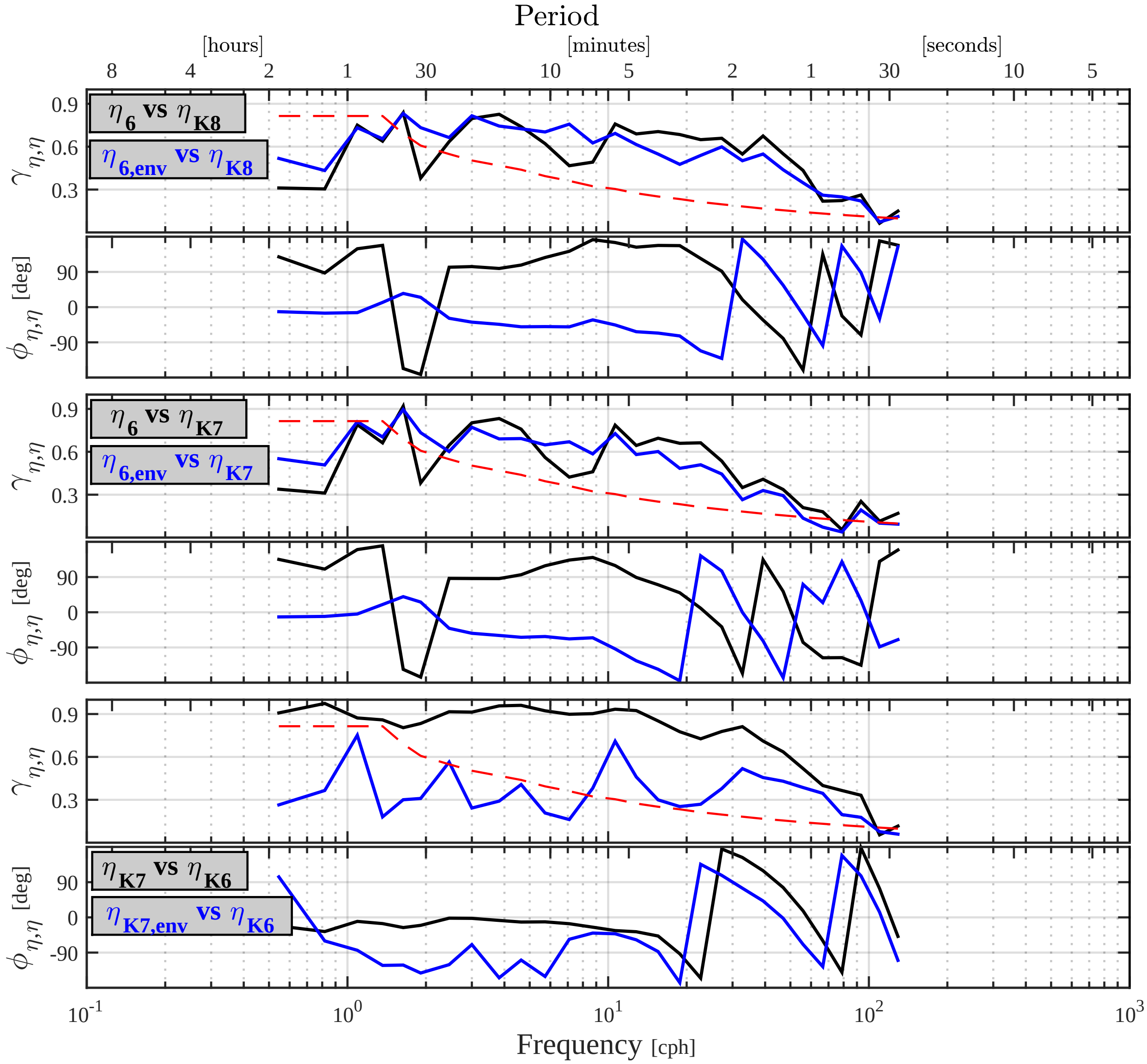

Figure 4.51: Coherence amplitude and phase at Waialua cross-shore array, for: (i) offshore-most η vs. shoreward η (black curves); and, (ii) offshore-most ηenv vs. shoreward η (blue curves). The red dotted lines in the coherence amplitude plots mark the 95% levels of no significance.

CHAPTER 5
CONCLUSIONS

5.1 Summary

The observational results provided us a look at the infragravity (IG) wave field in Hale'iwa Harbor, and at the coast in the vicinity of the harbor. However, our hypotheses of possible energy pathways could not be fully addressed since the observations lacked the spatial and temporal detail necessary to improve our understanding of the dynamics of these waves. For this reason we incorporated a numerical model that helped us address many of the hypotheses, and even opened up new questions.

The observations reveal a long history of large IG oscillations inside Hale'iwa Harbor under tsunami and strong SS forcing. Interestingly, we found that under the right conditions, the harbor's IG response under SS forcing could be very similar to the response under tsunami forcing. Focusing on the harbor's response to SS forcing, we combined the observations with a long-term forecast of offshore SS conditions and generated a SS-driven surge forecast for Hale'iwa Harbor. To determine the relationship between the offshore forcing and harbor IG response, we tested several SS parameters, quantified the errors, and found out that the SS energy flux had the tightest relationship with the harbor IG variability. Since its initial release to the public, the reliability of the forecast has been regularly tested under various large SS events. To date, the forecast SCI levels seem to agree well with the observed SCI levels, enabling us to identify several days in advance potentially dangerous conditions of IG wave activity inside the harbor.

By combining our observational and numerical modeling results, we were able to come up with several conclusions regarding our hypotheses of energy pathways:

1. Both Hale'iwa Harbor and the coast have their own sets of normal modes. The gravest mode of Hale'iwa Harbor appears to lie in the 4-8 min period band, possibly having a period of $\sim$6 min. The coastal modes, on the other hand, have periods as long as

23 min, but some modes have very short periods (e.g., possibly in the 1-2 min period band). As a result, there appears to be some range of frequencies (potentially in the 1∼6 min period band) where an overlap exist between the harbor and coastal modes. Regardless, we find that these harbor/coastal modes are nearly irrelevant for explaining the elevated and uniform spectra that is observed inside the harbor and at the coast.

2. Under strong SS forcing conditions, both the observational and numerical modeling results have provided abundant evidence of bound wave energy outside the SS breaking zone. Within the surf zone, the evidence suggested that the IG wave field is dominated by free waves. At first, we believed that these free waves appear to have been predominantly generated by the time-varying breakpoint mechanism (or some other mechanism that is tied to the wave groupiness), and not the released-bound wave mechanism. However, the high levels of coherence amplitude and corresponding variance explained of bound waves offshore of the surf zone ($\sim 50-80\%$) suggests that the IG wave field within the surf zone could potentially be composed of a significant portion of released-bound waves.

3. At the coast, the observed energy growth analysis reveals dominance of leaky waves within the surf zone, and the numerical modeling evidence points out to freely propagating leaky waves as potentially being the ones dominating the flux of energy at the coast and particularly outside the harbor. We also found evidence of low-mode edge waves at a site on the coast, but it appears to be most energetic at relatively short IG periods (∼45-60 sec).

4. At the coast, we found observational evidence of SS-driven "setup" at Mokuleia site triggering oscillations at IG periods ranging from several minutes to hours. Numerical modeling results from a cross-shore array at Waialua Bay, located much closer to Hale'iwa Harbor (∼1.5 km west of Hale'iwa Harbor), reveal very similar findings. However, these results appear to be valid only for periods shorter than ∼20 min due to limitations that are tied to the size of the domain used by the numerical model.

5. Evidence of island/inter-island wide modes was also found using observations. These observations, however, showed that even under strong SS forcing such a mechanism generates spectral levels that are much lower than the ones observed at the North Shore coast of O'ahu Island, and inside Hale'iwa Harbor.

6. A coherence analysis between two deep-water sites offshore of O'ahu Island provided evidence of free IG waves that potentially originated from the region extending from Oregon to British Columbia (approximate latitudes: $44°N - 53°N$), a result that is in good agreement with the findings of *Aucan and Ardhuin* (2013). Using observations and conservation of energy flux we projected the deep-water spectra that is necessary to generate the observed shallow-water spectra. We found that free IG waves in the 1-20 min that arrive from remote sources could potentially force the harbor at certain IG periods when SS levels are minimal.

The fact that our observations show that the coastal oscillations play a dominant role inside Hale'iwa Harbor, implies that in order to have a good understanding of the dynamics of energetic harbor oscillations we must understand the dynamics at the coast. This is not a necessary a requirement for every harbor, but Hale'iwa Harbor and the complex coastline outside the harbor represent a good example of such a case.

5.2 Future Research

Practical aspect of study:

1. Include analysis of the short IG period band 0.5-2 min.

2. At a relatively late stage, we found a relationship between our SS energy flux parameter and the low frequency mesoscale variability inside the harbor (not shown here). At this point, the mesoscale variability is not incorporated in our forecast, but it could relatively easily be done in the future in order to further improve our forecast.

3. The harbor surge forecast and its validation could be improved if we incorporate real-time sea level and currents observations.

4. The same methodology that was employed here can be applied to other harbors. In particular, in Hawaiian Harbors such as Barbers Point, Kahului, and Hilo, that have a history of strong seiche events, particularly under tsunami forcing. These harbors are larger and also economically more important than Hale'iwa Harbor.

Scientific aspect of study:

1. This study could be contrasted by applying it to a different environment where the shelf is steeper than the one along the north shore and coastal IG oscillations may not be very important. For example, the numerical modeling results of (*Munger and Cheung* 2008) suggest that the west coast of O'ahu Island could potentially be such an environment, and this could mean that the dynamics in Barbers Point region are likely very different than the ones seen in this study.

2. We can use the model output to quantify different terms in the force balance. Such an analysis will improve our understanding of the physical mechanisms.

3. This work has produced some interesting results that were not expected and could be further explored in the future. One such result is the turbulent structure extending offshore from the channel outside of Hale'iwa Harbor. This structure appears at long IG periods (periods longer than ~4 min) and we believe that it results from very large SS forcing conditions generating a return flow in the form of rip currents.

References

Aucan, J., and F. Ardhuin (2013), Infragravity waves in the deep ocean: An upward revision, *Geophysical Research Letters*, *40*(13), 3435–3439.

Baldock, T. (2012), Dissipation of incident forced long waves in the surf zoneimplications for the concept of bound wave release at short wave breaking, *Coastal Engineering*, *60*, 276–285.

Baldock, T., and D. Huntley (2002), Long–wave forcing by the breaking of random gravity waves on a beach, *Proceedings of the Royal Society of London. Series A: Mathematical, Physical and Engineering Sciences*, *458*(2025), 2177–2201.

Baldock, T., D. Huntley, P. Bird, T. O'Hare, and G. Bullock (2000), Breakpoint generated surf beat induced by bichromatic wave groups, *Coastal Engineering*, *39*(2), 213–242.

Baldock, T., P. Manoonvoravong, and K. S. Pham (2010), Sediment transport and beach morphodynamics induced by free long waves, bound long waves and wave groups, *Coastal Engineering*, *57*(10), 898–916.

Becker, J., M. Merrifield, and H. Yoon (2016), Infragravity waves on fringing reefs in the tropical pacific: Dynamic setup, *Journal of Geophysical Research: Oceans.*

Bellotti, G. (2007), Transient response of harbours to long waves under resonance conditions, *Coastal Engineering*, *54*(9), 680–693.

Bellotti, G., and L. Franco (2011), Measurement of long waves at the harbor of marina di carrara, italy, *Ocean Dynamics*, *61*(12), 2051–2059.

Bowen, A., and R. A. Holman (1989), Shear instabilities of the mean longshore current: 1. theory, *Journal of Geophysical Research: Oceans (1978–2012)*, *94*(C12), 18,023–18,030.

Bowen, A. J. (1967), Rip currents, Ph.D. thesis, Wiley Online Library.

Bowen, A. J., and R. T. Guza (1978), Edge waves and surf beat, *Journal of Geophysical Research: Oceans (1978–2012)*, *83*(C4), 1913–1920.

Bowen, A. J., and D. L. Inman (1969), Rip currents: 2. laboratory and field observations, *Journal of Geophysical research*, *74*(23), 5479–5490.

Bowen, A. J., D. Inman, and V. Simmons (1968), Wave set-downand set-up, *Journal of Geophysical Research*, *73*(8), 2569–2577.

Bowers, E. (1977), Harbour resonance due to set-down beneath wave groups, *Journal of Fluid Mechanics*, *79*(01), 71–92.

Bowers, E. (1992), Low frequency waves in intermediate water depths, *Coastal Engineering Proceedings*, *1*(23).

Breaker, L. C., Y.-h. Tseng, and X. Wang (2010), On the natural oscillations of monterey bay: Observations, modeling, and origins, *Progress in Oceanography*, *86*(3), 380–395.

Bretschneider, C. L., H. Krock, E. Nakazaki, and F. Casciano (1986), Roughness of typical hawaiian terrain for tsunami run-up calculations: A users manual, *JKK Look Laboratory Report, University of Hawaii, Honolulu.*

Briggs, M. J., L. S. Lillycrop, G. S. Harkins, E. F. Thompson, and D. R. Green (1994), Physical and numerical model studies of barbers point harbor, oahu, hawaii, *Tech. rep.*, DTIC Document.

Caldwell, P. C., and J. P. Aucan (2007), An empirical method for estimating surf heights from deepwater significant wave heights and peak periods in coastal zones with narrow shelves, steep bottom slopes, and high refraction, *Journal of Coastal Research*, pp. 1237–1244.

Chapman, D. C., and G. S. Giese (1990), A model for the generation of coastal seiches by deep-sea internal waves, *Journal of physical oceanography*, *20*(9), 1459–1467.

Cheung, K. F., Y. Bai, and Y. Yamazaki (2013), Surges around the hawaiian islands from the 2011 tohoku tsunami, *Journal of Geophysical Research: Oceans*, *118*(10), 5703–5719.

Contardo, S., and G. Symonds (2013), Infragravity response to variable wave forcing in the nearshore, *Journal of Geophysical Research: Oceans*, *118*(12), 7095–7106.

Davis, R. E., and L. A. Regier (1977), Methods for estimating directional wave spectra from multi-element arrays, *J. mar. Res.*, *35*(3), 453–478.

De Jong, M., and J. Battjes (2004), Low-frequency sea waves generated by atmospheric convection cells, *Journal of Geophysical Research: Oceans (1978–2012)*, *109*(C1).

De Jong, M., L. Holthuijsen, and J. Battjes (2003), Generation of seiches by cold fronts over the southern north sea, *Journal of Geophysical Research: Oceans (1978–2012)*, *108*(C4).

Dong, G., J. Gao, X. Ma, G. Wang, and Y. Ma (2013), Numerical study of low-frequency waves during harbor resonance, *Ocean Engineering*, *68*, 38–46.

Douyere, Y. M. (2003), Analysis of harbor oscillation with a boussinesq model, Ph.D. thesis, University of Hawaii at Manoa.

Eckart, C. (1951), Surface waves on water of variable depth, *Wave Rep*, *100*, 51–12.

Elgar, S., and R. Guza (1985), Observations of bispectra of shoaling surface gravity waves, *Journal of Fluid Mechanics*, *161*, 425–448.

Elgar, S., T. H. C. Herbers, M. Okihiro, J. Oltman-Shay, and R. T. Guza (1992), Observations of infragravity waves, *Journal of Geophysical Research: Oceans*, *97*(C10), 15,573–15,577, doi:10.1029/92JC01316.

Filloux, J. H., D. Luther, and A. Chave (1991), Long-term seafloor measurement of water pressure: Normal modes and infragravity waves, *Proceedings of the XXth General Assembly IUGG*.

Gallagher, B. (1971), Generation of surf beat by non-linear wave interactions, *Journal of Fluid Mechanics*, *49*(01), 1–20.

Giese, G. S., D. C. Chapman, P. G. Black, and J. A. Fornshell (1990), Causation of large-amplitude coastal seiches on the caribbean coast of puerto rico, *Journal of physical oceanography*, *20*(9), 1449–1458.

Giese, G. S., D. C. Chapman, M. G. Collins, R. Encarnacion, and G. Jacinto (1998), The coupling between harbor seiches at palawan island and sulu sea internal solitons*, *Journal of physical oceanography*, *28*(12), 2418–2426.

González-Marco, D., J. P. Sierra, O. F. de Ybarra, and A. Sánchez-Arcilla (2008), Implications of long waves in harbor management: The gijón port case study, *Ocean & Coastal Management*, *51*(2), 180–201.

Gordon, M. (2006), Tsunami pays brief visit to islands, `http://the.honoluluadvertiser.com/article/2006/Nov/16/ln/FP611160365.html`, online from *Honolulu Advertiser* newspaper; accessed 22 February 2015.

Grimshaw, R. H., and D. C. Chapman (1992), Continental shelf response to forcing by deep-sea internal waves, *Dynamics of atmospheres and oceans*, *16*(5), 355–378.

Guedes, R. M., P. J. McComb, D. L. Johnson, and S. Gardiner (2015), Boussinesq modeling of the long wave response in port geraldton under existing and modified harbor layouts, manuscript, conference paper.

Haller, M. C., U. Putrevu, J. Oltman-Shay, and R. A. Dalrymple (1999), Wave group forcing of low frequency surf zone motion, *Coastal Engineering Journal*, *41*(02), 121–136.

Hasselmann, K. (1962), On the non-linear energy transfer in a gravity-wave spectrum, *J. Fluid Mech*, *12*(481-500), 15.

Heath, R. (1974), Sea level oscillations in wellington harbour, *New Zealand journal of marine and freshwater research*, *8*(2), 403–414.

Herbers, T., S. Elgar, R. Guza, and W. O'Reilly (1992), Infragravity-frequency (0.005-0.05 hz) motions on the shelf, *Coastal Engineering Proceedings*, *1*(23).

Herbers, T., S. Elgar, and R. Guza (1994), Infragravity-frequency (0.005-0.05 hz) motions on the shelf. part i: Forced waves, *Journal of Physical Oceanography*, *24*(5), 917–927.

Herbers, T., S. Elgar, and R. Guza (1995a), Generation and propagation of infragravity waves, *Journal of Geophysical Research: Oceans (1978–2012)*, *100*(C12), 24,863–24,872.

Herbers, T., S. Elgar, R. Guza, and W. O'Reilly (1995b), Infragravity-frequency (0.005-0.05 hz) motions on the shelf. part ii: Free waves, *Journal of physical oceanography*, *25*(6), 1063–1079.

Hughes, S. A. (1984), The tma shallow-water spectrum description and applications, *Tech. rep.*, DTIC Document.

Huntley, D. (1976), Long-period waves on a natural beach, *Journal of Geophysical Research*, *81*(36), 6441–6449.

Huntley, D. A., and C. S. Kim (1984), Is surf beat forced or free?, *Coastal Engineering Proceedings*, *1*(19).

Janssen, T., J. Battjes, and A. Van Dongeren (2003), Long waves induced by short-wave groups over a sloping bottom, *Journal of Geophysical Research: Oceans (1978–2012)*, *108*(C8).

Johnson, D., P. McComb, et al. (2011), Modelling long wave generation and propagation around and within ports.

Kostense, J. (1984), Measurements of surf beat and set-down beneath wave groups, *Coastal Engineering Proceedings*, *1*(19).

Leone, D. (2006), Tsunami alert passes after quake near japan, `http://archives.starbulletin.com/2006/11/16/news/story01.html`, online from *Star Bulletin* newspaper; accessed 22 February 2015.

Lippmann, T., R. A. Holman, and A. Bowen (1997), Generation of edge waves in shallow water, *Journal of Geophysical Research: Oceans (1978–2012)*, *102*(C4), 8663–8679.

List, J. H. (1992), A model for the generation of two-dimensional surf beat, *Journal of Geophysical Research: Oceans (1978–2012)*, *97*(C4), 5623–5635.

Longuet-Higgins, M. S., and R. Stewart (1962), Radiation stress and mass transport in gravity waves, with application to surf beats, *Journal of Fluid Mechanics*, *13*(04), 481–504.

Longuet-Higgins, M. S., and R. Stewart (1964), Radiation stresses in water waves; a physical discussion, with applications, in *Deep Sea Research and Oceanographic Abstracts*, vol. 11, pp. 529–562, Elsevier.

Lopez, M., M. Veigas, S. Astariz, A. Castro, and G. Iglesias (2014), Long waves and artificial neural networks, *Coastal Engineering Proceedings*, *1*(34), currents–31.

Luther, D. S., S. Sweet, R. Whitmire, B. J. Kilonsky, and H. Dail (1998), Archive of rapidly-sampled hawaiian sea level (arshsl): Contribution to the "early detection and forecast of tsunamis" project at the pacific marine environmental laboratory (pmel), `http://ilikai.soest.hawaii.edu/arshsl/techrept/arshsl.`, accessed 7 July 2015.

Luther, D. S., A. D. Chave, and S. C. Webb (2014), Pelagic infragravity waves forced by tidal non-linear interactions, aGU Ocean Sciences Meeting, February 23-28. Abstract ID: 15452; oral.

Masselink, G. (1995), Group bound long waves as a source of infragravity energy in the surf zone, *Continental Shelf Research*, *15*(13), 1525–1547.

McComb, P. J., D. L. Johnson, B. J. Beamsley, et al. (2009), Numerical study of options to reduce swell and long wave penetration at port geraldton, *Coasts and Ports 2009: In a Dynamic Environment*, p. 490.

McComb, P. J., S. Thiebaut, and R. M. Guedes (2015), Measured long wave spectra at port geraldton, open access article.

Middleton, J. H., M. L. Cahill, and W. W. Hsieh (1987), Edge waves on the sydney coast, *Journal of Geophysical Research: Oceans (1978–2012)*, *92*(C9), 9487–9493.

Molin, B. (1982), *On the generation of long-period second-order free-waves due to changes in the bottom profile*, Ship Research Institute.

Morison, M. L., and J. Imberger (1992), Water-level oscillations in esperance harbour, *Journal of waterway, port, coastal, and ocean engineering*, *118*(4), 352–367.

Munger, S., and K. F. Cheung (2008), Resonance in hawaii waters from the 2006 kuril islands tsunami, *Geophysical Research Letters*, *35*(7).

Munk, W. (1949), Surf beats, *Transactions, American Geophysical Union*, *30*, 849–854.

Munk, W., F. Snodgrass, and F. Gilbert (1964), Long waves on the continental shelf: an experiment to separate trapped and leaky modes, *Journal of Fluid Mechanics*, *20*(04), 529–554.

Nakaso, D., and M. Vorsino (2011), Economic damage from isle tsunami spreads, `http://www.staradvertiser.com/news/20110315_Economic_damage_from_isle_tsunami_spreads.html`, online from *Star Advertiser* newspaper; accessed 22 February 2015.

Okihiro, M., and R. Guza (1996), Observations of seiche forcing and amplification in three small harbors, *Journal of waterway, port, coastal, and ocean engineering*, *122*(5), 232–238.

Okihiro, M., R. Guza, and R. Seymour (1992), Bound infragravity waves, *Journal of Geophysical Research: Oceans (1978–2012)*, *97*(C7), 11,453–11,469.

Okihiro, M., R. Guza, and R. Seymour (1993), Excitation of seiche observed in a small harbor, *Journal of Geophysical Research: Oceans (1978–2012)*, *98*(C10), 18,201–18,211.

Oltman-Shay, J., and R. Guza (1987), Infragravity edge wave observations on two california beaches, *Journal of Physical Oceanography*, *17*(5), 644–663.

Oltman-Shay, J., P. Howd, and W. Birkemeier (1989), Shear instabilities of the mean longshore current: 2. field observations, *Journal of Geophysical Research: Oceans (1978–2012)*, *94*(C12), 18,031–18,042.

Pang, G. Y., and D. Nakaso (2011), Damage comes into focus, `http://www.staradvertiser.com/news/20110313_Damage_comes_into_focus.html`, online from *Star Advertiser* newspaper; accessed 22 February 2015.

Park, J., J. MacMahan, W. V. Sweet, and K. Kotun (2016), Continuous seiche in bays and harbors, *Ocean Sci*, *12*, 355–368.

Péquignet, A. C. N., J. M. Becker, M. A. Merrifield, and J. Aucan (2009), Forcing of resonant modes on a fringing reef during tropical storm man-yi, *Geophysical Research Letters*, *36*(3).

Péquignet, A.-C. N., J. M. Becker, and M. A. Merrifield (2014), Energy transfer between wind waves and low-frequency oscillations on a fringing reef, ipan, guam, *Journal of Geophysical Research: Oceans*, *119*(10), 6709–6724.

Rabinovich, A. B. (2009), Seiches and harbour oscillations, *Handbook of coastal and ocean engineering*, pp. 193–236.

Roeber, V., and K. F. Cheung (2012), Boussinesq-type model for energetic breaking waves in fringing reef environments, *Coastal Engineering*, *70*, 1–20.

Roeber, V., Y. Yamazaki, and K. F. Cheung (2010), Resonance and impact of the 2009 samoa tsunami around tutuila, american samoa, *Geophysical Research Letters*, *37*(21).

Ruessink, B. (1998), Bound and free infragravity waves in the nearshore zone under breaking and nonbreaking conditions, *Journal of Geophysical Research: Oceans (1978–2012)*, *103*(C6), 12,795–12,805.

Schäffer, H. A. (1993), Infragravity waves induced by short-wave groups, *Journal of Fluid Mechanics*, *247*, 551–588.

Sheremet, A., R. Guza, S. Elgar, and T. Herbers (2002), Observations of nearshore infragravity waves: Seaward and shoreward propagating components, *Journal of Geophysical Research: Oceans (1978–2012)*, *107*(C8), 10–1.

Shrira, V., V. Voronovich, and N. Kozhelupova (1997), Explosive instability of vorticity waves, *Journal of physical oceanography*, *27*(4), 542–554.

Symonds, G., D. A. Huntley, and A. J. Bowen (1982), Two-dimensional surf beat: Long wave generation by a time-varying breakpoint, *Journal of Geophysical Research: Oceans (1978–2012)*, *87*(C1), 492–498.

Thompson, E. F., L. L. Hadley, W. A. Brandon, D. D. McGehee, and J. M. Hubertz (1996), Wave response of kahului harbor, maui, hawaii., *Tech. rep.*, DTIC Document.

Thompson, R. O. (1979), Coherence significance levels, *Journal of the Atmospheric Sciences*, *36*(10), 2020–2021.

Thomson, R. E., and W. J. Emery (2014), *Data analysis methods in physical oceanography*, Newnes.

Thornton, E. B., and R. Guza (1982), Energy saturation and phase speeds measured on a natural beach, *Journal of Geophysical Research: Oceans (1978–2012)*, *87*(C12), 9499–9508.

Thotagamuwage, D. T., and C. B. Pattiaratchi (2014a), Observations of infragravity period oscillations in a small marina, *Ocean Engineering*, *88*, 435–445.

Thotagamuwage, D. T., and C. B. Pattiaratchi (2014b), Influence of offshore topography on infragravity period oscillations in two rocks marina, western australia, *Coastal Engineering*, *91*, 220–230.

Tucker, M. (1950), Surf beats: sea waves of 1 to 5 min. period, *Proceedings of the Royal Society of London. Series A. Mathematical and Physical Sciences*, *202*(1071), 565–573.

Ursell, F. (1952), Edge waves on a sloping beach, *Proceedings of the royal society of London. Series A. Mathematical and Physical Sciences*, *214*(1116), 79–97.

Van Giffen, I. (2003), Long wave case study for barbers point harbour, hawaii, Ph.D. thesis, TU Delft, Delft University of Technology.

Walden, A. (1986), Estimating confidence intervals for the gain and phase of frequency response functions, *Geophysical Journal International*, *87*(2), 519–537.

Webb, S., and C. Cox (1986), Observations and modeling of seafloor microseisms, *Journal of Geophysical Research: Solid Earth (1978–2012)*, *91*(B7), 7343–7358.

Webb, S. C., X. Zhang, and W. Crawford (1991), Infragravity waves in the deep ocean, *Journal of Geophysical Research: Oceans (1978–2012)*, *96*(C2), 2723–2736.

Wessel, P., and W. H. Smith (1991), Free software helps map and display data, *Eos, Transactions American Geophysical Union*, *72*(41), 441–446.

Wilson, B. W. (1971), Tsunami-responses of san pedro bay and shelf, ca, *Journal of the Waterways, Harbors and Coastal Engineering Division*, *97*(2), 239–258.

Woo, S.-B., and P. L.-F. Liu (2004), Finite-element model for modified boussinesq equations. ii: Applications to nonlinear harbor oscillations, *Journal of waterway, port, coastal, and ocean engineering*, *130*(1), 17–28.

Wright, L., R. Guza, and A. Short (1982), Dynamics of a high-energy dissipative surf zone, *Marine Geology*, *45*(1), 41–62.

Wyrtki, K., and G. Meyers (1976), The trade wind field over the pacific ocean, *Journal of Applied Meteorology*, *15*(7), 698–704.

Yamazaki, Y., Z. Kowalik, and K. F. Cheung (2009), Depth-integrated, non-hydrostatic model for wave breaking and run-up, *International Journal for Numerical Methods in Fluids*, *61*(5), 473–497.